



The University of  
**Nottingham**

UNITED KINGDOM · CHINA · MALAYSIA

## Chowdhury, Muhammad Enamul Hoque (2014) Simultaneous EEG-fMRI : novel methods for EEG artefacts reduction at source. PhD thesis, University of Nottingham.

### **Access from the University of Nottingham repository:**

[http://eprints.nottingham.ac.uk/14297/1/THESIS\\_MEHC.pdf](http://eprints.nottingham.ac.uk/14297/1/THESIS_MEHC.pdf)

### **Copyright and reuse:**

The Nottingham ePrints service makes this work by researchers of the University of Nottingham available open access under the following conditions.

- Copyright and all moral rights to the version of the paper presented here belong to the individual author(s) and/or other copyright owners.
- To the extent reasonable and practicable the material made available in Nottingham ePrints has been checked for eligibility before being made available.
- Copies of full items can be used for personal research or study, educational, or not-for-profit purposes without prior permission or charge provided that the authors, title and full bibliographic details are credited, a hyperlink and/or URL is given for the original metadata page and the content is not changed in any way.
- Quotations or similar reproductions must be sufficiently acknowledged.

Please see our full end user licence at:

[http://eprints.nottingham.ac.uk/end\\_user\\_agreement.pdf](http://eprints.nottingham.ac.uk/end_user_agreement.pdf)

### **A note on versions:**

The version presented here may differ from the published version or from the version of record. If you wish to cite this item you are advised to consult the publisher's version. Please see the repository url above for details on accessing the published version and note that access may require a subscription.

For more information, please contact [eprints@nottingham.ac.uk](mailto:eprints@nottingham.ac.uk)



The University of  
**Nottingham**

UNITED KINGDOM • CHINA • MALAYSIA

# **Simultaneous EEG-fMRI: Novel methods for EEG artefacts reduction at Source**

By

**Muhammad Enamul Hoque Chowdhury, M.Sc.**

Thesis submitted to the University of Nottingham for the degree of  
Doctor of Philosophy

July 2014

## Acknowledgements

*“All praise is due to Allah, Lord of the worlds”*

Although one name is written on the title page of this thesis, the work presented, in reality is the result of the combined efforts of a number of people, to all of whom, I owe a great deal. I would like to take this opportunity to express my gratitude to all of those. First and foremost I would like to thank my supervisor Prof Richard Bowtell for giving me the opportunity to work in this novel project and for his support, advice, ideas, accessibility and guidance with the extreme patience over the last three years. I am indebted to colleague Dr Karen Mullinger who wasn't my supervisor officially but helped me as I would expect from my second supervisor. I will be forever grateful for her friendly and professional support throughout the course of this work. I would also like to thank Dr Paul Glover especially for his excellent ideas regarding star-quad cable for RLAS system and other nice ideas to improve RLAS.

A big thank to Andre Antunes for helping with electromagnetic simulation and teaching me how to use his C++ code and also how to modify it for my studies. Special thanks must go to Alan Dorkes and Ian Thexton in workshop for their excellent help in producing mould for the phantom. I must also thank all those people who have volunteered for me.

I would like to thank my very good friends Zaid, Zubair, Bador, Tariq, Moin, Shakeel, Shamim, Farhan, Junaid, Imran, Shoaib, Aftab, Nouman, Sadig and Mahmood who have coloured my PhD time with their exceptional inspiration and help. I must especially thank Zaid and Iqbal Bhai for calming me down when things got tough and for making me realise the more important things in life. Thanks also to Enamul, Glyn, Tom, and Joe for their support and encouragement in finishing this work.

Finally I would like to thank my family members. I would like to express especial gratitude to my beautiful wife who always encouraged and helped me while I was in difficult situation and made me understand that I have the capability to do it! Thank you Samoon Bhai for all your support before and during this study; it would be really difficult without your help. I am extremely grateful to my parents for always believing in me. I can never express my gratitude to them, but instead, I hope I make them proud.

# Contents

## Abstract

## Chapter 1

### Introduction

1.1 Introduction to Neuroimaging.....	2
1.2 Why Simultaneous EEG-fMRI? .....	3
1.3 Challenges in Combining EEG and fMRI .....	4
1.4 Thesis Overview .....	6
1.5 References.....	8

## Chapter 2

### Brain activity: physiology and measurement

2.1 Introduction.....	14
2.2 Central Nervous System (CNS).....	14
2.2.1 Glial Cells.....	14
2.2.2 Neurons .....	14
2.3 Anatomy of the Human Brain.....	16
2.4 Neuronal Activity.....	17
2.4.1 Action Potentials .....	17
2.4.2 Postsynaptic Potential (PSP) .....	20
2.5 Source of the EEG Signal .....	22
2.5.1 Cortical Pyramidal Neurons .....	23
2.5.2 Local-Scale and Large-Scale Synchronization .....	23
2.6 EEG Recording Equipment and Techniques .....	24
2.6.1 EEG Rhythms.....	24
2.6.2 Event Related Potential (ERP) .....	26
2.6.3 Modes of EEG Recording .....	28
2.6.4 Electrode Placement: International 10-20 System .....	30
2.7 Advantages and Disadvantages of EEG .....	33
2.8 Magnetic Resonance Imaging (MRI).....	34

2.8.1 Proton Spin in External Magnetic Field.....	35
2.8.2 Magnetic Resonance Effect.....	36
2.8.3 Relaxation .....	36
2.8.4 Spatial Encoding in MR imaging.....	37
2.8.4.1 Slice Selection (SS) .....	37
2.8.4.2 Readout or Frequency Encoding (RO) .....	38
2.8.4.3 Phase Encoding (PE) .....	39
2.8.5 Spin Echo and Gradient Echo .....	40
2.8.6 Correction Gradients .....	42
2.8.6.1 Slice-Rephasing Gradient .....	42
2.8.6.2 Prephasing Readout Gradient .....	42
2.8.6.3 Crusher Gradients .....	43
2.8.6.4 Spoiler Gradients .....	44
2.8.7 k-Space.....	45
2.8.8 Echo Planar Imaging (EPI) .....	46
2.8.9 MR Instrumentation .....	47
2.8.9.1 Magnet .....	48
2.8.9.2 Shim Coils .....	48
2.8.9.3 Gradient Coils.....	49
2.8.9.4 RF Coils.....	49
2.8.9.5 Control and Processing System .....	50
2.9 Functional Magnetic Resonance Imaging (fMRI).....	51
2.9.1 The BOLD Contrast Mechanism .....	51
2.9.2 The Haemodynamic Response.....	52
2.9.3 Advantages and Disadvantages of fMRI.....	54
2.10 References.....	56

## **Chapter 3**

### **EEG artefacts produced during simultaneous acquisition of fMRI data and review of standard correction techniques**

3.1 Introduction.....	61
3.2 Prominent EEG Artefacts in Simultaneous EEG-fMRI.....	61
3.3 Artefact Removal Techniques.....	68
3.3.1 Gradient Artefact Correction Techniques .....	69

3.3.1.1 Interleaved EEG-fMRI .....	69
3.3.1.2 GA Reduction at Source .....	70
3.3.1.3 Filtering in the Frequency Domain.....	70
3.3.1.4 GA Reduction by Stepping Stone Sampling .....	71
3.3.1.5 Average Artefact Subtraction (AAS).....	71
3.3.1.6 Synchronisation of EEG and fMRI Data Acquisitions.....	76
3.3.1.7 Independent Component Analysis (ICA) .....	79
3.3.1.8 Modelling Gradient Artefact.....	80
3.3.2 Pulse Artefact Removal.....	83
3.3.2.1 Temporal Pattern PA Removal Approaches.....	84
3.3.2.2 Spatial Pattern PA Removal Approaches .....	86
3.3.2.3 Motion sensor based PA correction.....	88
3.3.2.4 Additional possible measures for PA correction .....	89
3.3.3 Motion Artefact (MA).....	90
3.3.3.1 MA Reduction .....	90
3.3.4 Vibration Artefact .....	92
3.4 Conclusion .....	93
3.5 References.....	94

## **Chapter 4**

### **Simultaneous EEG/fMRI: Current practices for obtaining high quality EEG data**

4.1 Introduction.....	104
4.2 MR Compatible Equipment .....	105
4.2.1 EEG systems that reside in the scanner control room.....	105
4.2.2 EEG systems that reside in the scanner enclosure .....	106
4.3 Safety Concerns in Simultaneous EEG-fMRI .....	109
4.3.1 Subject Safety.....	109
4.3.2 Equipment Safety .....	111
4.4 Data Acquisition Considerations .....	112
4.4.1 Band Limited Filter .....	112
4.4.2 Sampling Rate .....	112
4.4.3 EEG-MR clock synchronization .....	113

4.5 Best Current Practice for EEG Equipment Set-up.....	114
4.5.1 EEG Cap.....	115
4.5.2 EEG Amplifier and Cabling.....	115
4.5.3 Subject Positioning inside the Scanner .....	115
4.6 Conclusion .....	116
4.7 References.....	116

## **Chapter 5**

### **Simultaneous EEG-fMRI: evaluating the effect of the cabling configuration on the gradient artefact**

5.1 Introduction.....	120
5.2 Background.....	120
5.2 Methods.....	121
5.2.1 Study 1 .....	122
5.2.2 Study 2 .....	124
5.3 Analysis.....	125
5.3.1 Study 1 .....	126
5.3.2 Study 2 .....	126
5.4 Results.....	127
5.4.1 Study1 .....	127
5.4.2 Study 2.....	134
5.5 Discussion.....	138
5.6 Conclusions.....	141
5.7 References.....	141

## **Chapter 6**

### **Reference Layer Artefact Subtraction: electromagnetic simulations**

6.1 Introduction.....	144
6.2 Background and Theory.....	145
6.2.1 Maxwell’s Equation .....	146
6.2.2 Quasi-Static Limit .....	146
6.2.3 Boundary Conditions .....	147

6.2.4 Problem Formulation .....	148
6.2.5 Analytic expressions for the Magnetic field and Vector potential.....	152
6.3 Modelling & Methods.....	153
6.4 Analysis.....	154
6.5 Preliminary Experiments .....	156
6.6 Preliminary Results.....	157
6.7 Optimization Experiments .....	159
6.8 Optimization Results.....	160
6.9 Discussions .....	164
6.10 Conclusion .....	169
6.11 References.....	170

## **Chapter 7**

### **Reference Layer Artefact Subtraction: experimental study**

7.1 Introduction.....	174
7.2 General Equipment and Data Acquisition .....	175
7.3 Preliminary Experiment.....	177
7.3.1 Method .....	178
7.3.2 Analysis.....	179
7.3.3 Results and Discussion of the Preliminary Experiment.....	180
7.3.4 Conclusion to Preliminary Experiment.....	181
7.4 Constructing the Reference Layer set-up.....	181
7.5 RLAS Experiments .....	183
7.5.1 General Set-up.....	183
7.5.2 Experiment 1: RLAS vs. fEEG .....	184
7.5.3 Experiment 2: Verifying the fidelity of the RLAS approach.....	184
7.5.4 Experiment 3: Phantom.....	185
7.5.5 Experiment 4: Human Subjects.....	186
7.6 Analysis of RLAS Experiments.....	187
7.6.1 Artefact removal using RLAS.....	187
7.6.2 Artefact correction using AAS.....	187



7.6.3 Evaluation of correction methods .....	188
7.7 RLAS Results.....	189
7.7.1 RLAS vs. fEEG .....	189
7.7.2 Verifying the fidelity of the RLAS approach.....	190
7.7.3 Comparing artefact removal methods: .....	191
7.7.3.1 Phantom Data: .....	191
7.7.3.2. Human Subject Data: .....	195
7.8 Discussion.....	199
7.9 Conclusion .....	206
7.10 References.....	206

## **Chapter 8**

### **Conclusion**

8.1 Summary .....	210
8.2 Future Work .....	212
8.3 Concluding Remarks.....	216
8.4 References.....	216

## **Publications of Author**

## **Abstract**

This thesis describes the development and application of novel techniques to reduce the EEG artefacts at source during the simultaneous acquisition of EEG and fMRI data. The work described in this thesis was carried out by the author in the Sir Peter Mansfield Magnetic Resonance Centre, School of Physics & Astronomy at the University of Nottingham, between October 2010 and January 2013.

Large artefacts compromise EEG data quality during simultaneous fMRI. These artefact voltages pose heavy demands on the bandwidth and dynamic range of EEG amplifiers and mean that even small fractional variations in the artefact voltages give rise to significant residual artefacts after correction, which can easily swamp signals from brain activity. Therefore any intrinsic reduction in the magnitude of the artefacts would be highly advantageous, allowing data with a higher bandwidth to be acquired without amplifier saturation, and facilitating improved detection of brain activity. This thesis firstly explores a new method for reducing the gradient artefact (GA), which is induced in EEG data recorded during concurrent MRI, by investigating the effects of the cable configuration on the characteristics of the GA. This work showed that the GA amplitude and its sensitivity to movement of the cabling is reduced by minimising wire loop areas in the cabling between the EEG cap and amplifier.

Another novel approach for reducing the magnitude and variability of the artefacts is the use of an EEG cap that incorporates electrodes embedded in a reference layer, which has a similar conductivity to tissue and is electrically isolated from the scalp. With this arrangement, the artefact voltages produced on the reference layer leads are theoretically similar to those induced in the scalp leads, but neuronal signals are not detected in the reference layer. Therefore taking the difference of the voltages in the reference and scalp channels should reduce the artefacts, without affecting sensitivity to neuronal signals. The theoretical efficacy of artefact correction that can be achieved by using this new reference layer artefact subtraction (RLAS) method was investigated. This was done through separate electromagnetic simulations of the artefacts induced in a hemispherical reference layer and a spherical volume conductor in a time-varying magnetic field and the results showed that similar artefacts are induced on the surface of both conductors. Simulations are also

performed to find the optimal design for an RLAS system, by varying the geometry of the system.

A simple experimental realisation of the RLAS system was implemented to investigate the degree of artefact attenuation that can be achieved via RLAS. Through a series of experiments on phantoms and human subjects, it is shown here that RLAS significantly reduces the GA, pulse (PA) and motion (MA) artefacts, while allowing accurate recording of neuronal signals. The results indicate that RLAS generally outperforms the standard artefact correction method, average artefact subtraction (AAS), in the removal of the GA and PA when motion is present, while the combination of RLAS and AAS always produces higher artefact attenuation than AAS alone. Additionally, this work demonstrates that RLAS greatly attenuates the unpredictable and highly variable MA that are very hard to remove using post-processing methods.

# Chapter 1

---

## *Introduction*

## 1.1 Introduction to Neuroimaging

The human brain has challenged and puzzled scientists, philosophers and countless others for many centuries. It was not until the 2<sup>nd</sup> century, that the brain was thought to be central organ of sensations and thoughts. In the 4<sup>th</sup> and 5<sup>th</sup> centuries, the idea of localising brain function was developed, with higher brain functions believed to be associated with the ventricles (Bear *et al.*, 2001). The first real attempt to understand human brain function using scientific techniques was made in the 19<sup>th</sup> century, “the era of cortical localisation”, by a German anatomist, Franze Gall. Gall proposed the concept of distinct functional areas of the cerebral cortex. Many scientists were inspired by his idea and began investigating the functionality of the human brain cortex. However, the lack of non-invasive techniques meant that the studies were limited to gathering evidence from patients. In 1862, Paul Broca suggested that the human brain contained a specialised region of speech, named “Broca’s area” in the frontal lobe. Broca’s observations were based on a patient who suffered from damage in the left frontal lobe and consequent loss of speech (Bear *et al.*, 2001). By the beginning of the 20<sup>th</sup> century, new methods were introduced to investigate brain function and structure. Electroencephalography (EEG) was the first, truly, non-invasive method that was used to investigate the brain function. In the middle of the 20<sup>th</sup> century, Wilder Penfield revolutionised the understanding of cortical localisation using Electrocorticography (ECoG) or intracranial EEG (icEEG). Using these techniques he mapped the motor and somatosensory cortices by stimulating the brain during neurosurgery of epileptic patients using electrodes placed directly on the exposed surface of the brain. The second half of the 20<sup>th</sup> century witnessed the rapid development of medical imaging. Moreover, the advent of functional neuroimaging techniques helps to localise different mental processes of which areas are responsible for which processes. Functional neuroimaging techniques are now divided into two types: direct measurements of neural activity through electrophysiological recordings, and indirect measurements through measuring the haemodynamic response.

With the development of the imaging techniques of X-ray computerised tomography (CT) and magnetic resonance imaging (MRI) it was possible to more specifically locate the anatomical area of interest in the brain. Whilst the measurement of the electrical signals on the scalp, arising from the synchronous firing of the neurons in response to a stimulus, known as EEG, opened up new possibilities for studying brain function in normal subjects. However it was the advent of the functional imaging modalities of positron emission tomography

(PET), single photon emission computed tomography (SPECT), functional magnetic resonance imaging (fMRI), magnetic resonance spectroscopy (MRS), Event Related Optical Signal (EROS), Near Infrared Spectroscopy (NIRS), and magnetoencephalography (MEG) that led to a new era in the study of brain function. Each of the techniques has advantages and disadvantages for imaging brain function depending on the importance of the temporal or spatial information to an investigation. These techniques are complementary rather than competitive. Therefore, it is unsurprising that information from the different modalities is now being combined with the aim of gaining further insight into brain function. Two of the most obvious, and practical, of the above techniques to combine are EEG and fMRI.

### 1.2 Why Simultaneous EEG-fMRI?

The changes in blood flow and blood oxygenation in the brain are closely linked to neural activity. When nerve cells are active they consume oxygen carried by hemoglobin. The difference in magnetic properties of oxygenated and de-oxygenated hemoglobin results in a difference in the magnetic resonance (MR) signal in the surrounding tissue depending on the level of blood oxygenation. This is known as the Blood-Oxygen-Level Dependent (BOLD) contrast. Since its introduction in the early 1990's, BOLD fMRI (Ogawa *et al.*, 1990, 1993) has revolutionised the field of cognitive neuroscience by providing a non-invasive means of mapping human brain function *in vivo*. This BOLD contrast is used to detect areas of the brain that show a change in neural activation when the subject performs a task.

EEG allows brain activity (Berger 1929) to be monitored with high temporal resolution, on the order of milliseconds, but the ill-posed inverse problem (Michel *et al.*, 2001) and inhomogeneous conductivity profile in the head means that its spatial resolution is limited; i.e. it is difficult to decipher from EEG data where in the brain activity is occurring. fMRI allows the detection of brain activity with excellent spatial resolution, but the temporal resolution is compromised by the slow nature of the haemodynamic changes upon which it relies. Whilst EEG has been used for many decades and fMRI for around twenty years, these two techniques were only combined together in the mid 90's (Ives *et al.*, 1993; Huang-Hellinger *et al.*, 1995). Combining these techniques is intuitively beneficial because of the complementary properties of the two methods. The combination of EEG and fMRI data allows accurate spatial information provided by fMRI to be used in conjunction with detailed information about the timing of electrical activity from EEG.

Simultaneous EEG and fMRI has opened up many new avenues of investigation in functional neuroimaging. The applications of simultaneous EEG/fMRI have already proved to be far-reaching, including the study of the resting state (Laufs *et al.*, 2003) and the correlation of fluctuations in spontaneous electrical activity and the BOLD signal (Goldman *et al.*, 2002; Laufs *et al.*, 2003), as well as the provision of new information about the link between evoked electrical activity and the hemodynamic response (Eichele *et al.*, 2005; Debener *et al.*, 2006; Schubert *et al.*, 2008; Strobel *et al.*, 2008; Mobascher *et al.*, 2009; Warbrick *et al.*, 2009). Clinical applications of combined EEG-fMRI have also been demonstrated in epilepsy (Iannetti *et al.*, 2002; Salek-Haddadi *et al.*, 2002,2003; Lemieux 2004; Laufs *et al.*, 2007). Recently, the multi-modal EEG-fMRI technique has also been used to investigate sleep (Czisch *et al.*, 2002; Stern *et al.*, 2011) and has been shown to have potential uses in the study of sleep disorders (Ritter *et al.*, 2006). Despite the many examples of the successful application of simultaneous EEG-fMRI in neuroscience, current investigations are still generally limited by the reduction in the quality of EEG data that results when measurements are acquired during concurrent fMRI. To realize the benefits of combined EEG-fMRI, it is important to ensure that the data acquired when the two techniques are implemented simultaneously are not significantly compromised in quality compared with data acquired in separate recordings.

### 1.3 Challenges in Combining EEG and fMRI

Because of the hostile environment within an MR scanner, truly simultaneous recording of EEG and fMRI data is technically challenging as both methods mutually influence each other. The effect of the EEG equipment on patient safety (Lemieux *et al.*, 1997) and MR signal quality (Krakow *et al.*, 1999) has been reduced to an acceptable level (Mullinger *et al.*, 2008a). More troublesome is the influence of the MR system on the EEG signal quality. Both motion in the large steady static magnetic field ( $B_0$ ) of the MR scanner and the fast time-varying fields needed to create MR images induce artefacts in the EEG data (Allen *et al.*, 1998; Allen *et al.*, 2000), which are generally much larger in magnitude than the electrical signals produced by neurological activity of interest. The largest artefacts are produced by the temporally-varying magnetic field gradients used in fMRI. These gradients generate voltages in the conducting tissues of the human body and the wires of the EEG recording system by means of the process of electromagnetic induction. The resulting *gradient artefacts*, can be

more than a few mV in magnitude compared with a typical EEG amplitude of less than 100  $\mu$ V from neuronal signals. Pulsatile cardiac-related movements of the electrode leads in the high static magnetic field also induce voltages that are superimposed upon the cerebral signals (Ives *et al.*, 1993). The exact etiology of this *pulse artefact* is not well understood, as discussed in detail in Chapter 3 of this thesis. The pulse artefact waveform shows a complicated pattern of spatial variation over the surface of the scalp (Huang-Hellinger *et al.*, 1995) and can also vary in form across cardiac cycles in an individual subject (Bonmassar *et al.*, 2002; Debener *et al.*, 2007).

The process by which gradient artefact is generated is well understood and the predictable and periodic nature of the GA, means it is commonly dealt with using a template subtraction method either in the time (Allen *et al.*, 2000) or frequency (Sijbers *et al.*, 1999; Hoffmann *et al.*, 2000) domains. An average artefact template is calculated and then subtracted (average artefact subtraction (AAS)) from the raw EEG signal. Residual variances after artefact correction can be caused by jitter of the internal clocks of the EEG and fMRI systems leading to heterogeneous imaging artefacts. Several methods have been proposed to reduce jitter related residual variance (Negishi *et al.*, 2004; Goncalves *et al.*, 2007). In particular, a significant improvement of the corrected EEG signal quality was achieved by the introduction of EEG and fMRI clock synchronization so as to prevent jittering (Mandelkow *et al.*, 2006; Mullinger *et al.*, 2008b).

The correction techniques proposed so far are adequate for temporally stable data or slow drifts of the artefact properties, but cannot correct the GA properly when abrupt changes of the artefact properties occur, e.g. when the head of the subject moves during data acquisition (leading to motion artefact (MA) in the EEG data). Increased heterogeneity of the gradient artefacts impairs EEG signal quality (Laufs *et al.*, 2008) and head motions alter the geometry of electrodes and cables in the magnetic field and consequently the properties of the induced artefacts change.

Although the periodic nature of the PA means that it can also be corrected using AAS (Allen *et al.*, 1998), variation of the artefact across cardiac cycles reduces the efficacy that can be achieved in PA correction via AAS, compared with the performance that can be achieved in correcting the GA. A sliding window template based on the average of an optimum number of repetitions of the cardiac cycle (Allen *et al.*, 1998) is typically used for PA correction via



AAS to avoid the variation of the PA without losing the neuronal signals of interest. Given the limitations of using AAS for PA correction, it is not surprising that significant effort has been dedicated to devising improved techniques for PA correction. These include independent component analysis (ICA) (Briselli *et al.*, 2006; Mantini *et al.*, 2007), optimal basis sets (OBS) analysis (Naizy *et al.*, 2005; Debener *et al.*, 2007) and spatial filtering using adaptive beamformer methods (Brookes *et al.*, 2008). These artefact correction methods are reported to perform inconsistently between studies with greater efficacy of correction generally achieved at lower field strengths. Given that the amplitude of the PA scales with field strength (Debener *et al.*, 2008), this field strength dependence is not surprising. For example, Huang-Hellinger *et al.*, (1995) reported that alpha oscillations could be observed above the PA amplitude in some subjects with recordings made at 1.5 T. However, the PA generally swamps the scalp voltages resulting from brain activity at 3 T as the peak amplitude of the PA at 3 T can exceed 200  $\mu\text{V}$  (Debener *et al.*, 2007).

It is obvious that the signal- and contrast-to-noise-ratio of fMRI data will increase with magnetic field strength (Gati *et al.*, 1997). This provides a strong motivation for moving to higher field strengths, such as 7T, for fMRI data acquisition (Gati *et al.*, 1997; van der Zwaag *et al.*, 2009). However, the greater degradation of the EEG data at ultra-high field due to the larger residual PA (Debener *et al.*, 2008) and subject movements means that moving to higher field strengths may not always be beneficial in simultaneous EEG-fMRI studies. In order to realise the full benefit of high field in EEG-fMRI, better efficacy in removal of the MR related EEG artefacts is needed or, alternatively, new methods to reduce the artefacts at source are required. To achieve this, an improved understanding of the sources of the artefacts and variability are also needed.

### 1.4 Thesis Overview

The aim of this body of work is to produce a better understanding of the artefacts produced in simultaneous EEG-fMRI recordings. This knowledge is then employed in combining EEG and fMRI in such a way to obtain high quality data which in the future will allow a detailed exploration of neural activity and brain function. This project focused on devising improved methods for eliminating EEG artefacts at source in combined EEG-fMRI experiments. The thesis can be split into three parts: Chapter two introduces the concept EEG, MRI and fMRI in detail. Chapters three and four outline the causes of the EEG artefacts and standard

correction methods. Chapters five, six and seven describe experimental and simulation based work exploring different aspects of novel methods to reduce the EEG artefacts at source, while Chapter eight provides a conclusion of the results of these chapters.

**Chapter Two** aims to give the reader a basic understanding of neuronal activity and the anatomy of the brain. This chapter explores, in detail, how EEG signals relate to brain activity and also how the signal are recorded. The physics behind magnetic resonance imaging (MRI) is also briefly explored. This chapter describes the theory of how MR images are formed and gives a general overview of the gradients used in MR imaging. The chapter then leads onto an overview of why fMRI is possible, as well as the advantages and disadvantages of EEG and fMRI, when used individually and in combination. A detailed discussion of the main physical limitations that are faced when combining these imaging techniques is given in **Chapter Three**, along with a description of the current methods for overcoming these problems. An overview of how combined EEG-fMRI has already been implemented by various groups is also provided in this chapter. **Chapter Four** focuses on the EEG equipment used, safety issues and data acquisition considerations in simultaneous EEG-fMRI. In this chapter current practices that should be used to obtain the best possible quality of EEG data recording in a combined EEG/fMRI experiment are also described.

**Chapter Five** is the first describing the experimental work of this thesis and explores the effect of the cable configuration on the EEG artefacts produced when performing simultaneous EEG-fMRI experiments. This work demonstrates that particular cabling configurations can improve the acquired EEG data quality. **Chapter Six** explores the theoretical efficacy of artefact correction that can be achieved by using a new method, Reference Layer Artefact Subtraction (RLAS), through simulations of the artefacts induced in a hemispherical reference layer and a spherical volume conductor separately and also for RLAS system in a time-varying magnetic field. This is done by evaluating the differences in the voltage produced in the reference layer conductor and volume conductor, while the reference layer and insulating layer geometry parameters were varied. These simulations provide the theoretical optimal design for an RLAS system.

**Chapter Seven** explores the development of an experimental set-up for the RLAS approach in which gradient, movement and pulse artefacts could be simultaneously recorded on the scalp and on a reference layer. This allows experimental testing of the efficacy of artefact

correction that can be achieved by using an RLAS system. Initial experiments were carried out on simple spherical phantoms using different cable configurations to test the feasibility of RLAS. A series of experiments were then carried out on spherical phantoms and human subjects to test how well RLAS eliminates the GA, PA and MA when these artefacts are present individually and in combination.

**Chapter Eight** concludes this thesis by drawing conclusions from all the experimental work presented in the preceding chapters. Some discussion of future work that should be conducted in light of these findings is then given, with an emphasis placed on the realistic implementation of the novel EEG artefact reduction method, RLAS so as to improve EEG data quality and to enable the use of this method in conducting future studies based on simultaneous EEG-fMRI thus improving our understanding of the function of the brain.

## 1.5 References

- Allen, P. J., Josephs, O. and Turner, R. (2000). "A Method for removing Imaging Artifact from Continuous EEG Recorded during Functional MRI." *Neuroimage* **12**(2): 230-239.
- Allen, P. J., Poizzi, G., Krakow, K., Fish, D. R. and Lemieux, L. (1998). "Identification of EEG Events in the MR Scanner: The Problem of Pulse Artifact and a Method for Its Subtraction." *Neuroimage* **8**(3): 229-239.
- Anami, K., Mori, T., Tanaka, F., Kawagoe, Y., Okamoto, J., Yarita, M., Ohnishi, T., Yumoto, M., Matsuda, H. and Saitoh, O. (2003). "Stepping stone sampling for retrieving artifact-free electroencephalogram during functional magnetic resonance imaging." *Neuroimage* **19**(2): 281-295.
- Bear, M.F., Connors, B.W., Paradiso, M.A., (2001). *Neuroscience: Exploring the brain* - Second Edition. Philadelphia: Lippincott, Williams and Wilkins.
- Berger, H. (1929). "Uber das Elektrenkephalogramm des Menschen." *Psychiatrie Nerv.* **87**: 527-570.
- Bonmassar, G., Purdon, P. L., Jaaskelainen, I. P., Chiappa, K., Solo, V., Brown, E. N. and Belliveau, J. W. (2002). "Motion and ballistocardiogram artifact removal for interleaved recording of EEG and EPs during MRI." *NeuroImage* **16**(4): 1127–1141.

- Briselli, E., Garreffa, G., Bianchi, L., Bianciardi, M., Macaluso, E., Abbafati, M., Marciani, M. and Maraviglia, B. (2006). "An independent component ballistocardiogram analysis-based approach on artifact removing." Magn Reson Imaging **24**: 393-400.
- Brookes, M. J., Mullinger, K. J., Stevenson, C. M., Morris, P. G. and Bowtell, R. W. (2008). "Simultaneous EEG source localisation and artifact rejection during concurrent fMRI by means of spatial filtering " NeuroImage **40**(3): 1090-1104.
- Czisch, M., Wetter, T. C., Kaufmann, C., Pollmacher, T., Holsboer, F. and Auer, D. P. (2002). "Altered processing of acoustic stimuli during sleep: Reduced auditory activation and visual deactivation detected by a combined fMRI/EEG study." Neuroimage **16**(1): 251-258.
- Debener, S., Mullinger, K. J., Niazy, R. K. and Bowtell, R. W. (2008). "Properties of the ballistocardiogram artefact as revealed by EEG recordings at 1.5, 3 and 7 Tesla static magnetic field strength." International Journal of Psychophysiology **67**(3): 189-199.
- Debener, S., Strobel, A., Sorger, B., Peters, J., Kranczioch, C., Engel, A. K. and Goebel, R. (2007). "Improved quality of auditory event-related potentials recorded simultaneously with 3-T fMRI: removal of the ballistocardiogram artefact." Neuroimage **34**: 587-597.
- Debener, S., Ullsperger, M., Siegel, M. and Engel, A. K. (2006). "Single-trial EEG-fMRI reveals the dynamics of cognitive function." Trends in Cognitive Sciences **10**(12): 558-563.
- Eichele, T., Specht, K., Moosmann, M., Jongsma, M. L. A., Quiroga, R. Q., Nordby, H. and Hugdahl, K. (2005). "Assessing the spatiotemporal evolution of neuronal activation with single-trial event-related potential and functional MRI." Proc. Natl Acad. Sci. **102**(49): 17789–17803.
- Gati, J. S., S., M. R., Ugurbil, K. and Rutt, B. K. (1997). "Experimental Determination of the BOLD Field Strength Dependence in Vessels and Tissue." Magnetic Resonance in Medicine **38**(296): 302.
- Goldman, R. I., Stern, J. M., Engel, J. and Cohen, M. S. (2002). "Simultaneous EEG and fMRI of the alpha rhythm." NeuroReport **13**(18): 2487–2492.
- Goncalves, S. I., Pouwels, P. J., Kuijter, J. P., Heethaar, R. M. and de Munck, J. C. (2007). "Artifact removal in co-registered EEG/fMRI by selective average subtraction." Clin. Neurophysiology **118**: 2437-2450.

- Hoffmann, A., Jager, L., Werhahn, K. J., Jaschke, M., Noachtar, S. and Reiser, M. (2000). "Electroencephalography during functional echo-planar imaging: detection of epileptic spikes using post-processing methods." Magn. Res. Med. **44**: 791-798.
- Huang-Hellinger, F., Breiter, H., McCormack, G., Cohen, M., Kwong, K., Sutton, J., Savoy, R., Weisskoff, R., Davis, T., Baker, J., Belliveau, J. and Rosen, B. (1995). "Simultaneous functional magnetic resonance imaging and electrophysiological recording." Hum Brain Map **3**: 13-23.
- Iannetti, G. D., Di Bonaventura, C., Pantano, P., Giallonardo, A. T., Romanelli, P. L., Bozzao, L., Manfredi, M. and Ricci, G. B. (2002). "fMRI/EEG in paroxysmal activity elicited by elimination of central vision and fixation." Neurology **58**(6): 976-979.
- Ives, J. R., Warach, S., Schmitt, F., Edelman, R. R. and Schomer, D. L. (1993). "Monitoring a patient's EEG during echo planar MRI." Electroencephalography and Clinical Neurophysiology **87**(6): 417-420.
- Krakow, K., Woermann, F. G., Symms, M. R., Allen, P. J., Lemieux, L., Barker, G. J., Duncan, J. and S., F., D.R., (1999). "EEG-triggered functional MRI of interictal epileptiform activity in patients with partial seizures." Brain **122**: 1679-1688.
- Laufs, H., Daunizeau, J., Carmichael, D. W. and Kleinschmidt, A. (2008). "Recent advances in recording electrophysiological data simultaneously with magnetic resonance imaging." NeuroImage **40**(2): 515-528.
- Laufs, H. and Duncan, J. S. (2007). "Electroencephalography/function MRI in human epilepsy: what it currently can and cannot do." Curr. Opin. Neurol. **20**(4): 417-423.
- Laufs, H., Kleinschmidt, A., B., A., Eger, E., Salek-Haddadi, A., Preibisch, C. and Krakow, K. (2003). "EEG-correlated fMRI of human alpha activity." Neuroimage **19**: 1463-1476.
- Lemieux, L. (2004). "Electroencephalography-correlated functional MR imaging studies of epileptic activity " Neuroimaging Clinics of North America **14**(3): 487-506.
- Lemieux, L., Allen, P. J., Franconi, F., Symms, M. R. and Fish, D. R. (1997). "Recording of EEG during fMRI experiments : Patient safety." Magn. Res. Med. **38**(6): 943-952.
- Mandelkow, H., Halder, P., Boesiger, P. and Brandeis, D. (2006). "Synchronisation facilitates removal of MRI artefacts from concurrent EEG recordings and increases usable bandwidth." Neuroimage **32**(3): 1120-1126.
- Mantini, D., Perrucci, M. G., Cugini, S., Ferretti, A., Romani, G. L. and Del Gratta, C. (2007). "Complete artifact removal for EEG recorded during continuous fMRI using independent component analysis." Neuroimage **34**(2): 598-607.

- Michel, C. M., Thut, G., Morand, S., Khateb, A., Pegna, A. J., Grave de Peralta, R., Gonzalez, S., Seeck, M. and Landis, T. (2001). "Review: ELeCtric source imaging of human brain functions." Brain Research Reviews **36**(2-3): 108-118.
- Mobascher, A., Brinkmeyer, J., Warbrick, T., Musso, F., Wittsack, H. J., Saleh, A., Schnitzler, A. and Winterer, G. (2009). "Laser-evoked potential single-trial amplitudes covary with the fMRI BOLD response in the medial paon system and interconnected subcortical structures." Neuroimage **45**(3): 917–926.
- Mullinger, K. J., Brookes, M. J., Stevenson, C. M., Morgan, P. S. and Bowtell, R. W. (2008a). "Exploring the feasibility of simultaneous EEG/fMRI at 7 T." Magnetic Resonance Imaging **26**(7): 607-616.
- Mullinger, K. J., Morgan, P. S. and Bowtell, R. W. (2008b). "Improved Artefact Correction for Combined Electroencephalography/Functional MRI by means of Synchronization and use of VCG Recordings." Journal of Magnetic Resonance Imaging **27**(3): 607-616.
- Niazy, R. K., Bechmann, C. F., Iannetti, G. D., Brady, J. M. and Smith, S. M. (2005). "Removal of fMRI environment artifacts from EEG data using optimal basis sets." Neuroimage **28**(3): 720-737.
- Negishi, M., Abildgaard, M., Nixon, T., Constable, R. T. and (2004). "Removal of time-varying gradient artifacts from EEG data acquired during continuous fMRI." Clin. Neurophysiol. **115**: 2181-2192.
- Ogawa, S., Lee, T. M., Nayak, A. S. and Glynn, P. (1990). "Oxygenation-sensitive contrast in magnetic resonance image of rodent brain at high magnetic fields. ." Magn Reson Med **14**: 68-78.
- Ogawa, S., Menon, R. S., Tank, D. W., Kim, S. G., Merkle, H., Ellermann, J. M. and Ugurbil, K. (1993). "Functional brain mapping by blood oxygenation level dependent contrast magnetic resonance imaging." Biophysical Journal **64**: 803-812.
- Ritter, P. and Villringer, A. (2006). "Review: Simultaneous EEG-fMRI." Neuroscience and Behavioural reviews **30**: 823-838.
- Salek-Haddadi, A., Friston, K. J., Lemieux, L. and Fish, D. R. (2002). "Simultaneous EEGcorrelated ictal fMRI." Neuroimage **16**: 32-40.
- Salek-Haddadi, A., Friston, K. J., Lemieux, L. and Fish, D. R. (2003). "Review: Studying spontaneous EEG activity with fMRI." Brain Research Reviews **43**: 110-133.
- Schubert, R., Ritter, P., Wustenberg, T., Preuschhof, C., Curio, G., Sommer, W. and Villringer, A. (2008). "Spatial attention related SEP amplitude modulations covary

- with BOLD signal in S1-a simultaneous EEG-fMRI study." *Cereb. Cortex* **18**(11): 2686–2700.
- Sijbers, J., Michiels, I., Verhoye, M., Van Audekerke, J., Van der, L. A. and Van Dyck, D. (1999). "Restoration of MR-induced artifacts in simultaneously recorded MR/EEG data." *Magn Reson Imaging* **17**(9): 1383-1391.
- Stern, J. M., Caporro, M., Haneef, Z., Yeh, H. J., Buttinelli, C., Lenartowicz, A., Mumford, J. A., Parvizi, J. and Poldrack, R. A. (2011). "Functional imaging of sleep vertex sharp transients." *Clinical Neurophysiology* **122**: 1382-1386.
- Strobel, A., Debener, S., Sorger, B., Peters, J. C., Kranczoich, C., Hoechstetter, K., Engel, A. K., Brocke, B. and Goebel, R. (2008). "Novelty and target processing during an auditory novelty oddball: a simultaneous event-related potential and functional magnetic resonance imaging study." *Neuroimage* **40**(2): 869-883.
- van der Zwaag, W., Francis, S., Head, K., Peters, A., Gowland, P., Morris, P. and Bowtell, R. (2009). "fMRI at 1.5, 3 and 7T: characterising BOLD signal changes." *Neuroimage* **47**(4): 1425-1434.
- Warbrick, T., Mobascher, A., Brinkmeyer, J., Musso, F., Richter, N., Stoecher, T., Fink, G. R., Shah, N. J. and Winterer, G. (2009). "Single trial P3 amplitude and latency informed event related fMRI models yield different BOLD response patterns to a target detection task." *Neuroimage* **47**(4): 1532–1544.

# Chapter 2

---

*Brain activity: physiology and measurement*



## 2.1 Introduction

The neural activity of the human brain starts to develop between the seventeenth and twenty-third week of pre-natal development (Wolfe 2010). It is believed that from this early stage and throughout life, electrical signals generated by the brain represent both brain function and the physical state of the person. Understanding of the neuronal functions and neurophysiological properties of the brain together with the mechanisms underlying the generation of signals and their recordings is therefore vital for those who deal with these signals for detection, diagnosis, and treatment of brain disorders.

The entire human body is composed of cells. Each cell or group of cells has a specific job to perform. The cells that constitute the *central nervous system (CNS)* comprise the brain and the spinal cord. This system combined with the endocrine system provides most of the control functions for the body. Two main types of cells make up the CNS: *neurons* and *glial cells*.

## 2.2 Central Nervous System (CNS)

### 2.2.1 Glial Cells

*Glial cells* make up 90 percent of the brain's cells. Glial cells are nerve cells that don't carry nerve impulses. The various glial (meaning "glue") cells perform many important functions, including: digestion of parts of dead neurons, manufacturing myelin for neurons, providing physical and nutritional support for neurons, and more (Wolfe 2010). Since these cells do not contribute to the brain's electrical activity, the focus of the rest of the section is on neurons.

### 2.2.2 Neurons

There are approximately 100 billion neurons which are found primarily in the CNS. Neurons "communicate" with one another and form networks by means of electrical and chemical signalling i.e., neurons respond to stimuli and transmit information over long distances. Most neurons are composed of: a cell body (*soma*) which contains the nucleus; short projections called *dendrites*; and a single *axon* which is a long cylinder, as shown in Figure 2.1. The *axon* transmits an electrical impulse and is usually covered by a fatty substance called *myelin*. The *soma* is where the signals from the various dendrites come together and are passed on. The soma and the nucleus do not play an active role in the transmission of the neural signal. Instead, these two structures serve to maintain the cell and keep the neuron functional. The

*axon hillock* is located at the end of the soma and controls the firing of the neuron. If the total strength of the signal exceeds the threshold limit of the axon hillock, the structure will fire a signal (known as an *action potential*, see Section 2.4.1) down the axon (Wolfe 2010).

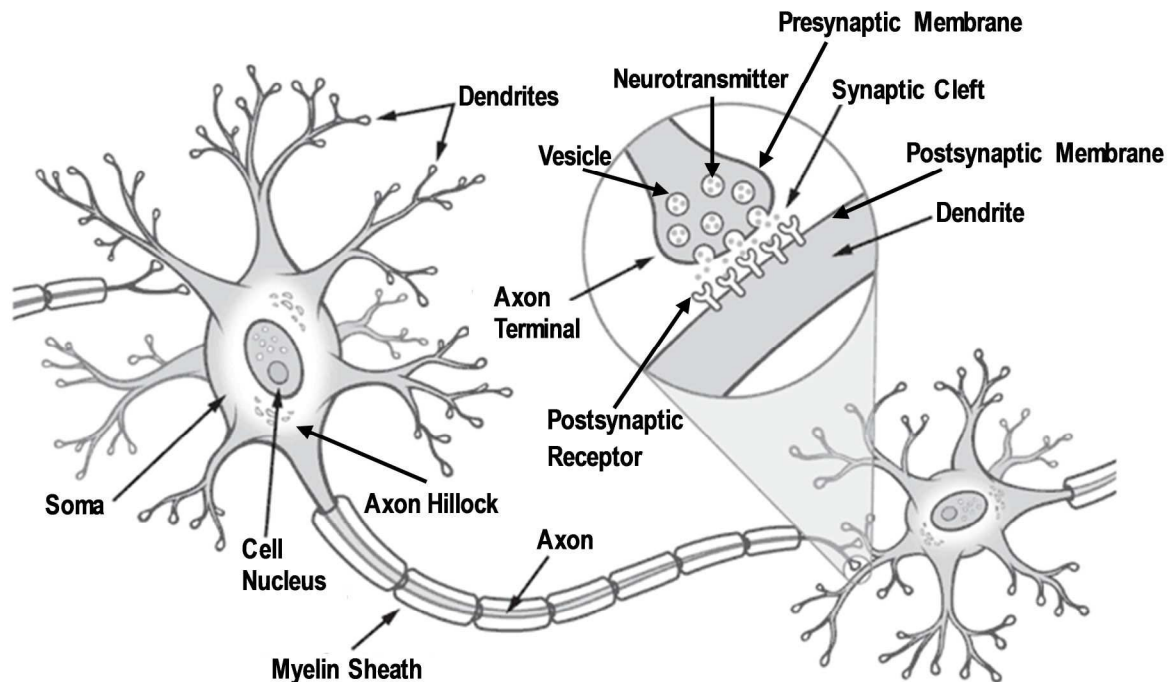


**Figure 2.1** Structural features of a typical nerve cell (i.e., neuron) and synapse. Adapted from (Ritchison 2013).

The number of dendrites in each neuron ranges between 6,000 and 10,000. In fact, dendrites are so numerous, they can account for 90% of the cell's surface (Wolfe 2010). The job of the dendrites is to receive information from other cells whereas the main job of the axon is to send information to other cells. The end of the axon splits into branches, each of which ends in an *axon terminal* or *bulb*. Communication between neurons occurs electrochemically by passing messages at the junction (known as the *synapse*) between axon terminals and spines on dendrites or cell bodies of the next neuron in the chain (see insert of Figure 2.1). This communication across the synapse produces a signal known as the *post-synaptic potential*, see Section 2.4.2.

Neurons come in many sizes. For example, a single sensory neuron originating at the fingertip has an axon that extends over the length of an arm, while neurons within the brain may have axons which extend only a few millimetres. Neurons can also have different shapes depending on their functions. The two main types of neuron are *stellate cells* and *pyramidal cells*. Stellate cells have symmetrically distributed dendrites and thus the average current flow within them is isotropic, whereas pyramidal cells have dendrites orientated perpendicular to

the cortical surface resulting in a current flow normal to the cortical surface. It is from these pyramidal cells that activity on the scalp can be detected using either *electroencephalography (EEG)* to measure the electrical potentials directly or *magnetoencephalography (MEG)* to measure the induced magnetic fields.

### 2.3 Anatomy of the Human Brain

Although it is important to understand the functionality of the individual neurons to comprehend brain function, the neuronal activity which is most commonly measured in humans arises from networks of neurons. It is therefore important to understand the main regions of the human brain and their function. The main components of the brain are the *cerebrum, cerebellum and brain stem* (Figure 2.2A). The cerebrum is the largest part of the brain and is divided into right and left hemispheres which are connected via the *corpus callosum*. The outer layer of the cerebrum is known as the *cerebral cortex*, which is about 1/32- to 1/4-inch thick, and is composed of the so-called grey matter. The cerebral cortex is made up of six layers of cells, their dendrites, and some axons. Studies of human brains by neurosurgeons, neurologists, and neuroscientists have shown that different areas (lobes) of the cerebral cortex have separate functions.

The cerebral cortex is divided into four lobes: *the frontal lobe, parietal lobe, temporal lobe and occipital lobe* (Figure 2.2B). The *frontal lobe* is separated from the parietal lobe by the *central sulcus*, whereas the temporal lobe is separated from these regions by the *lateral sulcus*. Different functions are carried out in each of these lobes and the lobes can be further divided into functional regions. For example somatosensory information is processed posterior to the central sulcus whereas the primary motor tasks are carried out anterior to that sulcus. In the primary auditory cortex, the primary auditory processing takes place deep inside the lateral sulcus. The visual cortex is located at the posterior of the brain in the occipital lobe. It should be noted that the information from a stimulus crosses over from left to right and vice versa in the brain. For example, a somatosensory stimulus applied to the left hand will mainly activate somatosensory cortex in the right hemisphere of the brain.

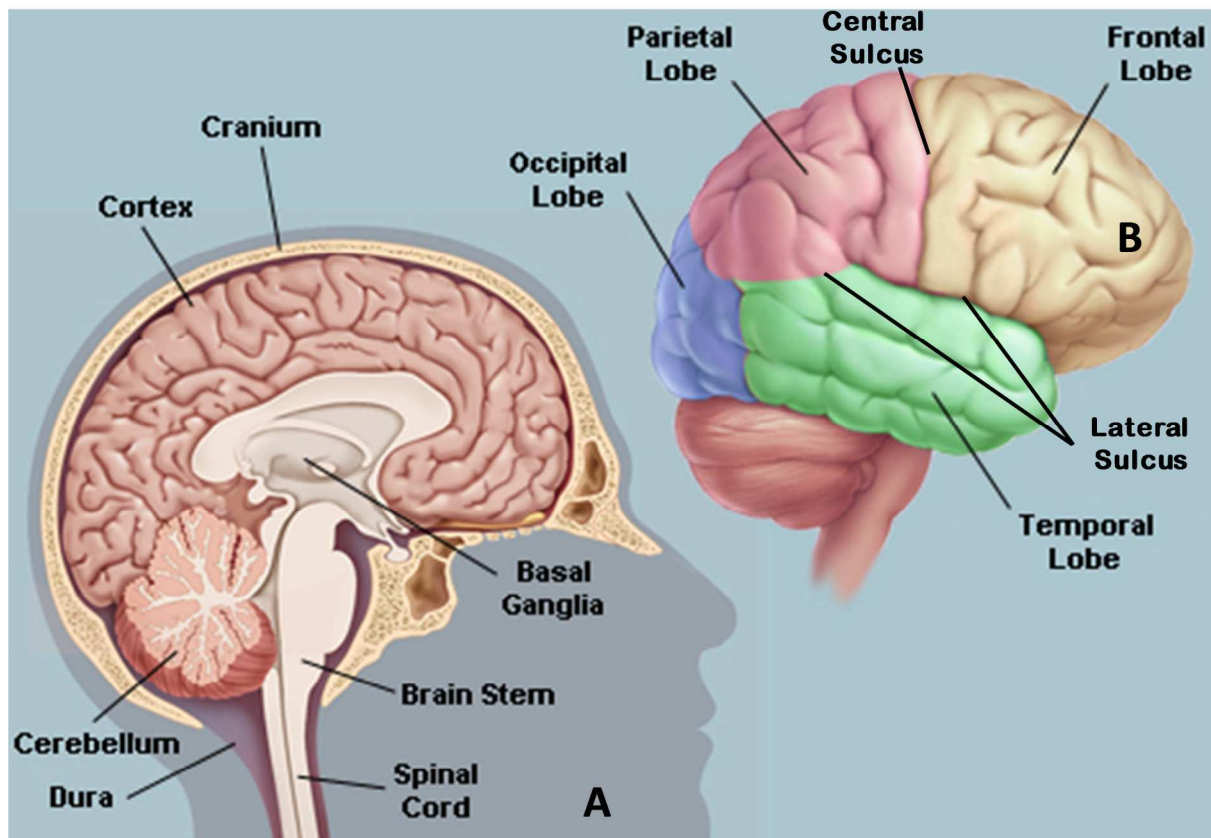


**Figure 2.2** An illustration of the main areas of: (A) a cross-section of the whole head and (B) the brain (Wolfe 2010).

## 2.4 Neuronal Activity

As briefly mentioned in Section 2.2.2, neuronal currents can be considered in two stages: along the axon (action potential) and in dendrites (post-synaptic potential).

### 2.4.1 Action Potentials

An *action potential* (AP) is simply an electrical current that travels down the axon of a neuron. An AP can only occur when charge separation occurs across a cell membrane. There are potassium ions ( $K^+$ ), sodium ions ( $Na^+$ ), chloride ions ( $Cl^-$ ), and large organic anions in the neuron. The neuron membrane has many channels which only allow  $Na^+$  and/or  $K^+$  to move through them. These special  $Na^+$  and  $K^+$  channels have gates that open and close in response to the membrane voltage (voltage-gated channels). When a neuron is resting (not transmitting an electrical message),  $Na^+$  and  $K^+$  ions move down their concentration gradients through their membrane channels to opposite sides of the membrane. Meanwhile, a specialized pump ( $Na^+/K^+$  pump) located in the membrane maintains the concentration gradient. In a neuron at rest, the outside concentration of  $Na^+$  is higher than inside the cell,

while the inside concentration of  $K^+$  is higher than outside the cell (as shown in Figure 2.3). This difference results in the inside of the axon being negative charged relative to the outside. This is called the *resting potential* (which is typically -70 mV).

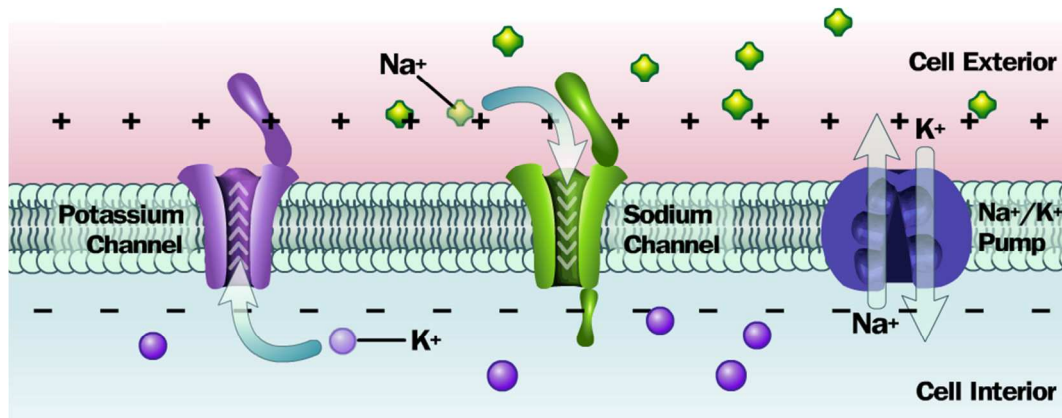


**Figure 2.3** Schematic representation of the resting state ion distribution in a cell. Adapted from (Bohan 2005).

A stimulus, which can be external (e.g. chemical, light, electricity, pressure, touch or stretching) or internal (stimulated by chemical activity at synapses (Sanei *et al.*, 2007)), must be above a threshold level to set off an AP. Very weak stimuli cause a small local electrical disturbance, but do not produce a transmitted AP. As soon as the stimulus strength goes above the threshold, an action potential appears and travels down the nerve. The spike of the AP is mainly caused by opening of  $Na^+$  channels. Opening the gates of  $Na^+$  channels allows  $Na^+$  to rush into the cell, carrying positive charge. This makes the membrane potential positive (*depolarization*), producing the spike. Figure 2.4 shows the stages of the process during evolution of an AP (Sanei *et al.*, 2007).

- I. When the dendrites of a nerve cell receive the stimulus, the  $Na^+$  channels will open. If the opening is sufficient to drive the interior potential from the resting potential, -70 mV, up to -55 mV, the process continues.
- II. As soon as the action threshold is reached, additional  $Na^+$  channels (sometimes called voltage-gated channels) open. The  $Na^+$  influx drives the interior of the cell membrane up to approximately +30 mV. The process is called *depolarization*.
- III. Then  $Na^+$  channels close and the  $K^+$  channels open. Since the  $K^+$  channels are much slower to open, the depolarization has time to be completed. If both the  $Na^+$  and  $K^+$  channels opened at the same time this process would drive the system towards neutrality and prevent the creation of the AP.
- IV. Having the  $K^+$  channels open, the membrane begins to repolarize back towards its rest potential.

- V. The *repolarization* typically overshoots the rest potential to a level of approximately -90 mV. This is called *hyperpolarization* and would seem to be counterproductive, but is important in the transmission of information. Hyperpolarization prevents the neuron from receiving another stimulus during this time, or at least raises the threshold for any new stimulus. Part of the importance of hyperpolarization is in preventing any stimulus already sent up an axon from triggering another AP in the opposite direction. In other words, hyperpolarization ensures that the signal is transmitted in one direction.
- VI. After hyperpolarization, the  $\text{Na}^+/\text{K}^+$  pumps eventually brings the membrane back to its resting state of -70 mV by restoring the original concentrations of  $\text{Na}^+$  and  $\text{K}^+$ .

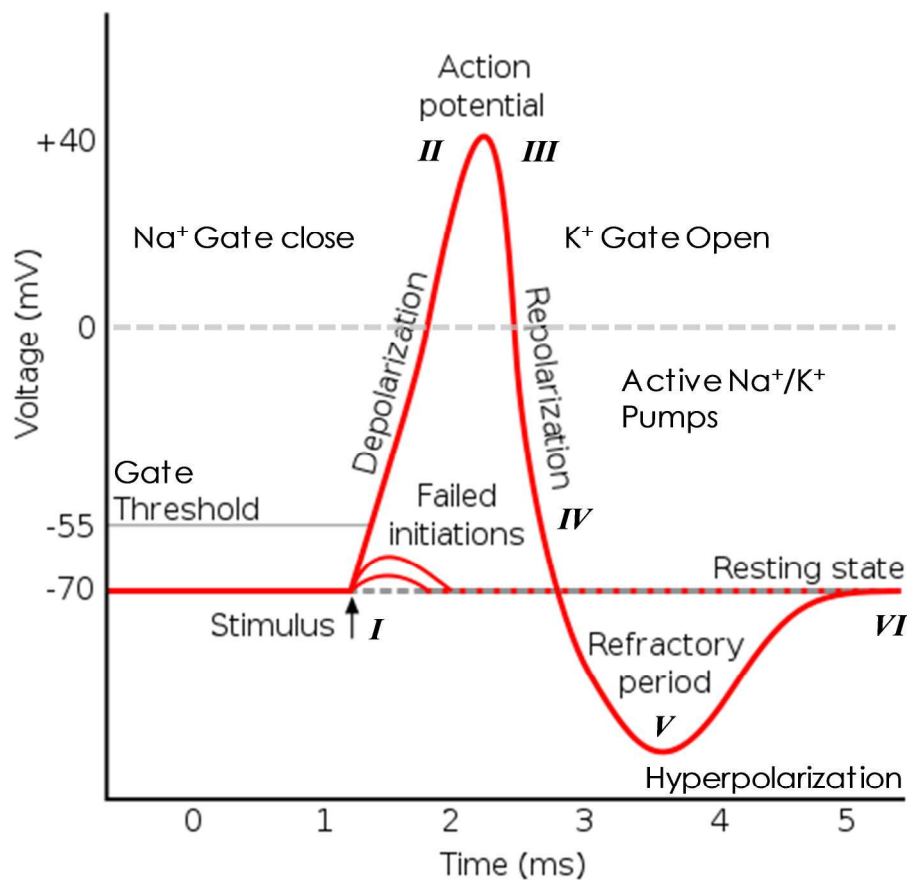


**Figure 2.4** Changing the membrane potential by closing the  $\text{Na}^+$  channels and opening  $\text{K}^+$  channels. Modified from (Sanei et al., 2007).

The APs typically last between 0.4 and 1.5 milliseconds. The nerve requires approximately two milliseconds before another stimulus is presented which is called the *refractory period*. During this time no AP can be generated.

### 2.4.2 Postsynaptic Potential (PSP)

The AP can traverse long axonal distances, reaching the nerve terminal without loss of amplitude. On arrival at the nerve ending, the AP generally stimulates the release of a neurotransmitter from the synaptic vesicles. The neurotransmitter then diffuses across the synaptic cleft, a gap of approximately 50 nm between the presynaptic and postsynaptic cells (Figure 2.1). On arrival at the postsynaptic cell, the neurotransmitter binds with proteins in the membrane causing one of two things to happen. In the case of an excitatory synapse, where the permeability to ions is increased, the membrane becomes depolarized, while it becomes hyperpolarized in the case of inhibitory synapses, where the permeability to ions is decreased. Ions (mainly  $\text{Na}^+$ ) then flow into the cell and along the dendrite towards the soma setting up a primary current and a voltage change, known as the *postsynaptic potential (PSP)* (Sanei et al., 2007).

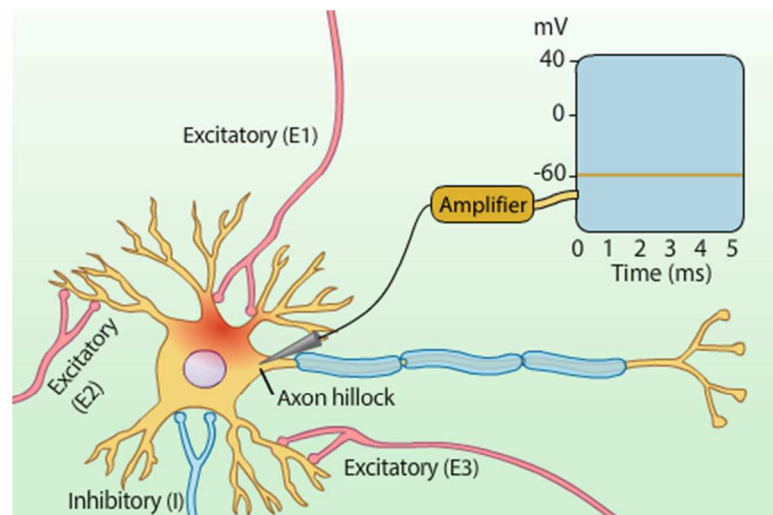


**Figure 2.5** Schematic showing three excitatory (E1, E2 & E3) and one inhibitory (I) synapse and PSP is shown to be recorded from Axon hillock. Adapted from (Purves et al., 2012).

The PSPs can be either depolarizing, often (but not always) resulting in excitatory postsynaptic potential (EPSP) (Fig. 2.6A) or hyperpolarizing, resulting in an inhibitory postsynaptic potential (IPSP) (Fig. 2.6B) (Shepherd 1974). PSPs generally move passively along the dendritic membrane, gradually becoming smaller as they spread. Therefore the PSPs from more distant synapses will decay more than PSPs from synapses close to the integration zone at the axon hillock. The PSPs produced at most synapses are usually well below the threshold for generating postsynaptic action potentials (Fig. 2.6C).

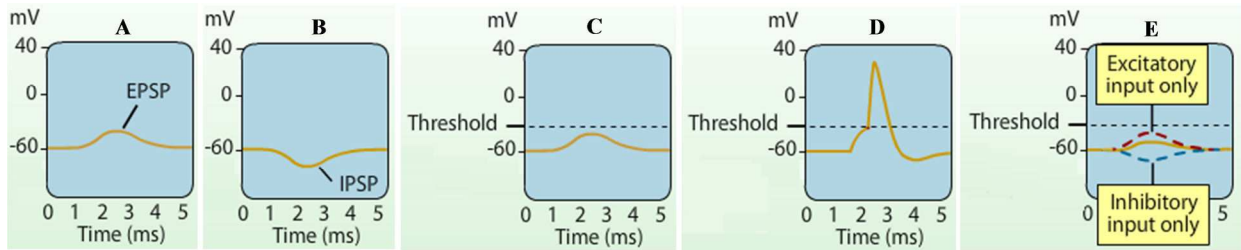


**Figure 2.6** Generation of PSP depending on excitatory (A), inhibitory (B) synapse; below threshold PSP (C), combined excitatory (D) and excitatory-inhibitory synapse (E). Modified from (Purves et al., 2012).

Suppose that two excitatory endings (E1 & E2 in Fig. 2.5) are activated, causing local depolarizations of the cell body. Considered alone, neither would be sufficient to trigger an action potential (Fig. 2.6A&C), but when combined, the two depolarizations sum to depolarize the membrane in the hillock region to threshold (Fig. 2.6D). When inhibitory synapses are also active (Fig 2.6B), the membrane potential tends to be stabilized below threshold because they induce hyperpolarizations or sub-threshold depolarizations that cannot reach threshold. These postsynaptic effects also spread passively, dissipating as they travel. Because some PSP excite and others inhibit the hillock, these effects partially cancel out each other. Thus the net effect is the difference between the two: the neuron subtracts the IPSPs from the EPSPs (Fig. 2.6E).

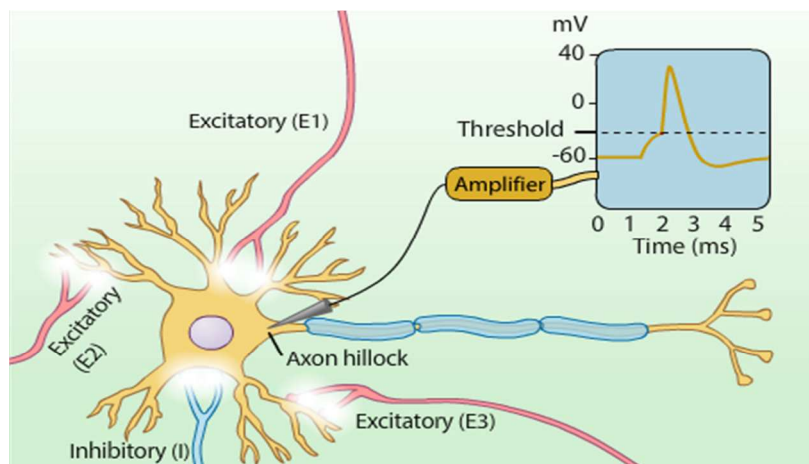


**Figure 2.7** Generation of PSP for three excitatory and one inhibitory synapse. Adapted from (Purves et al., 2012).

Postsynaptic effects that are not absolutely simultaneous can also be summed, because PSPs last between 10 and 20 milliseconds before fading away. The closer they are in time, the greater the overlap and the more complete the summation, which in this case is called *temporal summation*. The summation of potentials originating from different physical locations across the cell body is called *spatial summation*. Only if the overall sum of all the



potentials – both EPSPs and IPSPs – is sufficient to depolarize the cell at the axon hillock to the threshold level is an AP triggered (Fig. 2.7).

## 2.5 Source of the EEG Signal

Both EPSP and IPSP, rather than APs, represent the most significant source of scalp-recorded EEG signals (Purves *et al.*, 2012). In fact, although APs have higher amplitude ( $\sim 100$  mV vs  $\sim 10$  mV), PSPs have a longer duration, which increases the probability that they will occur with a temporal overlap. The PSPs also involve a larger membrane surface; these characteristics allow both temporal and spatial summation. APs last too short a time to contribute to scalp-recorded EEG, except during synchronous events such as sleep transient activity and epileptic discharges.

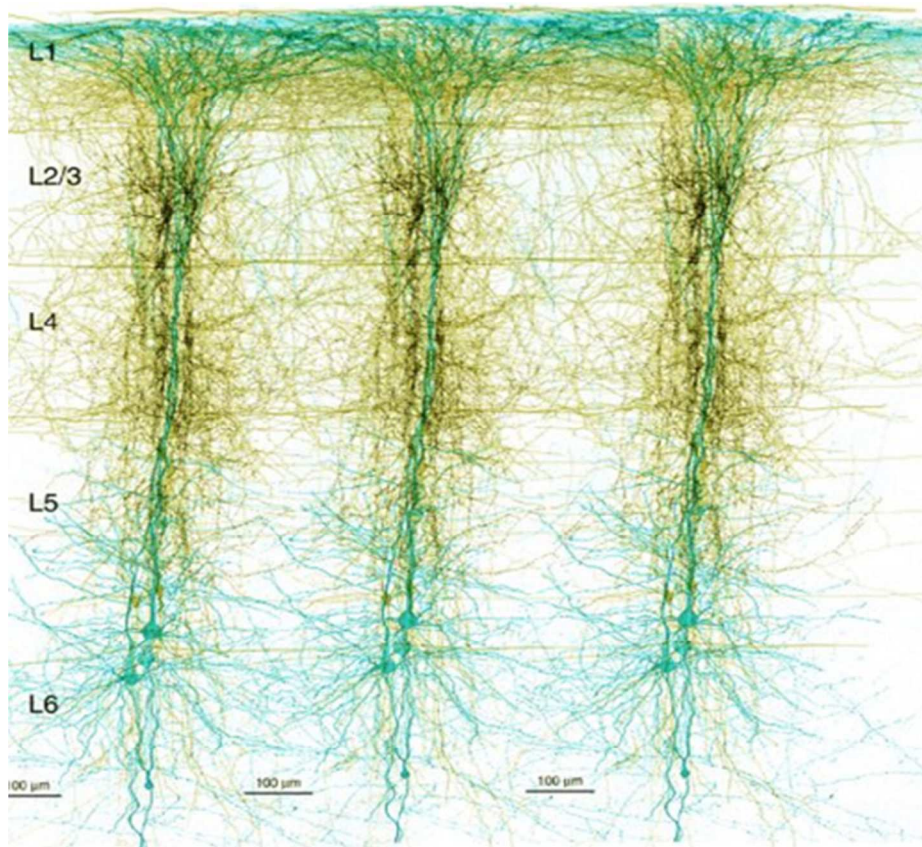


**Figure 2.8** *Pyramidal neurons: dendritic structure and synaptic integration. Modified from (Kandel 2000).*

To understand the contribution of a single neuron to the EEG, we can consider the flow of current produced by an EPSP on the tip of the dendrite of a cortical pyramidal neuron. Current flows into the dendrite at the site of generation of the EPSP, creating a current sink. It then must complete a loop by flowing down the dendrite and back out across the membrane

at other sites, creating a current source. Every neuron receiving synaptic inputs can therefore be thought of as a dipole with a specific orientation and polarity. A dipole corresponding to a single neuron is not detectable with EEG, but when thousands of neurons with similar orientation receive similar synaptic inputs, the dipoles sum together to produce strong voltage signals at the scalp (Adrian *et al.*, 1934). Although the sources of scalp EEG are not still completely clear, the findings and hypotheses that have been published in the literature are summarized below.

### 2.5.1 Cortical Pyramidal Neurons

Scalp-recorded EEG oscillations are hypothesized to be generated by the summation of excitatory and inhibitory PSPs in cortical pyramidal neurons (Speckmann *et al.*, 1993) (Fig. 2.8). Pyramidal cells of the cortex are parallel to a large degree, and the activity within them is synchronized by thalamocortical connections. “*The contribution to the electric field of neurons acting synchronously is approximately proportional to their number, and, for those firing non-synchronously, as a square root of their number*” (Blinowska *et al.*, 2006). This implies that the contribution of the neurons acting synchronously for generating EEG is much larger than those are not synchronised. Tens of thousands of synchronously activated pyramidal cortical neurons are assumed to be involved in the generation of an EEG oscillation. The coherent orientation of their dendritic trunks (parallel to each other and perpendicular to the cortical surface) allows summation and propagation of the EEG signal to the scalp surface (Nunez *et al.*, 2000).

### 2.5.2 Local-Scale and Large-Scale Synchronization

The signal recorded at the scalp is due to the spatial summation of current density induced by synchronized post-synaptic potential occurring in large clusters of neurons. Considering that the diameter of EEG electrodes (~10 mm) is several orders of magnitude larger than single neurons (~ 20  $\mu\text{m}$ ) and that the area of an electrode covers approximately 250,000 neurons (Baillet *et al.*, 2001), it is clear that many neurons must be activated synchronously in order to detect an EEG signal at the scalp.

Animal studies have described considerable synchronization among neighbouring neurons (local-scale synchronization) (Llinas *et al.*, 1999), as well as between neuronal assemblies of distant brain regions (large-scale synchronization) (Bressler *et al.*, 2001). Large scale

synchronization is a key mechanism for neuronal communication between spatially distributed brain networks (e.g. language processing (Weiss *et al.*, 2003)). Interestingly, higher frequency oscillations (e.g. gamma) appear to originate from smaller neuronal assemblies, whereas low frequency oscillations (e.g., theta) span larger neuronal populations (Buzsaki *et al.*, 2004).

## 2.6 EEG Recording Equipment and Techniques

Richard Caton (1842–1926) is regarded as the first scientist to investigate brain potentials. He worked on the exposed brains of cats and rabbits, measuring electric currents by means of a galvanometer, where a beam of light reflected from its mirror were projected onto a scale placed on a nearby wall (Gloor 1969). The results (presented in 1875) showed that “*feeble currents of varying directions pass through the multiplier when the electrodes are placed at two points of the external surface, or one electrode on the grey matter and one on the surface of skull.*” This observation can be regarded as a discovery of electroencephalographic activity. In 1924, German physician, Hans Berger first measured the traces of brain electrical activity in both normal and abnormal brains of humans. The first rhythm that he documented was the alpha rhythm which is prominent in restful wakefulness with the eyes closed and drastically reduced by opening the eyes. He also documented the observation that the beta rhythm ‘replaced’ the alpha rhythm when the eyes were open. Although today’s electronics and software for EEG analysis benefit from the most recent technological developments, the basic principle remains unchanged from Berger’s time.

### 2.6.1 EEG Rhythms

The EEG is a continuous recording of waves of varying frequency and amplitude. The following rhythms have been distinguished in EEG (Fig. 2.9) (Blinowska *et al.*, 2006): delta (0.5–4 Hz), theta (4–8 Hz), alpha (8–13 Hz), beta (13–30 Hz), and gamma (above 30 Hz). Gamma components are difficult to record due to the low amplitudes of these signals, which generally also decrease as the frequency increases. Therefore often it is necessary to use ECoG or icEEG rather than scalp EEG to measure the higher frequency gamma responses. The contribution of different rhythms to the EEG depends on the age and behavioural state of the subject (mainly the level of alertness).

- Delta ( $\delta$ ) rhythms are actually most obvious in children, although they form a predominant feature in an adult’s EEGs recorded during deep sleep. These waves

usually have large amplitudes (20–200  $\mu\text{V}$ ) and show strong coherence over the whole scalp in this stage of sleep.

- Theta ( $\theta$ ) rhythms (5–100 $\mu\text{V}$ ) can be found in awake children and also occasionally in awake adults, and when visible are usually found over the anterior region of the head. Theta rhythms are also common found in adults when drowsy or in the transition between being awake and sleep. The activity in the theta band also can occur in emotional or some cognitive states and can be connected with the slowing of alpha rhythms caused by pathology.
- Alpha ( $\alpha$ ) rhythms (5–100  $\mu\text{V}$ ) are predominant during wakefulness and are most pronounced in the posterior regions of the head. They are best observed when the eyes are closed and the subject is in a relaxed state, but awake. They are strongly attenuated by attention (especially visual) and by mental effort. Mu rhythms have a frequency band similar to alpha, but their topography and physiological significance are different. They are related to the function of motor cortex and are prevalent in the central part of the head. It is much harder to find the mu rhythm in adults than the alpha rhythm, and it is detectable in only about 10-20% of the healthy adult population. A person suppresses mu wave patterns when he or she performs a motor action or when he or she visualizes the performance of a motor action. The mu wave is even suppressed when one observes another person performing a motor action (Blinowska *et al.*, 2006).
- Beta ( $\beta$ ) activity (2–20 $\mu\text{V}$ ) is characteristic for states of increased alertness and focused attention (Blinowska *et al.*, 2006).
- Gamma ( $\gamma$ ) activity (2–10  $\mu\text{V}$ ) is connected with information processing (e.g. recognition of sensory stimuli) and the onset of voluntary movements (Blinowska *et al.*, 2006).

In general, it can be summarized that the slowest cortical rhythms are related to an idle brain and the fastest to information processing.

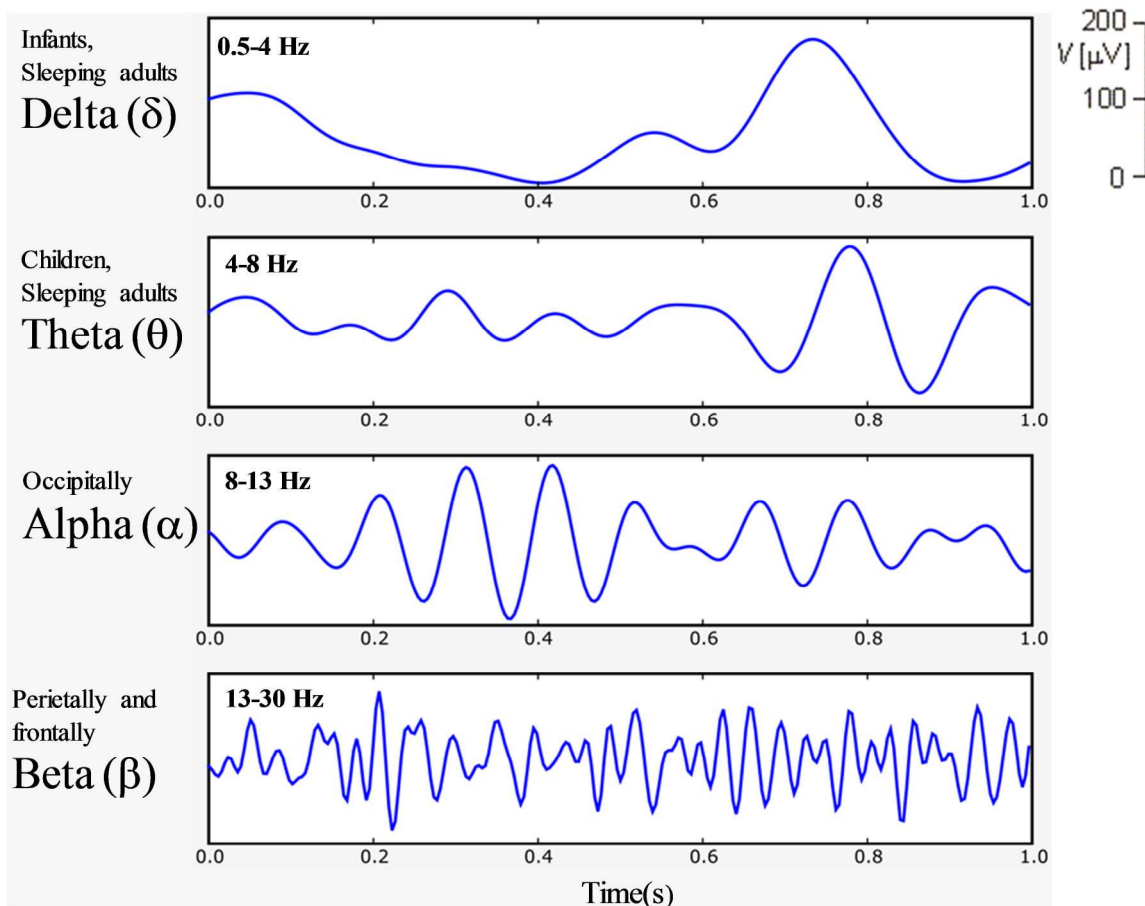


**Figure 2.9** Characteristic EEG rhythms, from the bottom:  $\beta$  (13–30 Hz),  $\alpha$  (8–13 Hz),  $\theta$  (4–8 Hz),  $\delta$  (0.5–4 Hz). Modified from (Blinowska et al., 2006).

### 2.6.2 Event Related Potential (ERP)

The Event Related Potential (ERP) is an EEG signal which can be used to investigate processing while subjects perform a task (e.g. processing a visual stimulus). Under such conditions, the data recorded directly from a subject contains more information than that recorded from the subject in normal awake or asleep conditions (Figure 2.10A) and in general, we are interested in the signal that is time and phase-locked to the stimulus. To obtain this information each point in time is marked when a stimulus occurs and average together a large number of trials so that everything that happens at fixed time-interval with respect to the stimulus and with the same phase is averaged in, with everything else that is non-phase locked the stimulus, being averaged out (Figure 2.10B).

This averaging process allows brain activity that is not related to the appearance of the stimulus to be filtered out, since such activity does not occur at a consistent time and phase relative to the stimuli. In the case of Fig. 2.10, the process of averaging therefore leaves an

ERP waveform showing electrophysiological activity related to processing of the visual stimulus. Many of an ERP waveform's peaks can be linked to specific cognitive mechanisms (Davis 2011). ERP's have high temporal resolution since it involves electrophysiology; however, as with all other EEG measures, the spatial resolution is poor.

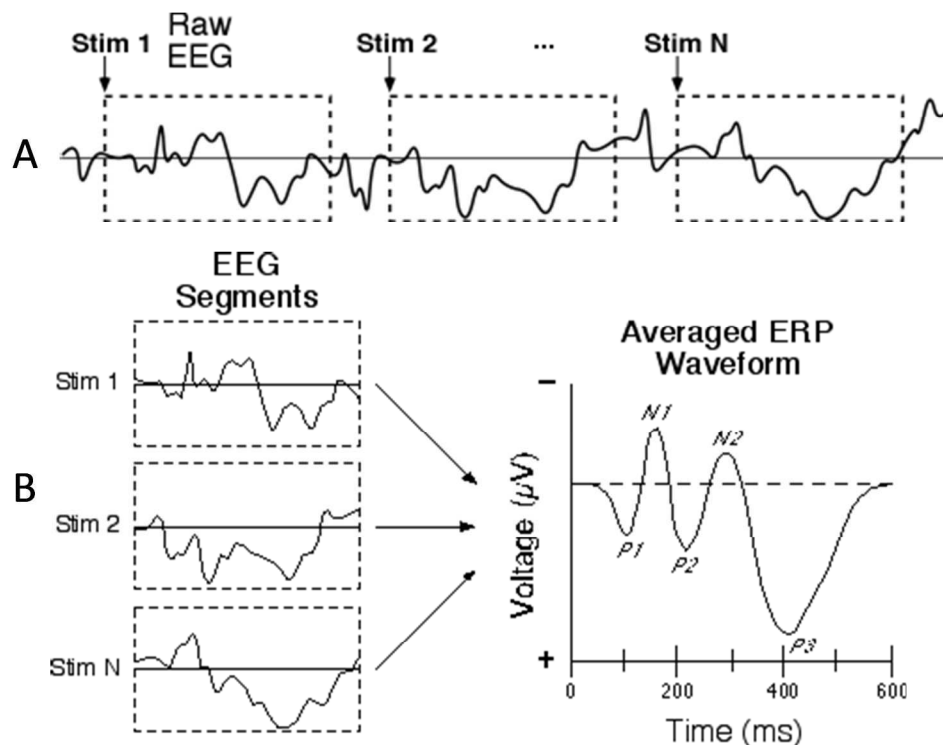


**Figure 2.10** Demonstration of eliciting ERP from the raw EEG data. (A) Raw EEG data recorded with multiple visual stimuli, (B) segmented EEG data averaged to generate ERP. Adapted from (Davis 2011).

Indeed, ERPs can be considered to result from a reorganization of the phases of the on-going EEG signals (Sayers *et al.*, 1974). However, it has also been shown that visual stimuli can reduce the amplitude of the on-going EEG amplitude (Vijn *et al.*, 1991) and thus can block or desynchronize the on-going alpha activity. These types of changes are time-locked to the event, but not phase-locked. This effect which relates to the effect of stimulation on the oscillatory rhythms may be considered to be due to a decrease or an increase in synchrony of the underlying neuronal populations. The former case is called event-related activity in desynchronization or ERD (Pfurtscheller 1977), and the latter event-related synchronization (ERS) (Pfurtscheller 1992). For example, the suppression of mu waves during a motor task is an example of ERD.

### 2.6.3 Modes of EEG Recording

EEG consists of measurements of a set of electric potential differences between pairs of scalp electrodes connected to opposite ends of a differential amplifier. Research protocols can use up to 256 electrodes (Baillet *et al.*, 2001). EEG recordings depend intimately on the positions of the individual electrodes and how they are paired. There are three different methods for pairing electrodes:

- **Unipolar Mode:** In this mode, one electrode or a pair of electrodes is common to all channels as in Fig. 2.11. This electrode is commonly known as the reference.

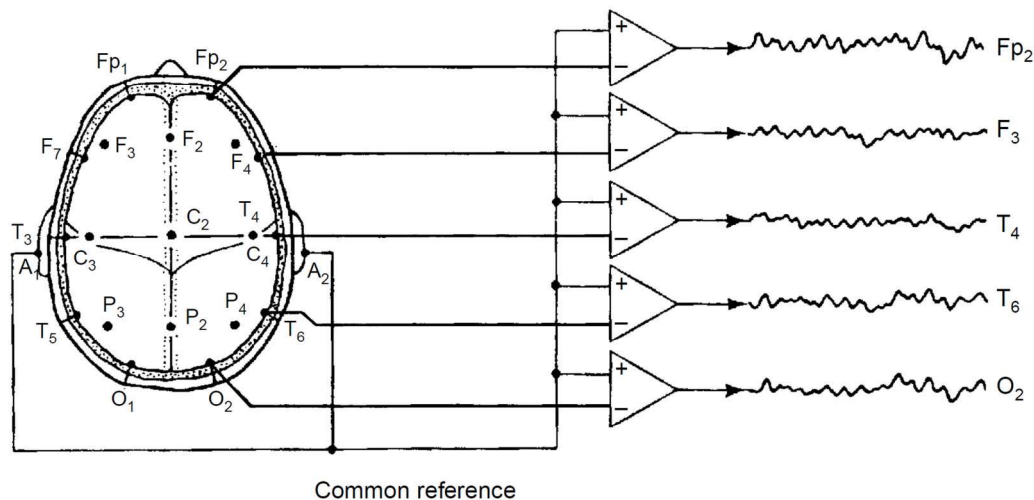


**Figure 2.11** Shows the unipolar mode configuration for recording EEG (Ananthi 2005).

Ideally, this common electrode is regarded as electrically inactive, placed on a region of the head with little on-going electrical activity from the brain. However, in practice, this is difficult to achieve and electrical activity near the reference electrode will appear in all channels. The ear is sometimes used as the site of the reference electrode, as this location is close to the brain, but doesn't show neuronal activity. This set up ensures that the electrode closest to the area of interest of the neuronal activity will show the largest amplitude. The use of a single reference allows some localisation of the neuronal activity. Although one electrode is common to all channels, to reduce interference and artefacts, it is desirable not to ground this common electrode and a separate ground electrode is often connected between the subject and the instrumentation ground (Ananthi 2005).

- **Bipolar Mode:** In bipolar mode, the channels are connected in series between electrode pairs as shown in Fig. 2.12. It may be noted from this figure that the change in the recorded EEG between these electrodes pairs (e.g., pair F<sub>8</sub>-T<sub>4</sub> and T<sub>4</sub>-T<sub>6</sub>)

suggest a local maximum/minimum at this location as  $T_4$  is common to these electrode pairings. The electrode immediately over a region where there is high neuronal activity (for example caused by an evoked potential) will cause a positive deflection in one recording channel and a negative deflection in the adjacent recording channel so that the electroencephalographer will see an apparent  $180^\circ$  phase difference between them. This “phase reversal” is accepted as the most reliable means of localization of discrete phenomena. In referential recordings, when the reference is inactive (or is the least active electrode), the site of maximal involvement is identified as the one having the greatest voltage. However, in bipolar recording, amplitudes can be misleading; in any given channel higher amplitude indicates a greater potential difference, not necessarily the most active site, while low amplitude could be due to two electrodes being equally active and cancelling or both electrodes being inactive. Therefore the comparisons between all electrodes on the head cannot easily be made.

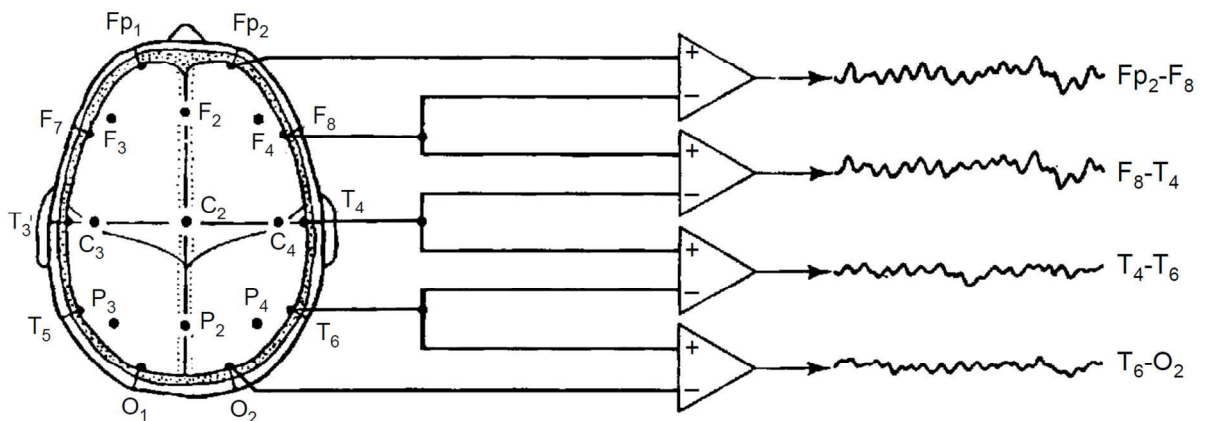


Figure 2.12 Shows the bipolar mode configuration for recording EEG (Ananthi 2005).

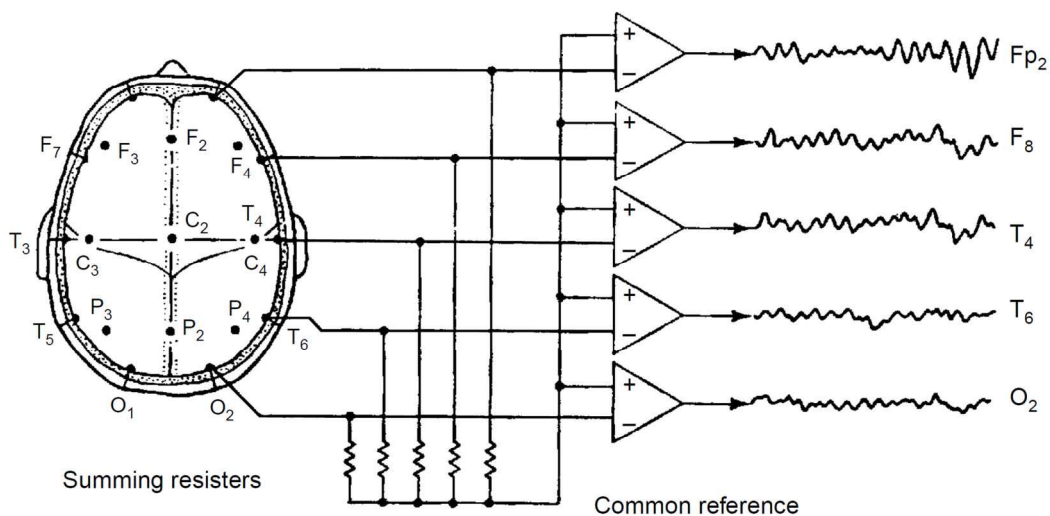


Figure 2.13 Shows the averaging mode configuration for recording EEG (Ananthi 2005).



- **Averaging Mode:** In this mode, one input lead of all amplifiers is taken to the common point of a summing network in which equal resistors are connected to each electrode (as shown in Fig. 2.14). The recording will now indicate deviations from the mean instantaneous potential of the electrode system. Thus an isolated neuronal feature, such as an evoked potential, is localized and will stand out in one or a small number of channels.

### 2.6.4 Electrode Placement: International 10-20 System

The placement of electrodes for any of these modes of EEG recording usually follows the international 10-20 system (Figure 2.14). This is so named, as the electrodes are spaced from one another either at 10% or 20% of the total distance between given anatomical landmarks on the head (Jasper 1958; Cooper *et al.*, 1969). The anatomical landmarks which are used for positioning the EEG electrodes are: first, the nasion which is the distinctly depressed area between the eyes, just above the bridge of the nose; second, the inion, which is the lowest point of the skull at the back of the head and is normally indicated by a prominent bump; third, left and right preauricular points (which are the depressions in the bone in front of the ears).

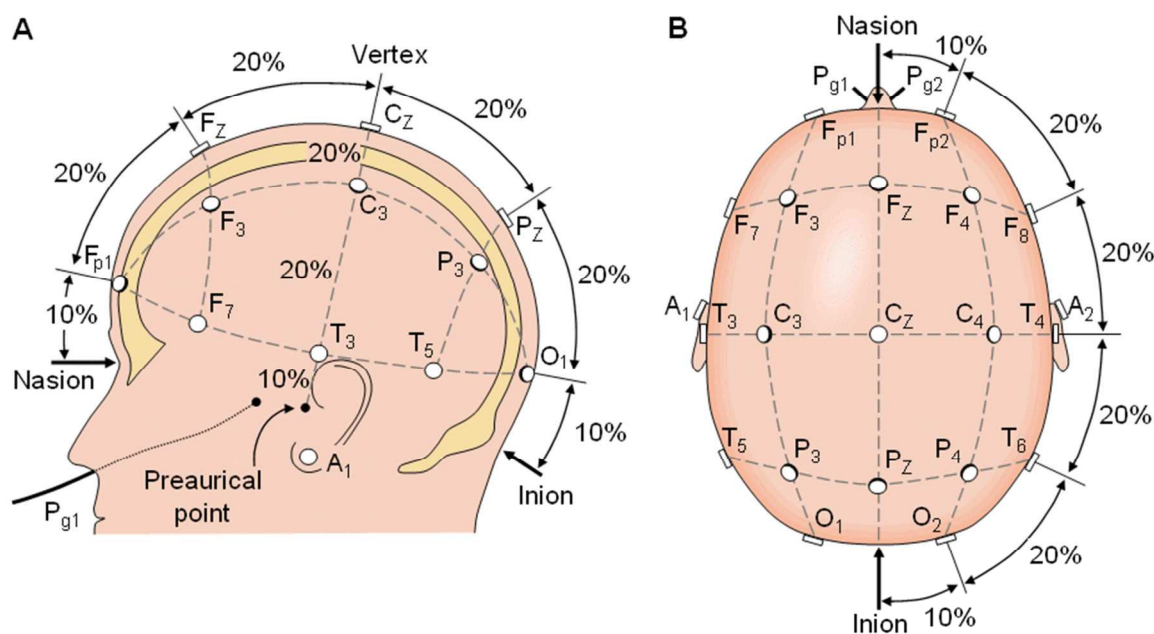


**Figure 2.14** The figure illustrating the international 10-20 system. Adapted from (Cooper *et al.*, 1969).

Each site has a letter to identify the lobe and a number to identify the hemisphere location. The letters F, T, C, P and O stand for frontal, temporal, central, parietal, and occipital lobes,

respectively. Note that no central lobe exists; the "C" letter is used only for identification purposes. A "z" (zero) refers to an electrode placed on the midline. Even numbers (2,4,6,8) refer to electrode positions on the right hemisphere, whereas odd numbers (1,3,5,7) refer to those on the left hemisphere and the smaller the number, the closer the position of the electrode is to the midline. In addition, the letter codes A, Pg and Fp identify the earlobes, nasopharyngeal and frontal polar sites respectively. The international 10-20 system has to be modified when an increased number of electrodes (such as 32 or 64) are added into the montage. For the caps used in these instances, the first 21 electrodes follow the 10-20 system and then are adapted to include the extra electrodes, with caps often following equidistance montages such as the one shown in Figure 2.15, which is used in the work presented in this thesis.

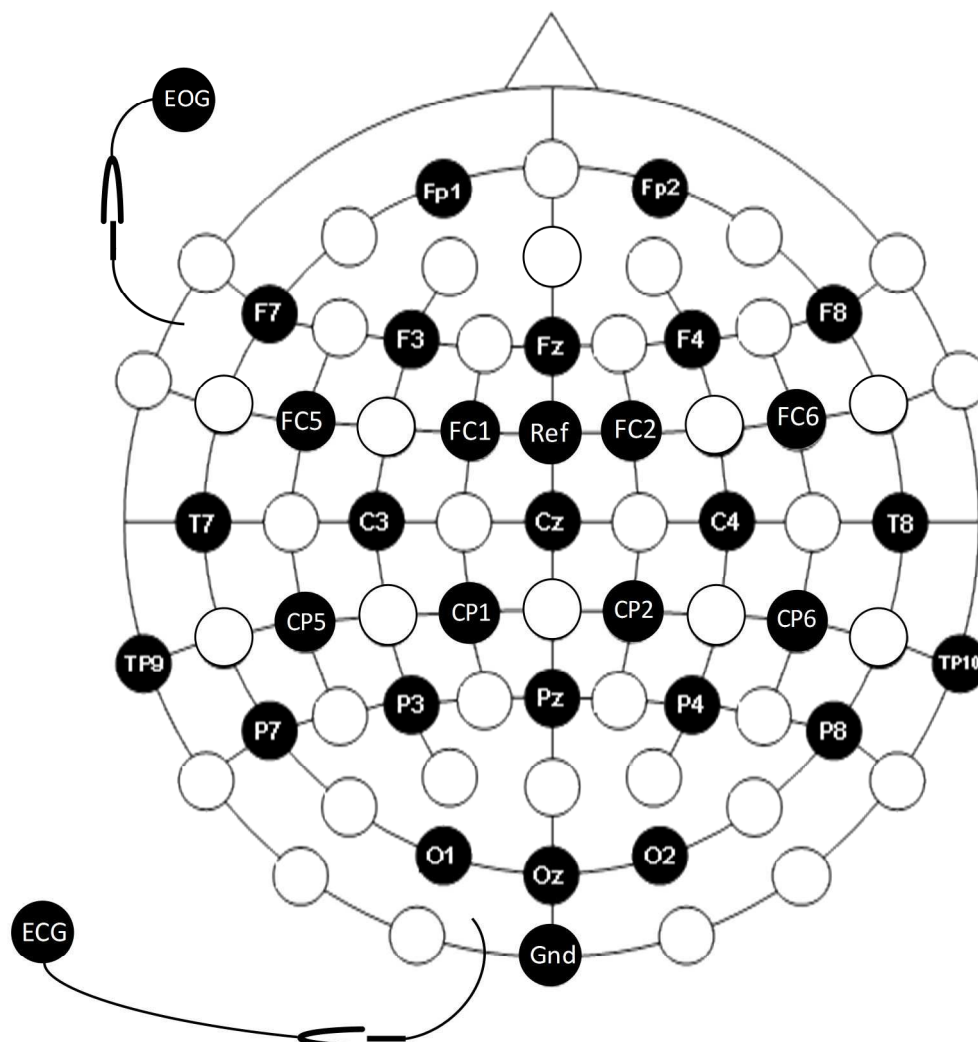


**Figure 2.15** The electrode configuration for the 32 channel cap used throughout this thesis (Courtesy of EasyCap GmbH).

The method employed by the recording system, used in this thesis, is the unipolar method. The reference electrode is placed on the top of the head, situated between electrodes Cz and Fz (Figure 2.14), in a position known as FCz. A ground electrode (GND) is also used in EEG recordings to remove interference from common mode voltages. The voltages at the reference and the other leads are measured relative to the GND, so only the differences in potential between the reference and the other lead are amplified. The EEG electrodes can be fitted to the head using an elastic cap, as used in this thesis, which is quick to use and ensures near uniform coverage of the scalp. Alternatively electrodes can be glued to the skin at selected locations directly above cortical regions of interest (Ananthi 2005). This is particularly useful for prolonged clinical observation. The key to using surface electrodes, which are used throughout this work, is to get a good electrical contact between the surface of the scalp and the electrode. To do this, the grease and dead skin cells are removed using alcohol and abrasive gels on the area where the electrode will be placed. Then a conductive gel is used to make a good electrical connection between the scalp and the electrode. In clinical EEG (recorded without other simultaneous measurements), it is reasonable to achieved electrode-scalp impedance below 5 k $\Omega$ . However, new high impedance amplifiers can produce high quality EEG data even when the scalp-electrode impedance is as high as 50 k $\Omega$  (Basar *et al.*, 1999). An impedance value below 20 k $\Omega$  was the target for all the electrode-scalp/phantom connections made during the experimental work presented in this thesis. The relatively high value was chosen for two reasons: firstly, a 5 k $\Omega$  resistor is already built into the electrodes for safety reasons (discussed in Chapter 4) rendering it impossible to reduce impedances below 5 k $\Omega$  and secondly, to reduce the length of time it takes to put the cap on subjects whilst not effecting data quality severely.

The signals recorded on the human scalp are fed into a set of differential amplifiers and the differential output is then hardware filtered to limit the recording frequency to a band of interest. Brain Amp MR compatible amplifiers (Brain Products GmbH, Germany) were used in this thesis. These use a high pass filter at 0.016 Hz and a low pass filter at 250 or 1000 Hz (user selectable) within the hardware. An analogue-to-digital converter is then employed to convert the analogue EEG signals to digital signals, which can be displayed and saved by a computer for further analysis. The best practices of recording and digitizing these EEG signals are described in detail in Chapter 4.

## 2.7 Advantages and Disadvantages of EEG

EEG is extensively used in neuroscience, cognitive science, cognitive psychology, neuro-linguistics and psychophysiological research, as well as in clinical investigation of neurological diseases. However, there are several other methods that can be used to study brain function, including fMRI, PET, MEG, MRS, ECoG, SPECT, NIRS and EROS. EEG hardware cost are significantly lower than that of most other techniques and the equipment itself is much more portable than the equipment used in fMRI, SPECT, PET, MRS, or MEG (Hamalainen *et al.*, 1993; Vespa *et al.*, 1999). EEG has very high temporal resolution, on the order of milliseconds. Therefore, neuronal signals are commonly sampled at rates of between 250 and 2000 Hz in clinical practice and also in research settings; although modern EEG amplifiers are capable of recording EEG data at a sampling rate of more than 20,000 Hz (Vespa *et al.*, 1999). This level of temporal resolution can only be obtained from two other non-invasive techniques, MEG and EROS. EEG is comparatively insensitive to subject movement and is a silent method, which make it suitable for study of the responses to auditory stimuli. There is no issue of claustrophobia in the case of EEG, unlike fMRI, PET, MRS, SPECT, and sometimes MEG (Hamalainen *et al.*, 1993; Vespa *et al.*, 1999; O' Regan *et al.*, 2010). In contrast to some of the techniques, such as MRI and MRS, EEG does not involve exposure to high-strength magnetic fields, which makes it easier to implement on participants with metallic implants in their body. Unlike PET, EEG does not involve exposure to radioactivity. EEG has the additional advantage that it is a fully non-invasive technique, unlike ECoG in which electrodes are placed directly on the surface of the brain (O' Regan *et al.*, 2010).

Therefore, as mentioned above, EEG enables the non-invasive measurement of the electrical activity of cortical neurons via electrodes placed on the scalp. This means that EEG is able to follow fast dynamics of the signal with a temporal resolution at the millisecond scale. However, the relatively low number of electrodes and the nature of the inverse problem of source localization, which is intrinsically ill-posed, mean that the EEG technique has poor spatial resolution. Another major drawback of EEG is that it can only reliably detect signals arising from the cortical surface; deep sources are difficult to detect. The electrical activity from deeper generators is dispersed and attenuated by volume conduction effects and therefore cannot easily be measured with EEG. It is also not possible to measure activity from small networks of neurons; rather a large number of neurons must have coherent activity to

be detectable (as discussed in Section 2.5.1). Another significant problem in using EEG is the effect of the heterogeneous conductivities of the tissues of the head. In particular the skull is not a good conductor (although the brain and scalp are highly conductive) and this causes blurring of the EEG signal, leading to further difficulties in source localisation. It is important in EEG experiments to make the electrode-scalp resistance as low as possible, with all electrodes having similar impedances. If the impedance differs significantly between electrodes, then neuronal activity may appear artificially higher at an electrode with low electrode-scalp impedance relative to those electrodes with high impedance. Moreover, it often takes a long time to connect a subject to an EEG system, as it requires precise placement of dozens of electrodes around the head and the use of gels, saline solutions and/or pastes to keep them in place and ensure good connections between the scalp and electrodes. Although the length of time differs dependent on the specific EEG set-up and number of channels being used; it takes considerably longer time to prepare a subject for EEG recordings than it does for MEG, fMRI, MRS, and SPECT (O' Regan *et al.*, 2010). As discussed in this section there are many instances when EEG can be helpful in studying brain function. However, there are some limitations to this technique, some of which can be addressed using fMRI. Therefore, how MRI works and how it can be used to study brain function will be covered in the next section.

### **2.8 Magnetic Resonance Imaging (MRI)**

MRI has become an important non-invasive imaging modality since its first implementation by Mansfield *et al.*, (1973) and Lauterbur (1973). Several more years were required to design and develop imaging hardware to the level necessary for producing high-quality diagnostic images of the human body. Despite its relatively slow beginning, MRI has become an indispensable diagnostic tool since the early 1980s, and because it provides unique contrast between soft tissues and high spatial resolution, MRI has revolutionized diagnostic imaging in medicine. MRI has also found a number of applications in the fields of biology, engineering, and materials science. MRI is based on the phenomenon of Nuclear Magnetic Resonance (NMR), independently discovered by Bloch and Purcell in 1946. This discovery, which resulted in the award of a shared Nobel Prize in 1952, has led to numerous applications in chemistry and biology. More recently NMR has moved into the exploration of more complex structures such as living tissues, and is nowadays applied in the clinic thanks to its potential to image the body (through MR imaging) at a millimetric scale. A relatively new

imaging technique (fMRI), relying on sensitivity of the NMR signal from brain tissue to the different magnetic properties of oxygenated and deoxygenated blood, has revolutionised research in functional brain mapping. The fundamental principles of MR imaging and Blood Oxygenation Level Dependent (BOLD) fMRI are described in detail in the following sections of this chapter.

### 2.8.1 Proton Spin in External Magnetic Field

The signal that is measured in magnetic resonance imaging (MRI) usually arises from the nuclei of the tissue's hydrogen atoms (i.e. protons) which possess a physical property known as *spin*. Each proton has a small magnetic dipole moment, but in general the spin vectors of hydrogen nuclei within the tissue are randomly oriented in all directions, which results in zero net magnetization being observed in the tissue. However, when the tissue is put into the strong magnetic field inside the magnetic resonance (MR) scanner's bore, the spins will align either anti-parallel or parallel to the *static magnetic field*,  $B_0$ .

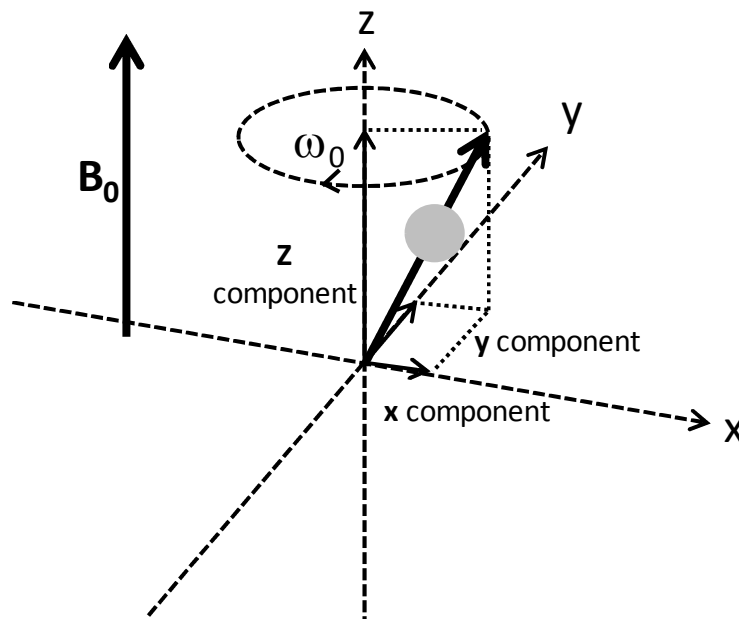


**Figure 2.16** Inside a magnetic field, a proton precesses about an axis parallel to the static magnetic field,  $B_0$ . The z-component of the spin vector (projection of the spin onto the z axis) is the component of interest because it does not change in magnitude or direction as the proton precesses. The x and y components vary with time at a frequency  $\omega_0$  proportional to  $B_0$  as expressed by Equation 2.1 (adapted from (Brown et al., 2003)).

A tiny majority of the spins adopt the parallel alignment and their magnetic moments add up, giving rise to a net *macroscopic magnetisation*,  $\mathbf{M}$  which is parallel to  $B_0$ . In the  $B_0$  field, individual protons precess about the magnetic field and are tilted slightly away from the axis of the magnetic field, but the axis of rotation is parallel to  $B_0$ , as shown in Figure 2.16. This precession is at constant rate which is proportional to the strength of the applied static magnetic field and is expressed by the Larmor equation (Eq. 2.1):

$$\nu_0 = \omega_0/2\pi = \gamma B_0/2\pi \quad (2.1)$$

where  $\nu_0$  is the Larmor frequency in MHz,  $B_0$  is the magnetic field strength in Tesla (T) that the proton experiences, and  $\gamma/2\pi$  is a constant for each nucleus in MHz/T, known as the gyromagnetic ratio (42.6 MHz/T) (Brown *et al.*, 2003).

### 2.8.2 Magnetic Resonance Effect

A radiofrequency (RF) pulse with the Larmor frequency and duration of a few milliseconds is transmitted which rotates the longitudinal magnetisation into the transverse plane. This pulse, also known as an excitation pulse, contains many frequencies spread over a narrow range or bandwidth (Westbrook *et al.*, 1993). After sending the initial RF pulse, a detector tuned to the Larmor frequency is switched on, and picks up the signal from the precessing transverse magnetisation. The existence of the net magnetisation inside the magnetic field is an indicator of the presence of protons, and the measurement of  $\mathbf{M}$  with a certain spatial resolution can be used to construct a proton density image. It is worth mentioning that the initial step of tipping the magnetisation only works if the frequency of the transmitted RF is exactly equal to the protons' Larmor frequency (resonance frequency) (Westbrook *et al.*, 1993).

### 2.8.3 Relaxation

The process by which protons release the energy that they absorbed from the RF pulse is called *relaxation*. After the *relaxation time*, the magnetisation has returned to its equilibrium state, parallel to  $B_0$ . Relaxation consists of two simultaneous processes:

- The longitudinal component of the magnetisation (i.e. the component parallel to the magnetic field) approaches its *equilibrium value* with a *time constant*  $T1$ , the *longitudinal relaxation time*. This process is also called *spin lattice relaxation* because spins transfer energy to the surrounding environment, the lattice (Westbrook *et al.*, 1993).
- The transverse component of the magnetisation (i.e. the component perpendicular to the  $B_0$  field) decays with the *time constant*  $T2$ , this is known as the *transverse relaxation time*. This process is also called *spin-spin relaxation* because it can result from interactions between spins which are in close proximity to one another (Westbrook *et al.*, 1993).

As discussed in Sections 2.8.1,  $\mathbf{M}$  is oriented along the  $z$  ( $B_0$ ) axis at equilibrium and no portion of  $\mathbf{M}$  lies in the  $x$ - $y$  plane. Absorption of energy from an RF pulse causes  $\mathbf{M}$  to rotate

into the  $x$ - $y$  plane, so that coherent, net magnetisation lies in the transverse plane at the end of the pulse. As time elapses, this coherence disappears, while at the same time the protons release their energy and reorient themselves along  $B_0$ . This disappearing coherence produces the free induction decay (FID) or MR signal. There are several potential causes for a loss of transverse coherence of  $\mathbf{M}$  including main field inhomogeneity, tissue-induced inhomogeneity and the imaging gradients. The decay of the FID following the RF excitation pulse is called  $T2^*$  decay. This decay is faster than  $T2$  decay since it is a combination of two effects:  $T2$  decay itself and dephasing due to magnetic field inhomogeneities. Some sources of proton dephasing can be reversed by the application of a  $180^\circ$  RF pulse, which has to be applied in a sequence such as one involving a  $90^\circ$  RF pulse, short delay, a  $180^\circ$  RF pulse, followed by a second short delay before actual acquisition of the signal (discussed in Section 2.8.4).

#### 2.8.4 Spatial Encoding in MR imaging

MRI uses the field dependence of the Larmor frequency to localise signals to different regions of space. The application of magnetic field gradients makes the magnetic field spatially dependent. These gradients are alterations to the main magnetic field such that the  $z$ -component of the magnetic field varies linearly with spatial position along one of the three Cartesian axes. They are generated by coils of wire located inside the bore of the magnet, through which current is passed. Three orthogonal physical gradients are used, one in each of the  $x$  (left/right),  $y$  (anterior/posterior), and  $z$  (superior/inferior) directions. The combination of gradient pulses, RF pulses, data sampling periods that are used to acquire an image is known as a pulse sequence.

##### 2.8.4.1 Slice Selection (SS)

The initial step in MRI is the application of a frequency-selective RF pulse to tip the magnetisation within a region of space (*slice*) into the transverse plane. This is accomplished by applying the RF pulse in conjunction with a gradient known as the slice selection gradient,  $G_{SS}$ . A frequency-selective RF pulse has two parts associated with it: a central frequency (e.g.,  $f_1, f_2, f_3$ ) and a narrow range or bandwidth of frequencies (typically  $\Delta f=1-2$  kHz). The gradient direction ( $x, y, \text{ or } z$ ) determines the slice orientation, whereas the gradient amplitude together with bandwidth and centre frequency of the RF pulse determines the slice thickness ( $\Delta z$ ) and slice position. Let us assume that within a certain axial slice the Larmor frequency



has an average value of  $f_1$  (Fig. 2.17 right). The RF pulse cannot influence protons in the upper or lower parts of the body, because their Larmor frequencies are higher or lower than  $f_1$ . Thus, only protons inside the selected slice are tilted (or “excited”) and can contribute to the MR signal. This process is repeated for different excitation frequencies (e.g.,  $f_2$ ,  $f_3$ ) in order to acquire multi-slice image datasets. The repetition time (TR) is the time from the application of one RF pulse to the application of the next RF pulse.

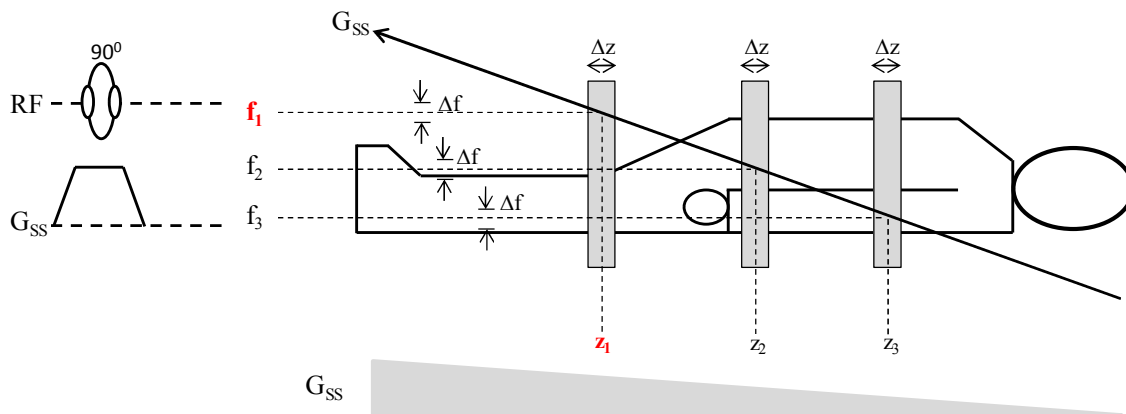


**Figure 2.17** Concept of slice selection: An RF pulse with a specific frequency  $f_1$  can only excite protons within a certain slice ( $z_1$ ), since the protons with different  $z$ -coordinates have different Larmor frequencies.

#### 2.8.4.2 Readout or Frequency Encoding (RO)

Once a slice has been selected, the signal coming from it must be located along the two dimensions of the image. In an imaging pulse sequence, the MR signal is always detected in the presence of a gradient known as the readout gradient,  $G_{RO}$ , which allows the signals in one of the two remaining dimensions (in-plane) to be distinguished. Figure 2.18 (right) shows three small brain regions and the signal that protons inside these regions produce while the readout gradient is switched on. The protons in the right of the head are exposed to a slightly reduced magnetic field, so they generate a signal with a slightly lower frequency than those in the left of the head (Fig 2.18,  $f_3$  compared with  $f_1$ ). The detected signal undergoes a frequency analysis (Fourier transform), resulting in production of the signal’s frequency spectrum. The positions of the signal-generating protons (or at least their  $x$ -coordinates) can then be deduced from the signal’s frequency spectrum. Thus, this process is called frequency encoding. It should be noted that the read-out gradient is switched on during acquisition only, not during the initial RF pulse. The use of magnetic field gradients to achieve spatial resolution was first proposed by Mansfield *et al.*, (1973) and Lauterbur (1973).

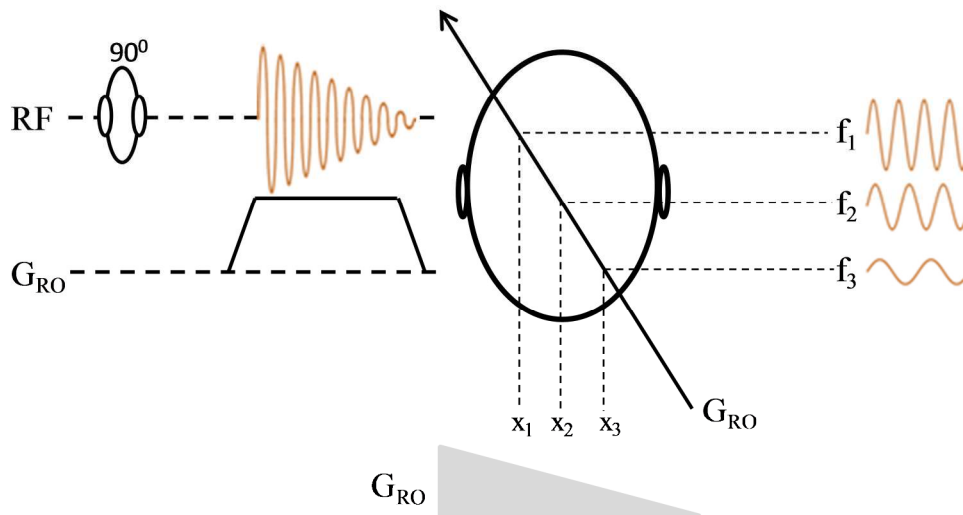


**Figure 2.18** The concept of frequency encoding: due to the read gradient ( $x$ -direction), the magnetic field increases linearly in the  $x$ -direction ( $x_3$  to  $x_1$ ) which linearly increases spin precession frequency ( $f_3$  to  $f_1$ ).

#### 2.8.4.3 Phase Encoding (PE)

The phase encoding gradient,  $G_{PE}$ , is oriented perpendicular to both  $G_{SS}$  and  $G_{RO}$  and is the only gradient that changes amplitude during the data acquisition loop of a standard two-dimensional (2D) imaging sequence. Any signal amplitude and phase variations occurring from one acquisition to the next are assumed to be caused by the influence of  $G_{PE}$  during the measurement. The effect of this gradient is shown in Fig. 2.19 (right) for three brain regions with the same  $x$ -coordinates but different  $y$ -coordinates: when the gradient  $G_{PE}$  is switched on, the protons in the anterior region have a higher Larmor frequency than the protons in the posterior regions.

The effect on the Larmor frequency only lasts as long as  $G_{PE}$  is switched on. Once  $G_{PE}$  is switched off and  $G_{RO}$  is switched on, the signals from both regions have the same Larmor frequencies because they have the same  $x$ -coordinate. However, the signals from the anterior and posterior regions have different phases as shown on the right-hand side of Fig. 2.19. It should be noted that an exact determination of the  $y$ -coordinates in a slice requires the repetition of the experiment depicted in Fig. 2.19 using different PE gradient amplitudes (shown in Figure 2.21). In summary, the  $x$ -coordinate can be deduced from the signal frequency and the  $y$ -coordinate from the evolution of the signal phase.

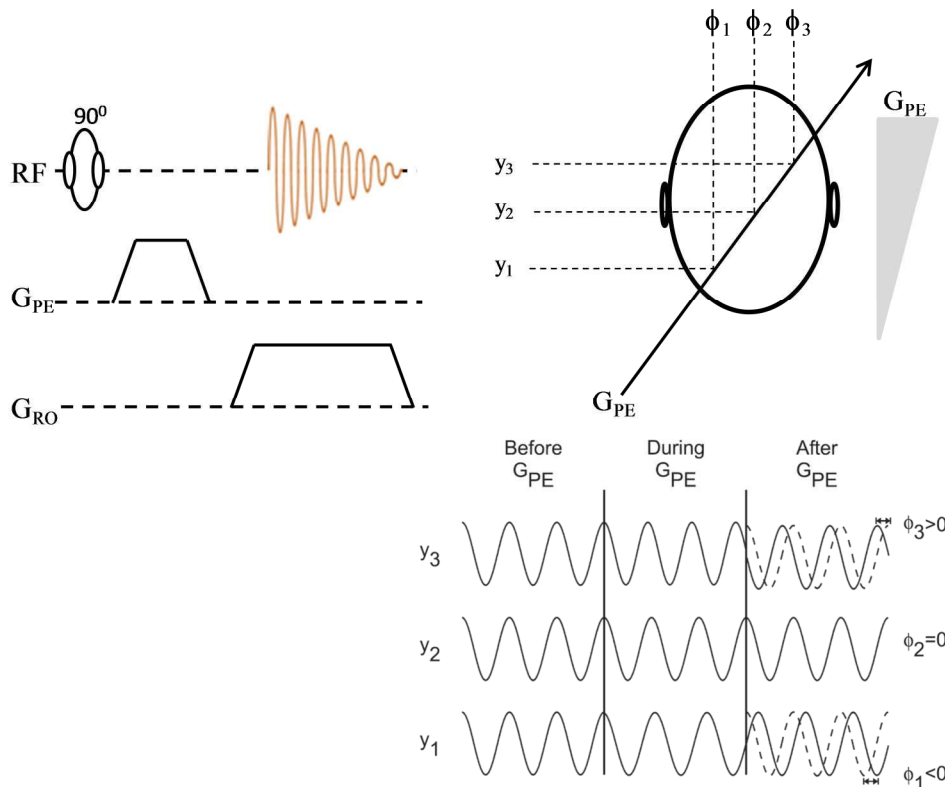


**Figure 2.19** The concept of phase encoding (PE): while the phase gradient is switched on, protons with different  $y$ -coordinates precess with different frequencies, leading to different phases when the acquisition begins.

### 2.8.5 Spin Echo and Gradient Echo

As discussed in Section 2.8.3, the initial  $90^\circ$  RF pulse rotates  $\mathbf{M}$  into the transverse plane. During the time  $t$ , proton dephasing will occur through  $T_2^*$  relaxation processes and the transverse coherence will diminish. Application of the  $180^\circ$  RF pulse inverts the sign of the accumulated phase. Since the rates and directions of precession for the protons do not change, the protons will then regain their transverse coherence after a further time  $t$ . This reformation of phase coherence induces another signal in the receiver coil, known as a spin echo.

In almost all imaging sequences, the signal is acquired while a gradient is applied in the readout-direction. As described above, this means that for the duration of the readout gradient the magnetic field varies linearly with position in the read-out direction. As a consequence, rapid signal decay is observed. However, after a reverse gradient (field magnitude increases in the negative readout-direction) has been applied, the signal builds up again after a while. This effect is known as gradient echo. Figure 2.20 schematically shows how a gradient echo is produced.

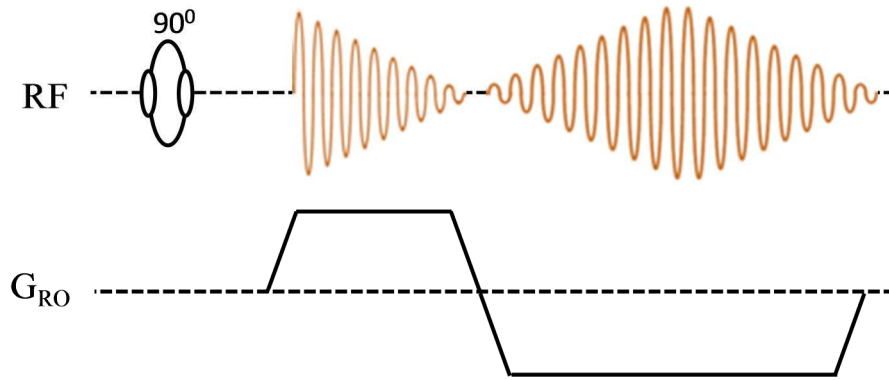


**Figure 2.20** Gradient echo: due to the magnetic field gradient, protons at different positions precess with different frequencies, resulting in signal losses due to dephasing. After inversion of the gradient, this process is reversed (rephasing) and the signal returns (gradient echo).

While the gradient is on, the spins dephase so that their contributions to the net magnetisation cancel each other, causing fast signal decay. In general, it can be said that any inhomogeneity of the static magnetic field will have a similar effect, resulting in accelerated signal decay. However, when the gradient is inverted, a spin that initially rotated quickly now precesses at a lower rate, and a spin that initially rotated slowly continues with a higher rate. This process continually reduces the phase difference between spins, so that the spins now rephase and the resulting signal (the gradient echo) builds up, attaining maximum strength when the spins are in phase again. Figure 2.21 shows a gradient echo imaging sequence with slice rephasing lobe and readout prephasing lobe (discussed in Section 2.8.6.1 and 2.8.6.2).

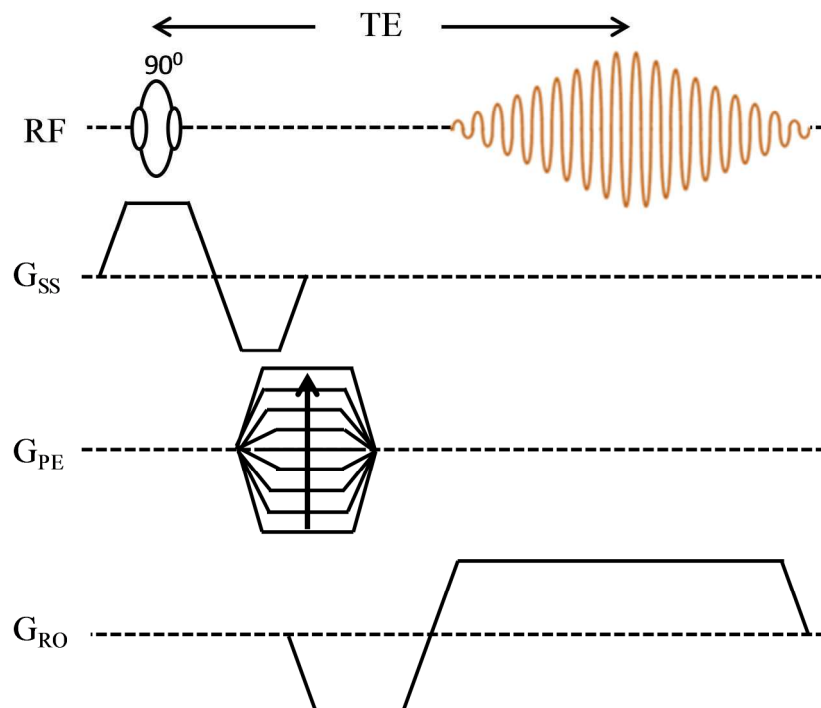


**Figure 2.21** A complete gradient echo imaging experiment.

The echo time, TE, is defined as the time difference between the RF excitation and the centre of the gradient echo. Gradient echo techniques are of major importance for functional imaging studies because neuronal activations lead to small changes of T2\* in the surrounding brain tissue and thus to intensity variations in T2\*-weighted gradient echo images. This effect, which is called the blood oxygenation level-dependent (BOLD) effect, will be discussed in a later section.

## 2.8.6 Correction Gradients

### 2.8.6.1 Slice-Rephasing Gradient

A slice-refocusing or rephasing lobe is associated with the slice-selection gradient of an excitation pulse. The slice-rephasing gradient lobe has opposite polarity compared to the slice-selection gradient (Fig. 2.22) and is used to compensate for the phase dispersion caused by the slice-selection gradient. Without the slice-rephasing gradient lobe, there is intra-voxel phase dispersion across the slice and signal loss results, as if a spoiler gradient (discussed in Section 2.8.6.4) had been applied.

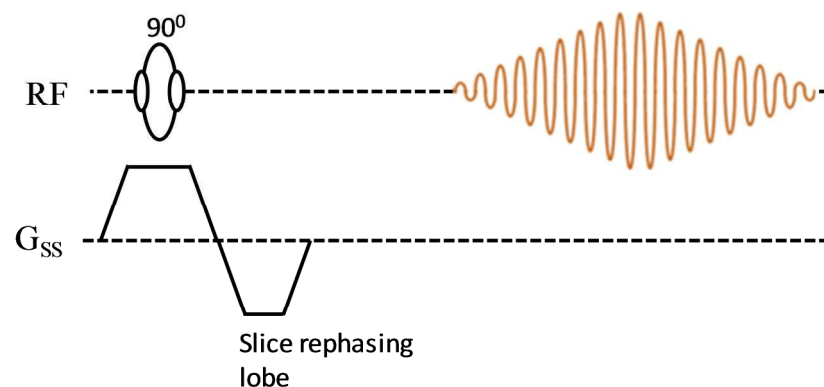


**Figure 2.22** A slice-rephasing lobe is used to compensate for the phase dispersion introduced by a slice-selection gradient.

### 2.8.6.2 Prephasing Readout Gradient

A readout gradient waveform typically consists of two portions, a pre-phasing gradient lobe (also known as dephasing gradient lobe or pre-excursion pulse) and a readout gradient lobe. In a spin-echo sequence, these two lobes are usually separated by an RF refocusing pulse with the pre-phasing gradient lobe before the inversion pulse and the readout gradient lobe after it (Figure 2.23a). In a gradient-echo pulse sequence, the two gradient lobes can be combined into a single continuous waveform (Figure 2.23b). The polarity of the pre-phasing gradient lobe is opposite to that of the readout gradient lobe. In pulse sequences with multiple spin echoes or gradient echoes, such as echo planar imaging (EPI), the second half of a

readout gradient can also serve as a separate pre-phasing gradient for subsequent readout. Thus, only a single separate pre-phasing gradient lobe is used at the beginning of the sequence, regardless of the length of the of the echo train (Section 2.8.8).

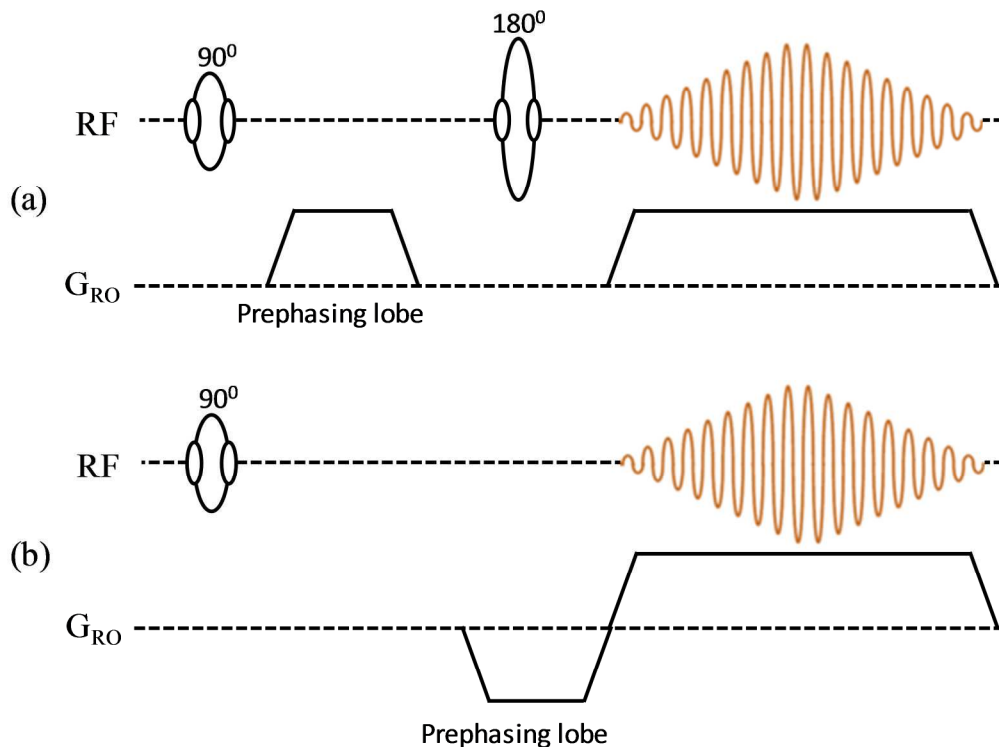


**Figure 2.23** A frequency-encoding gradient waveform in a (a) spin-echo pulse sequence and (b) gradient-echo pulse sequence.

### 2.8.6.3 Crusher Gradients

When a pulse sequence contains non-ideal refocusing RF pulses (i.e., flip angle  $\neq 180^\circ$ ) in the presence of imaging gradients, these signals can carry inconsistent spatial information encoded in their phase, leading to errors in the acquired k-space (discussed in Section 2.8.7) data. A crusher gradient is a correction gradient that eliminates the unwanted signals by introducing intra-voxel dephasing. It typically consists of two lobes with the same polarity, one applied immediately before a refocusing RF pulse and the other immediately after (Figure 2.24) (Bernstein *et al.*, 2004).

Although crusher gradients can be applied along any direction, in practice they are most commonly employed on the slice-selection axis, primarily because an imaging voxel typically has the largest dimension along this direction. A crusher gradient lobe can be combined with other gradient lobes (often with slice-selection gradients) in the pulse sequence, as long as the total gradient area is conserved (Figure 2.24).

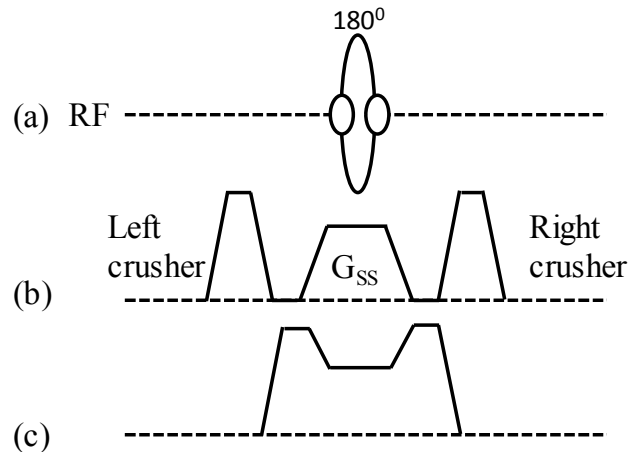


**Figure 2.24** Crusher gradients before (b) and after (c) combination with the slice-selection gradient ( $G_{SS}$ ) of a refocusing RF pulse (a).

#### 2.8.6.4 Spoiler Gradients

At the end of a pulse sequence or application of a preparatory RF pulse, residual transverse magnetization can remain. The residual transverse magnetization, if not eliminated, can produce a spurious signal that interferes with the desired signal in subsequent data acquisition, causing image artefacts (Haacke *et al.*, 1999; Bernstein *et al.*, 2004). A spoiler gradient, as the name implies, spoils or kills the unwanted MR signals that would otherwise produce artefacts in the image. Spoiler gradients are typically applied at the end of a pulse sequence (Figure 2.25a) or at the end of a preparatory RF pulse within a pulse sequence (Figure 2.25b).

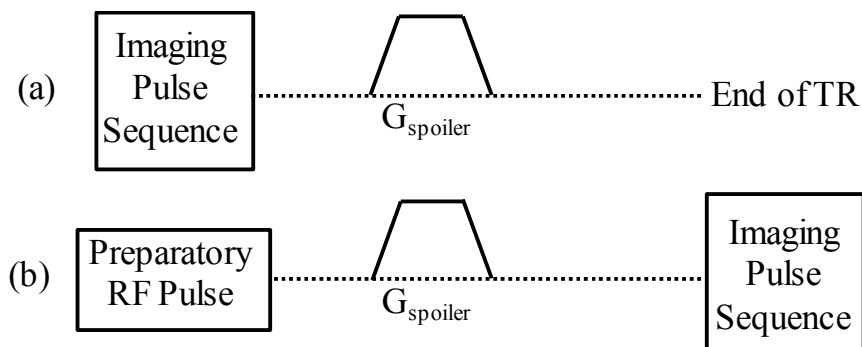


**Figure 2.25** Two examples of spoiler gradients. (a) A spoiler gradient that is applied at the end of a pulse sequence. (b) A spoiler gradient that is applied after a preparatory RF pulse (or pulses) but prior to an imaging pulse sequence.

Under the influence of a spoiler gradient, the transverse magnetization dephases along the direction of the gradient, leading to signal cancellation within a voxel. Meanwhile, the longitudinal magnetization experiences no effect from the spoiler gradient and thus is preserved to give rise to a signal in subsequent data acquisition. Spoiler gradients are unipolar

and can have either positive or negative polarity on a given gradient axis. The polarity is determined based on the other gradient waveforms within the pulse sequence. Although a spoiler gradient can be applied to any one, two, or all three logical (i.e., readout, phase-encoding, and slice-selection axes) or physical gradient axes, it is often sufficient to employ a spoiler gradient along a single axis. When spoiler gradients are required on more than one axis, they are typically applied simultaneously to minimize the length of the pulse sequence.

### 2.8.7 k-Space

k-space is a mathematical concept that is extremely useful for describing how MR sequences sample data. This is true for the EPI sequence, which lies at the heart of fMRI. In the k-space representation, the complex array of raw data points is treated as a two-dimensional grid of points ( $k_x$ ,  $k_y$ ), where each  $k_x$  value corresponds to a different complex time point in the readout direction and each  $k_y$  value corresponds to a different phase-encoding gradient amplitude. Therefore, each ( $k_x$ ,  $k_y$ ) data point corresponds to the echo signal amplitude influenced by the combination of readout and phase encoding gradient areas (Brown *et al.*, 2003; Hashemi *et al.*, 2004).

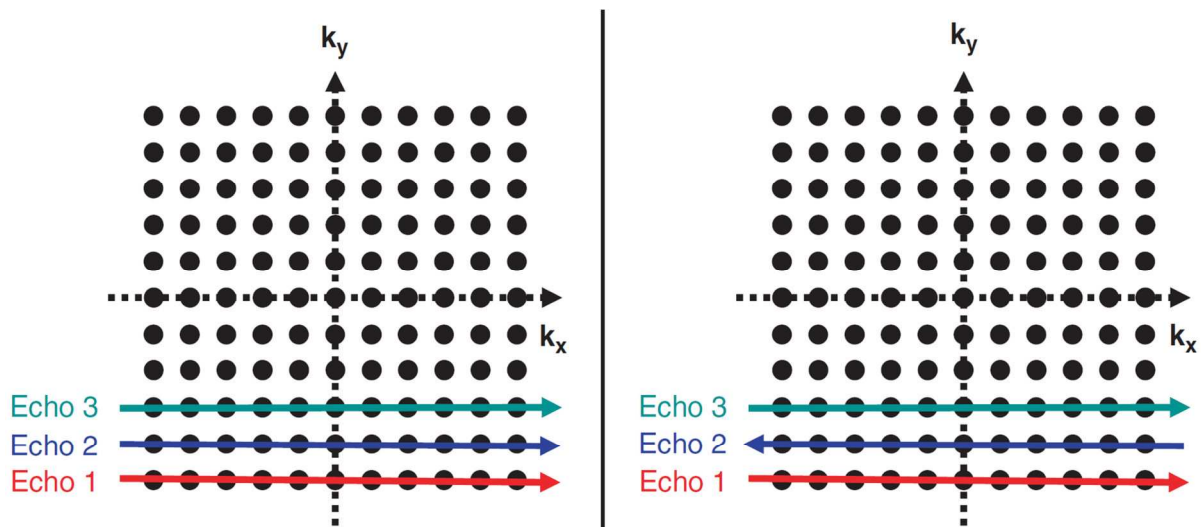


**Figure 2.26** Left: Schematic description of k-space coverage for the gradient echo experiment depicted in Fig. 2.21, filling horizontal lines successively from the left to the right. Right: schematic description of k-space coverage for the echo planar imaging (EPI) experiment depicted in Fig. 2.27, filling odd horizontal lines successively from the left to the right and even horizontal lines successively from the right to the left (Deichmann *et al.*, 2010).

Let us explain k-space using the gradient echo sequence depicted in Fig. 2.21 in which several gradient echoes are acquired using different values for the PE gradient. Let us start with the  $k_x$  values: the first data point of each gradient echo is preceded by the negative



gradient on the readout axis only, so it has a negative  $k_x$  value. The other data points are preceded by the initial negative gradient plus the positive read gradient of increasing duration, so they have increasing  $k_x$  values. However, all data points belonging to the same echo are preceded by the same PE gradient, so they have the same  $k_y$ -value, which is negative for the first echo because the PE gradient starts with a negative value. The different  $k$ -values of the data points belonging to the gradient echo can be depicted in a 2D,  $k$ -space diagram, as shown in Fig. 2.26 (left): obviously, the data points cover the bottom-most horizontal line (red line, Fig. 2.26, left) in  $k$ -space. For the next echo, the PE gradient has a higher value, so  $k_y$  is increased and the data points constituting this echo cover the next highest horizontal line in  $k$ -space (blue line, Fig. 2.26, left). In summary, one can say that for any particular MR imaging experiment, several data points with different combinations of  $k_x$  and  $k_y$  must be acquired, covering the complete 2D  $k$ -space, as shown in Fig. 2.26. For the experiment described in Fig. 2.21,  $k$ -space is covered in horizontal lines, with each line filled successively from the left to the right.

### **2.8.8 Echo Planar Imaging (EPI)**

The spin echo or gradient echo sequence is relatively time consuming, mainly because each repetition with a new PE gradient requires its own slice-selective excitation pulse and associated TR period. Echo Planar Imaging (EPI) was first proposed by Sir Peter Mansfield (Mansfield 1977) to avoid this limitation. In this pulse sequence, the whole 2D  $k$ -space is acquired with one RF excitation and therefore EPI has a much higher temporal resolution than conventional spin echo or gradient echo imaging sequences. After the slice-selective RF excitation, a series of gradient echoes are acquired by successive reversals of the read gradient. A short gradient pulse in the PE-direction, the so-called blip, is switched on between successive acquisitions. Thus, the degree of PE for a specific echo is given by the initial negative gradient in the PE-direction and the sum of the blips up to the echo acquisition time. In summary, this satisfies the conditions mentioned in Section 2.8.7 for imaging, so a full image can be constructed from the acquired data. The gradient reversals are performed very rapidly, allowing 2D echo planar images to be acquired in less than 100ms. Gradient echo EPI images are heavily  $T_2^*$  weighted, displaying reduced image intensity in areas affected by local magnetic field inhomogeneities. The  $T_2^*$ -weighting and speed of acquisition make this technique ideally suited for functional MRI.

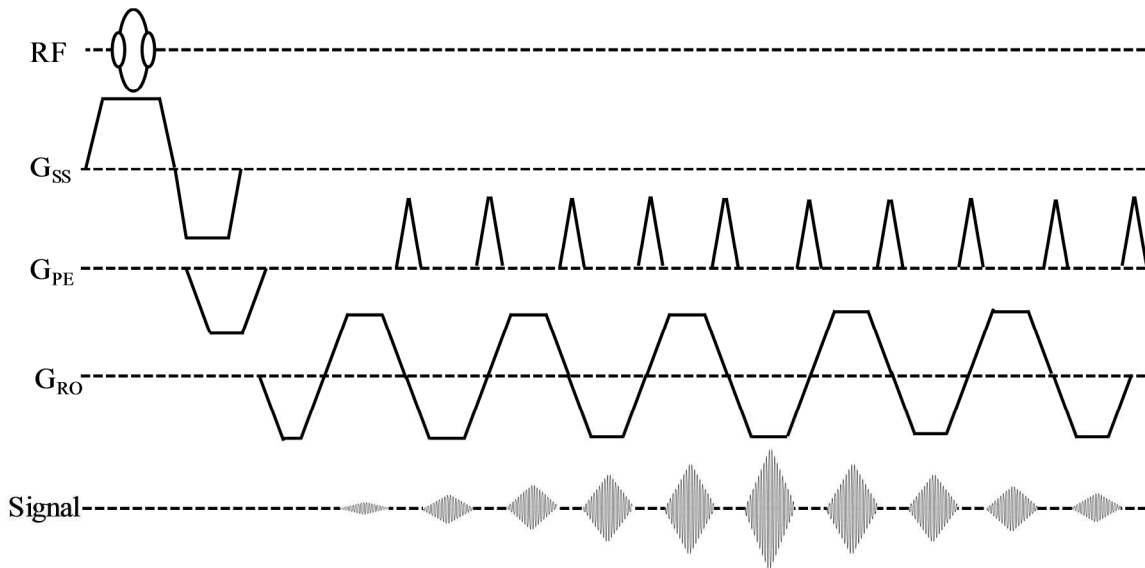


**Figure 2.27** Diagram of the basic gradient echo EPI sequence (Hashemi et al., 2004).

The sampling of  $k$ -space during an EPI sequence shown in Figure 2.26 (right) is simple to understand: for the first echo, the data points have increasing  $k_x$  values, ranging from a negative to a positive value, but the same negative  $k_y$  value due to the preceding PE gradient. Thus, this echo covers the bottom-most horizontal line in  $k$ -space, as shown by the red line in Fig. 2.26 (right). For the second echo,  $k_y$  is increased due to the intermediate PE blip. The  $k_x$  values of this echo range from a positive to a negative value, so this echo covers the next horizontal line in  $k$ -space, but in reverse order (blue line, Fig. 2.26, right). In summary, it can be said that  $k$ -space is covered in horizontal lines in EPI, with odd lines filled successively from the left to the right, and even lines from the right to the left.

### 2.8.9 MR Instrumentation

This section presents a brief description of the 3.0 T Philips Achieva scanner (Philips Medical Systems, Best, the Netherlands), situated in the Sir Peter Mansfield Magnetic Resonance Centre (SPMMRC) at the University of Nottingham which was used to acquire data for all the studies presented in thesis. Since these systems are commercially available, only a general overview will be described here. An MR system's hardware consists of: the magnet, shim coils, gradient coils, RF coils and associated electronics including computer control system for scanner operation and image reconstruction and processing. Figure 2.28 illustrates a schematic diagram of an MRI control system. Each of the components shown is described briefly below:

### 2.8.9.1 Magnet

The magnet should generate a strong magnetic field  $B_0$  with good spatial homogeneity and high temporal stability. A superconducting magnet is used in this system. This is made from wires of niobium-titanium (NbTi) alloy which has a critical superconducting temperature of approximately 10 K. To maintain this temperature and hence the superconducting state, the wires are kept immersed in liquid helium which has a boiling point of 4.2 K. The helium is contained in a dewar, which limits heat transfer from the magnet exterior to the helium. To keep the superconducting material below the critical temperature, liquid helium is generally used as a cryogenic coolant. The use of cryocooler pumps reduces the boil-off of the liquid helium by converting the helium gas back to a liquid by changes in pressure.

The high magnetic field generated by the unshielded superconducting magnets can extend beyond the magnet bore for many meters, as a “fringe field”. Therefore, magnetic field shielding is required to reduce the magnitude and the extent of this field. Shielding can be achieved using either passive or active shielding. Active shielding (used in a Philips 3 T scanner) employs a secondary counteracting superconducting coil wound on the outside of the main magnet coil. This cancels the undesired field outside the main magnet and reduces the fringe field to 0.5 mT at a distance of 3m radially from the bore. Passive shielding is often used for ultra-high field systems, involving the placing of a large amount of ferromagnetic material around the magnet.

### 2.8.9.2 Shim Coils

Shimming is the process of improving the static magnetic field homogeneity over a region of interest. Although the superconducting magnet inherently generates a field with good homogeneity, it is generally necessary to use shimming to improve this further. Two shimming methods are generally used to optimise the homogeneity of the static field: *passive* and *active* shimming. Passive shimming is usually performed during system installation to correct inhomogeneities in the main applied static field. This is achieved by placing small pieces of ferromagnetic material, normally iron, within the bore of the magnet. These ferromagnetic pieces attract and concentrate magnetic field lines, and thus correct the inhomogeneities in the static field (McGinley *et al.*, 1997). Once a subject is placed in the scanner, the different magnetic properties of air and tissue within the body introduce additional spatial variations in the field, leading to field inhomogeneities over the area of interest. These inhomogeneities can be corrected by the use of an active shimming method. In

active shimming, resistive coils are employed to generate small magnetic fields which either add or subtract from the main static field to correct field inhomogeneities.

### **2.8.9.3 Gradient Coils**

Gradient coils are used to induce linear spatial variations in the main field over the subject which are required for imaging, as described in Section 2.8.4. The three orthogonal gradients (resistive electromagnets) coils are mounted on a cylindrical former between the RF and the shim coils. The z-gradient,  $G_z$ , can be produced by Maxwell coils, while the transverse gradients,  $G_x$  and  $G_y$ , can be generated using saddle coils, such as those employed in a Golay coil arrangement.

The EPI technique used for fMRI studies, as performed in this thesis, puts a high demand on the gradient performance, as the sequence requires strong and rapidly switching gradients, whilst producing negligible eddy currents. For EPI, typical gradients strength and rise times are 20-40 mT/m and 150-200  $\mu$ s, respectively. To achieve this switching, the inductance of the gradient coils must be low, resulting in a large current requirement to reach appropriate magnetic field gradient amplitudes. It is the rapid switching of these gradients which is responsible for the noise heard within the MR scanner as the gradient coils flex as they experience time-varying forces resulting from the Lorentz force which the coil windings experience.

### **2.8.9.4 RF Coils**

RF coils are placed inside the gradient coil to excite the spin system of interest (discussed in Section 2.8.1). Coils may be arranged to surround the whole body, “body coil”, or part of the body (e.g., head coil). The transmit coil generates a strong, spatially uniform  $B_1$  magnetic field, oscillating at a range of frequencies centred at the Larmor frequency,  $\nu_0$ . The resulting MR signals emitted by the precessing spins after the excitation (as discussed in Section 2.8.2) are detected by RF receiver coils. A single RF coil may be used for both transmit and receive, however, to increase the SNR of the received signal it is often better to use separate transmit and receive coils so that the RF receiver coil can be placed close to the region of interest. Separate receiver coils are also needed when parallel imaging techniques, such as the SENSitivity Encoding technique (SENSE) (Pruessmann *et al.*, 1999) is used. This is achieved by using a number of small coils that receive signal simultaneously and independently from a

single excitation. By combining the data from each receiver coil, the final image is reconstructed and generated. The Philips system used in this work uses a transmit body coil and 8-element or 32-element SENSE receive head coils.

### 2.8.9.5 Control and Processing System

An MRI system requires a high level of computer processing power. A waveform generator produces the required waveforms for the gradients and the RF. The generated gradient waveforms are converted from analogue to digital form and then amplified via the gradient amplifiers ( $G_x$ ,  $G_y$  and  $G_z$ ). The generated RF waveforms are transmitted to the spectrometer which modulates the RF signal at the Larmor frequency and converts the waveform from analogue to digital. RF pulses are then delivered to the RF coil through an RF amplifier. The received MR signals detected by the RF coil are amplified via the pre-amplifier before being converted from analogue to digital in the spectrometer. The digitised MR signal is then sent to the image reconstruction computer. EPI acquisition requires fast computers capable of “real time” image reconstruction, of the order of  $<100$  ms per image. The reconstructed MR data is then stored and displayed.

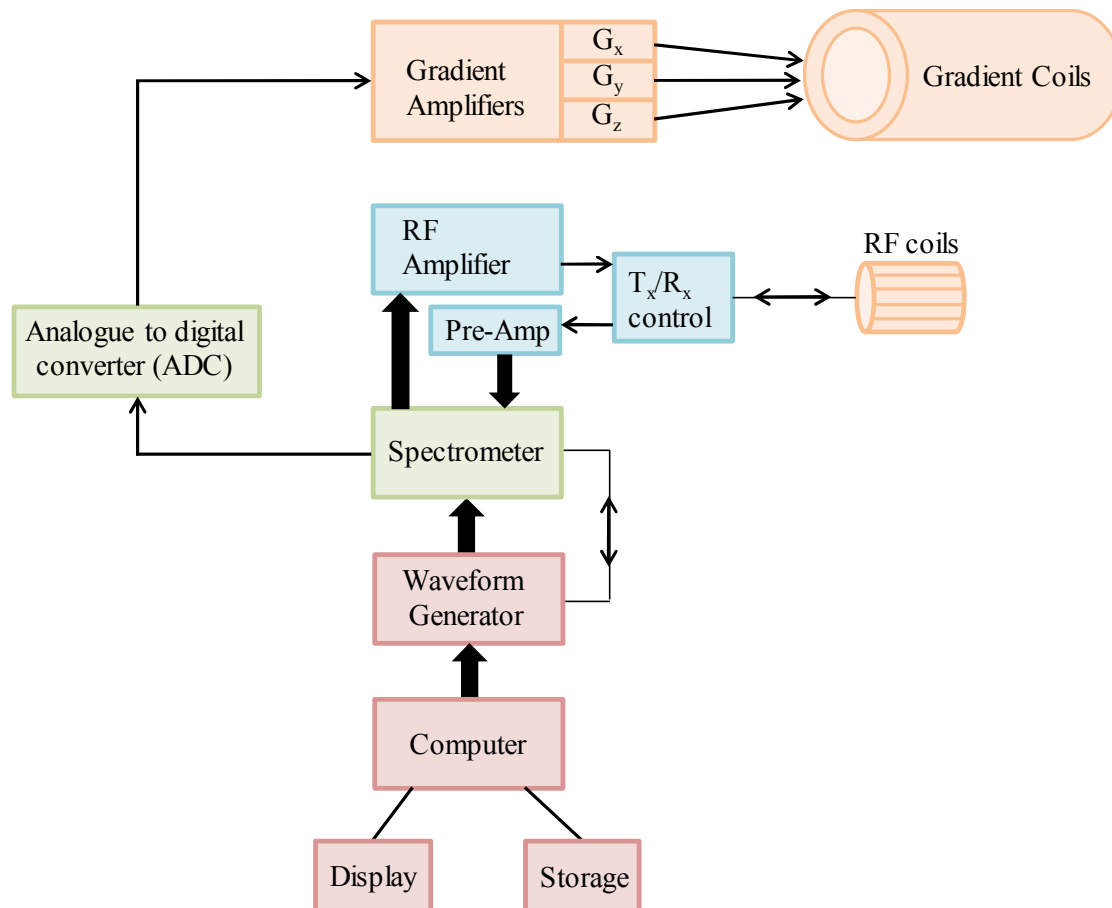


**Figure 2.28** An overview of an MRI control system.

## 2.9 Functional Magnetic Resonance Imaging (fMRI)

As briefly mentioned in Section 2.7, fMRI is a functional neuroimaging technique for measuring brain activity. Unlike EEG, this technique does not provide a direct measure of brain activity, but instead takes advantage of the fact that the changes in blood oxygenation and flow occur in response to neural activity. When a brain area is more active it consumes more oxygen and to meet this increased demand, blood flow increases to this area (Ogawa *et al.*, 1990; Belliveau *et al.*, 1991; Kwong *et al.*, 1992). The use of MRI as a cognitive neuroscience tool expanded greatly with the discovery of blood oxygenation level dependent (BOLD) functional imaging (Ogawa *et al.*, 1990; Kwong *et al.*, 1992). Now fMRI is a mainstay of neuroscience research. Compared to other functional imaging methods, fMRI offers much higher spatial resolution and it is entirely non-invasive, which has allowed improved the mapping of functional networks in the human brain. The advantages of fMRI have made it a popular tool for imaging normal brain function – especially for psychologists. Over the last couple of decades it has provided new insights in identifying regions linked to critical functions such as speaking, moving, sensing, or planning. fMRI can be used to plan for surgery and radiation therapy of the brain. Clinicians also use fMRI to detect the effects of tumors, stroke, head and brain injury, or diseases such as Alzheimer's on brain function.

### 2.9.1 The BOLD Contrast Mechanism

Ogawa *et al.*, (1990) first discovered the BOLD contrast in rats, when they observed that the intensity of the vascular signal in gradient-echo (GE) images decreased when blood was deoxygenated, and increased when the flow of freshly oxygenated blood increased. Later on, it was shown that BOLD contrast could be used to detect functional activation in humans (Ogawa *et al.*, 1990; Kwong *et al.*, 1992). In the resting brain, there is a given amount of oxygenated and deoxygenated haemoglobin in brain tissues. Deoxyhaemoglobin is paramagnetic, whilst oxyhaemoglobin is diamagnetic. This means that deoxyhemoglobin has the property that it disturbs any magnetic field surrounding it decreasing the MR signal intensity. When neural activity in a given brain area increases, via stimulation or task performance, the oxygen consumption local to that activated region increases and as a result the amount of deoxyhemoglobin is increased. This triggers an increase in the flow of fresh oxygenated blood i.e., both cerebral blood flow (CBF) and cerebral blood volume (CBV) increase to the activated area in order to meet the increased metabolic demands and this leads to an increase in oxygenated haemoglobin that exceeds the regional oxygen consumption.

The complex interplay between CBF, CBV, and blood oxygenation underlying the BOLD effect used in the majority of current fMRI studies, and are important for the quantitative mapping of the cerebral metabolic rate of oxygen (CMRO<sub>2</sub>). The increase in oxygen supplied to the active tissue is more than the additional oxygen that is used by the neurons, and hence there is a relative increase in the oxyhemoglobin concentration, and a decrease in deoxyhemoglobin concentration during brain activation. The increase in oxyhemoglobin concentration results in increased T<sub>2</sub>\* and leads to a signal increase in GE images (Ogawa *et al.*, 1990).

### 2.9.2 The Haemodynamic Response

Figure 2.29 shows a typical signal time course following neuronal activation associated with an external stimulus (e.g. a flashing light) or performance of a task (e.g. mental arithmetic), the so-called haemodynamic response. Initially, there is a slight signal decrease.

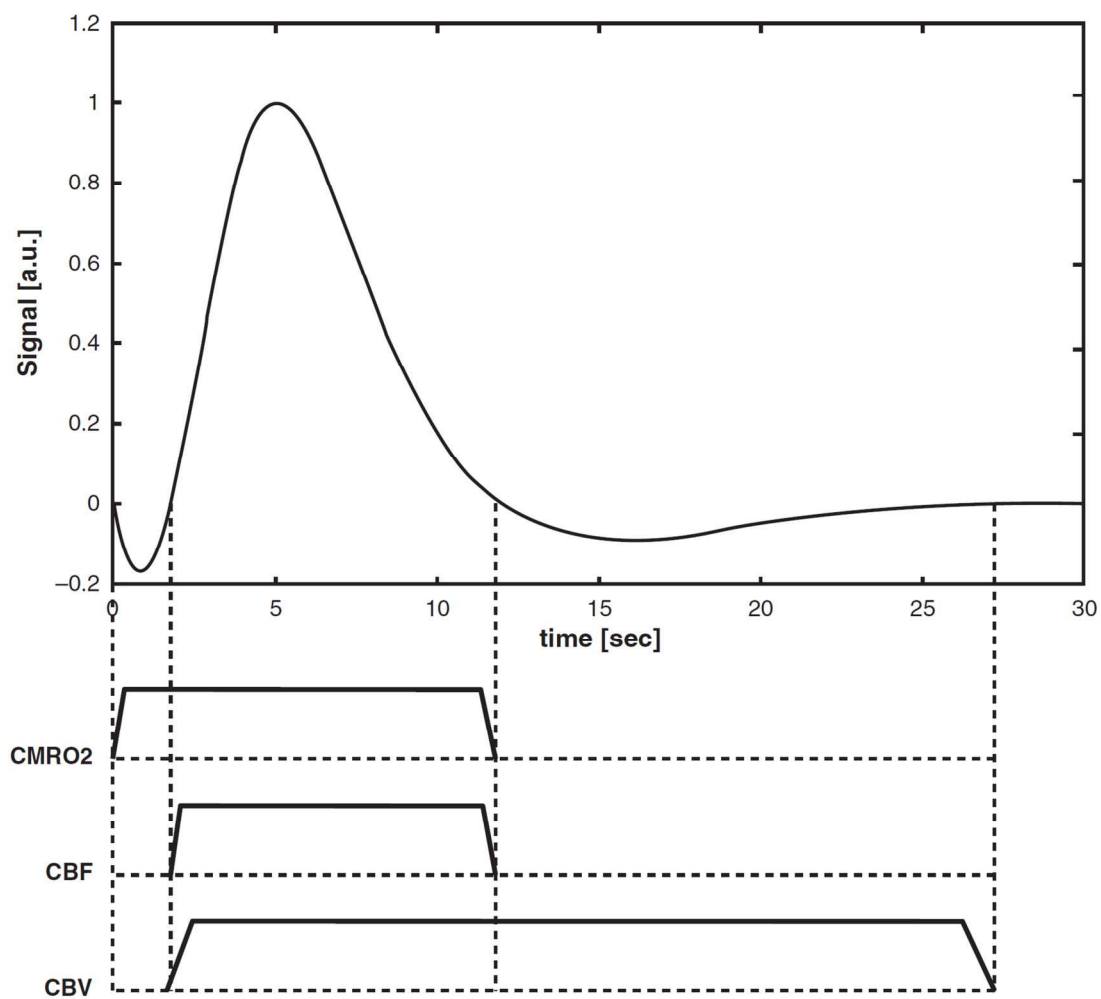


**Figure 2.29** A typical haemodynamic response function following a stimulus, showing a negative initial dip, a strong positive BOLD response, and a subsequent negative undershoot. (Goense *et al.*, 2010).

This initial dip is not always observed and has been reported mainly at high field strengths (Buxton 2001). Afterwards, there is a positive BOLD response that persists for about 5-10 s. For the remaining time, up to 30 s after the onset of the stimulus, there is a signal undershoot. The physiology behind these effects is only partially understood. In particular, it is not clear how the coupling between neuronal activity and blood flow is mediated (Attwell *et al.*, 2002), and which aspect or aspects of neuronal activity it best reflects. This is because changes in blood flow occur over a much slower timescale than changes in electrophysiological activity. Changes in electrophysiological activity may happen within milliseconds or tens of milliseconds, whereas changes in blood flow or BOLD response take anywhere from hundreds of milliseconds to seconds. Typically, peak blood flow and BOLD response are not achieved until 5–6 s after the onset of the stimulus. As a result, a vascular response to a synaptic input is still developing when a second stimulus might arrive at the active region and therefore the vascular response to subsequent stimuli is influenced by the preceding stimulus because of the temporal overlap between responses.

The important physiological parameters that influence the BOLD effect are  $CMRO_2$ , CBF, and CBV. The time courses of these parameters after activation for one of the commonly accepted explanations for the different components of the BOLD response are schematically sketched in Fig. 2.29. Directly after the onset of neuronal activation, the  $CMRO_2$  is increased. The consumption of oxygen leads to higher concentration of deoxyhemoglobin, which reduces the signal, resulting in the initial dip. However, after a very short while, the CBF and CBV increase, with opposing effects: due to the increased CBF, more oxyhemoglobin is transported to the site of activation, giving rise to a decreased concentration of deoxyhemoglobin and thus to a higher signal, as explained above. The increase in CBV is concomitant with a higher concentration of deoxyhaemoglobin, lowering the signal.

However, the effect of the CBF increase outweighs the signal reduction caused by the higher  $CMRO_2$  and CBV values, resulting in a positive BOLD response. According to the original balloon model by Buxton (Buxton 2001,2002; Buxton *et al.*, 2004), after about 10 s,  $CMRO_2$  and CBF return to their baseline levels. The relaxation of CBV is slower, so for a certain time there is an increased concentration of deoxyhaemoglobin due to the higher blood volume, which reduces the signal, resulting in the post-stimulus undershoot.



### 2.9.3 Advantages and Disadvantages of fMRI

The great advantage of fMRI is that it doesn't use radiation like X-ray CT and PET scans rather it uses MRI which, if done correctly, has virtually no risk. It can evaluate brain function safely, non-invasively and effectively. With advanced scanner hardware the achievable spatial resolution for structural imaging *in vivo* is around  $1 \times 1 \times 1 \text{ mm}^3$  at 3T. In principle fMRI can also be done at such resolutions, although it is constrained by the relatively low contrast-to-noise ratio (CNR) of the functional activation and the limited amount of time available for the acquisition of each image. Because of its speed, EPI (Mansfield 1977) is typically used for fMRI. However, EPI requires high-performance hardware, and the limitations of the gradients often restrict the maximally achievable resolution. Despite this, by using parallel imaging, high resolution fMRI can be done, and in human fMRI studies, typical resolution is  $3 \times 3 \times 3 \text{ mm}^3$ , and currently the highest resolution achieved is about  $0.5 \times 0.5 \times 0.5 \text{ mm}^3$  (Pfeuffer *et al.*, 2002; Yacoub *et al.*, 2005).

In the spatial domain, the resolution of the fMRI signal depends on the choice of fMRI contrast and the strength of the magnetic field. How well the functional activation is localized to the actual place of neural activation depends on the achievable fMRI resolution and the specificity of the hemodynamic signal. The achievable spatial resolution is determined by scanner hardware and the SNR. The specificity is determined by the fMRI method that is used and how closely the area of cortex where the hemodynamic response occurs reflects the area of cortex where actual neural activity occurs. BOLD signal originating from large vessels may occur remote from the site of activation, but BOLD signal from capillaries can reasonably be assumed to be closely related to the neural activity in that area. Hence, the specificity is not only determined by biological factors, but also by the choice of fMRI method, hardware, and sequence parameters (Ugurbil *et al.*, 2003; Harel *et al.*, 2006).

The disadvantages of fMRI include the fact that MR equipment set-up is very expensive and the data quality degrades and sometimes become unusable if the subject moves while the data are being acquired. Moreover, researchers still don't completely understand the origin of the measured BOLD signal. The major complaint from researchers is that fMRI can only look at indirect haemodynamic changes in the brain. It can't provide information about the activities of individual nerve cells (neurons), which are critical to mental function. Each area of the brain studied in fMRI is made up of thousands of individual neurons, each of which might

have a unique story to tell. Because certain areas of the brain that "light up" on analysis of fMRI data may represent a number of different functions, it's hard to tell exactly what kind of brain activity is being represented by the scan.

In the temporal domain, the BOLD response appears as a delayed, low-pass-filtered version of the neurophysiological response. This is because changes in blood flow and volume occur over a much longer timescale than changes in electrophysiological activity. As already discussed, changes in electrophysiological activity happen within milliseconds or tens of milliseconds, whereas, changes in blood flow, volume and thus the BOLD response take on the order of seconds to occur. Let us consider the specific example of neurons in the primary visual cortex. Subsequent to the onset of a visual stimulus, the response of primary visual cortex neurons begins within 20-50 ms, while a peak response is achieved within 30-70 ms (Maunsell *et al.*, 1992). The onset of the subsequent vascular response becomes apparent only after 1.5-2.5 s. How quickly the corresponding positive BOLD response can be measured depends on the paradigm, the signal-to-noise ratio (SNR), the amplitude of the response and the analytical parameters. Typically, peak blood flow and BOLD response are not achieved until 5-6 s after the onset of the stimulus. As a result, a vascular response to a synaptic input is still developing when a second stimulus arrives at the active region. This sluggish response therefore complicates the interpretation of the vascular response to subsequent stimuli as it is influenced by the preceding stimulus because of the temporal overlap between responses (Lauritzen 2005).

This chapter has identified the source of the responses measured using EEG and fMRI and outlined the theory and the acquisition techniques used in these methods. Explanations of why EEG has a high temporal resolution and low spatial resolution, with the opposite true for BOLD fMRI, have been given. The underlying principles of EEG and fMRI along with the hardware description discussed in this chapter are required to understand the experimental work of this thesis. This chapter along with the next chapter described why the work presented in this thesis has been carried out. The advantages and limitations of the combined use of these techniques will be covered in the remaining chapters of this work.

## 2.10 References

- Adrian, E. D. and Matthews, B. H. C. (1934). "The Berger rhythm: potential changes from the occipital lobes in man." Brain **57**: 355-385.
- Ananthi, S. (2005). A Text Book of Medical Instrumentations. New Age Intl Ltd., New Delhi. 978-81-224-2870-4.
- Attwell, D. and Iadecola, C. (2002). "The neural basis of functional brain imaging signals. ." Trends Neurosci **25**: 621-625.
- Baillet, S., Mosher, J. C. and Leahy, R. M. (2001). "Electromagnetic Brain Mapping." IEEE Signal Processing Magazine **18**: 14-30.
- Basar, E., Karakas, S. and Schurmann, M. (1999). "Are cognitive processes manifested in event-related gamma, alpha, theta and delta oscillations in the EEG?" Neuroscience Letters **259**: 165-168.
- Belliveau, J. W., Kennedy, D. N., McKinstry, R. C., Buchbinder, B. R., Weisskoff, R. M., Cohen, M. S., Vevea, J. M., Brady, T. J. and Rosen, B. R. (1991). "Functional mapping of the human visual cortex by magnetic resonance imaging." Science **254**: 716-719.
- Bernstein, M. A., King, F. K. and Zhou, X. J. (2004). Handbook of MRI Pulse Sequences. Elsevier, USA.
- Blinowska, K. and Durka, P. (2006). Electroencephalography (EEG). Wiley Encyclopedia of Biomedical Engineering. M. Akay, Wiley.
- Blinowska, K. and Durka, P. (2006). Electroencephalography(EEG), In: Wiley Encyclopedia of Biomedical Engineering. M. Akay. Wiley.
- Bohan, M. (2005). "MCB-HHMI Outreach." from [http://outreach.mcb.harvard.edu/animations/actionpotential\\_short.swf](http://outreach.mcb.harvard.edu/animations/actionpotential_short.swf).
- Bressler, S. L. and Kelso, J. A. (2001). "Cortical coordination dynamics and cognition." Trends in Cognitive Sciences **5**: 26-36.
- Brown, M. A. and Semelka, R. C. (2003). MRI Basic Principles and Applications. John Wiley & Sons, New Jersey, 3rd Ed.
- Buxton, R. B. (2001). "The elusive initial dip." NeuroImage **13**: 953-958.
- Buxton, R. B. (2002). Introduction to functional magnetic resonance imaging: principles and techniques. Cambridge University Press, Cambridge.
- Buxton, R. B., Uludag, K., Dubowitz, D. J. and Liu, T. T. (2004). "Modeling the hemodynamic response to brain activation." NeuroImage **23**: S220-233.

- Buzsaki, G. and Draguhn, A. (2004). "Neuronal oscillations in cortical networks." Science **304**: 1926-1929.
- Cooper, R., Osselton, J. W. and Shaw, J. C. (1969). EEG Technology. Butterworths, London, 2nd ed.
- Davis, U. C. (2011). "What is an ERP?". Retrieved on 15 Oct, 2013, from <http://erpinfo.org/what-is-an-erp>.
- Deichmann, R., Nöth, U. and Weiskopf, N. (2010). EEG-fMRI: Physiological Basis, Technique and Applications. Chapter 3 The Basics of Functional Magnetic Resonance Imaging. Springer, Berlin, 1.
- Gloor, P. (1969). Hans Berger on the Electroencephalogram of Man., Amsterdam.
- Goense, J. and Logothetis, N. K. (2010). Simultaneous EEG and fMRI: recording, analysis, and application. Chapter 1.2 Physiological Basis of the BOLD Signal. Oxford University Press. 978-0-19-537273-1.
- Haacke, E. M., Brown, R. W. and Thompson, M. R. (1999). Magnetic Resonance Imaging Physical Principles and Sequence Design. John Wiley & Sons, Canada.
- Hamalainen, M., Hari, R., Ilmoniemi, R. J., Knuutila, J. and Lounasmaa, O. V. (1993). "Magnetoencephalography-theory, instrumentation, and applications to noninvasive studies of the working human brain." Rev. Mod. Phys. **65**(2): 413-497.
- Harel, N., Ugurbil, K., Uludag, K. and Yacoub, E. (2006). "Frontiers of brain mapping using MRI." J Magn Reson Imaging **23**: 945-957.
- Hashemi, R. H., Bradley, W. G. and Lisanti, C. J. (2004). MRI: The Basics. Lippincott Williams & Wilkins, Philadelphia, 2nd Ed.
- Jasper, H. H. (1958). "Report of the Committee on Methods of Clinical Examinations in EEG: Appendix: The ten-twenty electrode system of the International Federation. ." Electroencephal. Clin. Neurophysiology **10**: 371-375.
- Kandel, E. R. (2000). Principles of neural science. McGraw-Hill., NY, London., 4th Ed. pp. 776-777.
- Kwong, K. K., Belliveau, J. W., Chesler, D. A., Goldberg, I. E., Weisskoff, R. M., Poncelet, B. P., Kennedy, D. N., Hoppel, B. E., Cohen, M. S., Turner, R., Cheng, H. M., Brady, T. J. and Rosen, B. R. (1992). "Dynamic magnetic resonance imaging of human brain activity during primary sensory stimulation." Proc Natl Acad Sci **89**: 5675-5679.
- Lauritzen, M. (2005). "Reading vascular changes in brain imaging: is dendritic calcium the key?" Nat Rev Neurosci **6**: 77-85.

- Lauterbur, P. C. (1973). "Image formation by induced local interactions: examples employing nuclear magnetic resonance." Nature **242**: 190-191.
- Llinas, R. R., Ribary, U., Jeanmonod, D., Kronberg, E. and Mitra, P. P. (1999). Thalamocortical dysrhythmia: A neurological and neuropsychiatric syndrome characterized by magnetoencephalography. Proceedings of the National Academy of Sciences of the United States of America, USA.
- Mansfield, P. and Grannell, P.M. (1973). "NMR 'diffractions' in solids." Journal of Physics C: Solid State Physics **6**: L422-L425.
- Mansfield, P. (1977). "Multi-planar image-formation using NMR spin echoes." Journal of Physics C: Solid State Physics **10**(3): L55-L58.
- Maunsell, J. H. R. and Gibson, J. R. (1992). "Visual response latencies in striate cortex of the macaque monkey. ." J. Neurophysiol. **68**: 1332-1344.
- McGinley, J., Srivastava, V. and DeMeester, G. (1997). "Passive shimming technique for MRI magnets." Magnetic Resonance Imaging **15**(3): 9-10.
- Nunez, P. L. and Silberstein, R. B. (2000). "On the relationship of synaptic activity to macroscopic measurements: does co-registration of EEG with fMRI make sense?" Brain Topography **13**: 79-96.
- O' Regan, S., Faul, S. and Marnane, W. (2010). Automatic detection of EEG artefacts arising from head movements. Conf Proc IEEE Eng Med Biol Soc.
- Ogawa, S., Lee, T. M., Nayak, A. S. and Glynn, P. (1990). "Oxygenation-sensitive contrast in magnetic resonance image of rodent brain at high magnetic fields. ." Magn Reson Med **14**: 68-78.
- Pfeuffer, J., Van De Moortele, P. F., Yacoub, E., Adriany, G., Andersen, P., Merkle, H., Ellermann, J. M., Ugurbil, K. and Hu, X. (2002). "Zoomed functional imaging in the human brain at 7 Tesla with simultaneously high spatial and temporal resolution." NeuroImage **17**: 272-286.
- Pfurtscheller, G. (1977). "Graphical display and statistical evaluation of event-related desynchronization (ERD)." Electroenceph clin Neurophysiol **43**: 757-760.
- Pfurtscheller, G. (1992). "Event-related synchronization (ERS): an electrophysiological correlate of cortical areas at rest." Electroenceph clin Neurophysiol **83**: 62-69.
- Pruessmann, K. P., Weiger, M., Scheidegger, M. and Boesiger, P. (1999). "SENSE: Sensitivity encoding for fast MRI." Magnetic Resonance in Medicine **42**(5): 952-962.

- Purves, D., Augustine, G. J., Fitzpatrick, D., Hall, W. C., LaMantia, A. and White, L. E. (2012). "Neuroscience." from <http://sites.sinauer.com/neuroscience5e/animations05.02.html>.
- Ritchison, G. (2013). "Neurons & the Nervous System." from <http://people.eku.edu/ritchisong/301notes2.htm>.
- Sanei, S. and Chambers, J. A. (2007). Introduction to EEG. In: EEG Signal Processing. Wiley, West Sussex, England: .pp. 1-17. 978-0-470-02581-9.
- Sayers, B., Mc, A., Beayley, H. A. and Henshall, W. R. (1974). "The mechanism of auditory evoked EEG responses." Nature **247**(481-483).
- Shepherd, G. M. (1974). The Synaptic Organization of the Brain. Oxford University Press, London.
- Speckmann, E., Elger, C. E. and Altrup, U. (1993). The Treatment of Epilepsy: Principles and Practices. In: Neurophysiologic basis of the EEG. E. Wyllie. Philadelphia: Lea & Febiger: pp.185-201.
- Ugurbil, K., Toth, L. and Kim, D. S. (2003). "How accurate is magnetic resonance imaging of brain function?" Trends Neurosci **26**(108-114).
- Vespa, P. M., Nenov, V. and Nuwer, M. R. (1999). "Continuous EEG monitoring in the intensive care unit: early findings and clinical efficacy." J Clin Neurophysiol. **16**(1): 1-13.
- Vijn, P., B., v. D. and Spekreijse, H. (1991). "Visual stimulation reduced EEG activity in man. ." Brain Research Reviews **550**(49-53).
- Weiss, S. and Mueller, H. M. (2003). "The contribution of EEG coherence to the investigation of language." Brain and Language **85**: 325-343.
- Westbrook, C. and Kaut, C. (1993). MRI in practice. Blackwell Science Ltd., London, 2nd Ed.
- Wolfe, P. (2010). Brain Matters: Translating Research into Classroom Practice. ASCD, Virginia, USA, 2nd Edition. 978-1-4166-1067-0.
- Yacoub, E., Van De Moortele, P. F., Shmuel, A. and Ugurbil, K. (2005). "Signal and noise characteristics of Hahn SE and GE BOLD fMRI at 7T in humans." NeuroImage **24**: 738-750.

# Chapter 3

---

*EEG artefacts produced during simultaneous acquisition of fMRI data and review of standard correction techniques*

### 3.1 Introduction

In the 1990's several groups (Ives *et al.*, 1993; Hill *et al.*, 1995; Warach *et al.*, 1996; Lemieux *et al.*, 1997) showed that the simultaneous recording of EEG and fMRI provides several advantages over interleaved EEG and fMRI recording protocols. These advantages arise because of the complementary properties of each imaging method (discussed in Section 2.9.3). These groups showed that the combination of the two modalities was technically feasible and safe for the subjects. However, the recording and analysis of simultaneous EEG-fMRI data is not without a number of difficulties. In these early studies they reported one particularly strong artefact, with steep signal slopes and huge amplitudes (far beyond physiological EEG amplitudes), which resulted from the sequentially switched magnetic gradients required for the MR imaging process (discussed in detail in Chapter 2).

Since the potential benefits of simultaneous EEG-fMRI recordings come at the expense of massive, unavoidable artefacts that corrupt the EEG signals recorded in the MR environment, it is not surprising that many researchers find it difficult to obtain satisfactory EEG data quality during simultaneous EEG-fMRI recordings, and may prefer to record the EEG and fMRI data separately (Bledowski *et al.*, 2007). However, over recent years significant progress has been made in artefact correction with the advent of more reliable hardware and software solutions. This chapter provides a review of the work that has already been carried out to overcome the technical difficulties associated with removing the artefacts. The following review focuses on the most prominent artefacts; it also discusses the limitations of currently available approaches to artefact reduction, as well as possible future directions of research in this area.

### 3.2 Prominent EEG Artefacts in Simultaneous EEG-fMRI

According to Faraday's law of induction, the induced electromotive force (EMF) is proportional to the time derivative of the magnetic flux and can therefore reflect changes in the magnetic field (gradient switching, RF) or changes in circuit geometry or position relative to the static  $B_0$  field due to body motion (Ives *et al.*, 1993; Lemieux *et al.*, 1997). These effects result in the induction of large voltages in the closed loops of the EEG system resulting from the EEG electrodes being galvanically coupled to the EEG amplifier input (by cables) and to the scalp surface. Therefore, physiological EEG data recorded inside the MRI scanner may appear either massively obscured or totally indiscernible due to the presence of



these induced artefact voltages. The magnitude of these artefacts depend on: the MR scanner's field strength ( $B_0$ ), the MR protocol applied, the subject's behaviour in the scanner, and the recording equipment used. Fig. 3.1 shows a typical example of a continuous EEG recording made inside a 3 T MRI scanner during fMRI data acquisition using an EPI pulse sequence. It shows the typical EEG data quality obtained in the MR scanner environment. The EEG signal recorded inside an MR scanner can be contaminated with the following artefacts:

- **Image Acquisition Artefact:** Image acquisition artefact is an unavoidable artefact which is caused by the switching of the magnetic field gradients, necessary for MR image acquisition. The two types of imaging artefact that has been identified until to-date are the gradient artefact (GA) and the radio frequency (RF) artefact. The largest rate of change of the magnetic field occurs during the application of the RF pulses (about 30,000 T/s) (Hill *et al.*, 1995). However, the

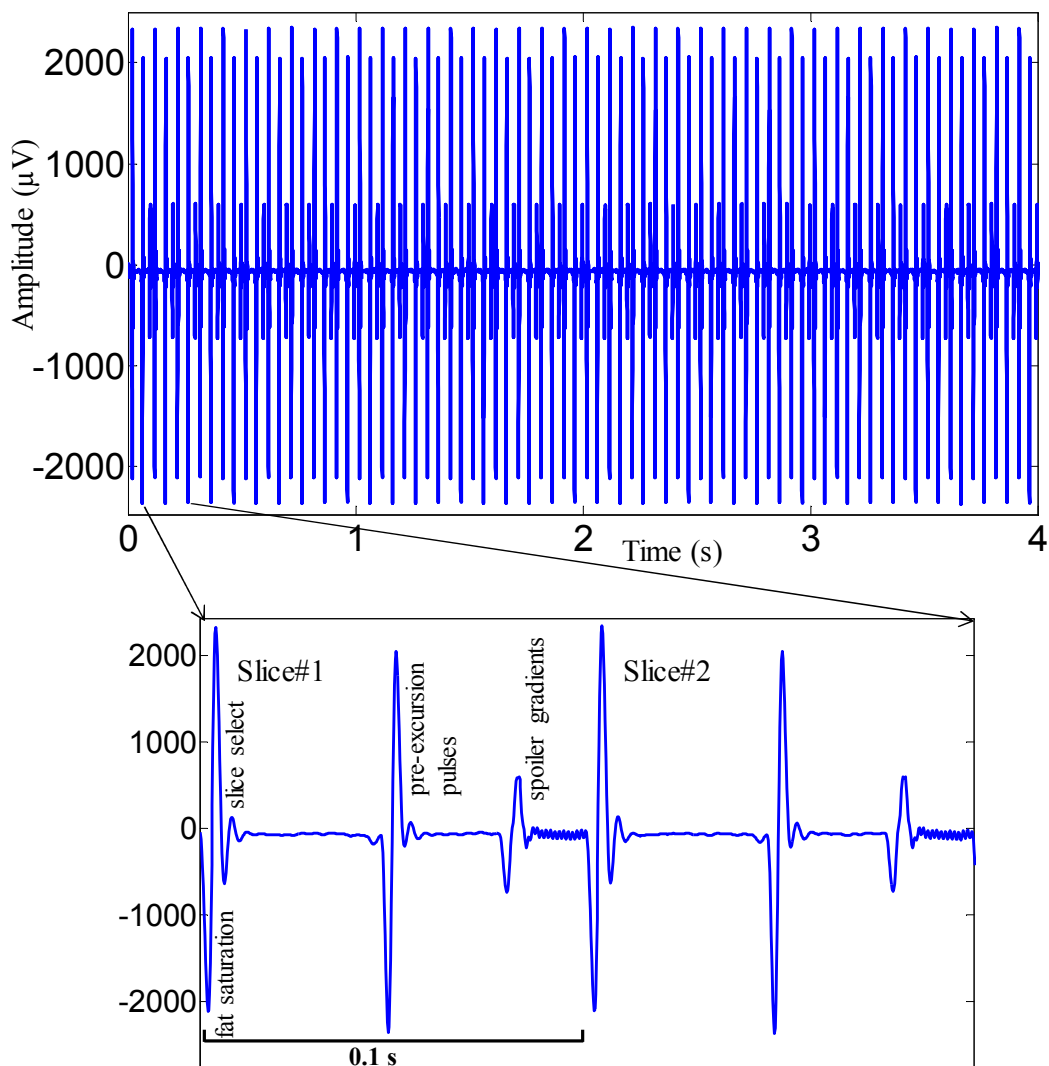


**Figure 3.1** Example of EEG recordings made during EPI image acquisition and showing the largest artefacts induced periods of the sequence (discussed in Section 2.8.1).

frequency of the RF pulses for spin excitation (e.g. 128 MHz at 3T), lies well outside the frequency range of conventional EEG amplifiers, resulting in greatly attenuated artefacts (Anami *et al.*, 2003). Spencer *et al.*, (2012) has showed that a signature of the RF pulse is still sometimes observed in EEG data recorded using standard EEG amplifiers, but this is much smaller than the artefacts generated by the MR gradients.

The contribution of the GA to the recorded EEG signals can easily be several orders of magnitude larger than the neural signal of interest (Felblinger *et al.*, 1999; Allen *et al.*, 2000). The rapidly varying magnetic field gradients (for example, the readout gradient switching frequency typically lies in the range of 500-1000 Hz), which cause the artefacts, are required for the spatial encoding of the MR signal and therefore used in fMRI sequences such as EPI, as discussed in detail in Chapter 2. The switching of these magnetic field gradients in the presence of the wire loops formed by the EEG electrodes, leads, amplifier and subject's scalp results in electromagnetic induction and therefore electrical signals which are detected by the EEG system. Thus, image acquisition artefact can obscure the whole acquisition bandwidth of the EEG signal in the multi-modal implementation of EEG-fMRI. In the early stage of this multi-modal approach, it was observed that the acquisition of an MR image results in complete obscuration of the physiological EEG (Ives *et al.*, 1993; Allen *et al.*, 2000). However, imaging artefacts induced in the EEG data have a strong deterministic component due to the pre-programmed nature of the MR sequence and therefore correction of the gradient artefact is generally considered a lesser problem than correction of other artefacts.

- **Pulse Artefact (PA):** Ives *et al.*, (1993) were the first to mention a second, weaker, MR specific artefact which can be observed as soon as the subject is placed in the MR environment. This artefact is always present in the scanner's magnetic field unlike the GA, which occurs only during MR image acquisition periods. This artefact is characterized by a repeatedly occurring waveform that is strongly linked to the heart beat and which may be a consequence of tiny head- and electrode movements caused by cardiac pulsation (Nakamura *et al.*, 2006). This is known as the 'ballistocardiogram' (BCG) or pulse artefact (PA). The PA does not display the same level of consistency as the GA and the artefact can vary on time scales as short as consecutive heart beats (Bonmassar *et al.*, 2002; Debener *et al.*, 2007), as well as

showing large variation across subjects (Hill *et al.*, 1995). The maximum amplitude of neural activity detected by EEG seldom exceeds  $50 \mu\text{V}$  and as such it may be completely obscured by the PA, whose amplitude can exceed  $200 \mu\text{V}$  at 3T (Debener *et al.*, 2007) and has some resemblance to epileptic spikes. The PA amplitude can be substantially larger than occipital EEG alpha oscillations. The peak amplitude can vary markedly across individuals, channels and MRI scanners. Although the PA is clearly visible on EEGs recorded inside the MR scanner even in the absence of scanning, the inability of current filtering methods to remove this artefact fully leads to significant degradation of the EEG data recorded in combined EEG/fMRI studies. This is because the frequency range of the PA ( $< 15 \text{ Hz}$ ) (Eichele *et al.*, 2010) coincides directly with the neuronal signals that are of interest in many EEG recordings (Bonmassar *et al.*, 2002).

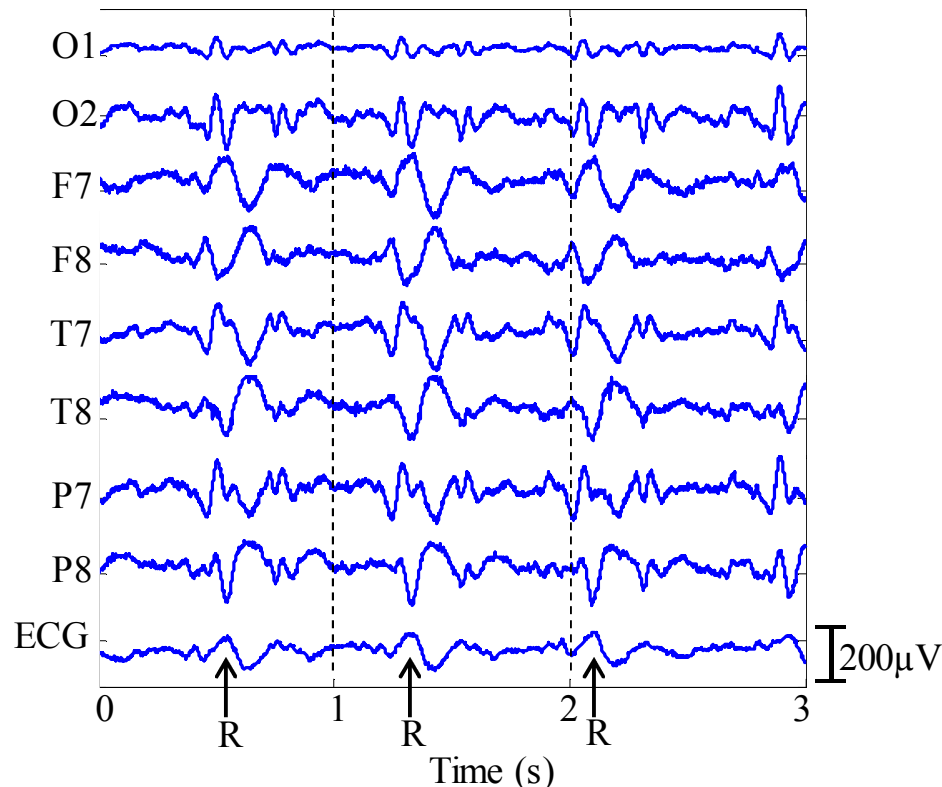


**Figure 3.2** Example of the pulse artefact in on-going EEG data recorded in a 3 T MRI scanner without MRI scanning. In these traces, R corresponds to the occurrence of the R-peak in the ECG recording.

A concurrent recording of the electrocardiogram (ECG) with EEG inside a 3 T MRI scanner reveals that the periodic distortion present in most EEG channels is related to the cardiac cycle. This is shown in Figure 3.2 where “R” denotes R peaks, a feature of

the cardiac cycle (Figure 3.3B for 0T) that is evident in the ECG. The exact aetiology of the PA is not known yet; it is likely that the pulsatile flow of blood associated with the cardiac cycle induces a rocking, nodding head motion (Anami *et al.*, 2002; Debener *et al.*, 2008; Yan *et al.*, 2010; Mullinger *et al.*, 2013). EEG electrodes (or cables) located near to blood vessels may experience motion related to the vessel pulsation, which could be another artefact source. Finally, the flow of blood, which is electrically conductive, in the magnetic field could be a source of artefact voltages that are recorded in the EEG (Eichele *et al.*, 2010). This is a result of the Hall Effect (a voltage difference is created on opposite sides of a moving conductor when placed in a strong magnetic field).

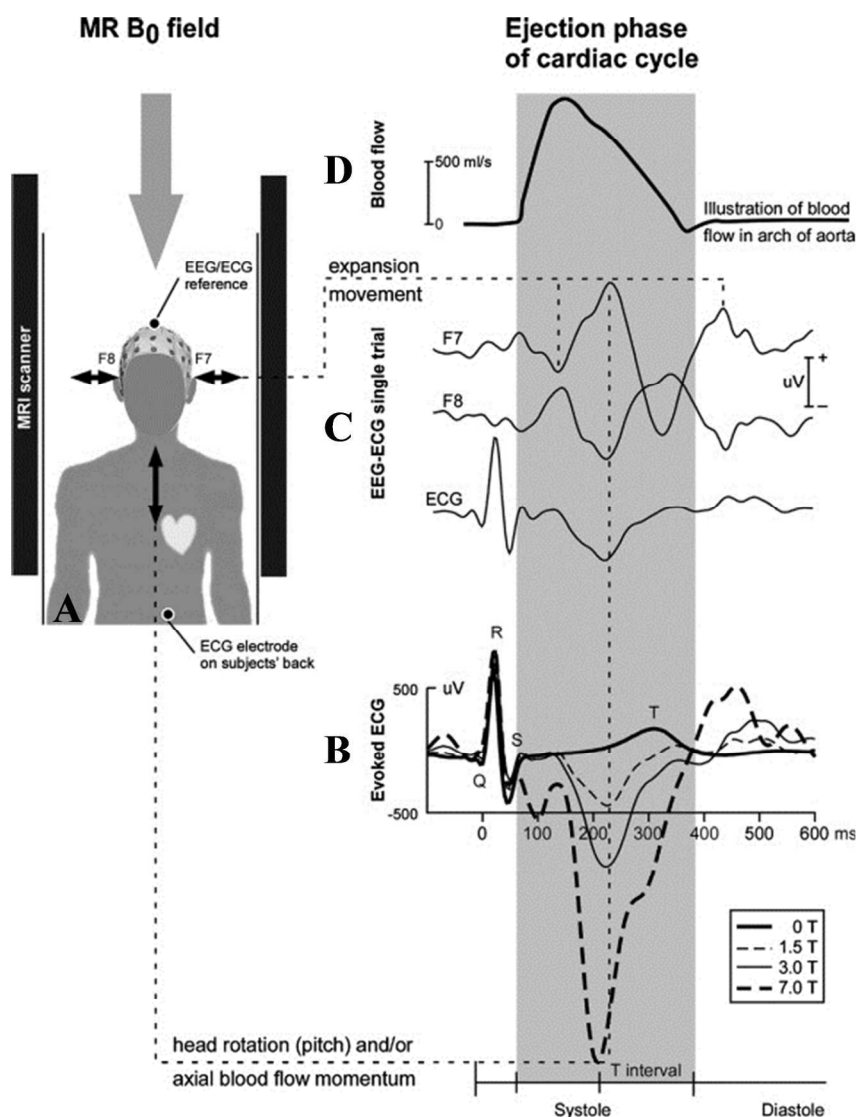


**Figure 3.3** A schematic diagram illustrating possible factors causing the PA. Two different types of movement are indicated, axial nodding rotation of the head and expansion movement at lateral and temporal scalp sites. The left part of the figure (A) illustrates a subject in supine position inside an MRI scanner. The locations of EEG electrodes, EEG/ECG reference site, and ECG recording site at the lower back are indicated. Lower right part of the figure (B) shows the evoked ECG from one individual, recorded outside the MRI (0 T) and inside three different MRI scanners (1.5, 3.0, 7.0 T). Above the evoked ECG traces, a typical single trial of ECG and EEG activity is shown (C), and on top (D), the blood-flow time course in the arch of aorta. As highlighted by the grey background, the BCG mostly occurs during the ejection phase of the cardiac cycle. Adapted from Debener *et al.*, (2008).

It is evident from Figure 3.3B that exposure to a strong magnetic field distorts the ECG signal most during the ST interval, whereas the QRS interval is unchanged compared to recordings made outside the MRI scanner. An additional deflection can

be observed between the onset of the S wave and the offset of the T wave (not present at 0 T). Careful comparison of the PA and ECG reveals a delay of approximately 200 ms between the ECG R peak (Figure 3.3B&C) and the peak artefact in the EEG traces (Allen *et al.*, 1998), indicating that the artefact is not simply a volume-conducted electrical ECG artefact, with fluctuations in the interval between PA occurrences reflecting fluctuations in the subject's heart rate.

In some previous work, it has been suggested that axial head rotation is the primary cause of the pulse artefact (e.g. Nakamura *et al.*, 2006), while others point to the possible local effect of pulsatile movements of scalp vessels on adjacent electrodes (Debener *et al.*, 2010). In addition to ballistic effects, motion of the blood (i.e. abrupt changes in blood velocity) can lead to the Hall Effect, which may also contribute to the PA (Debener *et al.*, 2010). These possible artefact contributions are summarised in Figure 3.3. More recent simulations (Yan *et al.*, 2010) and experimental work (Mullinger *et al.*, 2013) have strongly suggested that the primary source of the PA is head rotation.

Mullinger and colleagues tried to identify the relative contributions of cardiac-pulse-driven head rotation, the Hall Effect due to pulsatile blood flow and pulse-driven expansion of the scalp to the amplitude and variability of the PA. A bite-bar and vacuum cushion (Benar *et al.*, 2003) were used to restrain the head, thus greatly attenuating the contribution of cardiac-driven head rotation to the PA, while an insulating layer placed between the head and the EEG electrodes was used to eliminate the Hall voltage contribution. By using the RMS amplitude of the PA averaged over leads and time as a measure of the PA amplitude, Mullinger *et al.*, (2013) found that the head restraint and insulating layer reduced the PA by 61% and 42%, respectively, when compared with the PA induced with normal recording conditions. This indicates that cardiac-pulse-driven head rotation is the dominant source of the PA. The PA was reduced in RMS amplitude by 78% compared with the standard condition when both the insulating layer and head restraint in place, the remaining PA contribution resulting from scalp expansion or residual head motion. The variance of the PA across cardiac cycles was more strongly reduced by the insulating layer than the head restraint, indicating that the flow-induced Hall voltage

makes a larger contribution than pulse-driven head rotation to the variability of the PA.

- **Movement Artefact (MA):** A third significant artefact is the motion artefact (MA) which arises from the movement of the conducting loops, formed from the EEG leads and head, in the strong magnetic field of the MR scanner. The static  $B_0$  field becomes non-uniform away from the centre of the magnetic bore and movements of the electrode leads within the inhomogeneous field then result in the a change of flux linked and thus an EMF is induced in the lead loops (Eichele *et al.*, 2010). However, this source of artefact can be reduced significantly by simply twisting together electrode leads running from the subject's head to the amplifier inputs. This has the effect of reducing the area of the wire loops and thus reducing the EMF induced by movement (Goldman *et al.*, 2000). A further reduction of the induced EMF can be achieved by securely fixing the leads to a stationary surface, as the wires are then unable to cut lines of flux (Allen *et al.*, 1998; Mullinger *et al.*, 2008a).

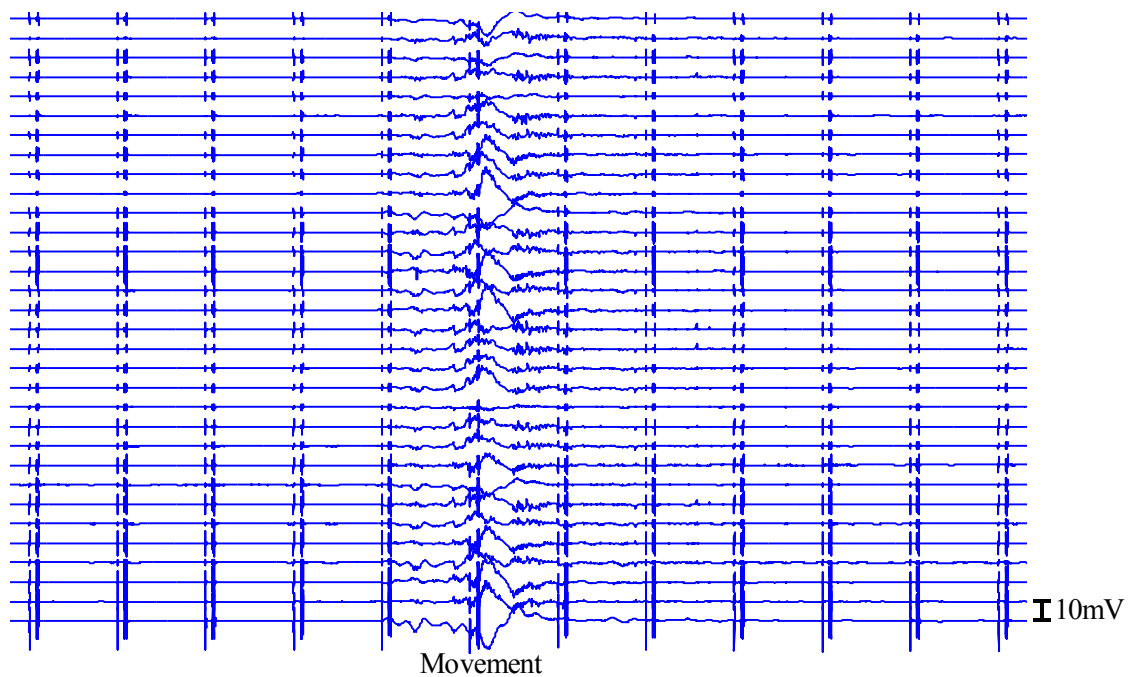


**Figure 3.4** Example of the motion artefact in on-going EEG data recorded in a 3 T MRI scanner during EPI image acquisition. Black bar denotes period of movement.

A severe problem with the implementation of simultaneous EEG-fMRI arises when subject movement occurs during a study (Fig. 3.4). Head rotation caused by talking, swallowing, coughing or turning, will also induce an EMF in the scalp-lead loops as the area of the loops normal to  $B_0$  will change. A second more subtle consequence of

subject movement is that it alters the morphology of the induced gradient artefacts on each lead. This is caused by the changes in the position and orientation of lead paths over time due to head movement. This change in morphology means that the artefact voltage waveforms recorded from each electrode vary over volume acquisitions making artefact correction difficult, as discussed in Section 3.3.1. Therefore, the combination of body motion with image acquisition artefacts can lead to random variations that represent a real challenge for artefact correction (Mullinger *et al.*, 2011; Jansen *et al.*, 2012).

- **Vibration Artefact (VA):** Another type of artefact is caused by the vibration which occurs in simultaneous EEG-fMRI recordings as a result of the gradient switching. This gradient switching causes the bed to vibrate when scanning occurs (Laufs *et al.*, 2008). Vibration artefacts can also be caused by the continuous running of the cryostat pump in some MR scanners, although in some systems this pump is automatically turned off during scanning and so is not a problem. In general VAs can be avoided by isolating the EEG amplifier and cabling from the scanner bed (Mullinger *et al.*, 2008a).

### 3.3 Artefact Removal Techniques

As already discussed in this chapter, it is impossible to identify the EEG neuronal signatures of interest from the raw EEG data collected in the MRI scanner without further processing of the raw data. In fact, a meaningful interpretation of the EEG signal is not possible without the application of artefact removal. The above mentioned artefact types obscure the original EEG signal and contaminate the data over a broad frequency range (0-3000 Hz) which contains the EEG signals of physiological interest, commonly 0-100 Hz (Ives *et al.*, 1993; Hill *et al.*, 1995; Allen *et al.*, 2000), as discussed in Chapter 2. It is assumed that the recorded EEG data is a linear mixture of original physiological EEG signal and the artefacts (Eichele *et al.*, 2010). Therefore it is impossible to inspect typical EEG features, like occipital alpha oscillations, without artefact removal techniques being applied first. To correct the artefacts, a number of groups have developed different techniques with different advantages. A more detailed description of the techniques is provided below:

### 3.3.1 Gradient Artefact Correction Techniques

As discussed in Section 3.2, the GA distorts the EEG spectrum over a broad frequency range, including the frequencies of interest ( $< 100$  Hz), and therefore cannot be fully accounted for by filtering (Allen *et al.*, 2000). The EEG is dominated by the harmonics of the slice repetition frequency (typically in the range of 10-25 Hz) convolved with harmonics of the volume repetition frequency (about 0.2-2 Hz) during periodic EPI BOLD scanning (Mandelkow *et al.*, 2006; Ritter *et al.*, 2008b). Therefore the power spectrum of the GA overlaps that of the neuronal EEG signals. Techniques to correct the GA have been developed by a number of groups with each technique exhibiting different advantages and disadvantages. The main methods are outlined here, although other variants do exist.

#### 3.3.1.1 Interleaved EEG-fMRI

Depending on the type of brain activity one is interested in studying, interruptions in MR scanning can be used to reduce the impact of gradient artefacts in the EEG data. In EEG-triggered fMRI, short series of fMRI images are acquired following the (random) occurrence of predefined EEG events such as epileptic discharges (Warach *et al.*, 1996; Seeck *et al.*, 1998; Krakow *et al.*, 1999; Symms *et al.*, 1999; Baudewig *et al.*, 2001; Lemieux *et al.*, 2001). This assumes that the peak of the BOLD changes associated with the neural activity of interest occurs with the same time delay as those of normal stimuli (typically 3-8 s); therefore, the delayed onset of fMRI acquisition relative to the neural response does not pose a problem for recording the BOLD response. However, this approach requires that the T1 saturation effects are modelled explicitly (Krakow *et al.*, 1999), and fMRI signal changes that occur over long time scales cannot be easily accounted for, given the irregular sampling.

In the periodic interleaved approach, MR acquisition is suspended at regular intervals, resulting in periods of EEG data acquisition free from GA (Ives *et al.*, 1993; Goldman *et al.*, 2000; Kruggel *et al.*, 2000; Sommer *et al.*, 2003; Ritter *et al.*, 2008a). Although interleaved protocols are generally less flexible and experimentally less efficient than continuous measurements, they are suitable for certain forms of brain activity such as slowly varying rhythms and evoked responses.



### 3.3.1.2 GA Reduction at Source

In concurrent EEG-fMRI, the GA can be reduced by minimising conductor loop area and avoiding conductor motion. By stabilising the subject's head with a vacuum cushion and fixing the EEG amplifiers and wires using sandbags, movement can be reduced (Anami *et al.*, 2003; Benar *et al.*, 2003). Goldman *et al.*, (2000) showed that the EEG artefact can be minimised by acquiring the EEG data using pairs of twisted single-lead electrodes. The voltages induced by motion and gradient switching in twisted dual leads cancel out since the currents induced in consecutive twists flow in opposing directions (Goldman *et al.*, 2000). Therefore, twisted dual leads for each EEG channel can provide greater gradient and motion artefact attenuation. Mullinger *et al.*, (2011) showed that positioning subjects so that their nasion was moved 4 cm axially from the scanner's iso-centre towards the feet significantly reduces the GA compared with the situation where the nasion is at iso-centre (discussed in detail in Section 3.3.1.8). This is a consequence of the reduction in the average magnetic field changes experienced by the EEG leads and head, which change in axial position with respect to the applied field gradients produces.

### 3.3.1.3 Filtering in the Frequency Domain

Gradient artefacts are periodic and distributed over a limited range of frequencies, suggesting that correction may be performed satisfactorily in the frequency domain. One such method is based on the comparison of the spectral content of EEG data acquired with and without simultaneous MR acquisition. The Fourier components of the signal corresponding to the MR-specific frequencies are set to zero for subsequent re-projection into signal space (Hoffmann *et al.*, 2000). The disadvantage of this method is that, due to a spectral overlap between the physiological EEG and GAs, some of the physiological EEG signal is removed as well. The method is also confounded by ringing artefact (Benar *et al.*, 2003), which results from discontinuities in the signals to be corrected. A similar approach relies on channel-wise subtraction of an average gradient artefact power spectrum, adapted by a scaling factor to the spectrum of the individual artefact, from the power spectrum of the artefact-distorted EEG (Sijbers *et al.*, 1999). To filter image acquisition artefacts in the frequency domain, one group (Grouiller *et al.*, 2007) first calculated the FT of the imaging artefact template (described in Section 3.3.1.5) and then applied weights to the spectral components of that FT. For spectral components of the artefact-corrupted EEG corresponding to strong spectral components in the artefact template, spectral filtering weights were inverted; thus, coefficients corresponding to the image acquisition artefact were attenuated. The corrected EEG spectra

were then converted back into the time domain. Grouiller *et al.*, (2007) reported their technique to be better than that of Hoffmann *et al.*, (2000) (where FT coefficients of the artefacts were set to zero) as this new technique improved signal preservation and reduced ringing.

### **3.3.1.4 GA Reduction by Stepping Stone Sampling**

The GA does not produce a continuously high voltage in EEG data recorded during simultaneous EEG-fMRI, rather large artefact voltages occur during short segments of each slice acquisition (Figure 3.1). A special MR sequence has been developed that allows EEG sampling at a digitisation rate of 1 kHz exclusively in the period in which the GA resides around baseline level (Anami *et al.*, 2003). This “stepping stone” sampling of EEG data is only possible in combination with synchronisation of the EEG digitisation and scanner clock. Anami *et al.*, (2003) reported that the GA amplitude is strongly attenuated to less than 5% of the raw artefact amplitude in the study. Consequently, a greater dynamic range is available for the physiological EEG, allowing resolutions of 0.1  $\mu\text{V}$  and below to be achieved (Ritter *et al.*, 2008a; Freyer *et al.*, 2009) which is particularly desirable when studying the gamma frequency band (30-100 Hz) where neuronal signals have a small amplitude and high frequency.

Hanson *et al.*, (2007) showed that the EEG can be recorded using surplus RF receive bandwidth. In this work, EEG signals amplified and digitised within the scanner are transmitted as radio waves that are detectable by the MR system. In contrast to the method by Anami *et al.*, (2003), GAs can be greatly reduced when sampled in periods free of gradient switching (approximately 100  $\mu\text{s}$  of silence following periods of gradient activity) using this stepping stone technique based on gradient field detection and a gating circuit (was opened for around 20  $\mu\text{s}$  to record EEG) that does not require modification of the MR sequence.

### **3.3.1.5 Average Artefact Subtraction (AAS)**

A processing method which is based on artefact template subtraction was proposed by Allen *et al.*, (2000). This widely applied technique can be used to significantly reduce GA amplitude so that EEG data acquired simultaneously with fMRI are usable. Allen’s technique for artefact removal relies on the reproducibility of the artefacts across successive image acquisitions. It involves the generation of a mean template of the artefacts for each lead, by means of averaging the EEG over a pre-specified number of TR-related epochs and

subtracting the template from the EEG traces in the current epoch. The epochs can be identified by recording a signal generated by the scanner that marks the beginning of each slice or volume acquisition. EEG traces corrected by mean template subtraction are shown in Figure 3.5B. The averaging procedures implemented in different algorithms differ with respect to the number and selection of averaging epochs and their weighting. The original template generation method consisted of a weighted sliding average of artefact epochs to account for possible changes of the artefact waveform over time and to account for a level of timing error (Figure 3.5C), and used adaptive noise cancellation (ANC) to further reduce residual image acquisition artefacts (Allen *et al.*, 2000; Becker *et al.*, 2005).

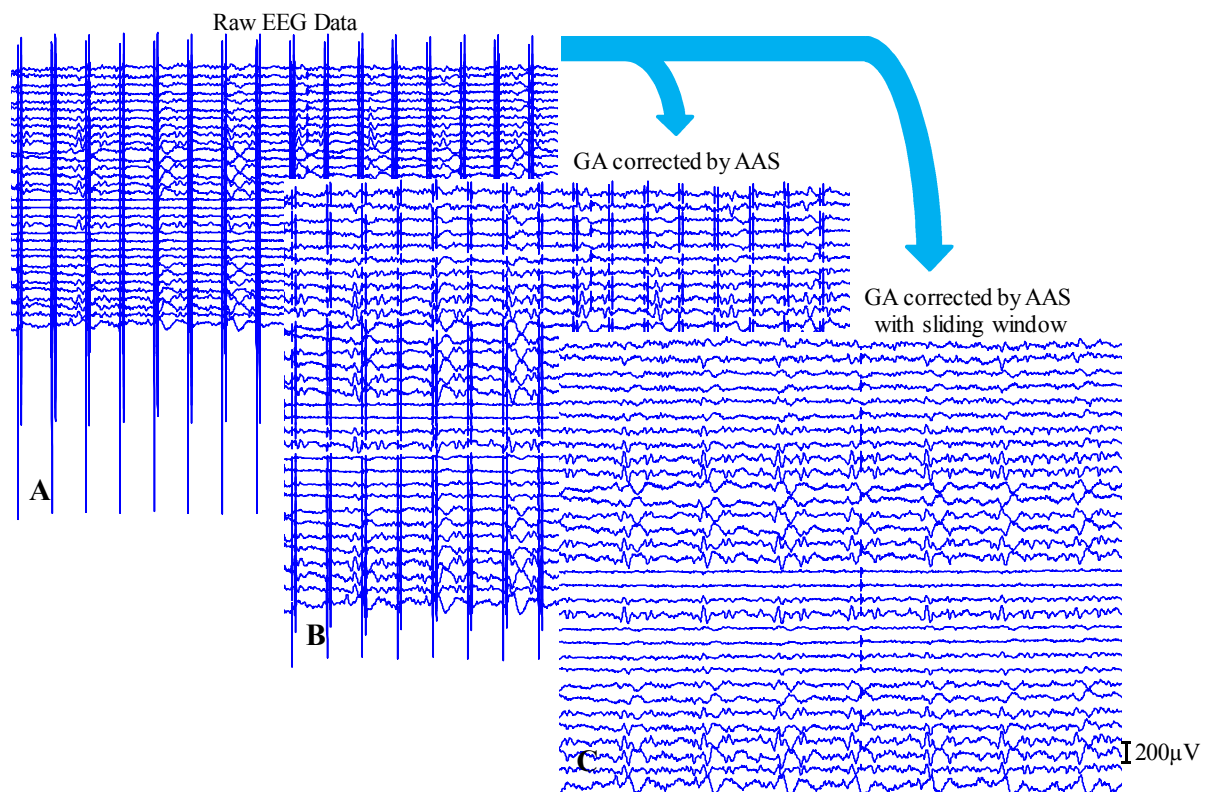


**Figure 3.5** Gradient artefact in EEG data (A). EEG channels with severe residual artefacts after cleaning with average artefact subtraction (B). EEG channels with residual artefacts after cleaning with sliding window AAS (C).

Although AAS (Allen *et al.*, 2000) is widely used to remove the gradient artefacts (Salek-Haddadi *et al.*, 2002), the waveform of the measured GA can change over time, thereby blurring the average waveform and decreasing the efficacy of this approach. Changes in the recorded GA waveform may be caused by:

- a) timing errors between fMRI scanning and EEG sampling (Cohen *et al.*, 2001),
- b) changes in electrode position and orientation over time due to head movement (as discussed in Section 3.2) (Moosmann *et al.*, 2009)

- c) mechanical vibrations that are caused by the switching gradient fields.

To overcome the problem (a), EEG data are typically sampled at 5 kHz which helps to characterize the GA completely. Anami *et al.*,(2003) proposed a way to solve problem (a) by using a single clock to control the EEG and fMRI acquisitions using customized hardware. Another approach is to record the fMRI trigger with a high temporal resolution and then to make the appropriate timing adjustment during average waveform subtraction (Allen *et al.*, 2000; Cohen *et al.*, 2001). Negishi *et al.*, (2004) have demonstrated an approach, in which the EEG is recorded with a relatively low sampling rate (1 kHz) after low-pass analogue filtering (cut-off frequency 80 Hz), followed by timing error detection and correction. One method of timing-error correction is to divide data into epochs, each containing an MRI volume or slice acquisition period. The epochs are then interpolated and subsequently aligned by maximising the cross-correlation to a reference period. After this adjustment, epochs are down-sampled to the original sampling frequency and subsequently averaged to yield an artefact template (Allen *et al.*, 2000; Negishi *et al.*, 2004). This approach does not require special hardware for synchronization of the EEG and MRI clocks or recording of the fMRI trigger with a high temporal resolution (discussed in Section 3.3.1.6). However, because timing errors are computed, there are possibilities for errors in the estimated timing errors. Another method of timing-error correction relies on the calculation of multiple image acquisition artefact templates, each representing a different version of the artefact waveform (Benar *et al.*, 2003). This algorithm is implemented in Brain Vision Analyzer (V.2.0.1.5528, Brain Products, Munich, Germany), providing so-called template drift detection (TDD) and subsequent template drift compensation. Using the drift information provided by TDD, different average-artefact templates are calculated. Each individual artefact is assigned to one template. Artefact correction is then obtained by subtracting the corresponding template from the respective artefact epoch.

When movements occur during the EEG data acquisition, the GA voltage waveforms recorded from each electrode vary over volume acquisitions, as outlined in (b), above. This variation in the GA waveforms means that the average artefact template does not exactly characterise individual occurrences of the gradient artefact. This problem is often partially solved by using a sliding time window to form the average artefact template (Allen *et al.*, 2000; Becker *et al.*, 2005). Moosmann *et al.*,(2009) have recently taken this concept further, by using information about the occurrence of subject movements derived from the MRI

realignment parameters, to guide the formation of templates, while Freyer *et al.*, (2009) analysed the similarity of the artefact produced by a particular image acquisition to the artefacts generated during all other image acquisitions and then formed a varying correction template by weighted summation over a limited number of the most similar artefact waveforms. These techniques help to reduce the effect of subject movement on GA correction, but do not eliminate this problem. ANC (Allen *et al.*, 2000; Wan *et al.*, 2006) and spatial filtering (Bonmassar *et al.*, 1999) have the ability to further reduce the problem caused by (b), although spatial filtering does not reduce noise components whose spatial pattern over the EEG electrodes fluctuate over time.

The Brain Vision Analyzer software offers three different methods of template estimation which use: (1) all epochs, (2) a sliding average of a certain number of epochs, or (3) a predefined number of initial scan epochs plus subsequent epochs exceeding a predefined cross-correlation with the initial template. There is an option to identify epochs by searching for steep gradients or high amplitudes in the EEG exceeding a defined threshold, instead of a specific scanner-generated signal. A modified approach for dynamic template estimation has been introduced by Freyer *et al.*, (2009) where artefact epochs in the template are weighted according to a Fourier spectrum-based similarity measure. This approach allowed the recovery of ultrahigh-frequency EEG signatures with amplitudes in the hundreds of nanovolt range even during image acquisition periods.

Niazy *et al.*, (2005) proposed a variant of the AAS method for the removal of gradient artefacts, known as fMRI artefact slice template removal (FASTR). In FASTR, a unique artefact template for each slice artefact in each EEG channel is constructed and then subtracted. Each slice template is constructed as the local moving average plus a linear combination of basis functions that describe the variation of residuals. The basis functions are derived by performing temporal principal component analysis (PCA) on the artefact residuals and selecting the dominant components to serve as a basis set. This technique has been shown to be superior to average artefact subtraction (Allen *et al.*, 2000) and applicable at a sampling rate as low as 2048 Hz. The FASTR algorithm, which is available in EEGLAB (Delorme *et al.*, 2004), has been successfully applied in a continuous EEG-fMRI study of pain-evoked responses at 3 T (Iannetti *et al.*, 2005). When the EEG signature of interest is of very high frequency, the beneficial outcome of a PCA-based post processing can be further enhanced by employing a band-specific PCA in the high-frequency band, in addition to the PCA on the

broad-band EEG. This cascaded, PCA post-processing enables the recovery of ultrafast EEG signatures, which would otherwise be obscured by residual imaging artefacts (Freyer *et al.*, 2009).

An alternative to average artefact template subtraction, but one that is closely related to it, allows correction of the GA in real time (Garreffa *et al.*, 2003). It is based on online subtraction of a model of the image acquisition artefact that is estimated using 48 s of initial data recorded prior to the EEG recording and subsequently fitted to the on-going EEG for subtraction. This technique has the advantage of allowing viewing of the physiological EEG signals in real time, but does not require EEG hardware modifications.

Wan *et al.*, (2006) used an adaptive finite impulse response (FIR) filter instead of the AAS method based on the frame-by-frame identification of the artefact. This method also assumes that the image acquisition artefacts are temporally stationary, except for a small frame-by-frame time-shift. Using a Taylor expansion based on the average artefact waveform, the time-shifted image acquisition artefact of each frame was estimated using the average artefact waveform and its derivatives, by least mean square (LMS) fitting. The algorithm outperformed simple average artefact template subtraction, which equals a zeroth-order FIR filter, but was not compared to artefact template subtraction combined with timing error correction.

A limitation of employing the sliding time window AAS technique (Allen *et al.*, 2000) occurs when choosing the window length, which is a compromise between optimally removing stationary and variable gradient artefacts without attenuating the brain signals (Mullinger *et al.*, 2008b). It is desirable, on one hand, to use a long sliding window to cover a sufficient number of slice (or volume) acquisitions so that brain signals can be averaged out of the computed template and thus are not removed by subtraction; on the other hand, a short sliding window is desirable for producing a more local artefact template that is better suited to filtering out a variable gradient artefact, but risks some loss of brain signals. This limitation often leads to unsatisfactory artefact removal by using AAS or its variants (Sijbers *et al.*, 1999; Goldman *et al.*, 2000; Goncalves *et al.*, 2007). Liu *et al.*, (2012) have shown how a singular value decomposition (SVD)-based filter can be used to overcome this compromise between removing the GA whilst leaving the brain signals. Whilst SVD (or equivalently PCA) is applied to the channel-wise signals that remain after AAS in all the above mentioned

techniques there are two distinctions that should be noted for the method proposed by Liu *et al.*, (2012) compared with the earlier methods (Negishi *et al.*, 2004; Niazy *et al.*, 2005; Mandelkow *et al.*, 2010). Firstly, although all the methods may help to reduce the residual artefacts remaining after AAS, there is no way to reverse the process and correct for the unwanted removal of brain signals when using PCA (Negishi *et al.*, 2004; Niazy *et al.*, 2005), which is however possible with the technique proposed by Lui *et al.*, (2012). Second, quantitative criteria for artefactual component selection are either lacking or loosely defined (Negishi *et al.*, 2004; Niazy *et al.*, 2005; Mandelkow *et al.*, 2010). For example, Niazy *et al.*, (2005) proposed to remove the first SVD component (or the first few) that explains the highest variance of the residual signal after AAS. This likely leads to over-correction because the first few SVD components always explain more variance than other components regardless of whether there are uncorrected artefacts in the signal or brain signals of interest. The SVD filter proposed by Liu *et al.*, (2012) uses data for all slice acquisitions to maximize the statistical power desired in order to avoid the removal of brain signals, with more than one SVD component able to be selected to account for the temporal variability of gradient artefacts.

### **3.3.1.6 Synchronisation of EEG and fMRI Data Acquisitions**

There are couple of key requirements for the successful implementation of the more standard mean template subtraction methods, which are described above (Sijbers *et al.*, 1999; Goldman *et al.*, 2000; Anami *et al.*, 2003; Mandelkow *et al.*, 2006; Goncalves *et al.*, 2007; Mullinger *et al.*, 2008c), in addition to the need for high reproducibility across repeated appearances of the artefacts. These requirements are:

- firstly, the EEG amplifiers must have a high enough dynamic range to prevent saturation by the large artefact voltages, thus allowing an undistorted artefact template to be produced.
- secondly, the artefact waveforms must be precisely and reproducibly sampled to provide an accurate template for each subtraction (Anami *et al.*, 2003; Mandelkow *et al.*, 2006; Mullinger *et al.*, 2008c).

The latter requires the timing of each appearance of the artefact waveforms to be accurately measured or precisely calculated. Temporal instability in the generation or sampling of the GA voltages and lack of synchronisation of the EEG sampling and gradient waveforms, can

both lead to partial failure of AAS. The large residual artefacts that arise as a consequence of this failure can easily overwhelm the signals of interest from the brain. Residual gradient artefacts can make recording activity across the gamma band particularly problematic in combined EEG-fMRI experiments (Ryali *et al.*, 2009). Therefore digital filtering of the EEG data after artefact correction with AAS is regularly employed to address this issue (Allen *et al.*, 2000; Benar *et al.*, 2003; Comi *et al.*, 2005; Gebhardt *et al.*, 2008; Ertl *et al.*, 2010; Mayhew *et al.*, 2010). This application of additional low-pass filtering, often with a low-frequency cut-off of less than 80 Hz, restricts the range of brain signals that can be investigated in concurrent EEG-fMRI experiments.

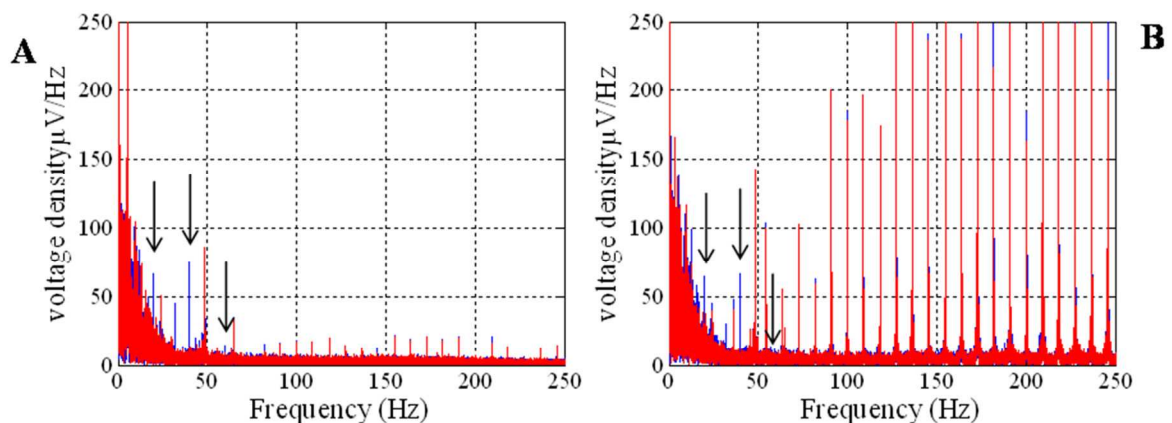


**Figure 3.6** The modulus of the Fast Fourier transform (FFT) of the signal from channel Oz, after gradient and pulse artefact correction periods for synchronized (A) and unsynchronized (B) data acquisition. Arrows indicate spikes of neuronal activity occurring at harmonics of the 10 Hz visual stimulus frequency (Adapted from Mullinger *et al.*, (2008a)).

Mandelkow *et al.*, (2006) provided the first demonstration that after synchronization of the EEG sampling to the MR scanner clock and ensuring that the chosen TR is a multiple of the EEG clock period, the GA can be sampled in a highly reproducible manner across repeated TR periods, allowing greatly improved gradient artefact correction by means of mean template subtraction and a consequently reduced need for low-pass filtering. When achieved, this negates the need for implementation of the timing-error correction methods outlined in Section 3.3.1.5. In their experiments on a phantom, Mandelkow *et al.*, (2006) showed that the usable EEG bandwidth, during concurrent MR image acquisition using a multi-slice EPI sequence, could be extended to 150 Hz by using synchronization. Mullinger *et al.*, (2008a) extended Mandelkow's work by showing that synchronization of the scanner clock to the EEG sampling improves GA correction in EEG data recorded from human subjects. They showed that synchronization of the EEG and MR scanner clocks significantly improves the



quality of the EEG data acquired in studies of neuronal function by means of combined EEG/fMRI, i.e., it increases the level of artefact attenuation at all frequencies, with particular improved performance at higher frequencies ( $>50$  Hz) provided that the chosen TR is a multiple of the EEG clock period (Mullinger *et al.*, 2008c).

A comparison of data acquired in the scanner with and without synchronization is shown in Figure 3.6. Although the differences in data recorded with and without synchronization are relatively small below 50 Hz, they rapidly become apparent at the higher frequencies. Synchronised EEG and fMRI digitisation has been used to study high-frequency (600 Hz) and very low amplitude (few 100 nV) components of the somatosensory evoked potential (Ritter *et al.*, 2008a; Freyer *et al.*, 2009) and spontaneous variations in the theta (3-6 Hz) and gamma (28-40 Hz) ranges (Giraud *et al.*, 2007).

In situations where the required clock synchronization through external hardware or precise control over the scanner software cannot be taken for granted, the retrospective methods of aligning the GA in image acquisitions offer a practical alternative to hardware synchronisation. These are typically needed when synchronisation cannot be achieved or the TR used is not a multiple of the EEG scanner clock period. A number of these retrospective correction methods have been discussed in Section 3.3.1.5. In addition to the aforementioned techniques, Mandelkow *et al.*, (2010) compared their retrospective method with prospective hardware synchronisation (Mandelkow *et al.*, 2006) and showed that prospective and retrospective synchronization show equivalent results in simulations within reasonable limits depending on the sampling rate and signal bandwidth. The advantages of retrospective synchronization are mostly limited to lower frequencies ( $<100$  Hz) depending on the relative contributions of the relative timing error and other artefacts (motion, respiration, BCG) to the residual GA and therefore it is obviously more desirable to use prospective synchronization; which is increasingly possible due to the commercial availability of synchronization hardware. Liu *et al.*, (2012) claim that the SVD filter is capable of removing GAs even with imperfect synchronization. However, this method is not very useful for real-time removal of GAs since it does not utilize the spatial dependency of gradient direction.

Apart from the temporal PCA and FASTR methods (discussed in Section 3.3.1.5), removal of GAs is mainly based on the assumption of a tight temporal relation between the EEG and scanner clocks, resulting in a highly reproducible artefact. Gonçalves *et al.*, (2007) presented

a variation of the average-subtraction algorithm, which can be used to correct EEG for GAs. It corrects for the time misalignment between EEG and fMRI data, which results from the desynchronization between the corresponding clocks, by interpolating the EEG data using an FFT algorithm, thus avoiding the use of extra hardware and MR sequence programming. de Munck *et al.*, (2013) have recently extended this work by estimating GA repetitions using a clustering algorithm, combined with selective averaging. They have shown that clustering of the GAs yields cleaner EEG data, after correction of data recorded during concurrent fMRI at 3 T using a sampling frequency of 2048 Hz. It has also been shown that this technique gives clean EEG even when the EEG is sampled only at a rate of 256 Hz (de Munck *et al.*, 2013).

### **3.3.1.7 Independent Component Analysis (ICA)**

Another approach to imaging artefact correction is independent component analysis (ICA) (Grouiller *et al.*, 2007; Mantini *et al.*, 2007; Ryali *et al.*, 2009). ICA is a signal processing technique that recovers independent sources from a set of simultaneously recorded signals that result from a linear mixing of the source signals (Mantini *et al.*, 2007). Since EEG and image acquisition artefacts are generated by different independent processes and are therefore uncorrelated, ICA seems to be an appropriate approach for artefact correction. Mantini and colleagues categorised the ICA sources into two signal categories: brain signals and artefacts. This was done by visual inspection or in an automated approach by correlation to reference signals. Only sources classified as non-artificial were back-projected and used for further analysis. This approach proved to be capable of not only removing residual image acquisition artefacts, but also pulse and ocular artefacts (see Section 3.3.2.2). Grouiller *et al.*, (2007) compared an ICA-based imaging artefact removal approach to three other approaches to imaging artefact correction: AAS (Allen *et al.*, 2000), FASTR (Niazy *et al.*, 2005) and Fourier transform (FT) filtering (Hoffmann *et al.*, 2000). They used the implementation of the Infomax ICA algorithm in the EEGLAB toolbox (Computational Neurobiology Laboratory, Salk Institute, La Jolla, CA, USA: <http://www.sccn.ucsd.edu/eeglab/>) (Delorme *et al.*, 2004). The authors selected the components that were correlated with the imaging artefact template. Selected components had a normalised cross-correlation coefficient higher than the average plus one standard deviation of that coefficient computed for all the components. The components representing image acquisition artefacts were excluded from the EEG reconstruction. Results for the performance of ICA, however, differed between simulations and real data. Results obtained by Grouiller *et al.*, (2007) indicate that ICA may not be applicable for efficiently estimating independent components in long time series of EEG data.

A theoretical reason for this might be the spatial non-stationarity of the EEG data and more particularly the imaging artefact signal, limiting the efficacy of ICA for GA correction.

### 3.3.1.8 Modelling Gradient Artefact

Yan *et al.*, (2009) showed the pattern of GAs induced on different leads by time-varying longitudinal and transverse gradients could be modelled based on the knowledge of the lead paths and head position in the gradient fields. This modelling work provided insight into ways in which the magnitude of the GA could be reduced at source. One of the ways suggested, a change in the axial positioning of the subject, has been further investigated (Mullinger *et al.*, 2011).

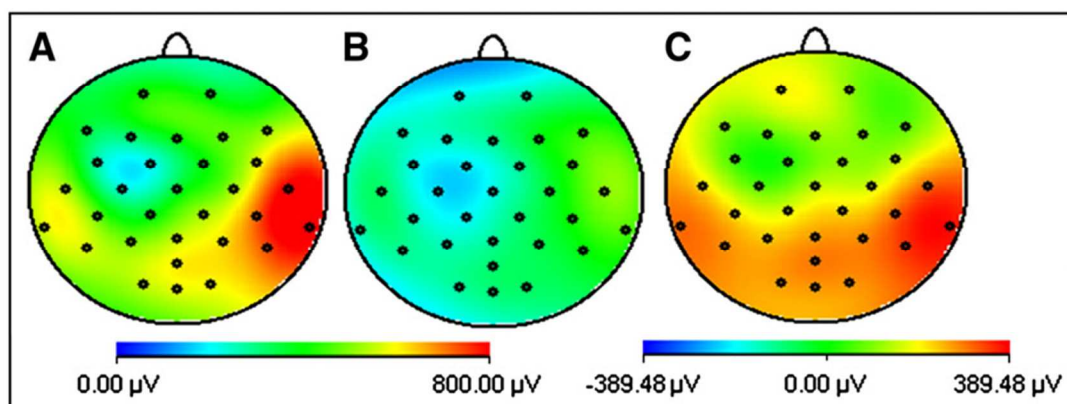


**Figure 3.7** Maps of the RMS (over time) of the gradient artefact produced by a multi-slice EPI acquisition with the nasion at (A) iso-centre; (B) +4 cm. Panel C shows the difference, A–B. Data averaged over six subjects. (Adapted from Mullinger *et al.*, (2011))

Figure 3.7 shows maps of the RMS value of the average gradient artefact over a typical fMRI slice acquisition with the subjects positioned with nasion at iso-centre (A) and at the optimal position corresponding to a shift of 4 cm in the direction of the feet (B), averaged over six subjects. Figure 3.7C shows the difference of these two maps with the positive values indicating that the GA is smaller in magnitude at the optimal position. This work showed that a significant reduction (40%) in the GA magnitude can be achieved by shifting the subject by 4 cm towards the feet relative to the standard subject position (nasion at iso-centre). In addition the residual GA after artefact correction was also reduced when small movements had occurred during data acquisition. This subject repositioning has the advantage that it can be used in conjunction with any of the artefact correction methods described above. A summary of the main methods with their advantages and disadvantages is shown in Table 3.1.

**Table 3.1** Summary of main GA correction methods and the relative merits of each of them.

<b>Sub-group</b>	<b>Authors</b>	<b>Method</b>	<b>Advantages</b>	<b>Disadvantages</b>
Interleaved EEG-fMRI	Warach <i>et al.</i> , 1996; Krakow <i>et al.</i> , 1999; <a href="#">ENREF 7</a> Lemieux <i>et al.</i> , 2001	EEG-triggered fMRI	<ul style="list-style-type: none"> <li>• EEG data acquired while gradients are not applied</li> </ul>	<ul style="list-style-type: none"> <li>• need to model MRI T1 saturation effects explicitly</li> </ul>
	Ives <i>et al.</i> , 1993; Goldman <i>et al.</i> , 2000; Ritter <i>et al.</i> , 2008a	periodic interleaved approach	<ul style="list-style-type: none"> <li>• periods of EEG data acquisition free from GA</li> </ul>	<ul style="list-style-type: none"> <li>• less flexible</li> <li>• experimentally less efficient</li> </ul>
GA reduction at source	Anami <i>et al.</i> , 2003; Benar <i>et al.</i> , 2003	vacuum cushion and sand bag	<ul style="list-style-type: none"> <li>• stabilising the subject's head</li> <li>• overall artefact reduction</li> <li>• can be used in conjunction with other correction</li> </ul>	<ul style="list-style-type: none"> <li>• not very effective at reducing the smaller motion events</li> </ul>
	Goldman <i>et al.</i> , 2000	twisted dual-lead electrodes	<ul style="list-style-type: none"> <li>• greater GA and MA attenuation</li> <li>• can be used in conjunction with other correction</li> </ul>	
	Yan <i>et al.</i> , 2009 Mullinger <i>et al.</i> , 2011	adjust subjects' positioning	<ul style="list-style-type: none"> <li>• significantly reduces the GA</li> <li>• can be used in conjunction with other correction methods</li> </ul>	
Filtering in the frequency domain	Hoffmann <i>et al.</i> , 2000	Frequency based approach	<ul style="list-style-type: none"> <li>• simple in implementation</li> </ul>	<ul style="list-style-type: none"> <li>• some of the physiological EEG signal is removed</li> <li>• ringing artefact</li> </ul>
	Grouiller <i>et al.</i> , 2007	Weighted FT method	<ul style="list-style-type: none"> <li>• improved signal preservation</li> <li>• reduced ringing</li> </ul>	<ul style="list-style-type: none"> <li>• computationally complex</li> </ul>
Stepping stone sampling	Anami <i>et al.</i> , 2003	“stepping stone” method	<ul style="list-style-type: none"> <li>• GA amplitude is strongly attenuated</li> <li>• greater dynamic range</li> </ul>	<ul style="list-style-type: none"> <li>• Non-standard MR sequence required</li> </ul>
	Gonçalves <i>et al.</i> , 2007	Selective average subtraction	<ul style="list-style-type: none"> <li>• corrects for the time misalignment between EEG and fMRI data</li> <li>• avoids the use of extra synchronization hardware and MR sequence programming</li> </ul>	<ul style="list-style-type: none"> <li>• only usable when EEG sampling frequency and low-pass filtering are sufficient in relation to MR gradient switching</li> </ul>
	De Munck <i>et al.</i> , 2013	clustering algorithm	<ul style="list-style-type: none"> <li>• gives clean EEG even with 256 Hz sampling frequency</li> </ul>	<ul style="list-style-type: none"> <li>• useful mainly for EEG-systems that are not time-locked to the MR scanner clock</li> </ul>
	Hanson <i>et al.</i> , 2007	EEG recorded using surplus RF receive bandwidth	<ul style="list-style-type: none"> <li>• does not require modification of the MR sequence</li> </ul>	<ul style="list-style-type: none"> <li>• customized hardware required</li> <li>• need to sample EEG in periods free of gradient switching</li> </ul>
Average Artefact Subtraction (AAS)	Allen <i>et al.</i> , 2000 Becker <i>et al.</i> , 2005	AAS with ANC	<ul style="list-style-type: none"> <li>• significantly reduce GA amplitude</li> <li>• easy to implement</li> <li>• ANC to compensate</li> </ul>	<ul style="list-style-type: none"> <li>• Template changes with timing error, movement and vibration</li> </ul>

			timing error	
	Negishi <i>et al.</i> , 2004	Temporal PCA	<ul style="list-style-type: none"> <li>• special hardware to synchronize EEG and MRI clocks not required</li> <li>• no need to record the fMRI trigger with a high temporal resolution</li> </ul>	<ul style="list-style-type: none"> <li>• possibilities for errors in the estimated timing errors</li> <li>• no way to reverse the process of correcting for the unwanted removal of brain signals which can occur when using PCA</li> </ul>
	Bonmassar <i>et al.</i> , 1999	spatial filtering	<ul style="list-style-type: none"> <li>• reduce template variation due to head movement and vibration</li> </ul>	<ul style="list-style-type: none"> <li>• does not reduce noise whose spatial pattern of influence on the EEG electrodes fluctuates over time</li> </ul>
	Moosmann <i>et al.</i> , 2009 Freyer <i>et al.</i> , 2009	AAS variant	<ul style="list-style-type: none"> <li>• reduce the effect of subject movement on GA correction</li> </ul>	<ul style="list-style-type: none"> <li>• does not eliminate the movement problem in GA correction</li> <li>• dependent on the fMRI motion parameters to characterise all movements (poor temporal resolution)</li> </ul>
	Garreffa <i>et al.</i> , 2003	Real-time AAS	<ul style="list-style-type: none"> <li>• online correction</li> </ul>	<ul style="list-style-type: none"> <li>• modified EEG equipment required</li> </ul>
	Niazy <i>et al.</i> , 2005	FASTR	<ul style="list-style-type: none"> <li>• superior to the use of AAS alone</li> <li>• works with sampling rate as low as 2048 Hz</li> </ul>	<ul style="list-style-type: none"> <li>• no way to reverse the process of correcting for the unwanted removal of brain signals which can occur when using PCA</li> <li>• quantitative criteria for artifactual component selection are lacking/loosely defined</li> </ul>
	Wan <i>et al.</i> , 2006	adaptive FIR filter	<ul style="list-style-type: none"> <li>• outperforms simple AAS</li> </ul>	<ul style="list-style-type: none"> <li>• not yet compared to AAS with timing error correction</li> </ul>
	Liu <i>et al.</i> , 2012	SVD filter	<ul style="list-style-type: none"> <li>• residual artefact reduction process can be reversed</li> <li>• artefact component selection criteria properly defined</li> </ul>	<ul style="list-style-type: none"> <li>• complex concept</li> <li>• does not utilize the spatial dependency of gradient direction</li> </ul>
Synchronisation of EEG and fMRI data acquisitions	Mandelkow <i>et al.</i> , 2006; Mullinger <i>et al.</i> , 2008c	Hardware synchronization	<ul style="list-style-type: none"> <li>• easy to implement</li> <li>• improve GA correction significantly</li> <li>• don't need to use 80 Hz low-pass filtering</li> </ul>	<ul style="list-style-type: none"> <li>• hardware dependent solution</li> <li>• improved performance mainly observed at</li> </ul>

				higher frequencies (>50 Hz)
	Mandelkow <i>et al.</i> , 2010	retrospective synchronization method	<ul style="list-style-type: none"> <li>• substitution for hardware synchronisation</li> </ul>	<ul style="list-style-type: none"> <li>• limited to lower frequencies (&lt;100 Hz)</li> </ul>
Independent Component Analysis (ICA)	Grouiller <i>et al.</i> , 2007; Mantini <i>et al.</i> , 2007; Ryali <i>et al.</i> , 2009 Grouiller <i>et al.</i> , 2007	Infomax ICA	<ul style="list-style-type: none"> <li>• capable of not only removing residual GA but also pulse and ocular artefacts</li> </ul>	<ul style="list-style-type: none"> <li>• not applicable for efficiently estimating independent components in long time series of EEG data.</li> </ul>
Artefact rejection by spatial filtering	(Brookes <i>et al.</i> , 2008)	Beamformer	<ul style="list-style-type: none"> <li>• can reduce PA and residual GA after AAS</li> </ul>	<ul style="list-style-type: none"> <li>• difficulty in accurately calculating the EEG forward solution</li> <li>• two spatially separate, but temporally co-varying sources will be suppressed</li> </ul>

### 3.3.2 Pulse Artefact Removal

As discussed in Section 3.2 there are multiple possible contributions to PA generation (Figure 3.3). The factors that can lead to differences in the PA are linked to the subject and experimental setup. Firstly, the variation of PA amplitude with field strength has important consequences for the choice of artefact removal technique (Debener *et al.*, 2008). Secondly, there are inter-individual differences in patterns of cardiac activity, such as changes in heart rate or peak latencies. For those individuals with a higher heart rate (shorter interbeat interval), the PA signature between adjacent cardiac cycles may overlap to some extent, which can further complicate artefact removal (Vincent *et al.*, 2007; de Munck *et al.*, 2013). Thirdly, the quality of the ECG recording may vary across subjects and/or sites, and it may not always be possible to identify the onset of every single cardiac cycle precisely. This can impair the performance of the PA removal procedures that rely on the detection of each cardiac cycle's onset.

Some authors (Goldman *et al.*, 2000; Benar *et al.*, 2003) recommended that an attempt should be made to reduce pulse artefacts prior to amplification by carefully laying out and immobilising the leads, twisting the leads, using a bipolar electrode chain arrangement and a head vacuum cushion. It is noteworthy that in EEG-fMRI studies in epilepsy, some investigators have found these measures to be sufficient, at least at 1.5 T, to allow useful analysis of the EEG of epileptic patients (Sammer *et al.*, 2005; Hamandi *et al.*, 2008).

However, it is more common to combine these efforts with post-processing artefact correction methods. A number of groups have developed a number of techniques to minimize the PA, with each technique exhibiting different advantages and disadvantages. The main methods are classified into couple of sub-categories which are outlined below:

### 3.3.2.1 Temporal Pattern PA Removal Approaches

This section describes the techniques of temporal template based PA correction which rely on identification of the R-peak of the cardiac cycle.

#### *Average Artefact Subtraction (AAS)*

Allen *et al.*, (1998) introduced the AAS algorithm, which has become one of the most frequently used methods for PA correction. The algorithm is predicated on the assumption that the EEG signals of interest (neuronal activity) and the ECG are not correlated, and that the artefact is relatively stable across a number of successive heartbeats. Therefore, in the ideal situation of a perfectly stable heartbeat, subtraction of the EEG averaged over a number of preceding heartbeats from the on-going EEG will result in the removal of the artefact. While different implementations and developments of the AAS exist (Laufs *et al.*, 2008), the basic principle of the AAS is common to all variants.

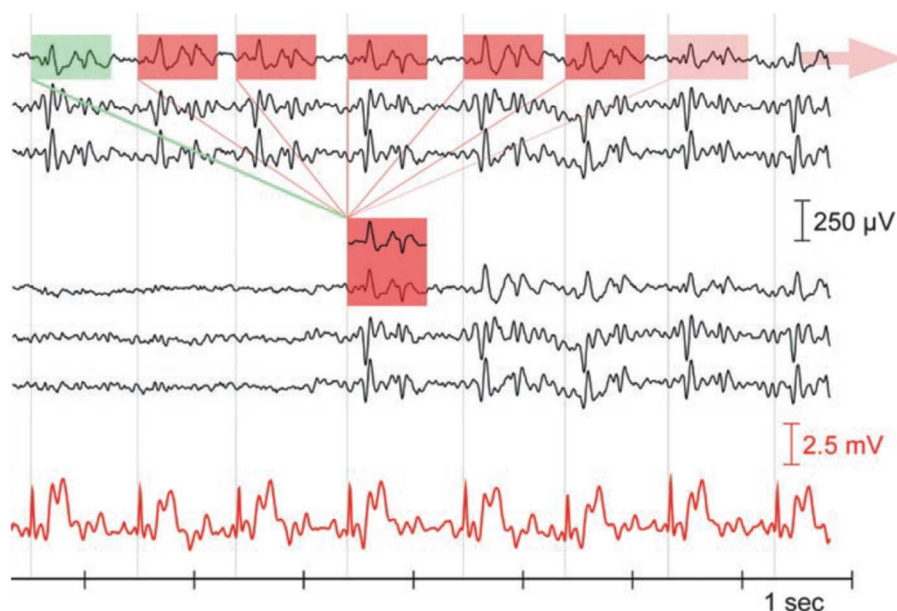


**Figure 3.8** Schematic of the average artefact subtraction procedure. For each channel, a waveform template is generated by averaging EEG epochs over adjacent cardiac cycles, with the time-locking event being derived from the ECG. The template generation is combined with a moving average procedure, and new templates are generated for each cardiac cycle. The procedure is repeated for each EEG channel. Adapted from (Debener *et al.*, 2010).

Figure 3.8 illustrates and highlights the main steps of the AAS method for PA correction (Debener *et al.*, 2010). As discussed in Section 3.3.1.5, the AAS approach requires knowledge of the precise onset of each occurrence of the artefact, in this case the cardiac cycle. For the PA correction, R-peaks from the ECG are used to define the artefact template. The averaged artefact template represents the evoked PA with the on-going EEG activity averaged out. The procedure is repeated for every EEG channel and can be implemented in real time. In theory, the quality of the template should increase with the number of epochs used. However, averaging more epochs reduces the sensitivity of the template to capture temporal fluctuations of the artefact. Therefore the number of cardiac cycles typically used to create a sliding window template is 21 (Allen *et al.*, 1998).

### ***AAS variant***

A lack of stability of the PA and reliable and precise detection of the onset of each cardiac cycle are the main causes of failure of AAS algorithm for PA correction. Deviations from the stability assumption result in inaccurate artefact estimation and therefore lead to greater residual artefact after subtraction. Shortening the moving average window size cannot fully compensate this problem, since, as previously discussed, a smaller moving average window is likely to remove physiological EEG signals. The choice of temporal length of the template is also potentially problematic due to inter-subject and dynamic variations in the R–R peak interval. A mismatch between template window length and artefact duration will also lead to greater residual artefact. The variation in the period of the cardiac cycle has led to the introduction of alternative template generation schemes that either scale the PA template with a percentage of the mean R-R period in the moving average window (Ellingson *et al.*, 2004) or that build a template which incorporates the PA data for all R-R period lengths present in the current moving average window (BrainVision Analyzer software, Brain Products GmbH, Munich, Germany). In the latter case, this template is then adaptively applied to each QRS period based on its R-R period, thus ensuring that no portion of the PA remains uncorrected due to a suboptimal template length. Alternative template constructions that are based on weighted averages (Goldman *et al.*, 2000) or median instead of mean values (Sijbers *et al.*, 2000) have been devised to improve quality of the template used for subtraction although these are not able to account fully for inter-artefact variability.



The R-peak can be difficult to identify due to ECG channel contamination resulting from gradient switching and the presence of flow artefacts leading to missed cycles or inaccurate template estimation window alignment, and consequently degraded template estimates and residual PAs. Accurate marker position improves the quality of the PA correction, in particular with regard to residual noise in the higher-frequency range of the EEG signal. To ensure good ECG recording quality, careful consideration of the positioning of the ECG electrodes is worthwhile. The ECG trace is generally recorded from a single electrode attached to the lower back and referenced against the reference electrode in the EEG cap (Debener *et al.*, 2005, 2007, 2008). This scheme ensures large R-peaks while avoiding respiratory and other movement related artefacts on the ECG channel. Mullinger *et al.*, (2008c) developed an alternative method that made use of the physiological monitoring apparatus attached to the MRI scanner, specifically the vectorcardiogram (VCG). The VCG is more commonly used for cardiac gating of MRI scans, and requires the application of four ECG electrodes. These multiple ECG signals are converted into planar VCG signals, leading to much more robust identification of the QRS complex, which can then be used to perform PA correction using AAS. In addition, the VCG signals are inherently less sensitive to gradient artefacts because of the short lead length and the low pass filtering that is applied at the hardware stage. The disadvantage of this approach is that four additional electrodes need to be applied to the participant's chest and, since the EEG and VCG are recorded by separate systems, they must be explicitly temporally synchronized in the post-processing steps.

Some implementations of the AAS algorithm, such as that in BrainVision Analyzer, already take jitter of R-peak information into account, and automatically align markers using statistical information to guide marker placement and ensure that the overall jitter is minimised before correction.

### **3.3.2.2 Spatial Pattern PA Removal Approaches**

The potential virtue of spatial approaches is that exact knowledge of the R-peak of each cardiac cycle is not necessarily required. Therefore, in principle, a spatial approach can avoid problems that are inherent to temporal approaches discussed above. Spatial approaches are already successfully used in clinical practice for the removal of eye blink and eye movement artefacts. This prior success motivated two different spatial PA correction approaches (Benar *et al.*, 2003): PCA and ICA. The assumption behind these is that the PA contribution is physiologically independent from on-going EEG activity in the case of ICA and orthogonal

to on-going EEG activity in the case of PCA. Therefore, the PA is presumed to be contained in a small number of components, whereas all other EEG activity should be represented by the remaining components. In the original work by Benar and colleagues, PA components were visually identified by exploring the similarity of all component time courses to the simultaneously recorded ECG signal (Benar *et al.*, 2003). Back-projection of components which were not assigned as PA components resulted in reconstructed EEG traces with reduced artefact. Benar *et al.*, (2003) found that both ICA and PCA were well suited for this task, as they eliminated the PA while preserving the relative amplitudes of neuronally generated epileptic spikes. However, the subjective selection of components is one drawback of this approach, since it makes its performance user dependent and leads to a requirement for training. Indeed, it can be rather difficult to visually identify and select the components that represent the PA beyond the first few strongest and most obvious ones. Srivastava *et al.*, (2005) proposed the identification of independent components based on their degree of correlation with the ECG, which has the advantage of eliminating subjective inspection of components by investigators.

Negishi *et al.*, (2004) and Niazy *et al.*, (2005) independently proposed a new way of constructing a PA template where the authors suggested generating PA templates based on a channel-wise temporal PCA, thereby relaxing the stability requirement. Niazy's optimal basis set (OBS) method uses the first few principal components as representations of distinct PA templates. These templates used to regress out the PA from the EEG data and the OBS approach thus accounts for greater temporal variation in the artefact shape. This is a freely available Matlab plug-in for the open-source EEGLAB environment (Delorme *et al.*, 2004). Since the number of necessary artefact templates is not known in advance and therefore needs to be determined by the user with the additional possibility that some signatures of neuronal activity may be confused with the PA template.

A comparison of a fully automatic implementation of ICA, OBS and OBS-ICA methods found that the latter two provided superior performance (Debener *et al.*, 2007). Possible explanations for the difference are as follows. First, the selection-by-correlation approach (Srivastava *et al.*, 2005) does not always identify the correct components (that is, those reflecting the PA) because the independent components identification and selection should not (solely) rely on the ECG correlation approach. This is because the ECG channel contains prominent features that are virtually absent in the EEG (QRS complex, T wave) and vice

versa (different morphology of the PA). Debener *et al.*, (2008) suggested an alternative approach for component identification where the components were identified by the amount of variance they contributed to the evoked PA, rather than based on the degree of correlation with the ECG. When compared to the identification-by-correlation criterion, they showed that this latter approach gives better results (Debener *et al.*, 2008). Second, it may be that ICA is not able to distinguish on-going and event related EEG neuronal activity from the PA due to the fact the PA violates the spatial stationarity assumption, which underlies temporal ICA.

Although several groups have reported success when using ICA for PA correction (Benar *et al.*, 2003; Briselli *et al.*, 2006; Nakamura *et al.*, 2006; Mantini *et al.*, 2007) other studies have shown less positive results using ICA (Debener *et al.*, 2007, 2008). A possible reason for this discrepancy is the different field strengths of the scanners used in these studies. Debener *et al.*, (2008) used the EEG data collected at different field strengths to investigate the efficacy of ICA for PA correction. They showed that at 1.5 T, the ICA decomposition was found to be comparable to that obtained from data recorded outside the MRI, while the decompositions for data recorded at 3 and 7 T were markedly different. This may result from the need for more components in ICA to model the PA at higher field strengths, and may be incompatible with the assumption of one (or a few) fixed sources (Nakamura *et al.*, 2006).

In summary, the spatial filtering approaches for PA correction developed till to-date such as ICA and PCA may not be as efficient as template methods (described in Section 3.3.2.1), particularly at fields of 3 T and higher. The application of ICA in combination with ECG triggered template subtraction methods such as AAS and OBS offers a possible way forward. Kim *et al.*, (2004) combined a wavelet-based denoising approach with recursive adaptive filtering as post processing, only in cases where AAS failed. Similarly, the use of adaptive noise cancellation following OBS is suggested by Niazy *et al.*, (2005) to increase performance. A comparison of ICA with the identification-by-correlation approach (Srivastava *et al.*, 2005), OBS (Niazy *et al.*, 2005), and a combination of both (Debener *et al.*, 2005) showed that ICA, when used on its own, while reducing the PA considerably, also reduced the signal-to-noise ratio (SNR) of event related potentials (ERPs). This suggests that artefact and signal could not be separated very well by ICA. However, when used after OBS, infomax ICA improved the ERP SNR and the ERP topography.

### **3.3.2.3 Motion sensor based PA correction**

Bonmassar *et al.*, (2002) utilized an adaptive Kalman filter approach for PA correction, which requires an extra motion sensor signal to be recorded as a reference signal. However, it might also be possible to use electrooculogram (EOG) signals instead (In *et al.*, 2006). While apparently producing good corrections, the Kalman filter approach appears to be computationally demanding, and is based on the questionable assumption that the EEG signal has a white noise characteristic (In *et al.*, 2006). A second novel method for recording motion has been proposed by Masterton *et al.*, (2007), who attached three loops as motion sensors on an electrode cap. This group reported a more complete model of head movements and, when employing a linear adaptive filter technique, good correction of the pulse-related artefact and other non-voluntary head movement artefacts.

LeVan *et al.*, (2013) investigated the possibility of directly recording the motion component of the PA using an optical motion-tracking system. Regressing out linear and quadratic functions of the measured motion parameters, they have shown a substantial reduction in RMS amplitudes of EEG data across cardiac cycles compared to AAS. A further major RMS reduction was shown to be obtained when applying the regression and AAS methods sequentially, resulting in RMS amplitudes that were not considerably different from those of EEG recorded outside the scanner, although with higher residual variability. In rigid-body motion (i.e., pure translations as well as rotations about the direction of the magnetic field) do not induce any current in the EEG wires (Yan *et al.*, 2009), leaving the rotations about the other axes as the main sources of the BCG artefact. LeVan *et al.*, (2013) also suggested that the large contributions of pure translational parameters and of non-linear terms to the PA waveforms may indicate that non-rigid motion of the EEG wires (originating from rigid head motion) is an important cause of the PA.

### **3.3.2.4 Additional possible measures for PA correction**

As wavelet-based nonlinear reduction of the PA (Wan *et al.*, 2006) is computationally demanding it is therefore unlikely to replace AAS in the near future. Vincent *et al.*, (2007) proposed a moving general linear model approach (mGLM), and showed evidence that this approach yielded improved performance compared to AAS. In particular, these authors address the issue of a PA that lasts longer than a cardiac cycle leading to overlap of consecutive PA. Although its significance remains to be fully determined, a recent study

showed that in 22% (1.5 T data) to 30% (3 T data) of the cases, the PA showed an overlap between successive cardiac cycles (de Munck *et al.*, 2013) when considering data from 29 healthy subjects and 15 patients with epilepsy. de Munck *et al.*, (2013) eliminated the constraints placed on PA correction using template methods by modelling the precise timings of artefact overlaps and represented those in a sparse matrix. Subsequently, the artefacts were disentangled with a least squares procedure. These authors also showed that ignoring the overlap of PAs leaves small residual artefacts that are indicative of epileptic spikes whereas this is not the case when the overlapping is accounted for, which would be advantageous in particular for EEG-fMRI applications in epilepsy.

In summary, the PA represents a rather complicated, dynamic contribution to the EEG signal. Thus, the development, application and comparison of PA removal procedures represent a real challenge which demands the attention of the EEG-fMRI research community.

### **3.3.3 Motion Artefact (MA)**

Motion artefact is primarily produced by any head rotation inside an MR scanner and is highly variable in both temporal and spatial pattern, as it is dependent upon both the type and speed of the movements. The MA can be as large as 10 mV in magnitude, and unfortunately can often be temporally correlated with task responses in fMRI experiments (Jansen *et al.*, 2012), leading to confounding effects in EEG-fMRI data analysis.

Jansen *et al.*, (2012) have shown that the artefacts induced by head movements can severely affect the inferences which can be drawn from the integration of simultaneously acquired EEG and fMRI data. This is because the EEG artefacts induced by head movements can dominate the neuronal signals even after the EEG data have been ‘cleaned up’ using stringent post-processing methods. The effect of such artefacts is potentially magnified in analyses using continuous EEG predictors of the fMRI signal. In studies where the analysis does not depend on the full time-span of recorded EEG data, it is possible to select only data segments that are unaffected by artefacts. However it is common to find movements around the times of greatest interest, such as when responses to stimuli occur, thus making it undesirable to discard such data segments. Finding methods by which to correct or reduce these artefacts is therefore imperative.

### 3.3.3.1 MA Reduction

Head motion alters the geometry of electrode and lead arrangements in the magnetic field and consequently the induced artefact properties change. The current methods available to facilitate the correction of the GA when there are head movements during data acquisition were explored in Section 3.3.1.5. Here the focus is how the MA itself can be reduced.

As already discussed, head motion can lead to severe image degradation and result in false-positive activation and is usually worse in patients than in healthy subjects. Lemieux *et al.*, (2007) performed general linear model fMRI data analysis on simultaneous EEG-fMRI data acquired in 34 cases with focal epilepsy. Signal changes associated with large inter-scan motion events (head jerks) were modelled using modified design matrices that include 'scan nulling' regressors. This group studied the data acquired with a simple head restraint method (soft cushions and straps supplied as standard by the scanner manufacturer) and also with more sophisticated head restraint methods (vacuum cushions (Benar *et al.*, 2003)). The vacuum cushion system appears effective in eliminating large head jerks (say, >1 mm), but less effective at reducing the smaller motion events. Consequently, it has been suggested that the motion modelling approach is useful even with the use of a vacuum cushion. However, the scan nulling approach is affected by the number of regressors it adds the model as a function of the amount of motion. This can be statistically inefficient, particularly if the scan nulling effect is small. Moreover, this technique can only be used to correct the effects of motion that is detected from the MRI data and it therefore has poor time resolution and can miss some of the MAs in the EEG data.

An alternative approach to attenuating the MAs in EEG data recorded during concurrent fMRI involves making use of reference signals. For example, Bonmassar *et al.*, (2002) used a piezoelectric movement sensor attached to the subject's head to monitor head motion during combined EEG/fMRI experiments. They then applied a linear adaptive filter so as to remove any signal from the EEG recordings that was linearly related to the reference signal from the movement sensor. This had the effect of attenuating both pulse (Section 3.3.2.3) and movement artefacts. Subsequently, Masterton *et al.*, (2007) showed that reference signals recorded from loops of carbon-fibre wire that were physically attached to, but electrically isolated from, the subject's head could similarly be used to ameliorate the MA. This approach relies on the reference signals being similar in form to the artefacts induced in the EEG

recordings. Therefore, the above methods are limited in efficacy by the differences between the artefact voltages induced by complex head movement in the combination of the EEG leads and the volume conductor formed by the human head, and the signal from a single motion sensor or the voltages induced in wire loops attached to the head. These implementations did not address the changes in the GA due to head movement.

The correction of the MA using post-processing methods is extremely difficult due to the inherent variability and unpredictable nature of head movements, which means that methods such as AAS or ICA are not really suited to MA removal (Allen *et al.*, 2000; Jansen *et al.*, 2012). The development of improved, easy to use, methods for removing the MA at source is therefore highly desirable for the advancement of EEG-fMRI.

### 3.3.4 Vibration Artefact

This artefact is caused by vibration of the MR scanner bed (Laufs *et al.*, 2008) in simultaneous EEG-fMRI recording due to the gradient switching or by the continuous running of the cryostat pump in some MR scanners. Post-hoc data correction for vibration related artefacts is still an unsolved problem. Template subtraction is often not applicable because, unlike the gradient and pulse artefact, the vibration-related artefacts do not have a characteristic, repetitive, temporal shape. In addition since all electrodes are similarly affected, correction algorithms using spatial filters (e.g. ICA) are not feasible. Therefore to minimise the vibration, the cryostat pump is often switched off during simultaneous fMRI/EEG measurements (Bonmassar *et al.*, 2002; Wan *et al.*, 2006; Assecondi *et al.*, 2010; Bagshaw *et al.*, 2010; Ritter *et al.*, 2010).

Mullinger *et al.*, (2008d) reported a study involving a series of EEG recordings made at 7T while various elements of the scanner hardware were sequentially turned off. These elements included the magnet's cryostat pumps, the cooling air-flow to the magnet bore, the gradient amplifiers and the screened room lighting. In addition, a variety of measures for limiting vibration of the EEG amplifier and leads were assessed. Initially, the amplifier was mounted on the beam that runs through the scanner bore and which is suspended from the ends of the magnet, on which the patient bed moves. Padding was placed between the amplifier and the beam, and the amplifier was weighted down in an attempt to limit vibration. Subsequently, the amplifier was mounted on a cantilever arrangement projecting into the rear of the magnet.

This was supported from the floor of the screened room and so was mechanically isolated from scanner vibrations as much as possible. The optimal set-up for limiting scanner-induced noise was found to involve switching off the magnet's cryostat pumps and mounting the EEG amplifier on a cantilever.

Nierhaus *et al.*, (2013) described another scanner-induced artefact in the EEG recorded concurrent with fMRI. They have reported that Siemens Magnetom (Tim Trio and Verio) scanners' internal ventilation system for fresh air supply induces a frequency peak in the power spectrum of the EEG. The exact frequency of the peak is dependent on the ventilation level, but overall appears to be in the gamma frequency range of the EEG. The ventilation-induced artefact could be eliminated most easily by switching off the ventilation during simultaneous EEG recordings. This, however, causes a temperature rise within the scanner bore. Nierhaus *et al.*,(2013) reported that short measurement blocks of ~10 min with short breaks for fresh air supply were still comfortable for the subjects they have scanned. In cases of longer acquisition periods, an external ventilation system placed before or behind the scanner bore can replace the built-in ventilation of the scanner.

### 3.4 Conclusion

This chapter has described the different types of artefacts caused by the static and changing magnetic fields of the MR scanner and the possibilities for their removal. The GA, due to its large amplitude, is initially dominant in the raw EEG data, but it has been shown to be more easily removed than the cardiac and motion related artefacts. This is mainly due to the fact that the GA is caused by an external source that is predictable in its temporal properties.

Template-based correction methods have been shown to be most successful and convenient as a first step of GA removal. Modifications for dealing with motion-induced alteration of the positions of the electrodes and cables were discussed. Future work should focus on how to avoid or attenuate MR-related imaging artefacts altogether or at least reduce the heterogeneity of the GA across a scan period in order to further increase signal quality. Dedicated fMRI sequences should be designed that are tuned for EEG-fMRI recordings, as pioneered by Anami and colleagues (Anami *et al.*, 2003). Silent fMRI sequences developed by Schmitter *et al.*, (2008) could be advantageous because acoustic resonance peaks of the



MR system during the gradient switching process are avoided. Consequently this would result in less vibration induced motion of the EEG electrodes and cables.

Removal of cardiac-related artefacts remains challenging since their origins are physiological. As the fMRI community moves on to higher field strengths to increase BOLD sensitivity, the problems of the residual PA and MA increase as these artefacts scale with MR field strength. Therefore the issues of removing these artefacts become even more challenging and important. This chapter showed the importance of adapting the methods and especially the combination of methods for artefact correction to the given situation. Improved artefact correction techniques may result from a better understanding of the mechanisms that give rise to the GA (Yan *et al.*, 2009), the PA (Yan *et al.*, 2010; Mullinger *et al.*, 2013) and MA (Goldman *et al.*, 2000; Masterton *et al.*, 2007; LeVan *et al.*, 2013). In other words, a better knowledge about the different mechanisms causing each of the artefacts should help to optimize recording conditions as well as offline data correction approaches, and thus contribute to a better EEG signal quality during simultaneous fMRI.

### 3.5 References

- Allen, P. J., Josephs, O. and Turner, R. (2000). "A Method for removing Imaging Artifact from Continuous EEG Recorded during Functional MRI." *Neuroimage* **12**(2): 230-239.
- Allen, P. J., Poizzi, G., Krakow, K., Fish, D. R. and Lemieux, L. (1998). "Identification of EEG Events in the MR Scanner: The Problem of Pulse Artifact and a Method for Its Subtraction." *Neuroimage* **8**(3): 229-239.
- Anami, K., Mori, T., Tanaka, F., Kawagoe, Y., Okamoto, J., Yarita, M., Ohnishi, T., Yumoto, M., Matsuda, H. and Saitoh, O. (2003). "Stepping stone sampling for retrieving artifact-free electroencephalogram during functional magnetic resonance imaging." *Neuroimage* **19**(2): 281-295.
- Anami, K., Saitoh, O. and Yumoto, M. (2002). "Reduction of ballistocardiogram with a vacuum head-fixating system during simultaneous fMRI and multi-channel monopolar EEG recording." *Recent Adv Hum Brain Mapp* **1232**: 427-431.
- Assecondi, S., Vanderperren, K., Novitskiy, N., Ramautar, J. R., Fias, W., Staelens, S., Stiers, P., Sunaert, S., Van Huffel, S. and Lemahieu, I. (2010). "Effect of the static magnetic

- field of the MR-scanner on ERPs: evaluation of visual, cognitive and motor potentials." Clin. Neurophysiol. **121**: 672–685.
- Bagshaw, A. P. and Bénar, C. G. (2010). Scanning strategies for simultaneous EEG-fMRI recordings. In: In: Simultaneous EEG and fMRI: Recording, Analysis and Application. M. Ullsperger and S. Debener. USA Oxford University Press.
- Baudewig, J., Bittermann, H. J., Paulus, W. and Frahm, J. (2001). "Simultaneous EEG and functional MRI of epileptic activity: a case report." Clin. Neurophysiology **112**: 1196-1200.
- Becker, R., Ritter, P., Moosmann, M. and Villringer, A. (2005). "Visual Evoked Potentials Recovered From fMRI Scan Period." Human Brain Mapping **26**: 221-230.
- Benar, C., Aghakhani, Y., Wang, Y., Izenberg, A., Al-Asmi, A., Dubeau, F. and Gotman, J. (2003). "Quality of EEG in simultaneous EEG–fMRI for epilepsy." Clin. Neurophysiol **114**(3): 569-580.
- Bledowski, C., Linden, D. E. and Wibral, M. (2007). "Combining electrophysiology and functional imaging: different methods for different questions." Trends Cogn Sci **11**: 500-502.
- Bonmassar, G., Purdon, P. L., Jaaskelainen, I. P., Chiappa, K., Solo, V., Brown, E. N. and Belliveau, J. W. (2002). "Motion and ballistocardiogram artifact removal for interleaved recording of EEG and EPs during MRI." NeuroImage **16**(4): 1127–1141.
- Briselli, E., Garreffa, G., Bianchi, L., Bianciardi, M., Macaluso, E., Abbafati, M., Marciani, M. and Maraviglia, B. (2006). "An independent component ballistocardiogram analysis-based approach on artifact removing." Magn Reson Imaging **24**: 393-400.
- Brookes, M. J., Mullinger, K. J., Stevenson, C. M., Morris, P. G. and Bowtell, R. W. (2008). "Simultaneous EEG source localisation and artifact rejection during concurrent fMRI by means of spatial filtering " NeuroImage **40**(3): 1090-1104.
- Cohen, M. S., Goldman, R. and Jerome, J. E. (2001). Simultaneous EEG and fMRI made easy. Proc Org Hum Brain Mapping, Brighton, UK.
- Comi, E., Annovazzi, P., Silva, A. M., Cursi, M., Blasi, V., Cadioli, M., Inuggi, A., Falini, A., Comi, G. and Leocani, L. (2005). "Visual evoked potentials may be recorded simultaneously with fMRI scanning: a validation Study." Hum. Brain Mapp **24**: 291–298.
- de Munck, J. C., van Houdt, P. J., Gonçalves, S. I., van Wegen, E. and Ossenblok, P. P. W. (2013). "Novel artefact removal algorithms for co-registered EEG/fMRI based on selective averaging and subtraction." NeuroImage **64**(407-415).

- Debener, S., Kranczioch, C. and Gutberlet, I. (2010). EEG Quality: Origin and Reduction of the EEG Cardiac-Related Artefact. In: EEG-fMRI Physiological Basis, Technology, and Applications. C. Mulert and L. Lemieux. Verlag Berlin Heidelberg Springer.
- Debener, S., Mullinger, K. J., Niazy, R. K. and Bowtell, R. W. (2008). "Properties of the ballistocardiogram artefact as revealed by EEG recordings at 1.5, 3 and 7 Tesla static magnetic field strength." International Journal of Psychophysiology **67**(3): 189-199.
- Debener, S., Strobel, A., Sorger, B., Peters, J., Kranczioch, C., Engel, A. K. and Goebel, R. (2007). "Improved quality of auditory event-related potentials recorded simultaneously with 3-T fMRI: removal of the ballistocardiogram artefact." Neuroimage **34**: 587-597.
- Debener, S., Ullsperger, M., Siegel, M., Fiehler, K., Yves von Cramon, D. and Engel, A. K. (2005). "Trial-by-Trial Coupling of Concurrent Electroencephalogram and Functional Magnetic Resonance Imaging Identifies the Dynamics of Performance Monitoring." Journal of Neuroscience **25**(50): 11730-11737.
- Delorme, A. and Makeig, S. (2004). "EEGLAB: an open source toolbox for analysis of single-trial EEG dynamics including independent component analysis." Journal of Neuroscience Methods **134**: 9-21.
- Eichele, T., Moosmann, M., Wu, L., Gutberlet, I. and Debener, S. (2010). Removal of MRI Artifacts from EEG Recordings. In: Simultaneous EEG and fMRI: Recording, Analysis and Application. M. Ullsperger and S. Debener. USA Oxford University Press.
- Ellingson, M. L., Liebenthal, E., Spanaki, M. V., Prieto, T. E., Binder, J. R. and Ropella, K. M. (2004). "Ballistocardiogram artefact reduction in the simultaneous acquisition of auditory ERPS and fMRI." NeuroImage **22**(4): 1534-1542.
- Ertl, M., Kirsch, V., Leicht, G., Karch, S., Olbrich, S., Reiser, M., Hegerl, U., Pogarell, O. and Mulert, C. (2010). "Avoiding the ballistocardiogram (BCG) artifact of EEG data acquired simultaneously with fMRI by pulse-triggered presentation of stimuli." J. Neurosci. Meth. **186**: 231-241.
- Felblinger, J., Slotboom, J., Kreis, R., Jung, B. and Boesch, C. (1999). "Restoration of electrophysiological signals distorted by inductive effects of magnetic field gradients during MR sequences." Magn Reson Med **41**(4): 715-721.

- Freyer, F., Becker, R., Anami, K., Curio, G., Villringer, A. and Ritter, P. (2009). "Ultrahigh-frequency EEG during fMRI: Pushing the limits of imaging-artifact correction." Neuroimage **48**(1): 94-108.
- Garreffa, G., Carni, M., Gualniera, G., Ricci, G. B., Bozzao, L., De Carli, D., Morasso, P., Pantano, P., Colonnese, C. and Roma, V. (2003). "Real-time MR artifacts filtering during continuous EEG/fMRI acquisition." Magn Reson Imaging **21**(10): 1175-1189.
- Gebhardt, H., Blecker, C. R., Bischoff, M., Morgen, K., Oschmann, P., Vaiti, D. and Sammer, G. (2008). "Synchronized measurement of simultaneous EEG-fMRI: a simulation study." Clin. Neurophysiology **119**(12): 2703–2711.
- Giraud, A. L., Kleinschmidt, A., Poeppel, D., Lund, T. E., Frackowiak, R. S. and Laufs, H. (2007). "Endogenous cortical rhythms determine cerebral specialization for speech perception and production." Neuron **56**(6): 1127-1134.
- Goldman, R. I., Stern, J. M., Engel, J. J. and Cohen, M. S. (2000). "Acquiring simultaneous EEG and functional MRI." Clin. Neurophysiology **11**: 1974-1980.
- Goncalves, S. I., Pouwels, P. J., Kuijter, J. P., Heethaar, R. M. and de Munck, J. C. (2007). "Artifact removal in co-registered EEG/fMRI by selective average subtraction." Clin. Neurophysiology **118**: 2437-2450.
- Grouiller, F., Vercueil, L., Krainik, A., Segebarth, C., Kahane, P. and David, O. (2007). "A comparative study of different artefact removal algorithms for EEG signals acquired during functional MRI." NeuroImage **38**: 124-137.
- Hamandi, K., Laufs, H., Nöth, U., Carmichael, D. W., Duncan, J. S. and Lemieux, L. (2008). "BOLD and perfusion changes during epileptic generalised spike wave activity." NeuroImage **39**(2): 608-618.
- Hanson, L. G., Lund, T. E. and Hanson, C. G. (2007). "Encoding of electrophysiology and other signals in MR images." Magn Reson Imaging **25**(5): 1059-1066.
- Hill, R. A., Chiappa, K. H., Huang-Hellinger, F. and Jenkins, B. G. (1995). "EEG during MR imaging: Differentiation of movement artifact from paroxysmal cortical activity." American Academy of Neurology **45**: 1942-1943.
- Hoffmann, A., Jaeger, L., Werhahn, K. J., Jaschke, M., Noachtar, S. and Reiser, M. (2000). "Electroencephalography During Functional Echo-Planar Imaging: Detection of Epileptic Spikes Using Post-processing Methods." Magn Reson in Medicine **44**: 791-798.

- Hoffmann, A., Jager, L., Werhahn, K. J., Jaschke, M., Noachtar, S. and Reiser, M. (2000). "Electroencephalography during functional echo-planar imaging: detection of epileptic spikes using post-processing methods." Magn. Res. Med. **44**: 791-798.
- Iannetti, G. D., Niazy, R. K., Wise, R. G., Jezzard, P., Brooks, J. C., Zambreanu, L., Vennart, W., Matthews, P. M. and Tracey, I. (2005). "Simultaneous recording of laser-evoked brain potentials and continuous, highfield functional magnetic resonance imaging in humans." NeuroImage **28**(3): 708-719.
- In, M. H., Lee, S. Y., Park, T. S., Kim, T. S., Cho, M. H. and Ahn, Y. B. (2006). "Ballistocardiogram artifact removal from EEG signals using adaptive filtering of EOG signals." Physiological Measurement **27**: 1227-1240.
- Ives, J. R., Warach, S., Schmitt, F., Edelman, R. R. and Schomer, D. L. (1993). "Monitoring a patient's EEG during echo planar MRI." Electroencephalography and Clinical Neurophysiology **87**(6): 417-420.
- Jansen, M., White, T. P., Mullinger, K. J., Liddle, E. B., Gowland, P. A., Francis, S. T., Bowtell, R. and Liddle, P. F. (2012). "Motion-related artefacts in EEG predict neuronally plausible patterns of activation in fMRI data." Neuroimage **59**(1-3): 261-270.
- Kim, K. H., Yoon, H. W. and Park, H. W. (2004). "Improved ballistocardiac artifact removal from the electroencephalogram recorded in fMRI. ." J. Neurosci. Methods **135**: 193-203.
- Krakow, K., Woermann, F. G., Symms, M. R., Allen, P. J., Lemieux, L., Barker, G. J., Duncan, J. and S., F., D.R., (1999). "EEG-triggered functional MRI of interictal epileptiform activity in patients with partial seizures." Brain **122**: 1679-1688.
- Kruggel, F., Wiggins, C. J., Herrmann, C. S. and von Cramon, D. Y. (2000). "Recording of the event-related potentials during functional MRI at 3.0 Tesla field strength." Magn. Res. Med. **44**: 277-282.
- Laufs, H., Daunizeau, J., Carmichael, D. W. and Kleinschmidt, A. (2008). "Recent advances in recording electrophysiological data simultaneously with magnetic resonance imaging." NeuroImage **40**(2): 515-528.
- Lemieux, L., Allen, P. J., Franconi, F., Symms, M. R. and Fish, D. R. (1997). "Recording of EEG during fMRI experiments : Patient safety." Magn. Res. Med. **38**(6): 943-952.
- Lemieux, L., Salek-Haddadi, A., Josephs, O., Allen, P., Toms, N., Scott, C., Krakow, K., Turner, R. and Fish, D. R. (2001). "Event-related fMRI with simultaneous and

- continuous EEG: description of the method and initial case report." Neuroimage **14**: 780-787.
- Lemieux, L., Salek-Haddadi, A., Lund, T. E., Laufs, H. and Carmichael, D. W. (2007). "Modelling large motion events in fMRI studies of patients with epilepsy." Magn Reson Imaging **25**(6): 894-901.
- LeVan, P., Maclaren, J., Herbst, M., Sostheim, R., Zaitsev, M. and Hennig, J. (2013). "Ballistocardiographic artifact removal from simultaneous EEG-fMRI using an optical motion-tracking system." NeuroImage **75**: 1-11.
- Liu, Z., de Zwart, J. A., van Gelderen, P., Kuo, L. and Duyn, J. H. (2012). "Statistical feature extraction for artifact removal from concurrent fMRI-EEG recordings." NeuroImage **59**: 2073-2087.
- Mandelkow, H., Brandeis, D. and Boesiger, P. (2010). "Good practices in EEG-MRI: The utility of retrospective synchronization and PCA for the removal of MRI gradient artefacts." NeuroImage **49**: 2287-2303.
- Mandelkow, H., Halder, P., Boesiger, P. and Brandeis, D. (2006). "Synchronisation facilitates removal of MRI artefacts from concurrent EEG recordings and increases usable bandwidth." Neuroimage **32**(3): 1120-1126.
- Mantini, D., Perrucci, M. G., Cugini, S., Ferretti, A., Romani, G. L. and Del Gratta, C. (2007). "Complete artifact removal for EEG recorded during continuous fMRI using independent component analysis." Neuroimage **34**(2): 598-607.
- Masterton, J., Abbott, D. F., Fleming, S. and Jackson, G. D. (2007). "Measurement and reduction of motion and ballistocardiogram artefacts from simultaneous EEG and fMRI recordings." NeuroImage **37**: 202-211.
- Mayhew, S., Dirckx, S. G., Naizy, R. K., Iannetti, G. D. and Wise, R. G. (2010). "EEG signatures of auditory activity correlate with simultaneously recorded fMRI responses in humans." Neuroimage **49**(1): 849-864.
- Moosmann, M., Schonfelder, V. H., Specht, K., Scheeringa, R., Nordby, H. and Hugdahl, K. (2009). "Realignment parameter-informed artefact correction for simultaneous EEG-fMRI recordings." Neuroimage **45**(4): 1144-1150.
- Mullinger, K. J., Brookes, M. J., Geirsdottir, G. B. and Bowtell, R. (2008b). Average gradient artefact subtraction: the effect on neuronal signals. Human Brain Mapping, Melbourne, Elsevier.

- Mullinger, K. J., Brookes, M. J., Stevenson, C. M., Morgan, P. S. and Bowtell, R. W. (2008a). "Exploring the feasibility of simultaneous EEG/fMRI at 7 T." Magnetic Resonance Imaging **26**(7): 607-616.
- Mullinger, K. J., Debener, S., Coxon, R. and Bowtell, R. W. (2008d). "Effects of simultaneous EEG recording on MRI data quality at 1.5, 3 and 7 tesla." International Journal of Psychophysiology **67**: 178-188.
- Mullinger, K. J., Havenhand, J. and Bowtell, R. (2013). "Identifying the sources of the pulse artefact in EEG recordings made inside an MR scanner." NeuroImage **71**: 75-83.
- Mullinger, K. J., Morgan, P. S. and Bowtell, R. W. (2008c). "Improved Artefact Correction for Combined Electroencephalography/Functional MRI by means of Synchronization and use of VCG Recordings." Journal of Magnetic Resonance Imaging **27**(3): 607-616.
- Mullinger, K. J., Yan, W. X. and Bowtell, R. W. (2011). "Reducing the Gradient Artefact in Simultaneous EEG-fMRI by Adjusting the Subject's Axial Position." NeuroImage **54**(3): 1942-1950.
- Nakamura, W., Anami, K., Mori, T., Saitoh, O., Cichocki, A. and Amari, S. (2006). "Removal of ballistocardiogram artifacts from simultaneously recorded EEG and fMRI data using independent component analysis." IEEE Trans Biomed Eng **53**: 1294–1308.
- Negishi, M., Abildgaard, M., Nixon, T., Constable, R. T. and (2004). "Removal of time-varying gradient artifacts from EEG data acquired during continuous fMRI." Clin. Neurophysiol. **115**: 2181-2192.
- Niazy, R. K., Bechmann, C. F., Iannetti, G. D., Brady, J. M. and Smith, S. M. (2005). "Removal of fMRI environment artifacts from EEG data using optimal basis sets." Neuroimage **28**(3): 720-737.
- Nierhaus, T., Gundlach, C., Goltz, D., Thiel, S. D., Pleger, B. and Villringer, A. (2013). "Internal ventilation system of MR scanners induces specific EEG artifact during simultaneous EEG-fMRI." NeuroImage **74**: 70-76.
- Ritter, P., Becker, R., Freyer, F. and Villringer, A. (2010). EEG quality: the image acquisition artefact. In: In: EEG-fMRI. C. Mulert and L. Lemieux. Berlin Heidelberg Springer: 153-171.
- Ritter, P., Freyer, F., Curio, G. and Villringer, A. (2008a). "High frequency (600 Hz) population spikes in human EEG delineate thalamic and cortical fMRI activation sites. ." NeuroImage **42**(2): 483-490.

- Ritter, P., Moosmann, M. and Villringer, A. (2008b). "Rolandic alpha and beta EEG rhythms' strengths are inversely related to fMRI-BOLD signal in primary somatosensory and motor cortex." Hum Brain Map **30**(4): 1168-1187.
- Ryali, S., Glover, G. H., Chang, C. and Menon, V. (2009). "Development, validation, and comparison of ICA-based gradient artifact reduction algorithms for simultaneous EEG-spiral in/out and echo-planar fMRI recordings." Neuroimage **48**(2): 348–361.
- Salek-Haddadi, A., Friston, K. J., Lemieux, L. and Fish, D. R. (2002). "Simultaneous EEGcorrelated ictal fMRI." Neuroimage **16**: 32-40.
- Sammer, G., Blecker, C. R., Gebhardt, H., Kirsch, P., Stark, R. and Vaitl, D. (2005). "Acquisition of typical EEG waveforms during fMRI: SSVEP, LRP, and frontal theta." NeuroImage **24**(4): 1012-1024.
- Schmitter, S., Diesch, E., Amann, M., Kroll, A., Moayer, M. and Schad, L. R. (2008). "Silent echo-planar imaging for auditory FMRI." Magma **21**: 317-325.
- Seeck, M., Lazeyras, F., Michel, C. M., Blanke, O., Gericke, C. A., Ives, J. R., Delavelle, J., Golay, X., Haenggeli, C. A., de Tribolet, N. and Landis, T. (1998). "Non-invasive epileptic focus localization using EEGtriggered functional MRI and electromagnetic tomography." Electroencephalogr.Clin.Neurophysiol **106**: 508-512.
- Sijbers, J., Michiels, I., Verhoye, M., Van Audekerke, J., Van der, L. A. and Van Dyck, D. (1999). "Restoration of MR-induced artifacts in simultaneously recorded MR/EEG data." Magn Reson Imaging **17**(9): 1383-1391.
- Sijbers, J., Van Audekerke, J., Verhoye, M., Van der Linden, A. and Van Dyck, D. (2000). "Reduction of ECG and gradient related artefacts in simultaneously recorded human EEG/MRI data." Magn Reson Imaging **18**(7): 881-886.
- Sommer, M., Meinhardt, J. and Volz, H. P. (2003). "Combined measurement of event-related potentials (ERPs) and fMRI." Acta Neurobiol.Exp.(Wars.) **63**: 49-53.
- Spencer, S. G., Mullinger, K. J., Peters, A. and Bowtell, R. W. (2012). Modelling and Removing the Gradient Artefact using a Gradient Model Fit (GMF). Proc. Intl. Soc. Mag. Reson. Med. 20, Abstract#2083, Melbourne.
- Srivastava, G., Crottaz-Herbette, S., Lau, K. M., Glover, G. H. and Menon, V. (2005). "ICA-based procedures for removing ballistocariogram artifacts from EEG data acquired in MRI scanner." Neuroimage **24**(1): 50-60.
- Symms, M. R., Allen, P. J., Woermann, F. G., Polizzi, G., Krakow, K., Barker, G. J., Fish, D. R. and Duncan, J. S. (1999). "Reproducible localization of interictal epileptiform discharges using EEG-triggered fMRI." Phys. Med. Biol. **44**: N161-N168.



- Vincent, J. L., Larson-Prior, L. J., Zempel, J. M. and Snyder, A. Z. (2007). "Moving GLM ballistocardiogram artefact reduction for EEG acquired simultaneously with fMRI." Clin. Neurophysiology **118**(5): 981-998.
- Wan, X., Iwata, K., Riera, J., Kitamura, M. and Kawashima, R. (2006). "Artifact reduction for simultaneous EEG/fMRI recording: adaptive FIR reduction of imaging artifacts." Clin. Neurophysiology **117**(3): 681-692.
- Warach, S., Ives, J. R., Schlaug, G., Patel, M. R., Darby, D. G., Thangaraj, V., Edelman, R. R. and Schomer, D. L. (1996). "EEG-triggered echo-planar functional MRI in epilepsy." Neurology **47**: 89-93.
- Yan, W. X., Mullinger, K. J., Brookes, M. J. and Bowtell, R. W. (2009). "Understanding Gradient Artefacts in Simultaneous EEG/fMRI." Neuroimage **46**(2): 459-471.
- Yan, W. X., Mullinger, K. J., Geirsdottir, G. B. and Bowtell, R. W. (2010). "Physical Modeling of Pulse Artefact Sources in Simultaneous EEG/fMRI." Human Brain Mapping **31**: 604-620.

# Chapter 4

---

*Simultaneous EEG/fMRI: Current practices for obtaining high quality EEG data*

## 4.1 Introduction

The post-processing methods currently available for correcting the EEG artefacts produced during concurrent fMRI require a number of criteria to be satisfied during data acquisition in order to produce high quality EEG data. Over the previous decade the optimal experimental set-up for recording high quality data has evolved as the understanding of the causes of the artefacts has improved. This has guided the modification of experimental methods so as to reduce the artefacts at source leading to improvement of the performance of post-processing correction algorithms. Technically, the MR scanner bore has to be seen as a “hostile” environment for the recording of EEG due to the artefacts that are induced in recordings, as described in Chapter 3. The cap, electrodes, and electrode leads are exposed to the strong homogeneous static magnetic field of the scanner and also to the rapidly time-varying magnetic fields generated by gradient switching (described in Chapter 2). The effects of these magnetic fields on the EEG data are discussed in detail in Chapter 3. Finally, the cap, electrodes, and electrode leads are also exposed to the radio frequency (RF) energy emitted during the scan sequence; see Chapter 2 and (Grandolfo *et al.*, 1992; Schenck 2000; DenBoer *et al.*, 2002; Nitz *et al.*, 2005). According to Faraday’s law, the RF field also induces currents in an electrically conductive object. Therefore the RF energy emitted during slice excitation can produce large electrical currents in the leads, particularly if they form loops, and the thermal energy dissipates at the points of highest thermal resistance, which (if no safety precautions are taken in the hardware design) typically occurs at the contact point between the electrode pin and the scalp across the conductive EEG gel. Therefore EEG during fMRI can be associated with the risk of heating and potentially also of burning of the subject (Angelone *et al.*, 2004; Angelone *et al.*, 2006; Laufs *et al.*, 2008).

This chapter therefore focuses on the EEG equipment used in simultaneous EEG-fMRI, as well as safety issues and data acquisition considerations, it also describes the current optimal approach for obtaining high quality EEG and fMRI data simultaneously using MR hardware and pulse sequences which are widely available, along with commercially supplied EEG equipment. Implementation of the suggested acquisition methods, in conjunction with the use of appropriate post-processing methods, yields EEG and fMRI data which are of good enough quality to allow a number of important neuroscience questions to be answered.

## 4.2 MR Compatible Equipment

The manufacturers of currently available EEG/MR equipment take different approaches both to the “hostility” of the MR recording environment and to the reduction of the imaging artefacts, mainly, the gradient artefacts. Currently available MR-compatible EEG systems fall into two categories (Gutberlet 2010): EEG systems that reside in the scanner control room during recording, and EEG systems that reside in the scanner enclosure (i.e. the RF shielded room) or even in the scanner bore during combined recordings.

### 4.2.1 EEG systems that reside in the scanner control room

Positioning the EEG system in the scanner control room used has both advantages and disadvantages for combined EEG/MR recordings. One major advantage is that the amplifier system is not exposed to the strong magnetic field of the MR system and therefore does not have to be designed specifically for MR compatibility and MR safety. In fact, such EEG systems can be technically equivalent to their non-MR-compatible counterparts, which means that there is almost none of the cost that would otherwise be incurred by the design, manufacturing, testing, and marketing of an amplifier specifically intended for use inside the scanner bore. Another potential advantage is that there can be no direct electromagnetic influence either on the amplification circuitry or on the electronics that control the amplifier itself. The operation of the amplifier is thus not compromised by the MR environment; this condition is otherwise quite challenging to achieve.

However, the most notable drawback of this set-up is that the distance between the amplifier and the electrodes on the subjects head is very long, typically on the order of 8-10 meters, since the orientation of most MR scanners is with the subject’s head pointing away from the scanner control room (Gutberlet 2010). This means that the electrode leads have to extend through the full length of the MR scanner enclosure and then through a wave-guide panel into the MR control room to connect to the amplifier. This is technically challenging as the induction of gradient artefacts in the electrode leads varies with the length of the cables used, and longer cables will also cause EEG signal decay and instability (Laufs *et al.*, 2008). However, the most critical aspect of this set-up is that the entire electrode lead matrix needs to be passed through the MR filter panel into the scanner control room, which requires a conduit with a diameter large enough to pass through the cable matrix including its multi-channel connector. Furthermore, this setup creates an electrical connection between the

scanner enclosure and the scanner control room, which can lead to severe leakage of RF energy into the screened MR scanner enclosure, affecting the MR image quality. RF leakage can only be counteracted with the help of special RF filter devices installed on the MR filter panel, which makes such EEG/MR setups rather bulky and a more or less a permanent installation (Gutberlet 2010).

#### 4.2.2 EEG systems that reside in the scanner enclosure

These setups could have the EEG amplifier located outside or inside the scanner bore. The major advantage with these setups is that the mass of cables coming from the electrode cap does not have to be routed over a long distance, thus reducing the chance for significant MR gradient and RF signal induction and cable movement artefacts. And finally and most importantly, the connection that forwards the signals from the amplifier to the recording computer, after analog/digital (AD) conversion, can be constructed with fibre-optic leads. These leads are immune to magnetic or RF coupling and consequently also do not hold the risk of creating an RF leak between the scanner control room and the shielded room in which the scanner is sited (Allen *et al.*, 2000; Gutberlet 2010).

- **EEG amplifier located outside the scanner bore:** An EEG system enclosed in a shielded box equipped with RF filters, fibre optical transmission links, and powered by a rechargeable battery case can then safely be placed inside the MR scanner chamber, although not inside the scanner bore. This solution has the advantage of lower development cost compared with systems that are placed in scanner bore. A commercially available EEG/MR system in this category is the Net Amps 300TM amplifier from Electrical Geodesics Inc. (EGI, Eugene, USA). This system uses a “Field Isolation Containment System” (FICS), essentially a magnetically shielded box, to achieve MR compatibility (Gutberlet 2010). This FICS box also contains the additionally required components mentioned above such as RF filters, optical-electrical converters for signal transmission, and a rechargeable battery. The amplifier itself is modified only slightly, compared to the standard amplifier version, to enhance its compatibility with the MR environment (personal communication, Phan Luu, EGI). The system uses an MR compatible version of EGI’s HydroCel Geodesic Sensor Net (HCGSN) 120 and is specified to work with up to 256 channels of EEG. Figure 4.1 shows the “Field Isolation Containment System” with the NetAmps 300TM amplifier positioned halfway between the MR console and scanner (Gutberlet

2010). The HCGSN MR Net is the only MR conditional device of the EGI system that has been tested for MR safety to enter the bore of a magnet.

**GES 300 MR Package within the MR Environment**

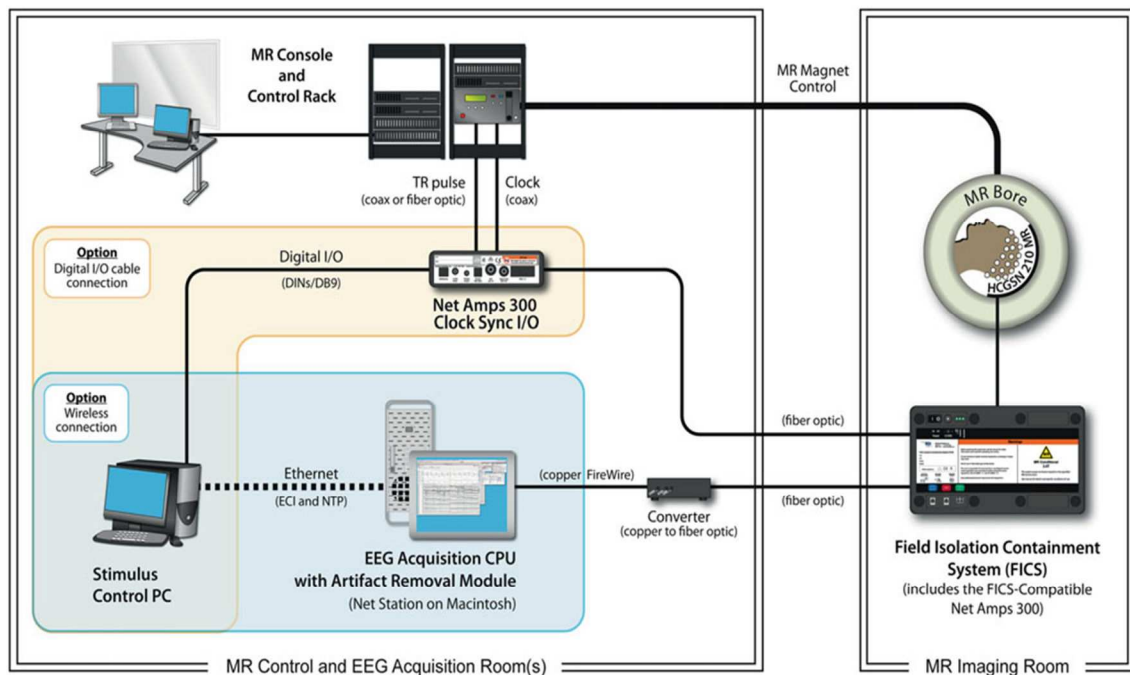


**Figure 4.1** A schematic diagram of the arrangement of a shielded amplifier used in the scanner environment. The amplifier resides in the MR chamber and communicates with the recording equipment in the MR control room via fibre optical connections. Volume onset pulses, clock signals, and some stimulus related events are received in the scanner control room, converted to optical pulses and forwarded to the amplifier in the MR chamber, where the event codes are reintegrated with the EEG/MR data acquired and are sent back to the scanner control room for storage (Adapted from (Gutberlet 2010)).

- **EEG amplifier located inside the scanner bore:** Currently, there is only one commercially available EEG/MR system explicitly designed to work directly inside the scanner bore. The advantage of this set-up is that the length of all electrical connections can be minimised, thereby minimising the influence of the gradient switching and motion of leads on the data acquired. The BrainAmp MR system by Brain Products (Brain Products GmbH, Gilching, Germany) is a modular amplifier consisting of units of 32 unipolar channels each. It is specified for up to 128 channels and for field strengths of up to 4T, but due to its design has been shown to work without fault in field strengths of up to 7T (Mullinger *et al.*, 2008c). A special bipolar amplifier is also available for the derivation of bipolar (e.g., EMG, EKG) or sensor-based signals (e.g. galvanic skin response, temperature, respiration) and can be combined with the EEG amplifiers. The BrainAmp MR amplifier system is battery

powered and communicates with the recording software via a two channel fibre-optic connection made through an intelligent USB interface located in the scanner

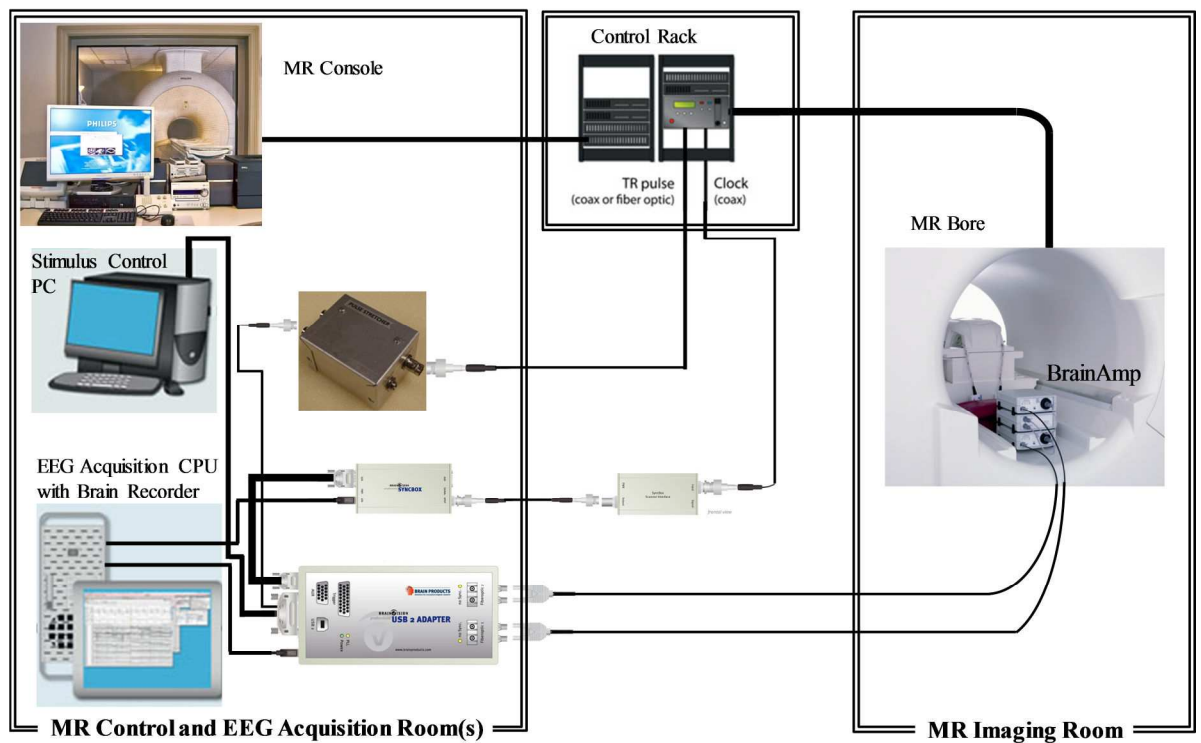


**Figure 4.2** A schematic diagram of the arrangement of a BrainAmp amplifier used in the scanner environment. The amplifier resides in the MR bore and communicates with the recording equipment in the MR control room via fibre optical connections. Volume onset pulses, clock signals, and some stimulus related events are received in the scanner control room.

control room (Mullinger *et al.*, 2013). This USB interface contains most of the more sensitive electronic circuitry needed to operate the amplifiers, such as the acquisition clock electronics and the circuit for the synchronization with an external clock signal, and also contains the logic for integrating external events. In this way, all electronically critical components of the EEG system can be kept in the scanner control room, while the amplifier itself can be made robust enough to reside in the scanner bore and directly behind the head coil for virtually any field strength. Also, having been designed explicitly for use inside the scanner, this EEG system does not require any shielding enclosure or external RF filters for its operation, thus giving it a small footprint compared with amplifiers which must reside outside of the bore. Furthermore, since the only connection between the amplifier and the scanner control room is through fibre-optic cables of approximately 4 mm diameter, this system not

only has a small footprint, but also is highly mobile and can be set up and removed in a few minutes. Figure 4.2 shows a schematic diagram of the arrangement of a BrainAmp amplifier system which can be used anywhere in the scanner environment.

### **4.3 Safety Concerns in Simultaneous EEG-fMRI**

As mentioned in the introduction to this chapter, recording EEG in the MR scanner raises important safety issues. First, there is the hazard associated with the introduction of ferromagnetic materials into the scanner. Secondly, currents induced in the electrodes and attached wires by the changing fields applied during imaging can present a hazard due to the following mechanisms: eddy current heating of the electrode heads; currents induced in loops formed between the electrode leads; and currents induced along electrode leads. There are several safety limits which must be adhered to when using these systems on humans:

- a. the maximum permissible cerebral temperature is 38°C, implying a maximum temperature increase due to scanner induced heating must be less than 1°C (Gutberlet 2010);
- b. the maximum permissible temperature of an applied part in skin contact (such as an electrode) is 43°C;
- c. the maximum permissible tissue contact currents ranges from 0.5 mA rms (>>1 kHz) to 10 mA rms (> 100 kHz) (Gutberlet 2010).

Again, the RF energy will dissipate on the input stages of the amplifier, and sophisticated engineering efforts are required to guard the input stages against this energy dissipation and at the same time retain the sensitivity and frequency response desired from the EEG amplifier. This is only a significant risk if safety guidelines are not satisfied. Hardware design and set-up, as well as careful selection of which MR sequences are run with the EEG hardware present must therefore be considered. This issue highlights the importance of the choice of the experimental protocol employed when performing a simultaneous EEG-fMRI experiment not only to achieve high data quality but also for subject safety.

#### **4.3.1 Subject Safety**

Patient safety during combined EEG/fMRI recordings is the highest concern. The MR scanner is an environment where physical forces are either present at all times, such as with the static magnetic field (Schenck 2000), or are induced during the MR acquisition with the



switched gradient magnetic fields (DenBoer *et al.*, 2002) and with the RF excitation of the tissue to be scanned (Grandolfo *et al.*, 1992; Nitz *et al.*, 2005), all of which pose particular dangers to the subject undergoing a combined EEG/fMRI experiment.

The most significant risk for the subject or patient is the heating of tissue due to the RF energy emitted during slice excitation. Placing EEG electrode caps with multiple electrodes on the scalp and establishing contact to the scalp with the help of a conductive gel creates surfaces of high electrical conductivity and with high thermal resistance. The RF energy causes large surface current densities in these materials, effectively shielding the inside of the skull from the RF energy emitted (Angelone *et al.*, 2004; Angelone *et al.*, 2006; Laufs *et al.*, 2008). This typically means that higher amount of RF power is transmitted to achieve the desired flip angle and to avoid image deterioration. At the same time, the RF induced current will be dissipated at the electrode terminal as warming or even heating at the scalp/gel border (Achenbach *et al.*, 1997; Nitz *et al.*, 2001). All scalp electrodes must have current limiting resistors conductively attached to the electrode surface which will effectively work as RF shielding resistors. The RF shielding resistors will reduce the current in the long leads and therefore suppressing the energy induced by MR gradients and RF pulses. The value of resistance typically varies in from 5 to 15 k $\Omega$  (electrodes from the EasyCap, which was used in this thesis work, are designed with 5 k $\Omega$  resistors), depending on the length of the cable assembly (Lemieux *et al.*, 1997). In order to avoid direct contact with the skin, a modern electrode's body is made of plastic. Moreover, heat resistant sheathing is used to avoid any potential heating of the lateral electrode lead causing heating/burns of the skin. When possible, it is best to use a head-sized transmit coil to minimize the risk of RF heating of the EEG cap and associated cables (Mullinger *et al.*, 2013).

Another safety relevant issue is RF energy coupling into cable loops, which would again dissipate the energy through heat emitted, e.g., to the body tissue or to the material of the loop itself (Lemieux *et al.*, 1997). If an electrode cable assembly is looped, the RF induction effect can be severe enough to cause the cable sheath to melt at the points where a cable crosses its own path to form a loop. It is therefore important that loops are always avoided (Dempsey *et al.*, 2001a; Dempsey *et al.*, 2001b). The scalp electrode leads should be routed as straight as possible toward a bundled exit from the cap and on to a common connector or common input and the leads must be routed on top of the textile cap fabric to avoid direct

lead contact with the skin (Gutberlet 2010). All electrode leads must be fixed to the textile fabric to avoid lead movement and inadvertent loop formation. Peripheral leads such as those for ECG acquisition, which have to be routed along the subject's back, must be sheathed in heat resistant tubing. With these precautions it is possible to minimize the safety risks to the subjects and to adhere to the regulations of the amount of heating allowed in tissue when conducting simultaneous EEG-fMRI experiments.

### 4.3.2 Equipment Safety

Possible dangers to the MR hardware and electronics are likely in cases where additional equipment is introduced into the scanner bore or is attached to the scanner electronics. In the case of additional equipment, this could mean stimulation devices as well as non-MR compatible bio-signal sensors or electrodes (Gutberlet 2010). The prime risk is that such equipment can contain ferromagnetic materials, which could cause attraction to and damage of the interior of the scanner bore (Schenck 2000), although in this case, patient safety would be much more at risk than scanner hardware. Only non-ferromagnetic leads and electrodes must be used in EEG caps. Leads are typically made from carbon fibres or stranded copper, and electrodes are most commonly made from high quality sintered Ag/AgCl materials or from gold (Goldman *et al.*, 2000).

Another possible danger to the scanner hardware is electrical connections made between the EEG system and the scanner electronics. Such connections would typically be needed to obtain a master clock signal from the MR device that can be used to drive the EEG amplifier clock and to achieve clock synchrony between the two devices (as described in Section 3.3.1.6). Attaching such devices can harm the scanner electronics, e.g., by drawing too much current from the clock output terminal or by detuning the MR system clock, due to influences of the synchronization hardware attached (Gutberlet 2010). It is therefore of the utmost importance that any devices attached to the MR scanner electronics are built to the highest technical standards. Optical decoupling of all connections between the scanner and the device should be employed (if possible), with all necessary power for operation being sourced from the synchronization device.

## 4.4 Data Acquisition Considerations

In simultaneous EEG-fMRI, there are several EEG data acquisition parameters, such as the bandwidth of the low pass filter (input stage of the amplifier), the sampling rate and the amplifier gain which are very important considerations. Synchronization of the EEG and MR system clock is also important for minimizing EEG artefact.

### 4.4.1 Band Limited Filter

As discussed in Chapter 3, the gradient artefact signal covers a broad spectrum extending from very low frequencies that are well within the typically used EEG spectrum, all the way to several kHz (Allen *et al.*, 2000). At the sample rate of 5000 Hz, often employed for EEG during fMRI, the highest frequency represented in the recorded data is of course 2500 Hz (Nyquist frequency), which would seem like a broad recording bandwidth. However, the bandwidth of the gradient artefact signal often extends well beyond 2500 Hz. In fact, for recordings done in most newer scanner models, with their strong and fast gradient systems, the analogue band limiter often times has to have its edge frequency set as low as 10% of the Nyquist frequency (e.g. 250 Hz @ 30 dB/Octave) in order to attenuate aliasing artefacts sufficiently (Gutberlet 2010). As a logical consequence, the effective bandwidth of the EEG amplifier would then also be limited to a value of 250 Hz. For the majority of studies AC-coupling with a filter of 0.016-250 Hz is optimal although DC-coupling or a higher (1 kHz) low-pass filter may be required if ultra-low or high frequency neuronal signals are of interest, respectively (Mullinger *et al.*, 2013).

### 4.4.2 Sampling Rate

Correction of the MR gradient-induced artefacts in the EEG requires that the true onset of each slice/volume's gradient activity can be detected and marked in the EEG data (discussed in detail in Chapter 3 Section 3.3.1.6). Almost all modern MR scanners have a configurable TTL or fibre optical output readily available at the scanner console, which gives a short signal pulse at the exact time point of every slice or volume acquisition onset that can be used to produce appropriate EEG markers.

It is also important to sample the EEG data with a high enough sampling rate, since the higher EEG data rates will sample the fast rising gradient signal at shorter time intervals and the resulting smaller amplitude steps between successive EEG sample points. This high

sampling will therefore help to reduce the uncertainty in correction of the gradient artefact using AAS. In theory this would mean that the EEG sampling rate should be at least twice as high as the true highest frequency in the gradient switching spectrum. However, it can be shown empirically that an EEG sample rate of 5000 Hz is perfectly adequate for EEG recordings. The reason for this is that the data would typically be down sampled (e.g. to 250 or 500 Hz) and subsequently low pass filtered during the artefact correction process or by the band limiter filter, the combination of which effectively eliminates all potentially existing (high frequency) gradient correction residuals. Using higher sample rates therefore typically does not improve the data quality, unless down sampling and low pass filtering are not used for whatever reason.

#### 4.4.3 EEG-MR clock synchronization

Hardware methods for EEG-MR clock synchronization require a physical (electrical) connection to the MR scanner electronics hardware providing access to a clock signal that is phase synchronous with the scanner's gradient system. This MR clock signal is then used to generate the new EEG acquisition clock signal which is synchronized to the MR clock (Mandelkow *et al.*, 2006).

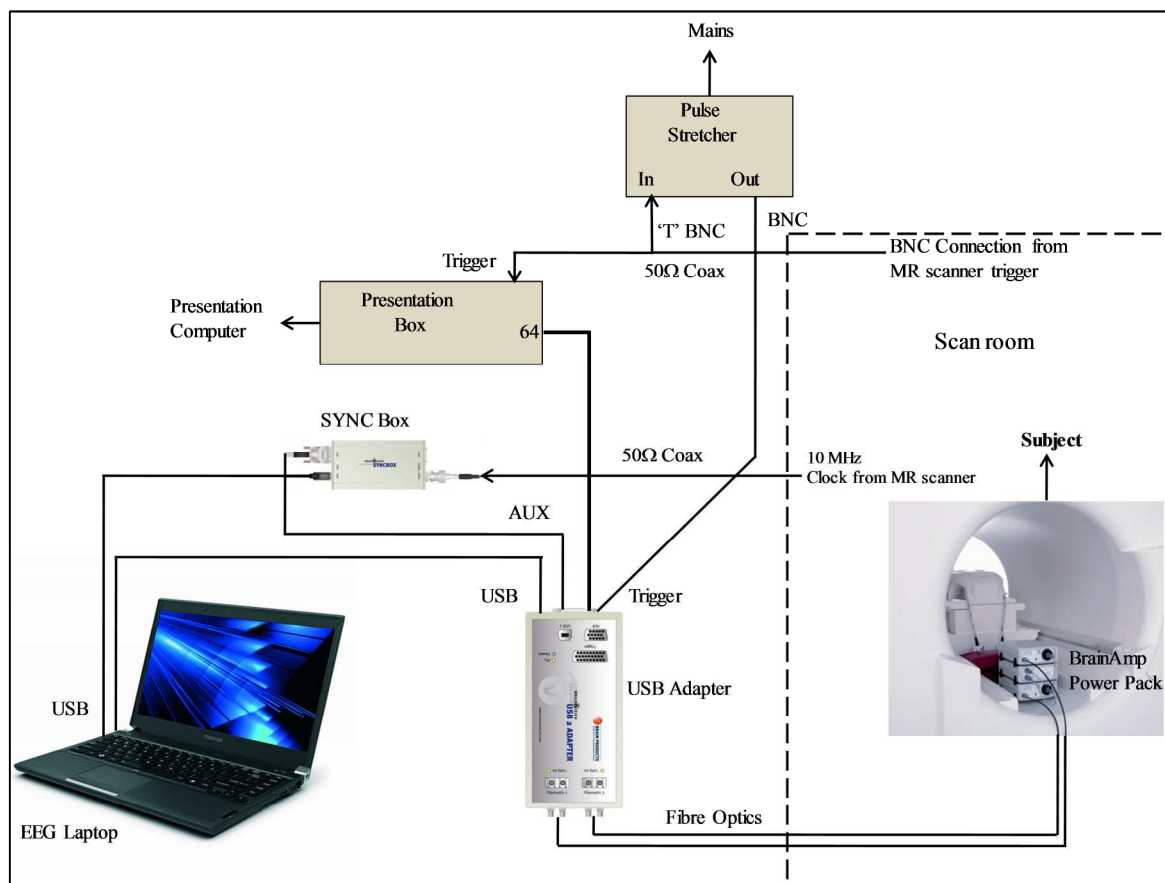


**Figure 4.3** A schematic diagram of an EEG/MR setup utilizing hardware clock synchronization.

All major commercially available MR scanners provide clock signal outputs which are typically unused by the MR system itself during normal operation. This makes them freely available for clock synchronization. The frequency of these clock signals may vary, but all major scanner brands have a 10 MHz clock that can be used for this purpose. The synchronization hardware has to optically decouple this signal from the MR scanner for technical safety reasons (described in Section 4.3.2), but also to avoid drawing power from the MR system circuit. This signal is then fed into a clock divider circuit, which down samples the 10 MHz signal into a clock signal that can be used directly by the EEG amplifier (Gutberlet 2010). Figure 4.3 shows a schematic example of a typical MR-EEG clock synchronization setup.

#### 4.5 Best Current Practice for EEG Equipment Set-up

While the previous sections introduced some theoretical considerations, this section will cover practical aspects of experimental set-up for a simultaneous EEG-fMRI experiment. The choice of hardware to provide patient safety and comfort, while delivering high quality EEG and fMRI data is discussed here.

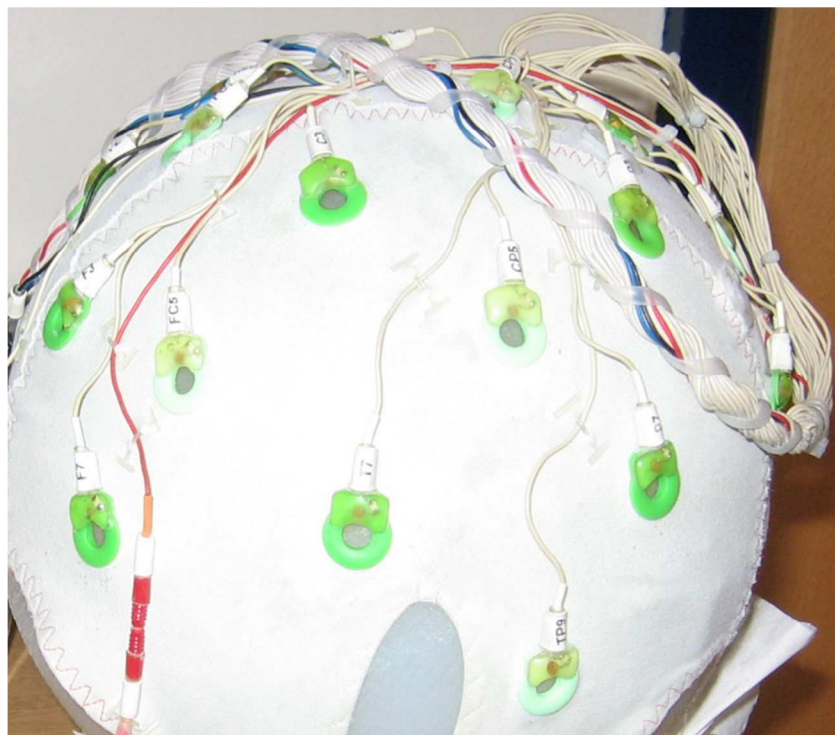


**Figure 4.4** Picture of a commonly used MR-compatible EEG cap system (BrainCap MR, Brain Products GmbH, Gilching, Germany). Safety features on this cap are: (1) plastic electrode holders to avoid direct contact of Ag/AgCl element with the scalp, (2) RF shielding resistor on electrode (e.g., white small “rectangle” on electrode T7), (3) fixation of electrode leads with nylon “Ts,” and (4) routing of electrode leads together in bundles in increasing numbers ).

### 4.5.1 EEG Cap

Electrode caps help to keep wires in a predefined position (Baumann *et al.*, 1999), without loops and direct electrical contact to the subject or one another, yet bundled together (Figure 4.4). Twisting of all wires together had been proposed to be beneficial in minimizing EEG artefacts, with the idea that induced fields cancel each other out (Goldman *et al.*, 2000), but for this to work it is assumed that all electrodes and leads have very similar resistances. Even if achieved in practice, any remaining voltage difference would still be amplified. Generally, cables should be fixed to protect them against motion, such as gradient switching-generated vibrations (Allen *et al.*, 2000), using a tape or bandage (Anami *et al.*, 2003).

### 4.5.2 EEG Amplifier and Cabling

Insertion of padding under the EEG amplifier and application of weights on its upper surface has been shown to result in some reduction of the artefact pick-up by the EEG amplifier, but greater artefact attenuation can be obtained by mounting the EEG amplifier on a wooden table with the ribbon cable (cable between the amplifier and the cap) attached to a cantilevered beam. This set-up ensures that the cable path is kept consistent throughout the experiment and that the entire system is isolated from the scanner bed vibrations (Figure 4.5). The vibration due to the air supply from the internal ventilation system and any other possible sources are damped using the sand bag placed on cantilevered beam.

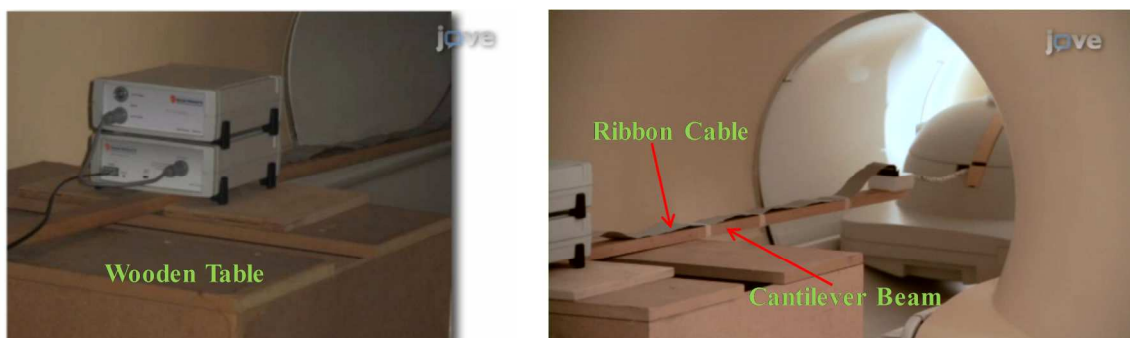


**Figure 4.5** The set-up of the amplifier on the wooden table and the cable on a cantilever beam to isolate it from any bed vibrations (Mullinger *et al.*, 2013).

### 4.5.3 Subject Positioning inside the Scanner

In typical fMRI experiments, the subjects are positioned with nasion at isocentre and this position has also been adopted for EEG-fMRI experiments; however, the optimal position of the subject in the MR scanner is not with nasion at isocentre (as discussed in Chapter 3 Section 3.3.1.8), rather it is with the subject displaced 4 cm axially in the foot direction from this original location (Mullinger *et al.*, 2011). To achieve this it should be ensured that Fp1 and Fp2 electrodes on the EEG cap are placed at the isocentre of the MR scanner in the z-

axis. This positioning significantly reduces the gradient artefact produced by time-varying gradients applied in the RL and FH directions compared with the situation where the nasion is at isocentre.

### 4.6 Conclusion

In recent years, the hardware and software used for simultaneous recordings of EEG and fMRI have matured to the point that many of the technical challenges have been overcome to allow recordings which can be used to investigate aspects of brain function. Several different EEG/MR systems are now commercially available, along with powerful post-processing software (both commercial and open-source) for the correction of the gradient and pulse artefacts as discussed in Chapter 3. However, even with an optimised experimental set-up using current technology, as described in this chapter, and the best post-processing, as described in Chapter 3, there are still significant limitations on the frequency bands (particularly delta, theta and gamma) and low-voltage signals which can be investigated confidently using simultaneous EEG-fMRI. Remaining problems with artefact removal are mostly related to subject motion, due to the inherent variability and unpredictable nature of head movements the available post-processing methods are not really suited to removal of artefacts related to motion (Allen *et al.*, 2000; Jansen *et al.*, 2012). Therefore it is desirable to develop new methods to reduce the amplitude and the variability of the EEG artefacts at source to minimise residual artefacts after post-processing. The following experimental chapters describe in this work which have been carried out in order to address these outstanding issues and to improve the quality of EEG data acquired during simultaneous fMRI.

### 4.7 References

- Achenbach, S., Moshage, W., Diem, B., Bieberle, T., Schibgilla, V. and Bachmann, K. (1997). "Effects of magnetic resonance imaging on cardiac pacemakers and electrodes." *Am Heart J* **134**: 467-473.
- Allen, P. J., Josephs, O. and Turner, R. (2000). "A Method for removing Imaging Artifact from Continuous EEG Recorded during Functional MRI." *NeuroImage* **12**(2): 230-239.
- Anami, K., Mori, T., Tanaka, F., Kawagoe, Y., Okamoto, J., Yarita, M., Ohnishi, T., Yumoto, M., Matsuda, H. and Saitoh, O. (2003). "Stepping stone sampling for retrieving

- artifact-free electroencephalogram during functional magnetic resonance imaging." Neuroimage **19**(2): 281-295.
- Angelone, L. M., Potthast, A., F, S., Iwaki, S., Belliveau, J. W. and Bonmassar, G. (2004). "Metallic electrodes and leads in simultaneous EEG-MRI: specific absorption rate (SAR) simulation studies. ." Bioelectromagnetics **25**(285-295).
- Angelone, L. M., Vasios, C. E., Wiggins, G., Purdon, P. L. and Bonmassar, G. (2006). "On the effect of resistive EEG electrodes and leads during 7 T MRI: simulation and temperature measurement studies." Magn Reson Imaging **24**(801-812).
- Baumann, S. B. and Noll, D. C. (1999). " A modified electrode cap for EEG recordings in MRI scanners." Clinical Neurophysiology **110**: 2189-2193.
- Dempsey, M. F. and Condon, B. (2001a). "Thermal injuries associated with MRI." Clin Radiol **56**: 457-465.
- Dempsey, M. F., Condon, B. and Hadley, D. M. (2001b). "Investigation of the factors responsible for burns during MRI." J Magn Reson Imaging **13**: 627-631.
- DenBoer, J. A., Bourland, J. D., Nyenhuis, J. A., Ham, C. L., Engels, J. M., Hebrank, F. X., Frese, G. and Schaefer, D. J. (2002). "Comparison of the threshold for peripheral nerve stimulation during gradient switching in whole body MR systems. ." Journal of Magnetic Resonance Imaging **15**: 520-525.
- Goldman, R. I., Stern, J. M., Engel, J. J. and Cohen, M. S. (2000). "Acquiring simultaneous EEG and functional MRI." Clin. Neurophysiology **11**: 1974-1980.
- Grandolfo, M., Polichetti, A., Vecchia, P. and Gandhi, O. P. (1992). "Spatial distribution of RF power in critical organs during magnetic resonance imaging." Ann N Y Acad Sci **649**: 176-187.
- Gutberlet, I. (2010). Simultaneous EEG and fMRI: recording, analysis, and application. Chapter 2.1: Recording EEG Signals Inside the MRI. Oxford University Press.
- Jansen, M., White, T. P., Mullinger, K. J., Liddle, E. B., Gowland, P. A., Francis, S. T., Bowtell, R. and Liddle, P. F. (2012). "Motion-related artefacts in EEG predict neuronally plausible patterns of activation in fMRI data." NeuroImage **59**(1-3): 261-270.
- Laufs, H., Daunizeau, J., Carmichael, D. W. and Kleinschmidt, A. (2008). "Recent advances in recording electrophysiological data simultaneously with magnetic resonance imaging." NeuroImage **40**(2): 515-528.



- Lemieux, L., Allen, P. J., Franconi, F., Symms, M. R. and Fish, D. R. (1997). "Recording of EEG during fMRI experiments : Patient safety." Magn. Res. Med. **38**(6): 943-952.
- Mandelkow, H., Halder, P., Boesiger, P. and Brandeis, D. (2006). "Synchronisation facilitates removal of MRI artefacts from concurrent EEG recordings and increases usable bandwidth." NeuroImage **32**(3): 1120-1126.
- Mullinger, K. J., Brookes, M. J., Stevenson, C. M., Morgan, P. S. and Bowtell, R. W. (2008c). "Exploring the feasibility of simultaneous EEG/fMRI at 7 T." Magnetic Resonance Imaging **26**(7): 607-616.
- Mullinger, K. J., Castellone, P. and Bowtell, R. (2013) Best Current Practice for Obtaining High Quality EEG Data During Simultaneous fMRI. JOVE DOI: 10.3791/50283
- Mullinger, K. J., Yan, W. X. and Bowtell, R. W. (2011). "Reducing the Gradient Artefact in Simultaneous EEG-fMRI by Adjusting the Subject's Axial Position." NeuroImage **54**(3): 1942-1950.
- Nitz, W. R., Brinker, G., Diehl, D. and Frese, G. (2005). "Specific absorption rate as a poor indicator of magnetic resonance-related implant heating." Invest Radiol **40**: 773-776.
- Nitz, W. R., Oppelt, A., Renz, W., Manke, C., Lenhart, M. and Link, J. (2001). "On the heating of linear conductive structures as guide wires and catheters in interventional MRI. ." J Magn Reson Imaging **13**: 105-114.
- Schenck, J. F. (2000). "Safety of strong, static magnetic fields." Journal of Magnetic Resonance Imaging **12**: 2-19.

# Chapter 5

---

*Simultaneous EEG-fMRI: evaluating the effect of the cabling configuration on the gradient artefact*

## 5.1 Introduction

The great potential of simultaneous EEG/fMRI is evident from the variety of applications of this multi-modal approach which have been explored. These range from investigating correlations between electrical and BOLD activity in the resting state (Goldman *et al.*, 2002; Laufs *et al.*, 2003) to source localization of epileptic activity (Lemieux *et al.*, 2001; Salek-Haddadi *et al.*, 2002). However, the presence of residual EEG artefacts still limits the avenues which can be investigated using EEG/fMRI. Chapter 3 outlines the causes of artefacts in EEG data recorded simultaneously with MRI and describes the methods that have been developed to correct these artefacts, whilst Chapter 4 describes the current practices that are used to obtain the best possible quality of EEG data recording in combined EEG/fMRI experiments. However, as already discussed in this thesis the EEG data quality inside the MR environment is still much poorer than that acquired outside this hostile environment. This chapter explores the effect of the cable configuration on the EEG artefacts and demonstrates that particular cabling arrangements can improve the quality of EEG data recorded in combined EEG/fMRI experiments.

## 5.2 Background

It is clear from the above discussion that it is essential to focus on how to avoid or attenuate MR-related imaging artefacts altogether or at least to reduce the variability of the GA across a scan period in order to increase the EEG signal quality. Improved artefact correction techniques may result from a better understanding of the mechanisms that give rise to the GA. Yan *et al.*, (2009) showed how the pattern of GAs induced on different leads by time-varying longitudinal and transverse gradients could be modelled based on knowledge of the lead paths and head position in the gradient fields. This modelling work provided insight into ways in which the magnitude of the GA could be reduced at source. One of the suggestions, a change in the axial positioning of the subject, has already been investigated (Mullinger *et al.*, 2011). The advantages of this change in positioning were discussed in Chapter 3, Section 3.3.1.8 and are now employed in the best experimental set-up. The modelling work (Yan *et al.*, 2009) also suggested that a further reduction in the magnitude and variability of the induced artefacts could be achieved by using a twisted cable instead of the flat ribbon cable, currently employed in the BrainAmp EEG amplifier (used in all experiments in this thesis), to complete the connection from the EEG cap to the amplifier. In essence, a twisted cable would minimise the area of the wire loops so that the maximum rate of change of magnetic flux

produced by the time-varying magnetic field gradients over the EEG leads is minimised (Figure 5.1A&B).

The aim of the study described in this chapter is to measure the effects of the cable configuration on the characteristics of the GA. In this work, two, 1-m long cable configurations were studied: Firstly, a ribbon cable in which the wires run in parallel, effectively forming loops of significant area; and secondly a twisted cable consisting of wires that are twisted together thus minimising the area of the wire loops. The first part of the study focused on the measurement of GA amplitude for both cables using a customised pulse sequence in which controlled gradient pulses were sequentially applied along the three (x, y and z) Cartesian axes (Mullinger *et al.*, 2011). In the second part of the study, we tested the effect of each cable configuration on the GA induced in the entire EEG system with the EEG cap present. This was done by using a standard fMRI sequence, as employed in typical EEG-fMRI studies.

### 5.2 Methods

For each of the following experiments 32 channels of EEG data were recorded (Brain Products, Munich, Germany). A BrainAmp MR-plus EEG amplifier (Brain Products, Munich, Germany) with Vision Recorder (Version 1.10) was used for recording data in a Philips Achieva 3 T MR scanner (Philips Medical Systems, Best, The Netherlands). EEG data were sampled at 5 kHz. The EEG clock was synchronised to the MR scanner clock for all experiments and the trigger pulses from the MR scanner marking each volume acquisition were recorded by the EEG system (Mandelkow *et al.*, 2006; Mullinger *et al.*, 2008c).

A 1m-long ribbon cable (Figure 5.1B) and twisted cable (Figure 5.1A) running axially along the magnet bore were used sequentially to connect the EEG amplifier to a signal tester box (Figure 5.1C) and to the connector box of the 32-channel EEG cap in the experiment. The signal tester box provides shorted wiring connections between all the channels with the REF channel which consequently helps to test the amplifier without connecting it to cap. The cables were attached to a wooden, cantilevered beam to ensure they were kept straight and isolated from scanner vibration. The EEG amplifier was placed just outside the bore of the magnet at the head end of the scanner on a table (as shown in Chapter 4, Figure 4.5), which isolated it from vibrations of the scanner (Mullinger *et al.*, 2008a). A 32 channel EEG cap

(EasyCap, Herrsching, Germany) was employed for the relevant experiments, with 31 sintered Ag/AgCl ring-electrodes following the extended international 10-20 system and the reference electrode positioned at FCz. The additional electrode was used as an electroculography (EOG) channel and was attached beneath the left eye. The electrodes used had a 1.2 cm outer diameter and 0.6 cm inner diameter, including plastic adapters and 5 k $\Omega$  resistors. Light-duty braided copper wires, with an approximate diameter of 0.3 mm were used for connection of the EEG electrodes to the connector box.

The conducting spherical phantom, employed in some of the experiments, was 0.19 m in diameter and constructed from 4% (by total weight) agar (Sigma Aldrich) in distilled water. 0.5% NaCl was added to the water to yield a conductivity of about 0.5  $\Omega^{-1} \text{ m}^{-1}$ , which approximately reflects the conductivity of tissues of the human head (blood  $\sim 0.6 \Omega^{-1} \text{ m}^{-1}$  and gray/white matter  $\sim 0.12 \Omega^{-1} \text{ m}^{-1}$ ) (Bencsik *et al.*, 2007) and 4 ml/l of Milton sterilizing fluid added to prevent bacterial growth (Yan *et al.*, 2009). The contents were boiled to make a viscous gel, which was then poured into a spherical fibre-glass mould. After the agar had set, the mould was removed to yield the desired spherical phantom. Abralyte 2000 conductive and abrasive gel was used to provide an electrical contact between the electrodes and the scalp or agar phantom surface. The quantity of gel placed between the electrodes and the surface of the phantom was equivalent to the amount typically used when EEG recordings are made on human subjects (<1 ml per electrode). The EOG lead was connected to the “face” of the phantom.

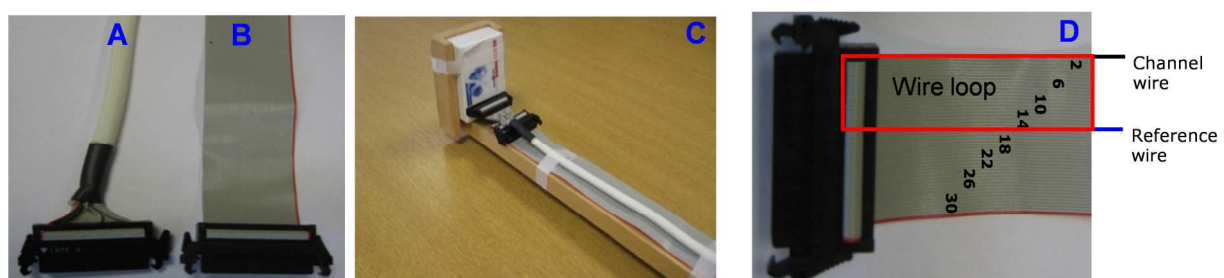


**Figure 5.1** A picture of the twisted cable (A); ribbon cable (B); how the cables were attached to the signal tester box (C) and the formation of wire loops with respect to reference channel in the ribbon cable (D).

### 5.2.1 Study 1

In order to assess how the cable configuration affected the magnitude of the GA produced by each of the three orthogonal gradients, EEG recordings were made during execution of a

modified EPI sequence. This incorporated three additional gradient pulses applied sequentially in the right-left (RL), anterior-posterior (AP), and foot-head (FH) directions prior to each slice acquisition, as described by Mullinger *et al.*, (2011) and shown in Figure 5.2A. Each trapezoidal pulse was made up of two ramps of 10 ms duration, during which the gradient changed at a rate of  $dG/dt = 2 \text{ T m}^{-1}\text{s}^{-1}$  and a 10-ms period during which the gradient remained constant. A 20-ms gap was inserted between successive gradient pulses. The modified sequence allowed easy separation of the effects of the three different gradients by providing clearly defined periods during which each single gradient varied in time in a well-defined manner. For this experiment the cabling was terminated in two different ways:

- i) using the signal tester box so that the cables were the dominant source of the GA.
- ii) using the EEG cap on the agar phantom to test the interaction of the artefacts induced on the cables with those due to the wires of the EEG cap.

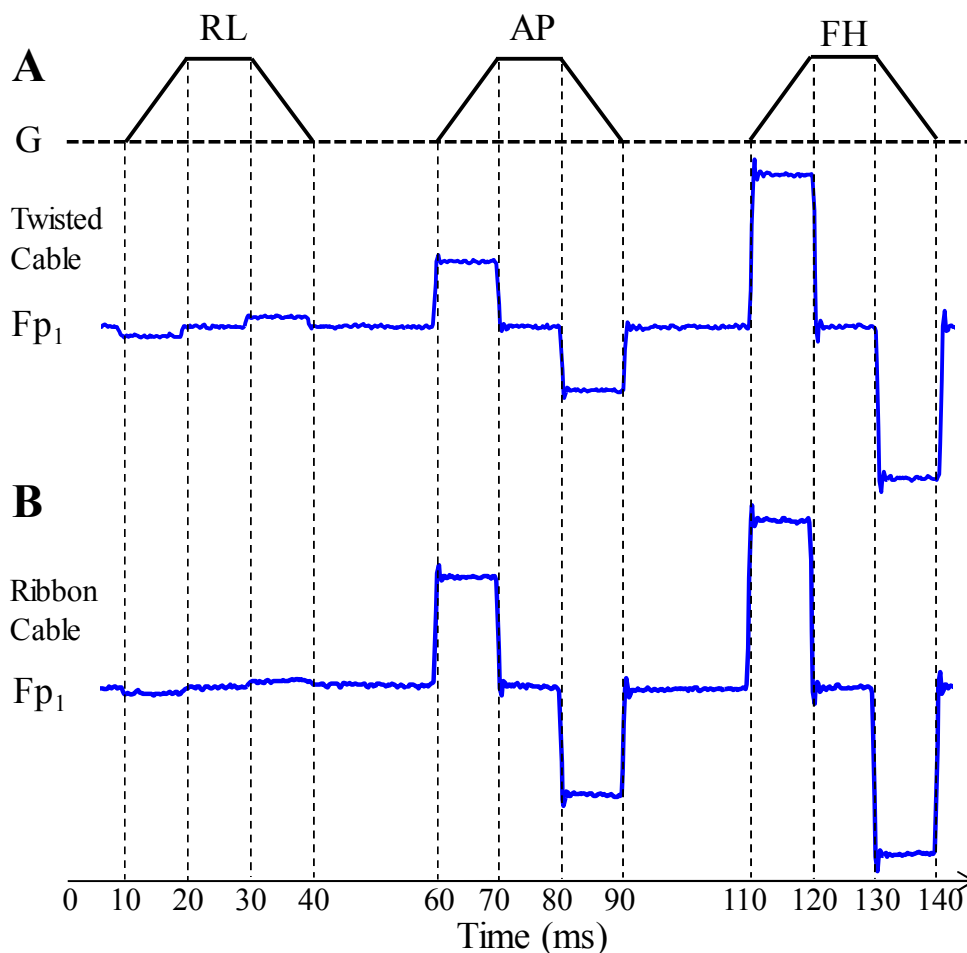


**Figure 5.2** Illustration of the sequence used to characterise the artefacts generated by time-varying gradients along each Cartesian axis. (A) Schematic illustration of the gradient pulses applied in the right-left (RL), anterior-posterior (AP), and foot-head (FH) directions. (B) Artefact voltages generated by these pulses on example lead (Fp1) for both cables. Adapted from Mullinger *et al.*, (2011).

The cantilevered beam (Figure 5.1C) to which the cables were attached ensured that the cable paths were kept consistent between the recordings made using the different cables. The cable arrangement positioning was defined such that the signal tester box or phantom was placed at isocentre in the FH direction (z-coordinate of the MR-system) and RL direction and at a fixed position in the AP direction (posterior to isocentre). For each of the cables and each termination method, recordings were made with the cable assembly located at two different AP positions that were 5mm apart. With termination method (i) the signal tester box and cable positions were also varied in the FH direction from -20 cm to +10 cm in 10-cm steps, with positive values corresponding to a shift toward the head direction.

The EEG amplifier was set with a frequency range of 0.016-1000 Hz and a 30 dB/octave roll-off at high frequency to enable full characterisation of the artefacts produced by the customised gradient pulses. For each cable position, the GA from thirty pulses applied along each of the three gradient axes were recorded.

### 5.2.2 Study 2

To evaluate the effect of the cable configuration on the GA generated in typical fMRI studies, EEG data were recorded during a standard EPI sequence (shown in Figure 5.3A). Experiments were carried out with the same ribbon cable and twisted cable and cabling positions used in Study 1. Data were acquired for both cables which were terminated using:

- i) the cable tester box used in Study 1.
- ii) the EEG cap on the agar phantom used in Study 1.
- iii) the EEG cap on a subject (with approval from the local research ethics committee).

Here the subject position was defined by the z-coordinate of the MR-system, and the nasion was displaced 4 cm axially from the scanner's iso-centre towards the feet (i.e. optimally positioned as described in Chapter 3, Section 3.3.1.8). The definition of iso-centre for set-ups (i) and (ii) were the same as described in Study 1. Two sets of data were recorded for each of the termination methods with the cabling moved 5 mm in the AP direction between recordings. For this study the EEG amplifier was set with a frequency range of 0.016-250 Hz and a 30 dB/octave roll-off at high frequency as typically used in EEG-fMRI studies which ensures that saturation of the amplifiers is avoided. For each of the set-ups and cable

positions described, EEG data were recorded for a 2-minute period while a standard axial, multi-slice EPI sequence (TR = 2 s, TE = 40 ms, 40 volumes, 64×64 matrix, 3×3 mm<sup>2</sup> in-plane resolution, flip angle=85<sup>0</sup>, SENSE factor = 2 and 3 mm slice thickness) was executed. Twenty transverse slices were acquired with equidistant temporal spacing in each TR period.

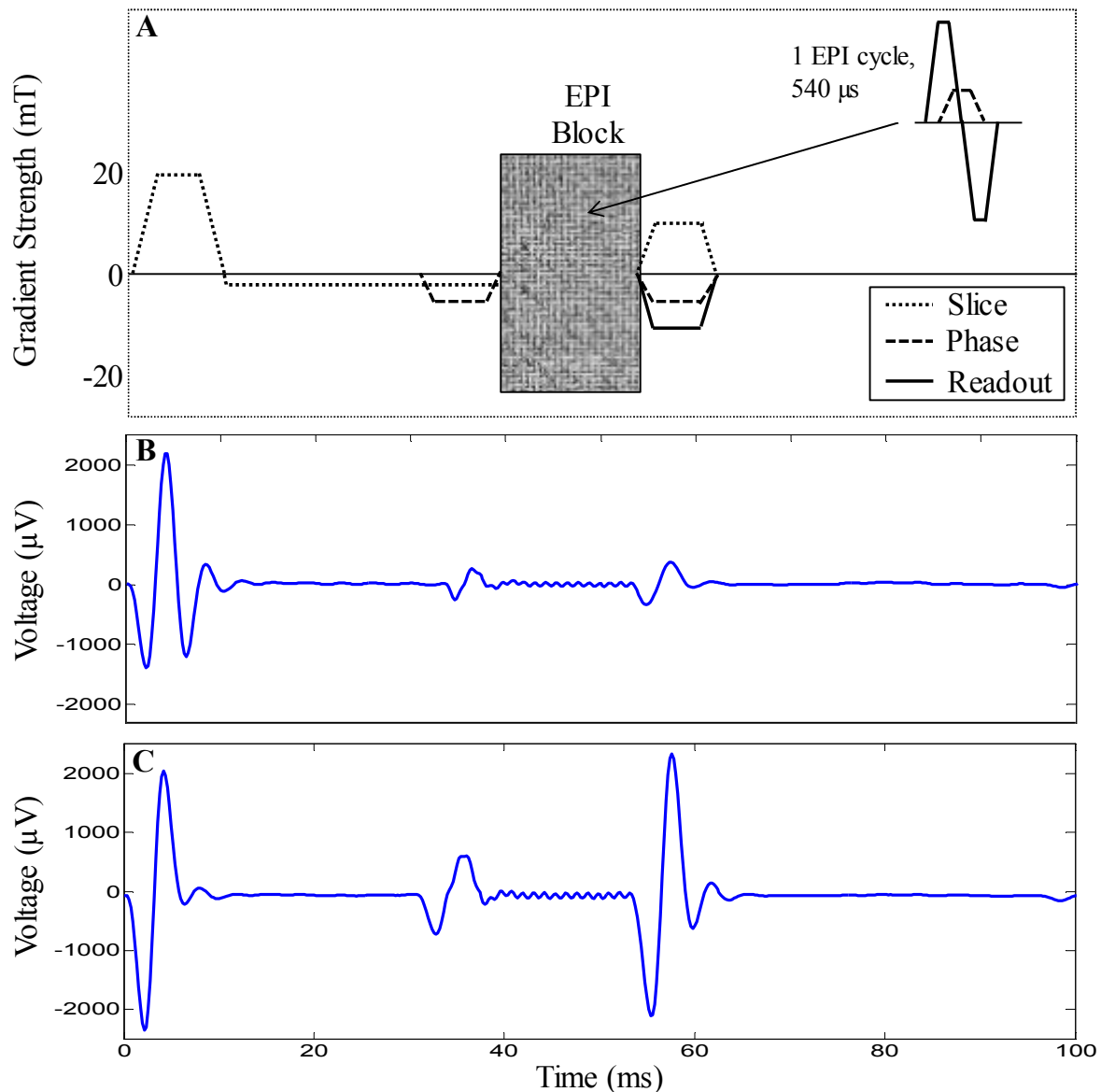


**Figure 5.3** Graphs showing the gradient artefact corresponding gradient waveforms for the EPI sequence shown in A, recorded on electrode Fp1. The gradient artefact is averaged over all slice acquisitions for cable bundle (B) and ribbon cable (C).

### 5.3 Analysis

Initial data processing and analysis were carried out in Brain Vision Analyzer2 (Version 2.0.1; Brain Products, Munich, Germany) while MATLAB (The MathWorks) was used for further quantification of differences in induced GA between cables and positions.



### 5.3.1 Study 1

Since the gradient pulses in the customised EPI sequence (Fig. 5.2A) commenced with a 10-ms period during which the rate of change of gradient,  $dG/dt$ , is constant and positive, followed 10 ms later by a 10 ms period in which  $dG/dt$  is constant and negative. Equal and opposite artefact voltages are generated during the two ramping periods (Mullinger *et al.*, 2011). To form a robust measure of the artefact voltage on each channel, the GA was averaged over the 30 pulses. Then the average voltage over the central 5 ms of each ramp period was evaluated, before taking the difference between the two values to eliminate the effect of any baseline offset and high-frequency fluctuations. The change in the amplitude and variation of the GA with the cable configuration was characterised by calculating the range and the root-mean-square amplitude (RMS) of the artefact voltages measured across the 31 channels and then averaging these measures over 30 repetitions.

Assuming that the artefact voltages induced in the twisted cable are very small compared with those in the ribbon cable, the differences between voltages recorded with the ribbon cable and twisted cable correspond to voltages induced in the ribbon cable only. Therefore using this assumption, voltages recorded with the entire EEG system and phantom present using the twisted cable predominately correspond to voltages induced in the cap and phantom (as the amplifier sits outside of the gradient field). Artefact maps were generated to show the spatial distribution of the artefacts coming from the EEG cap, ribbon cable only and entire EEG system with the ribbon cable in place. These maps were designed to show the spatial interaction of the artefacts induced in the various components of the EEG system.

### 5.3.2 Study 2

For each of the data sets acquired, EEG data were baseline corrected (0 to -100 ms) and then the RMS voltage of the induced GA over leads was calculated over an EPI slice acquisition for the two AP positions. The RMS over the time of the slice artefact RMS voltage for each data set was also calculated to give a single measure of the GA produced for each cable and position. The difference in the RMS voltage induced slice-GA between the two cable positions was calculated by subtracting baseline-corrected slice EPI data at each position and then the RMS over time of the slice artefact RMS voltage difference was calculated to measure the fractional change due to the 5 mm AP movement for the ribbon cable and twisted cable when the cables were attached to the EEG cap on the phantom and subject. To

assess any contribution of subject movement to any changes in GA the MRI data were realigned using SPM8 (FIL, London, <http://www.fil.ion.ucl.ac.uk/spm/software/spm8/>) and realignment parameters inspected.

## **5.4 Results**

### **5.4.1 Study1**

Figure 5.1D shows that for the ribbon cable the distance between an individual wire and the wire that is connected to the reference electrode varies linearly with channel number. Consequently the area of the loop formed by an individual wire and the reference wire also increases linearly with channel number.

The channel wires 1 and 32 are furthest from the reference wire and thus form the largest wire loops, whereas channel wires 16 and 17 are closest to the reference wire thus producing the smallest wire loops. The twisted cable reduces the discrepancy in the effective distance of the channel wires from the reference wire, resulting in more a homogeneous size of wire loop.

Comparison of the average gradient artefact (Figure 5.2B) and the customized gradient waveforms (Figure 5.2A) indicates that the largest artefacts are generated in the recording from lead Fp1 by the individual gradient pulses used in AP and FH direction. A comparatively smaller EEG artefact is generated by the RL gradient pulse. In the case of this customised EPI sequence, the EEG data are recorded with the higher EEG amplifier bandwidth in order to obtain a step-response in the EEG artefact while each individual gradient is linearly ramped on or off. The exact amplitude of the artefact corresponding to the gradient pulses varies according to the positions of the electrodes and associated leads relative to the applied field gradients and indeed may change between scan sessions if the electrodes are not positioned identically within the scanner on each occasion. However, the general features of the artefact waveforms described above are common to all channels.

The effect of the variation of the wire loop size with channel number can be seen in Figure 5.4. It should be noted that the artefacts shown in 5.4 come from both the cabling and the tester box. This figure shows the induced GA voltages for each of the orthogonal gradients

over channels for the ribbon cable (Figure 5.4A&C) and twisted cable (Figure 5.4 B&D) in each of the AP positions (0 mm, Fig. 5.4 A&B and +5 mm, Fig 5.4C&D). Figure 5.4 shows

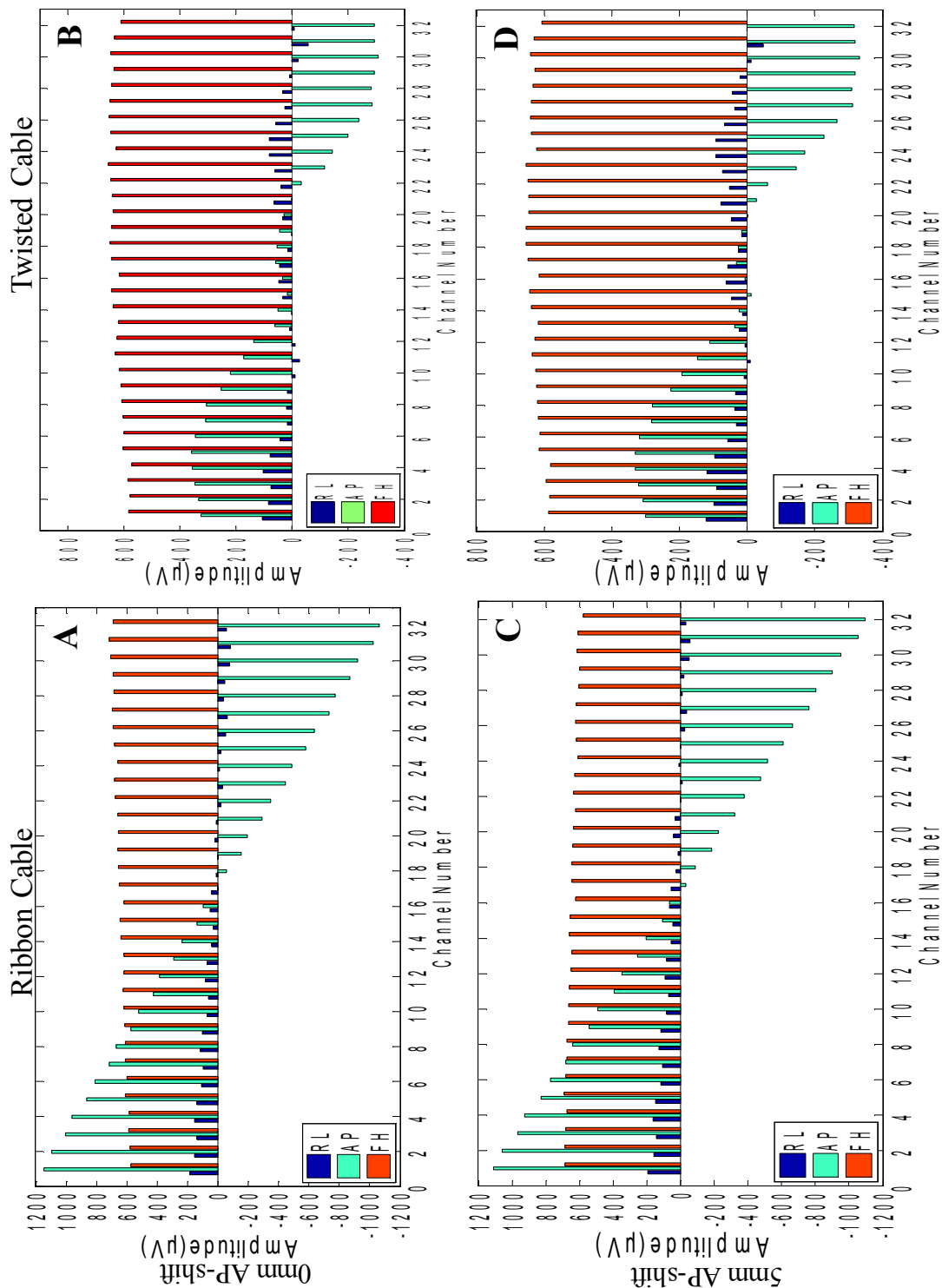


**Figure 5.4** Induced artefact voltage for the three orthogonal gradients for ribbon cable at **A: 0 mm AP-shift**, **C: 5 mm AP-shift** and for twisted cable at **B: 0 mm AP-shift**, **D: 5 mm AP-shift** connected to the signal tester box.

that the ribbon cable exhibits a linear variation in amplitude of the AP gradient artefact (range at 0 mm = 2218  $\mu\text{V}$ ) and a relatively linear variation for the RL gradient (range at 0 mm = 256  $\mu\text{V}$ ), as expected from the wire configuration. When the twisted cable was employed smaller artefacts were induced by the AP gradient over all channels which resulted in a 1532

$\mu\text{V}$  reduction of in the range of the artefact. Slight reductions in the range ( $76 \mu\text{V}/35 \mu\text{V}$ ) of the artefacts induced by the RL/FH gradients were also observed. These results are reflected in the mean RMS artefact amplitude at 0 mm AP-shift for the AP, RL and FH gradients which were 668/232, 83/51 and 645/625  $\mu\text{V}$  respectively for the ribbon cable/twisted cable.

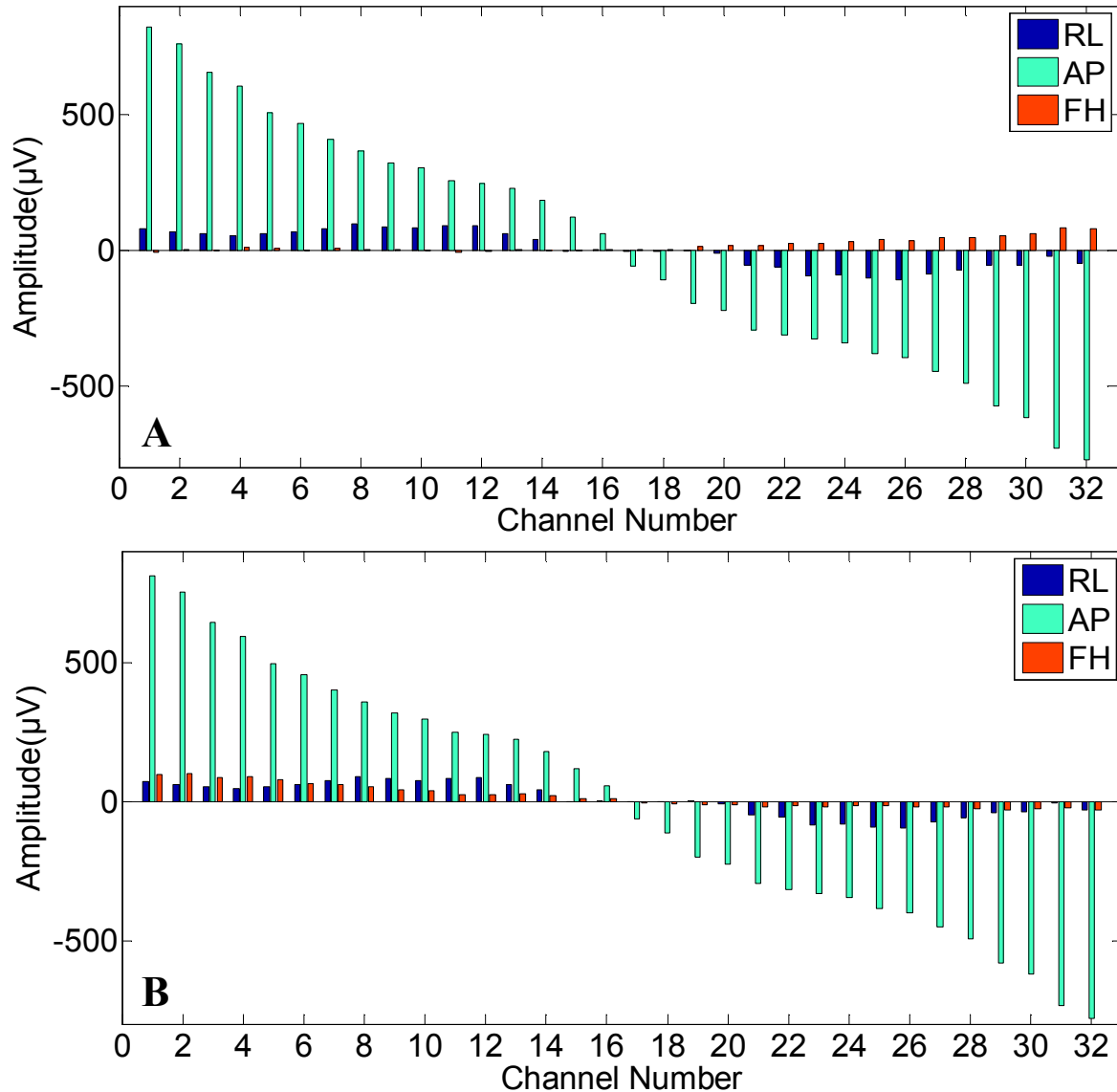


**Figure 5.5** Variation of the difference (ribbon cable – twisted cable) in the induced GA voltage over channels using the signal tester box for two AP-positions of the cables (**A**: 0 mm AP-shift & **B**: 5 mm AP-shift).

By taking the difference between the artefacts induced in the two cables, any artefact voltages generated in the signal tester box and amplifier were removed, revealing the differences in the voltages induced in the two different cables. Figure 5.5 shows the difference in the induced artefact between cables for the 0 mm (Figure 5.4(A-B)) and the 5 mm shift (Figure 5.4(C-D)). This shows that the largest differences are when the AP gradient is applied. Figure

5.6 shows the effect of the 5 mm shift in the AP direction for both the cables for the three orthogonal gradients. This shows the largest change in artefact amplitude with this shift in cable position for the ribbon cable is for the FH gradient. The change in artefact amplitude for this gradient also varies linearly with channel number showing a sensitivity to the loop area in the plane of the ribbon cable. The maximum differences in artefact amplitude when the twisted cable was used were considerably smaller. This is reflected in the mean RMS of the difference voltage between positions which took values of: 32/27, 18/14 and 67/7  $\mu\text{V}$  for ribbon cable/twisted cable for the AP, RL and FH gradients respectively.

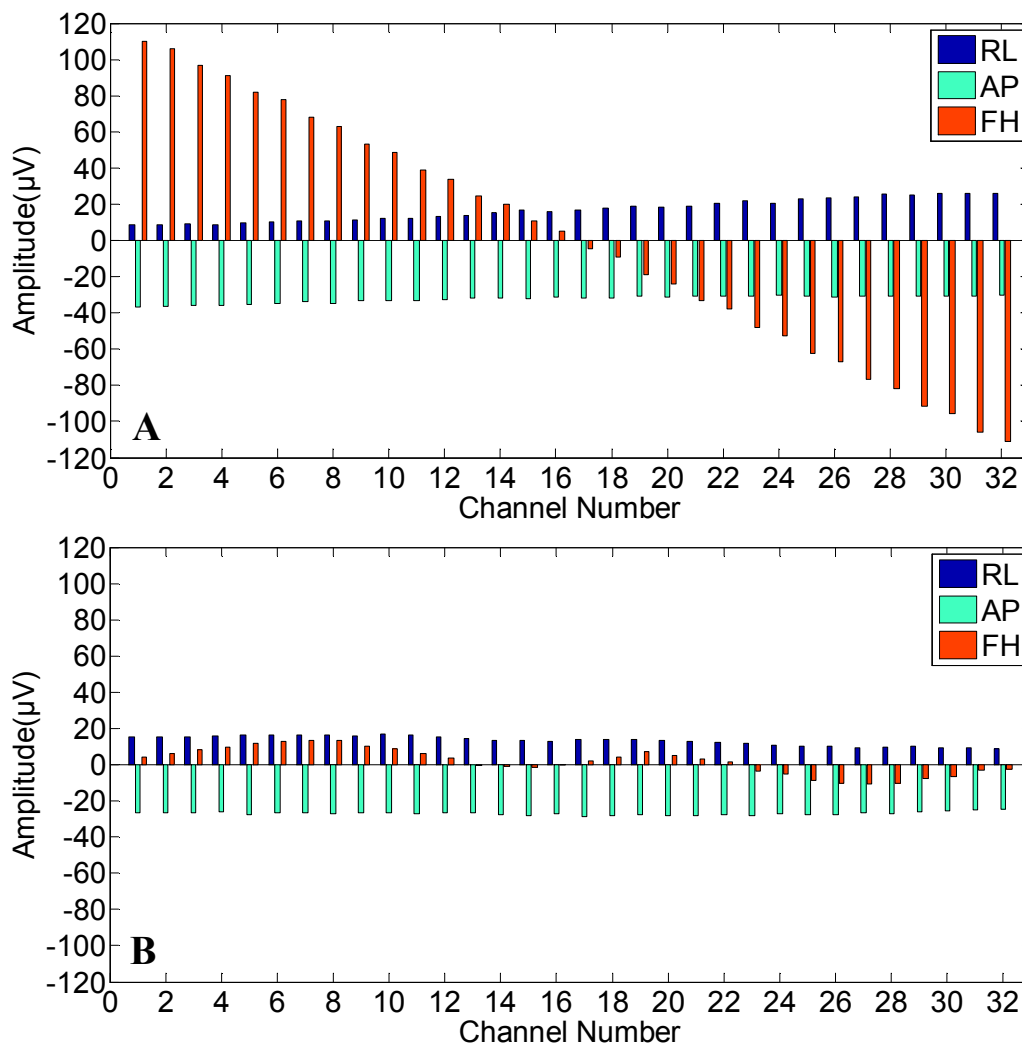


**Figure 5.6** Variation of the difference in the induced GA voltage over channels, using the signal tester box for a 5 mm AP-shift of the cables (**A**: Ribbon Cable, Fig 5.4 A-C, & **B**: Twisted cable, Fig. 5.4 B-D).

A similar pattern was observed when movements in the FH direction were performed as shown by the RMS and range values in Figure 5.7.

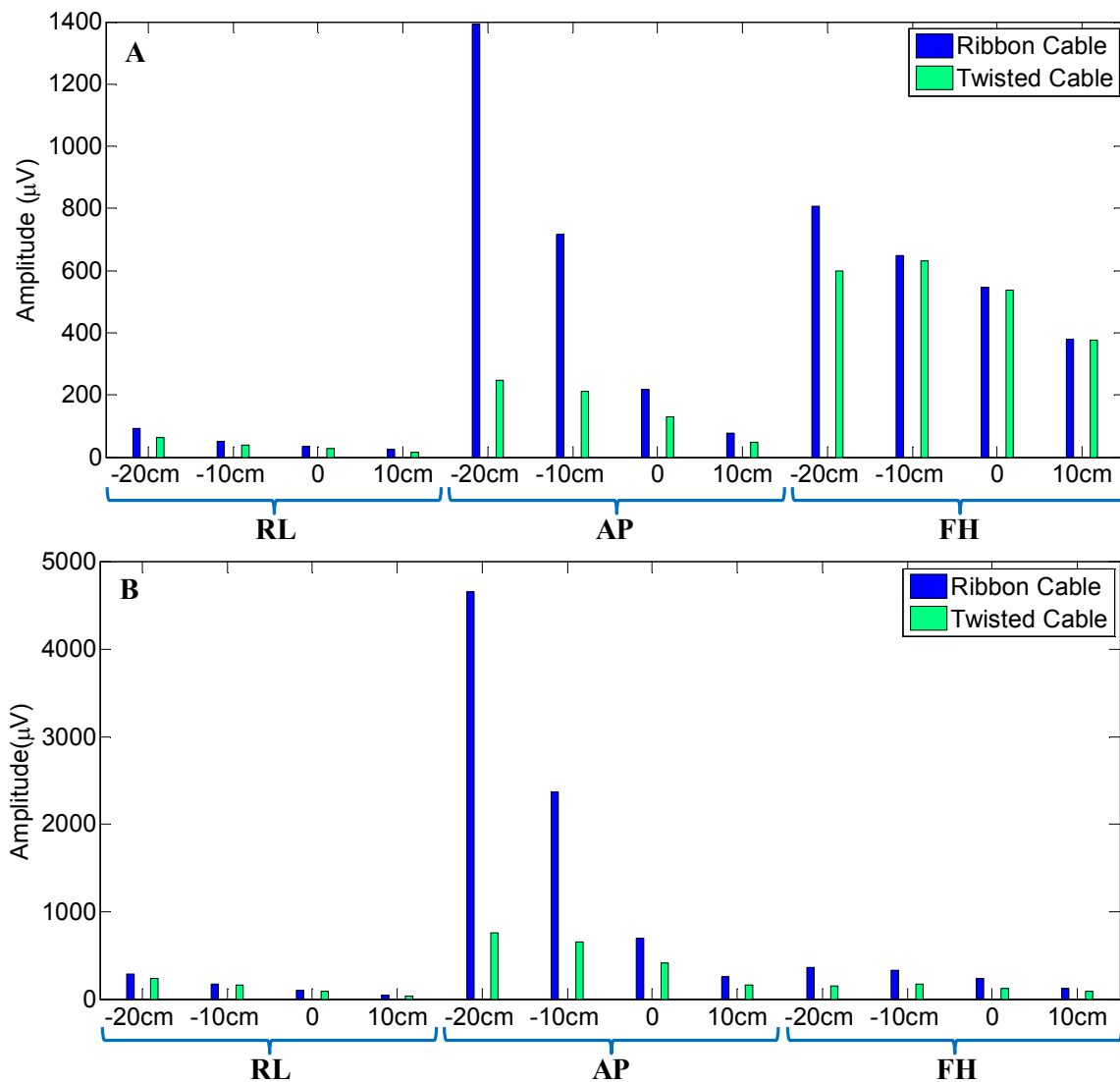


**Figure 5.7** Variation in RMS (A) and range (B) of the GA produced by the RL, AP and FH gradients for movements of the ribbon and twisted cabling in the z-direction from -20 cm to +10 cm.

The induced GA voltages over channels for the ribbon cable and twisted cable connected to the 32-electrode cap on the phantom can be seen in Figure 5.8 for the 0 mm AP position. This shows that the addition of the EEG cap alters the pattern of the induced artefacts as the artefacts induced in the cap and cable bundle (which connects to the ribbon/twisted cable) interact with the artefacts induced in the ribbon/twisted cable. However, by comparing Figure 5.5A and 5.8C it is clear that the contribution from the altered cabling remains the same despite the difference in the artefact induced by the presence of the EEG cap compared with the signal tester box.

By assuming that the artefact voltages induced in the twisted cable are very small compared with those induced in the ribbon cable, voltages recorded with the entire EEG system and

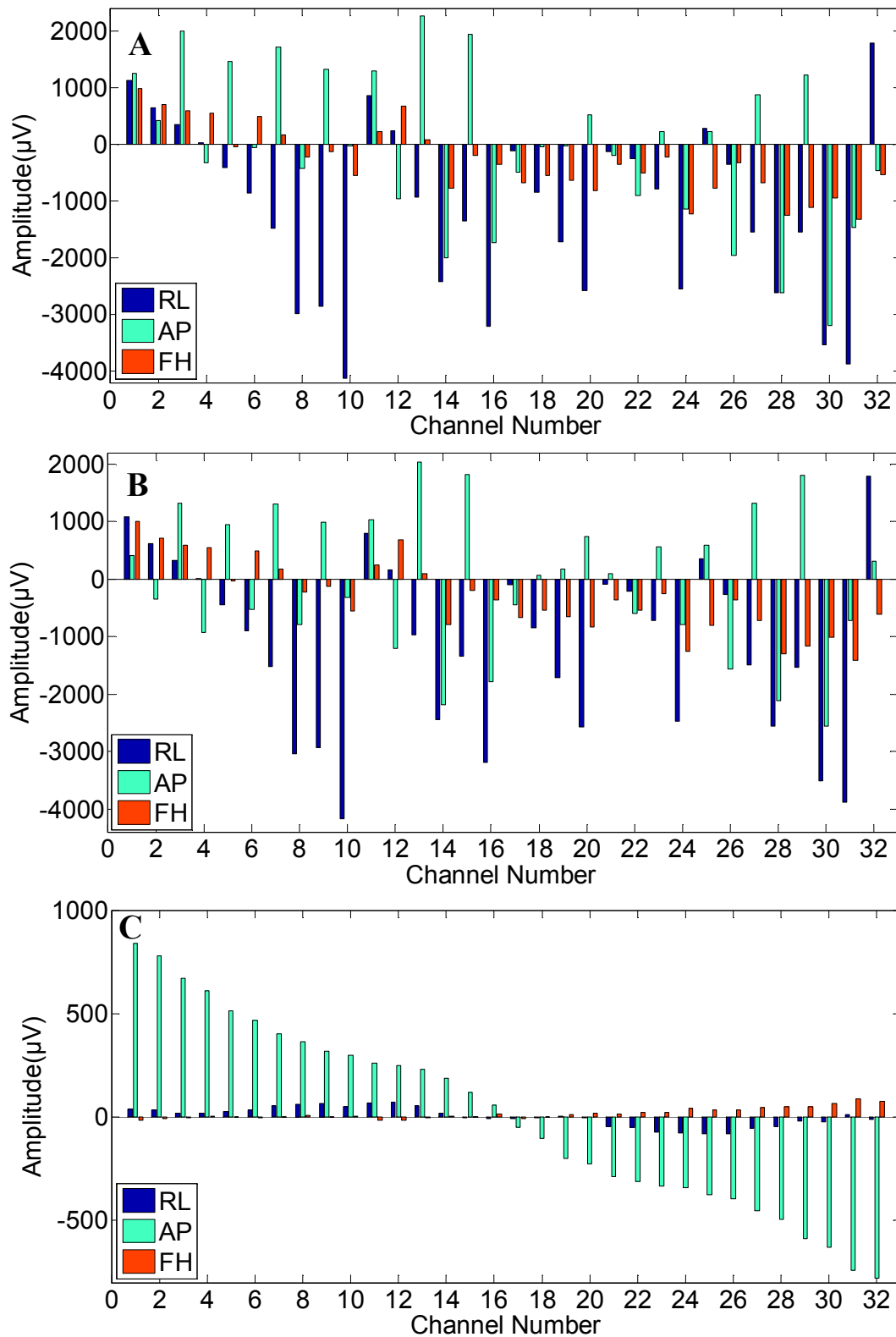


**Figure 5.8** Induced artefact voltage for the three orthogonal gradients at 0 mm shift in AP with agar phantom for **A:** ribbon cable & **B:** twisted cable and **C:** difference between the ribbon and twisted cable responses (A-B).

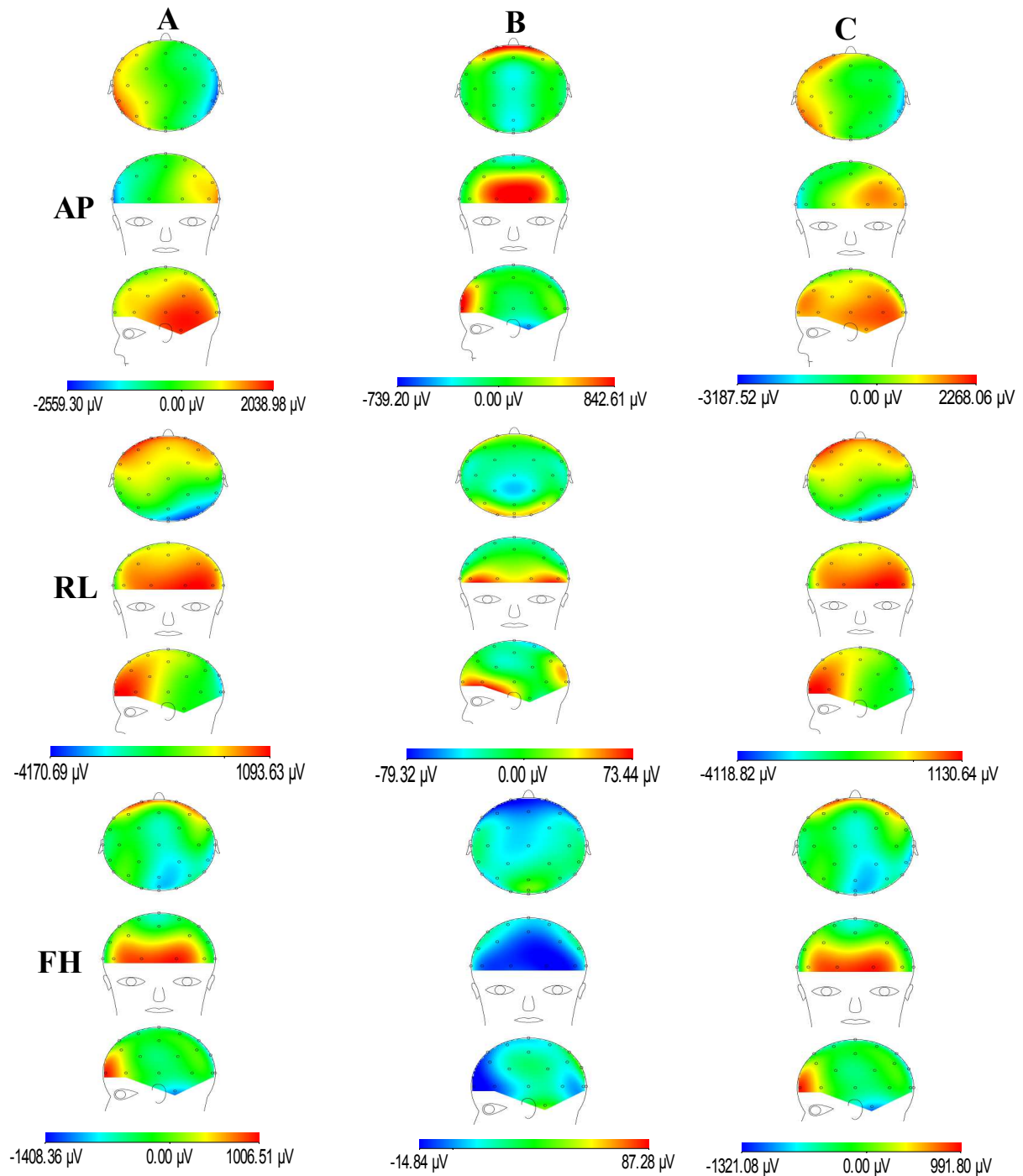


**Figure 5.9** Artefact map for the three orthogonal gradients showing **A**: the cap contribution, **B**: the ribbon cable contribution & **C**: the total artefact (cap with ribbon cable) for the spherical agar phantom.

phantom present using the twisted cable predominately correspond to voltages induced in the cap and phantom. This assumption enables the production of artefact maps for the voltage contribution from the different aspects of the EEG system (EEG cap, ribbon cable only and entire EEG system), which are shown in Figure 5.9.



The contribution of the EEG cap to the artefact voltages (Figure 5.9A) is much greater than that of the ribbon cable (Figure 5.9B) for all three gradients, but the difference in spatial patterns of the induced voltages in the two aspects of the system interact to produce the artefact patterns observed with the standard set up of the of 32-electrode cap with the ribbon cable (Figure 5.9C).

#### 5.4.2 Study 2

Comparison of the average GA (Figure 5.3 B&C) and the gradient waveforms (Figure 5.3A) indicates that the largest artefacts are generated in the recording from lead Fp1 by the gradient pulses used for slice selection at the start of each slice acquisition and those used for crushing transverse magnetization after signal acquisition (at  $t \sim 55$  ms). A slightly smaller artefact is generated by the gradient pulses used for the k-space pre-excursion in the phase-encode direction just prior to signal acquisition. Counterintuitively, the large switched magnetic field gradients used to form the EPI echo train and the associated gradient blips used for phase encoding, do not generate significant artefacts despite, in the former case, reaching rates of change of gradient of  $100 \text{ Tm}^{-1}\text{s}^{-1}$ . This is a consequence of the fact that the dominant spectral contribution to these gradient waveforms occurs at approximately 900 Hz and harmonics of this frequency, which are well above the 250 Hz cut-off frequency used in the EEG recording (Eichele *et al.*, 2010). The effect of the low-pass filtering is also evident from the form of the average artefact trace. This shows that the gradient artefacts generated by each gradient ramping period of a few hundred microseconds persist over a period of a few milliseconds in the EEG trace. The exact form of the artefact varies according to the positions of the electrodes and associated leads relative to the applied field gradients and indeed may change between scan sessions if the electrodes are not positioned identically within the scanner on each occasion. However, the general features of the artefact waveforms described above are common to all channels.

Figure 5.10 shows that when a conventional EPI sequence is used, GA voltage amplitudes induced in the cabling are generally smaller for the twisted cable than for the ribbon cable at the periods of peak artefact generation. This is also illustrated by the RMS voltage of the

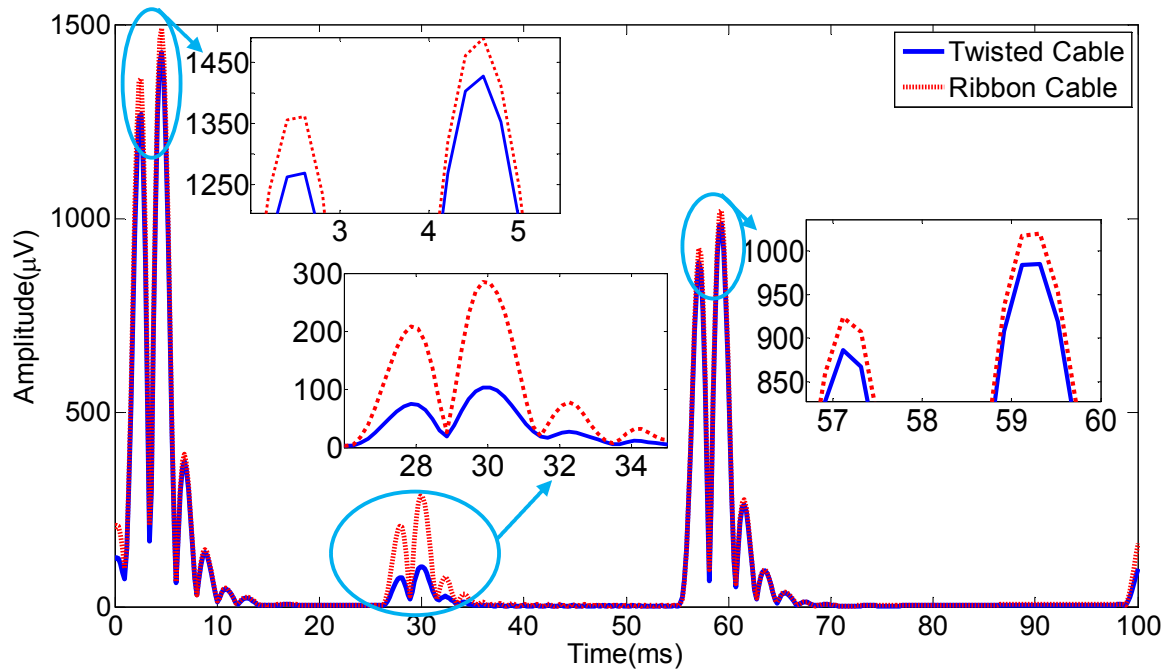


**Figure 5.10** RMS voltage over channels of the average slice artefact for twisted cable (blue solid line) and ribbon cable (red dashed line) for 0 mm shift in AP direction using the signal tester box.

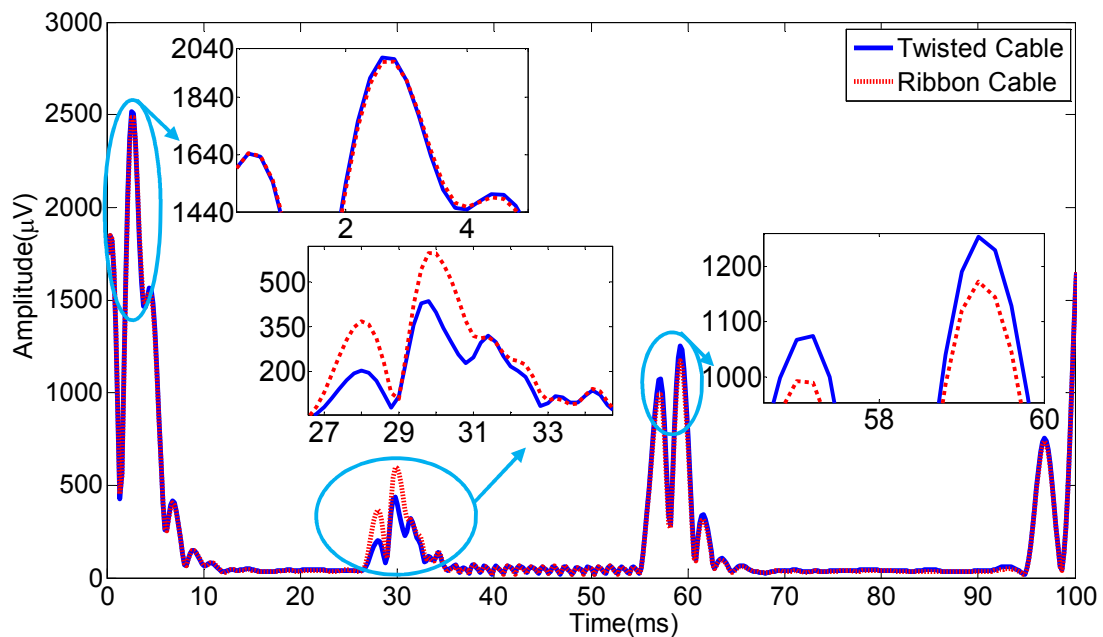


**Figure 5.11** RMS voltage over channels of the average slice artefact for twisted cable (blue solid line) and ribbon cable (red dashed line) for 0 mm shift in AP direction for the subject.

artefact over time which was found to be 272/256  $\mu\text{V}$  for the ribbon cable/twisted cable respectively. The relatively small difference in the RMS voltage over time is due to the large periods of time during the slice TR period where there are no gradient artefacts that contribute to the induced GA and thus no difference is observed between cables. However, when the EEG cap is present, the GA voltages induced are slightly larger for the twisted

cable than the ribbon cable during the slice select and spoiler pulses, as shown in Figure 5.11. This is presumably a consequence of a destructive interference between the artefact contributions from the cap and ribbon cable.

The effect of moving the cable in the AP direction for data recorded from a subject and the phantom are shown in Figure 5.12 and 5.13 respectively. Here the cables are attached to the EEG cap on the subject such that the changes in the artefact due to the movement of the

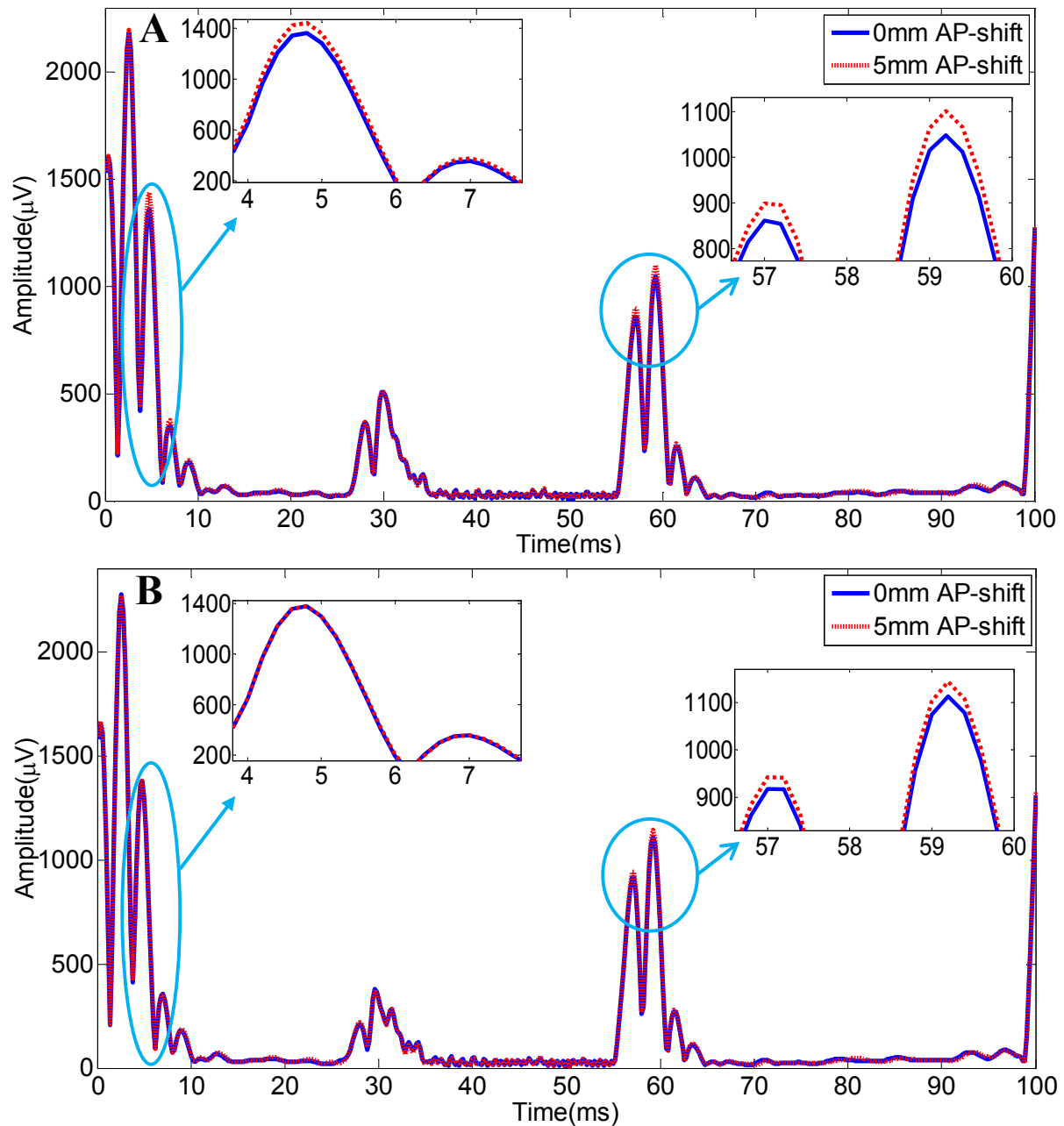


**Figure 5.12** RMS voltage of the average slice artefact averaged across channels for ribbon cable (A) & twisted cable (B) without (blue solid line) and with (red dashed line) 5-mm shift of cabling in AP direction for the subject.

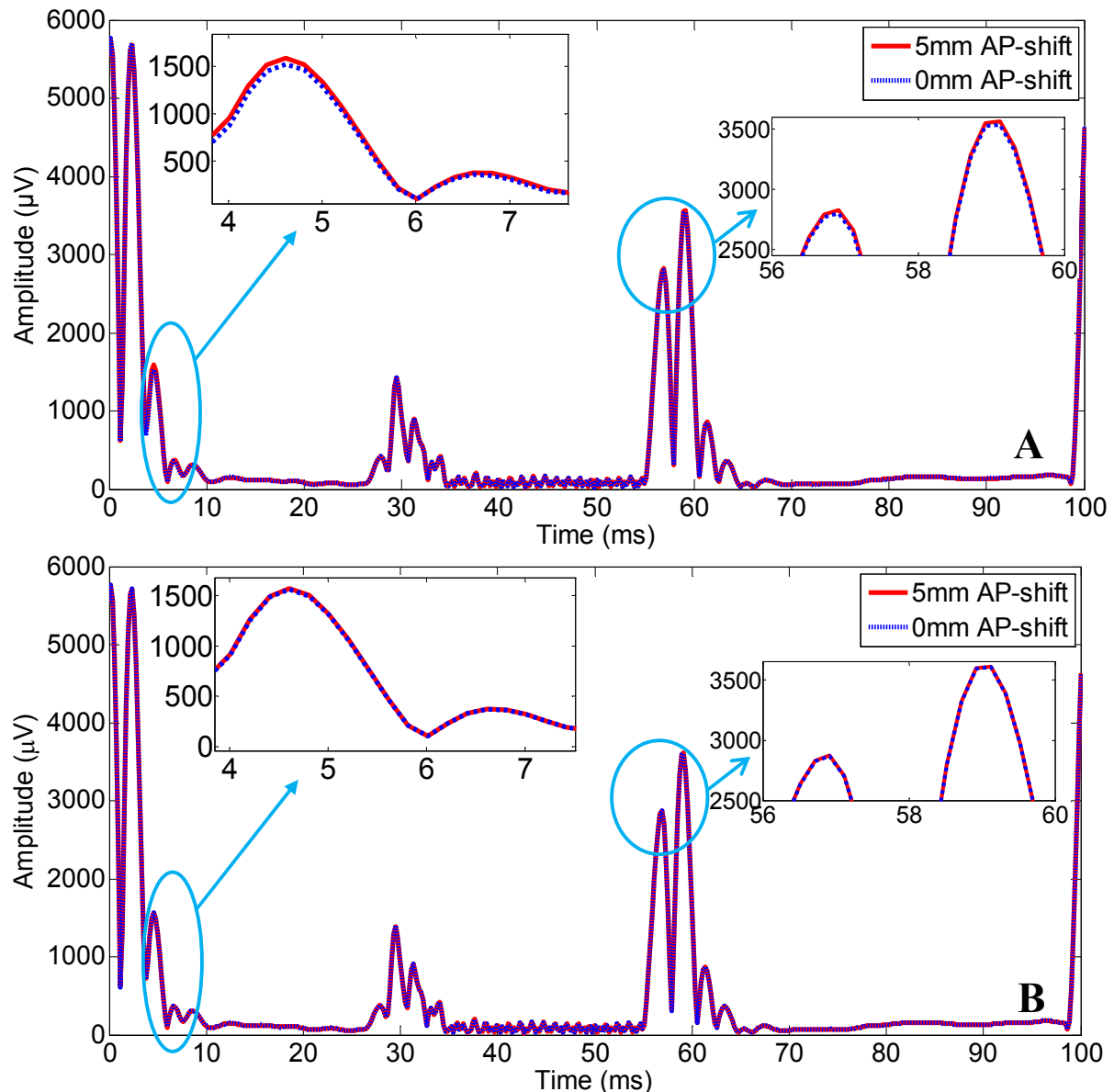


**Figure 5.13** RMS voltage of the average slice artefact averaged across channels for ribbon cable (**A**) & twisted cable (**B**) without (blue solid line) and with (red dashed line) 5-mm shift of cabling in AP direction for the phantom.

cabling are relatively small compared with the overall amplitude of the artefact induced in the system. However, the inserts clearly show differences during the slice select and crusher gradients when the ribbon cable is moved (Figure 5.12 A) with small differences occurring only during the spoiler gradients when the twisted cable is moved (Figure 5.12 B). This is reflected in the larger change in the RMS artefact amplitude observed with the 5mm AP movement when the ribbon cable was used in the set up: 374  $\mu\text{V}$  to 383  $\mu\text{V}$ ; compared to when the twisted cable was employed: 384  $\mu\text{V}$  to 387  $\mu\text{V}$ . Similar results were also observed when the phantom (Figure 5.13), rather than subject, was employed with the RMS amplitude changing from 1054  $\mu\text{V}$  to 1060  $\mu\text{V}$  for the 5 mm AP shift when the ribbon cable was

employed, whereas the change when the twisted cable was used was from 1061  $\mu\text{V}$  to 1062  $\mu\text{V}$ . The RMS artefact amplitude from Fig. 5.12 revealed an overall smaller fractional change in the RMS GA amplitude for the twisted cable than the ribbon cable (4.7 compare with 8.5%) for a 5 mm AP shift in the presence of the EEG cap; in agreement with data collected on the phantom where the percentage change in RMS GA amplitude was 0.7/2.8% for the twisted/ribbon cable with a 5 mm AP shift (Figure 5.13).

## 5.5 Discussion

The GA amplitudes (RMS across leads) for the ribbon cable/twisted cable (AP = 668/232, RL = 83/51, and FH = 645/625  $\mu\text{V}$  respectively) proved that, as expected, the induced GA is larger for the ribbon cable than the twisted cable for all three gradients. The most significant difference in the induced GA between the cables (Fig. 5.4&5.5) was for the AP gradient. This is because the greatest rate of change of flux is generated in the loops of the ribbon cable (which lie in the x-z plane) by the concomitant ( $B_y$ ) field associated with the AP gradient. A linear variation in artefact amplitude with channel number was also observed when the AP gradient was applied to the ribbon cable. This results from the linear increment in loop area with channel number in the ribbon cable.

Figure 5.6 clearly demonstrates that larger differences in the induced voltages are produced by small positional changes when the ribbon cable is employed rather than the twisted cable. Taking the RMS of the voltage changes with position across leads for the ribbon cable/twisted cable, it was found that the twisted cable is less sensitive to changes in GA resulting from AP or FH movement of the cabling between acquisitions. This demonstrates the advantage of using a twisted cable rather than ribbon cable if any movement of the cabling is likely to occur during data acquisition. Subject movement or vibrations caused by the MR scanner can be transferred along the cabling and are the most probable source of cable movement in EEG-fMRI experiments. Therefore these results highlight the importance of ensuring the ribbon cable is fixed to a cantilevered beam to decouple it from subject movement and MR scanner vibrations. If such a set-up cannot be achieved due to practical limitations of the environment then employing a twisted cabled, which is less susceptible to changes in the artefacts due to movement, will be advantageous as the variations in the GA morphology will be minimised allowing the optimal performance of GA correction techniques.

The GA voltages induced in the combination of the cabling and leads on the EEG cap shown in Figure 5.8 appear to be randomly dispersed. However, the pattern observed is due to the wiring configuration on the EEG cap employed here which dominates the artefacts induced in the cables, as expected from previous simulations and experiments (Yan *et al.*, 2009). Figure 5.9C shows that despite the random distribution of artefacts relative to channel number the induced artefacts form a structured spatial pattern. The contribution of the GA induced in the ribbon cable (Fig 5.9B) interacts with that of the cap (Fig 5.9A), and whilst the amplitude of the GA in the ribbon cable is significantly smaller than that produced by the leads in the EEG cap, it is clear that the overall GA induced in the whole EEG system is effected by the presence of the ribbon cable. Therefore the artefacts due to the cabling is likely to be the explanation for previously reported discrepancies between experimental and modelled GA data (Yan *et al.*, 2009).

As previously hypothesised, the greatest changes in the GA induced in the ribbon cable by movements in the AP direction were found to be caused by the FH gradient (Fig. 5.6). This is a consequence of the linear variation with AP position of the concomitant ( $B_y$ ) field that is associated with a FH gradient. However when the movement is in the FH direction the greatest change in the GA induced in the ribbon cable occurs due to the AP gradient. This is a consequence of the linear variation with FH position of the concomitant ( $B_y$ ) field that is associated with the AP gradient.

The interaction of the artefacts induced in the ribbon cable and the EEG cap will be dependent on the design of the EEG cap and the channel numbering of the electrodes and hence wire loops. For example we know that the largest positive voltages from an AP gradient will be produced on channels 1-5 of the ribbon cable (Fig 5.5) and the largest negative voltages from the same gradient interacting with the EEG cap will be produced on the right side of the head (Fig. 5.9A). Therefore to minimise voltages induced by the AP gradient, these channels (1-5) of the ribbon cable should be assigned to the electrodes which are placed on the right side of the head (e.g., FC6, T8, CP6, P8 and TP10 (Figure 2.16)), ensuring the voltages induced in the two components would cancel. Similarly channels 27-32 of the ribbon cable should be assigned to the electrodes placed on the left side of the head (e.g., F7, FC5, T7, TP9 and P7 (Figure 2.16)). By reducing the maximum induced voltage in the EEG system, the dynamic range of the amplifier which is required can also be reduced.

This demonstrates how the presence of the ribbon cable may be advantageous if considered in conjunction with the EEG cap. Therefore, when a new cap is designed these interactions could be used to prevent saturation of amplifier channels.

The effect of artefact cancellation between the cap and ribbon cable was seen to some extent with the cap design used here. Figure 5.11 shows that whilst, on average over all the EEG channels, the artefacts induced by the pre-excursion gradients were smaller when the twisted cable was employed in conjunction with the EEG cap, the fat suppression, slice select and spoiler gradients induced a larger artefact when the twisted cable rather than the ribbon cable was used in conjunction with the EEG cap. This pattern of the effect of the different components of the pulse sequence was despite all aspects of the induced artefact being smaller in the twisted cable than ribbon cable when the signal tester box was used, so that the cabling was the dominant source of the artefact (Figure 5.10). Figure 5.10 shows that the largest reduction in artefact induced in the cabling by using the twisted cable is during the pre-excursion pulse which may explain how the results shown in Figure 5.11 arise. As shown in Figure 2.28 of Chapter 2, the pre-excursion pulse is on the phase encoding axis which for axial EPI slice acquisition is generally the AP gradient. Therefore, the pre-excursion pulse comprises of a large gradient applied in the AP direction which given the findings of the first study explain why this period of the EPI sequence is most affected by the change in cabling.

Despite the interactions between the EEG cap and the cabling making the total induced GA amplitude hard to predict, it is clear from Figure 5.12 and 5.13 that the effect of movement of the cabling still results in smaller GA amplitude changes when the twisted cable rather than the ribbon cable is used. This was reflected in the measured fractional changes in artefact amplitude for the ribbon/twisted cable for the subject (4.7/8.5%) and the phantom (0.7/2.8%). The fractional changes were larger on the subject than the phantom which may be due to a small head movement between data acquisitions in addition to the planned, controlled cable movements. By realigning the EPI images it was possible to assess the degree of movement of the subject, which showed that there was less than 1mm (translation) during each scan period and therefore this is unlikely to be the source of differences between the subject and phantom results. More likely is the fact that the overall RMS amplitude of the GA differed between the phantom (1054  $\mu\text{V}$ ) (Figure 5.13) and subject (374  $\mu\text{V}$ ) (Figure 5.12), probably due to positioning of the phantom/subject. However, despite these slight differences the

overall pattern of the changes in GA amplitude were the same for both the phantom and subject with the largest changes induced by an AP movement occurring during the slice-select and spoiler gradient pulses. As shown in Figure 2.25 of Chapter 2, the slice-select and spoiler gradient pulses are on the slice selection axis and for axial slice acquisition, they are associated with the FH gradient. Therefore, both of these pulses have a large gradient component in the FH direction and are therefore in agreement with our findings from Study 1.

## **5.6 Conclusions**

Here it is shown that the artefacts induced in a ribbon cable are much larger and more sensitive to movement than those of the twisted cable. The high sensitivity to movement of the ribbon cable highlights the need to isolate this cable from all movement by attaching the cabling to a cantilever beam when performing EEG-fMRI experiments. If this is not possible then a twisted cable should be used to attach the EEG cap to the amplifier. Although the changes in amplitude due to movement appear small relative to the total GA, any reduction in the variation of the GA during an fMRI time series is advantageous since residual GA can easily swamp brain signals. A ribbon cable, if isolated from all movement, however, may prove advantageous in reducing the total GA induced in the EEG system. We suggest that through careful design of the EEG cap with consideration of the geometry of the ribbon cable it may be possible to reduce the dynamic range that is required for the amplifiers by cancelling GA contributions in various aspects of the system.

## **5.7 References**

- Bencsik, M., Bowtell, R. and Bowley, R. M. (2007). "Electric fields in the human body by time-varying magnetic field gradients: numerical calculations and correlation analysis." *Phys. Med. Biol.* **52**: 1-17.
- Eichele, T., Moosmann, M., Wu, L., Gutberlet, I. and Debener, S. (2010). Removal of MRI Artifacts from EEG Recordings. In: *Simultaneous EEG and fMRI: Recording, Analysis and Application*. M. Ullsperger and S. Debener. USA Oxford University Press.
- Goldman, R. I., Stern, J. M., Engel, J. and Cohen, M. S. (2002). "Simultaneous EEG and fMRI of the alpha rhythm." *NeuroReport* **13**(18): 2487–2492.



- Laufs, H., Krakow, K., Sterzer, P., Eger, E., Beyerle, A., Salek-Haddadi, A. and Kleinschmidt, A. (2003). "Electroencephalographic signatures of attentional and cognitive default modes in spontaneous brain activity fluctuations at rest." Proceedings Of The National Academy Of Sciences Of The United States Of America **100**(19): 11053-11058.
- Lemieux, L., Salek-Haddadi, A., Josephs, O., Allen, P., Toms, N., Scott, C., Krakow, K., Turner, R. and Fish, D. R. (2001). "Event-related fMRI with simultaneous and continuous EEG: description of the method and initial case report." Neuroimage **14**: 780-787.
- Mandelkow, H., Halder, P., Boesiger, P. and Brandeis, D. (2006). "Synchronisation facilitates removal of MRI artefacts from concurrent EEG recordings and increases usable bandwidth." Neuroimage **32**(3): 1120-1126.
- Mullinger, K. J., Brookes, M. J., Stevenson, C. M., Morgan, P. S. and Bowtell, R. W. (2008a). "Exploring the feasibility of simultaneous EEG/fMRI at 7 T." Magnetic Resonance Imaging **26**(7): 607-616.
- Mullinger, K. J., Morgan, P. S. and Bowtell, R. W. (2008c). "Improved Artefact Correction for Combined Electroencephalography/Functional MRI by means of Synchronization and use of VCG Recordings." Journal of Magnetic Resonance Imaging **27**(3): 607-616.
- Mullinger, K. J., Yan, W. X. and Bowtell, R. W. (2011). "Reducing the Gradient Artefact in Simultaneous EEG-fMRI by Adjusting the Subject's Axial Position." NeuroImage **54**(3): 1942-1950.
- Salek-Haddadi, A., Friston, K. J., Lemieux, L. and Fish, D. R. (2002). "Simultaneous EEG correlated ictal fMRI." Neuroimage **16**: 32-40.
- Yan, W. X., Mullinger, K. J., Brookes, M. J. and Bowtell, R. W. (2009). "Understanding Gradient Artefacts in Simultaneous EEG/fMRI." Neuroimage **46**(2): 459-471.

# Chapter 6

---

*Reference Layer Artefact Subtraction:  
electromagnetic simulations*

## 6.1 Introduction

The cause of the artefacts in EEG data recorded simultaneously with MRI and the methods that have been developed to correct artefacts were described in detail in Chapter 3. It is clear from the previous discussion that problems arise with the implementation of AAS (Allen *et al.*, 1998; Allen *et al.*, 2000) and other techniques for GA and PA correction when subject movement occurs during a study (Allen *et al.*, 2000; Masterton *et al.*, 2007; Jansen *et al.*, 2012). An alternative approach to attenuating the artefacts in EEG data recorded during concurrent fMRI involves making use of reference signals. For example, Bonmassar *et al.*, (2002) used a piezoelectric movement sensor attached to the subject's head to monitor head motion during combined EEG/fMRI experiments. They then applied a linear adaptive filter so as to remove any signal from the EEG recordings that was linearly related to the reference signal from the movement sensor, thus attenuating pulse and movement artefacts. Subsequently, Masterton *et al.* (2007) showed that reference signals recorded from loops of carbon-fibre wire that were physically attached to, but electrically isolated from, the subject's head could similarly be used to ameliorate the PA and MA. This approach relies on the reference signals being similar in form to the artefacts induced in the EEG recordings. Therefore, the above methods are limited in efficacy by the differences between the artefact voltages induced by complex head movement in the combination of the EEG leads and the volume conductor formed by the human head, and the signal from a single motion sensor or the voltages induced in four 10 cm diameter loops of insulated carbon-fibre wire sewn into place upon the outside surface of a neoprene EEG cap attached to the head. These implementations did not address correction of the GA, and more particularly changes in the GA due to head movement.

The reference signal approach was extended to address these issues with the development of the “fEEG” system (Dunseath *et al.*, 2009). This system used an EEG cap incorporating a reference layer (RL), which carries a second set of electrodes and leads that directly overlay those attached to the scalp. The reference layer is electrically conducting (with a similar conductivity to tissue), but is electrically isolated from the scalp so that the electrodes in this layer do not pick up brain signals. Assuming that the current paths formed by the reference layer and associated leads are very similar to those formed by the scalp leads and the head, similar voltages should be recorded from the scalp and reference layer leads in the presence of time-varying magnetic field gradients or head rotation. Consequently taking the difference

of the signals from associated reference layer and scalp leads should cancel out the artefacts, but leave neuronal signals unaltered. In the fEEG system this differencing was implemented in hardware. However, since there are no publications describing the performance of the fEEG system, a number of uncertainties over the efficacy of the reference layer approach remain. In particular, it is not known how similar the artefact voltages induced in a thin reference layer by gradient switching or head rotation are to the voltages produced in the human head by these effects, nor is it clear how comparable the artefacts induced in the leads attached to the reference layer can be made to those produced in the leads attached to the scalp electrodes.

The aim of the work described in this chapter was therefore to simulate the artefacts induced in a hemispherical reference layer and a spherical volume conductor separately by a time-varying magnetic field gradient. This electromagnetic modelling allows us to test the theoretical efficacy of artefact correction that can be achieved by using Reference Layer Artefact Subtraction (RLAS), making the assumption that the voltages induced in leads attached to the associated reference layer and scalp electrodes can be made identical. A series of simulations were carried out on simple spherical volume conductor with isotropic conductivity to evaluate the differences in the voltage produced in the reference layer conductor and volume conductor, while the reference layer and insulating layer geometry parameters were varied. This parameter optimization study was aimed at finding the theoretical optimal design for an RLAS system. Moreover, the effect of head rotation, reference layer slip, head-shift along transverse or longitudinal directions to the optimal design of a reference layer, was also investigated in this study.

## **6.2 Background and Theory**

To characterise the artefacts induced it is necessary to consider the theory relating the electric field induced in a conducting sphere and hemispherical RL to the imposed vector potential, and consequently to the external current distribution, under quasi-static conditions. This is outlined below. Next, this theory is used to evaluate the form and magnitude of the electric field induced in a conducting sphere and RL by perfectly linear, longitudinal and transverse gradients, in the situation where the sphere is centred within the gradient field and also when it is shifted along the transverse or longitudinal directions. In this analysis, the field gradient is defined in terms of a simple analytic form of the vector potential.

### 6.2.1 Maxwell's Equation

For a non-magnetic material such as biological tissue, Maxwell's equations (Griffiths 1981; Jackson 1998) are:

$$\nabla \times \mathbf{B} = \mu_0 \left( \mathbf{J} + \frac{\partial \mathbf{D}}{\partial t} \right) = \mu_0 \left( \mathbf{J} + \varepsilon_0 \varepsilon_r \frac{\partial \mathbf{E}}{\partial t} \right) = \mu_0 \mathbf{J} + \frac{\varepsilon_r}{c^2} \frac{\partial \mathbf{E}}{\partial t} \quad (6.1)$$

$$\nabla \cdot \mathbf{B} = 0 \quad (6.2)$$

$$\nabla \times \mathbf{E} = -\frac{\partial \mathbf{B}}{\partial t} \quad (6.3)$$

$$\nabla \cdot \mathbf{D} = \rho_f(\mathbf{r}, t) \text{ or, } \nabla \cdot \mathbf{E} = \frac{1}{\varepsilon_0 \varepsilon_r} \rho_f(\mathbf{r}, t) \quad (6.4)$$

where  $\rho_f(\mathbf{r})$  is the charge density,  $\mathbf{J}$  is the current density,  $\mu_0$  is the permeability of free space,  $\mathbf{r}$  is the space vector,  $t$  is time and  $\mathbf{D} = \varepsilon_0 \varepsilon_r \mathbf{E}$  is the electric displacement (where  $\varepsilon_0$  is the permittivity for vacuum and  $\varepsilon_r$  is the relative permittivity). The magnetic induction,  $\mathbf{B}$ , and the electric field,  $\mathbf{E}$ , can be written in terms of the scalar and vector potentials  $V(\mathbf{r}, t)$  and  $\mathbf{A}(\mathbf{r}, t)$  as:

$$\mathbf{B} = \nabla \times \mathbf{A}(\mathbf{r}, t) \quad (6.5)$$

and

$$\mathbf{E} = -\nabla V(\mathbf{r}, t) - \frac{\partial \mathbf{A}(\mathbf{r}, t)}{\partial t} \quad (6.6)$$

This electric field  $\mathbf{E}$  generates a current according to Ohm's law  $\mathbf{J} = \sigma \mathbf{E}$  where  $\sigma$  is the conductivity.

### 6.2.2 Quasi-Static Limit

The frequencies,  $\omega/2\pi$  (where  $\omega$  is the angular gradient switching frequency), present in the gradient waveforms used in MRI are generally less than 10 kHz (Bowtell *et al.*, 2000; Bencsik *et al.*, 2002) and the average conductivity of biological tissue is  $\sigma \approx 0.2 \text{ S m}^{-1}$  (Bencsik *et al.*, 2007; Glover *et al.*, 2008; Glover 2009), therefore the system can be regarded as quasi-static which allows us to make the following assumptions:

- Suppose the fields change on a time scale of  $10^{-4}$  s (Bowtell *et al.*, 2000; Sánchez *et al.*, 2012). The time taken for an electromagnetic wave to travel through the head is much less than the gradient reversal period ( $2\pi/\omega$ ) which is of the order of  $10^{-4}$  s. Under these circumstances it is a good approximation to ignore the propagation effects in these systems.
- The skin depth at the gradient frequencies is much larger than the diameter of the head. The large ratio of skin depth to head diameter means that the current induced

inside the head is not sufficient to perturb the externally applied magnetic fields. Therefore it is a good approximation to ignore the contribution to the vector potential arising from the currents in the head.

- The ratio of the displacement to conduction current is of order  $\omega\varepsilon/\sigma$ . In general the permittivity,  $\varepsilon = \varepsilon_0\varepsilon_r$  of biological tissues varies with frequency, changing from about  $10^{-7}$  at 10 kHz to  $10^{-5}$  at 10 Hz. Over this frequency range  $\omega\varepsilon/\sigma$  varies from  $10^{-2}$  to  $10^{-3}$ . Therefore, at such frequencies, displacement currents will be approximately two orders of magnitude smaller than conduction currents.

The assumptions above are explored in detail in (Bowtell *et al.*, 2000; Sánchez *et al.*, 2012). With these approximations, displacement current can be neglected and all the current densities in the system,  $\mathbf{J}(\mathbf{r}, t)$ , can therefore be thought of as arising from conduction.

### 6.2.3 Boundary Conditions

At first sight there appears to be no source of the scalar potential since there is no net charge on the body. However, as shown below, the changing magnetic field induces an electromagnetic potential (EMF) that separates charges, which accumulate on the surface. The amplitude and sign of the charges vary with surface position. These surface charges produce a scalar potential.

Taking the divergence of the Maxwell equation  $\nabla \times \mathbf{B} = \mu_0(\mathbf{J} + \frac{\partial \mathbf{D}}{\partial t})$  gives,

$$\nabla \cdot (\nabla \times \mathbf{B}) = \mu_0 \nabla \cdot \left( \mathbf{J} + \frac{\partial \mathbf{D}}{\partial t} \right) \quad (6.7)$$

The divergence of a curl of any vector field is zero, i.e.,  $\nabla \cdot (\nabla \times \mathbf{B}) = 0$  therefore Eq. (6.7) can be written:

$$\nabla \cdot \left( \mathbf{J} + \frac{\partial \mathbf{D}}{\partial t} \right) = 0 \quad (6.8)$$

This implies that the component of  $(\mathbf{J} + \frac{\partial \mathbf{D}}{\partial t})$  which is normal to the boundary of the sphere can deposit charge there, giving rise to a surface charge density; the surface charge density generates a scalar potential which acts to reduce the electric field; the electric field component normal to the boundary then decays exponentially with time constant  $\tau = \varepsilon_0\varepsilon_r/\sigma$ , for a sufficiently low frequency of oscillation,  $\omega$ ,  $\omega\tau \ll 1$  it can therefore be assumed that the normal component of the electric field at the boundary is zero. This situation corresponds to the quasi-static approximation of Maxwell's equations (Bowtell *et al.*, 2000; Bencsik *et al.*, 2002; Liu *et al.*, 2003; Bencsik *et al.*, 2007) which is used below.

### 6.2.4 Problem Formulation

Since  $\nabla \times \mathbf{B} = 0$  still holds,  $\mathbf{B}$  can be defined in terms of a vector potential,  $\mathbf{A}$  (Griffiths 1981; Jackson 1998):

$$\mathbf{B} = \nabla \times \mathbf{A} \quad (6.9)$$

Then Faraday's law (6.3) can be written  $\nabla \times \mathbf{E} = -\frac{\partial \mathbf{B}}{\partial t} = -\frac{\partial(\nabla \times \mathbf{A})}{\partial t} = -\nabla \times \frac{\partial \mathbf{A}}{\partial t}$

$$\nabla \times \left( \mathbf{E} + \frac{\partial \mathbf{A}}{\partial t} \right) = 0 \quad (6.10)$$

This means that the quantity with vanishing curl in (6.9) can be written as the gradient of some scalar function, namely, a *scalar potential*  $\Phi$  (Griffiths 1981; Jackson 1998),

$$\mathbf{E} + \frac{\partial \mathbf{A}}{\partial t} = -\nabla \Phi \quad (6.11)$$

or

$$\mathbf{E} = -\frac{\partial \mathbf{A}}{\partial t} - \nabla \Phi \quad (6.12)$$

$\mathbf{E}$  comprises two components, the field due to varying potentials within the body,

$$\mathbf{E}_{grad} = -\nabla \Phi$$

and a component induced by the external time varying magnetic field, governed by Faraday's law

$$\mathbf{E}_{induced} = -\frac{\partial \mathbf{A}}{\partial t}$$

Equation (6.8) can be re-written as,

$$\nabla \cdot \mathbf{J} + \frac{\partial(\nabla \cdot \mathbf{D})}{\partial t} = 0 \quad (6.13)$$

Substituting Eq. (6.4) in above equation results,

$$\nabla \cdot \mathbf{J} + \frac{\partial \rho_f(\mathbf{r}, t)}{\partial t} = 0 \quad (6.14)$$

The *divergence theorem* (*Gauss's theorem or Green's theorem*) (Griffiths 1981; Jackson 1998) states that for any well behaved vector field,  $\mathbf{A}(\mathbf{x})$ , defined within a volume,  $V$ , surrounded by the closed surface,  $S$ , the relation

$$\oiint \mathbf{A} \cdot d\mathbf{S} = \int_V \nabla \cdot \mathbf{A} \, d^3x \quad \text{or} \quad \oiint \mathbf{A} \cdot \mathbf{n} \, da = \int_V \nabla \cdot \mathbf{A} \, d^3x \quad (6.15)$$

holds between the volume integral of the divergence of  $\mathbf{A}$  and the surface integral of the outwardly directed normal component of  $\mathbf{A}$  ( $\mathbf{n}$  is the vector orthogonal to the surface,  $S$ ).

Equation (6.14) can be re-written as,

$$\int_v (\nabla \cdot \mathbf{J}) d^3x = -\int_v \frac{\partial \rho_f(\mathbf{r}, t)}{\partial t} d^3x \quad (6.16)$$

Now the divergence theorem allows us to write Eq. (6.16) as

$$\oint \mathbf{J} \cdot d\mathbf{S} = -\int_v \frac{\partial \rho_f(\mathbf{r}, t)}{\partial t} d^3x = -\frac{\partial}{\partial t} (\int_v \rho_f(\mathbf{r}, t) d^3x) \quad (6.17)$$

or

$$\oint \mathbf{J} \cdot d\mathbf{S} = -\frac{\partial Q}{\partial t} \quad (6.18)$$

This equation shows us that the sum of the current densities normal to the surfaces of a closed volume is equal to the variation of the charge inside that volume.

In the quasi static approximation limit (Antunes *et al.*, 2012), the Eq. (6.18) becomes

$$\oint \mathbf{J} \cdot d\mathbf{S} = 0 \quad (6.19)$$

Given that  $\mathbf{J} = \sigma \mathbf{E}$  Equation (6.19) can be re-written in the quasi static approximation limit,

$$\oint \sigma \mathbf{E} \cdot d\mathbf{S} = 0 \quad (6.20)$$

$$\text{Or, } \oint \sigma (\mathbf{E}_{grad} + \mathbf{E}_{induced}) \cdot d\mathbf{S} = 0 \quad (6.21)$$

Using Eq. (6.12), Eq. (6.22) can be re-written as

$$\oint \sigma \left( -\frac{\partial A}{\partial t} - \nabla \Phi \right) \cdot d\mathbf{S} = 0 \quad (6.22)$$

where the infinitesimal area element,  $d\mathbf{S} = da \cdot \mathbf{n}$ , the time derivative of the vector potential,  $\frac{\partial A}{\partial t}$ .

This is the governing equation subject to the boundary condition that the component of the current density (and, therefore, the E-field) normal to the surface of the conductive object is zero. This relationship can be solved for the scalar potential using a finite difference approximation method. The basic idea is to break the volume to be modelled into a cuboidal array of  $N_p$  cells (also described as volume elements).



Here, the computational space has been divided into a large number of cubic cells, with a single value of electrical conductivity per cell and then Eq. (6.22) is approximated for each elementary cell. After discretization and rearrangement (Liu *et al.*, 2003,2003; Li *et al.*, 2007; Antunes *et al.*, 2012), the scalar potential for cell (i, j, k) can be expressed as

$$\Phi_{i,j,k} = \frac{\sum_{m=0}^1 (\Phi_{i+m,j,k} \sigma_{i+m,j,k}^a + \Phi_{i,j+m,k} \sigma_{i,j+m,k}^a + \Phi_{i,j,k+m} \sigma_{i,j,k+m}^a) - f(\mathbf{E}_{induced})h}{\sum_{m=0}^1 (\sigma_{i+m,j,k}^a + \sigma_{i,j+m,k}^a + \sigma_{i,j,k+m}^a)} \quad (6.23)$$

where  $f(\mathbf{E}_{induced})$  is defined as

$$f(\mathbf{E}_{induced}) = \sum_{m=0}^1 \left( \begin{aligned} & \left( \sigma_{i+m,j,k}^a \frac{\partial A}{\partial t(i+m,j,k)} \right) \cdot \hat{S}_x^m + \\ & \left( \sigma_{i,j+m,k}^a \frac{\partial A}{\partial t(i,j+m,k)} \right) \cdot \hat{S}_y^m + \\ & \left( \sigma_{i,j,k+m}^a \frac{\partial A}{\partial t(i,j,k+m)} \right) \cdot \hat{S}_z^m \end{aligned} \right) \quad (6.24)$$

in which  $i, j, k$  indicate the cell index,  $m$  indicates two faces (represented by “0, 1”) in  $x, y, z$  directions, respectively,  $\hat{S}$  is the unit vector normal to the cell faces and  $h$  is the cell size,  $\sigma^a$  is the local average conductivity.

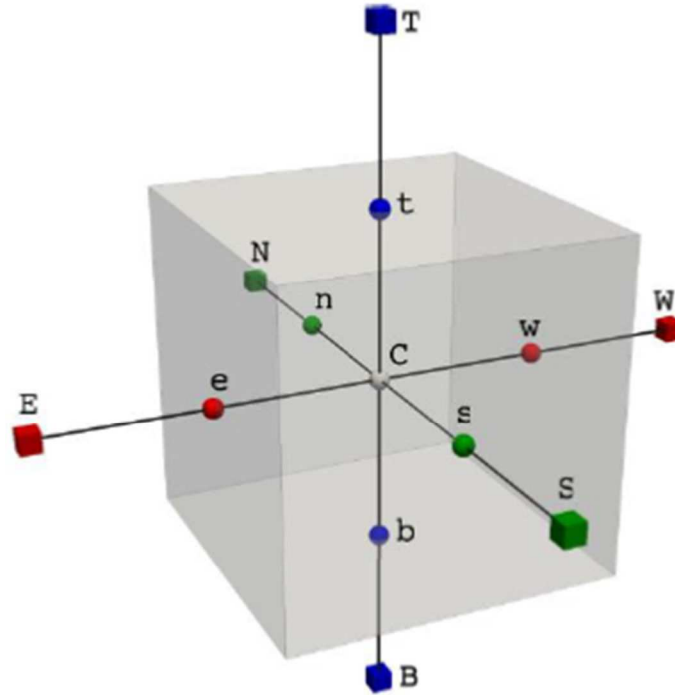


**Figure 6.1** Illustration of a cubic volume element with the notation used for cell faces.

Hence the value of the potential in a certain cell depends on the potentials and conductivities of its 6 immediate neighbours, and on a separate term which depends on the external field. For points centred on each of the faces the subscripts  $e, w, s, n, b, t$  will be used (standing for east, west, south, north, bottom, top). For points centred on the adjacent voxels,  $E, W, S, N, B,$

$T$  will be used.  $C$  is the centre point of the voxel. The discretization of the spatial derivatives using a central difference scheme holds (Zhang 1995; Liu *et al.*, 2003; Li *et al.*, 2007):

$$\left(\frac{\partial \Phi}{\partial x}\right)_e \approx \left(\frac{\Phi_E - \Phi_C}{\Delta x}\right) \quad (6.25)$$

$$\left(\frac{\partial \Phi}{\partial y}\right)_n \approx \left(\frac{\Phi_N - \Phi_C}{\Delta y}\right) \quad (6.26)$$

$$\left(\frac{\partial \Phi}{\partial z}\right)_t \approx \left(\frac{\Phi_T - \Phi_C}{\Delta z}\right) \quad (6.27)$$

The remaining components of the gradient are ignored since they are orthogonal to  $\mathbf{n}$  in the case of the discretization with cuboids.

From Eq. (6.22), using these relations (Liu *et al.*, 2003)

$$\begin{aligned} & \sigma_e \left(\frac{\partial A_x}{\partial t}\right)_e \Delta y \Delta z + \sigma_e \left(\frac{\Phi_E - \Phi_C}{\Delta x}\right) \Delta y \Delta z \\ & - \sigma_w \left(\frac{\partial A_x}{\partial t}\right)_w \Delta y \Delta z + \sigma_w \left(\frac{\Phi_W - \Phi_C}{\Delta x}\right) \Delta y \Delta z \\ & + \sigma_n \left(\frac{\partial A_y}{\partial t}\right)_n \Delta x \Delta z + \sigma_n \left(\frac{\Phi_N - \Phi_C}{\Delta y}\right) \Delta x \Delta z \\ & - \sigma_s \left(\frac{\partial A_y}{\partial t}\right)_s \Delta x \Delta z + \sigma_s \left(\frac{\Phi_S - \Phi_C}{\Delta y}\right) \Delta x \Delta z \\ & + \sigma_t \left(\frac{\partial A_z}{\partial t}\right)_t \Delta x \Delta y + \sigma_t \left(\frac{\Phi_T - \Phi_C}{\Delta z}\right) \Delta x \Delta y \\ & - \sigma_b \left(\frac{\partial A_z}{\partial t}\right)_b \Delta x \Delta y + \sigma_b \left(\frac{\Phi_B - \Phi_C}{\Delta z}\right) \Delta x \Delta y = 0 \end{aligned} \quad (6.28)$$

The  $\Delta y \Delta z$ ,  $\Delta x \Delta z$ ,  $\Delta x \Delta y$  elements correspond to the orthogonal infinitesimal area element  $dS$ .

The above equation can be rewritten if the following substitutions are made

$$\begin{aligned} \beta_e &= \sigma_e \frac{\Delta y \Delta z}{\Delta x}, \beta_w = \sigma_w \frac{\Delta y \Delta z}{\Delta x}, \beta_n = \sigma_n \frac{\Delta x \Delta z}{\Delta y}, \beta_s = \sigma_s \frac{\Delta x \Delta z}{\Delta y}, \\ \beta_t &= \sigma_t \frac{\Delta x \Delta y}{\Delta z}, \beta_b = \sigma_b \frac{\Delta x \Delta y}{\Delta z} \end{aligned}$$

and the Eqn. (6.28) becomes

$$-(\beta_e + \beta_w + \beta_n + \beta_s + \beta_t + \beta_b) \Phi_C + \beta_e \Phi_E + \beta_w \Phi_W + \beta_n \Phi_N + \beta_s \Phi_S + \beta_t \Phi_T + \beta_b \Phi_B = \Psi \quad (6.29)$$

where  $\Psi = \sigma_e \left(\frac{\partial A_x}{\partial t}\right)_e \Delta y \Delta z - \sigma_w \left(\frac{\partial A_x}{\partial t}\right)_w \Delta y \Delta z + \sigma_n \left(\frac{\partial A_y}{\partial t}\right)_n \Delta x \Delta z$

$$- \sigma_s \left(\frac{\partial A_y}{\partial t}\right)_s \Delta x \Delta z + \sigma_t \left(\frac{\partial A_z}{\partial t}\right)_t \Delta x \Delta y - \sigma_b \left(\frac{\partial A_z}{\partial t}\right)_b \Delta x \Delta y \quad (6.30)$$

Here  $\sigma_i$  corresponds to the conductivity at the cell face and this is given by

$$\sigma_e = \frac{2\sigma_E \sigma_C}{\sigma_E + \sigma_C} \quad (6.31)$$

for the east face and similarly for the other faces.

Application of Eq. (6.29) to all the elements of the discretized mesh gives rise to a linear system of equations (Liu *et al.*, 2003) that can be represented as

$$\mathbf{C}\mathbf{x} = \mathbf{b} \quad (6.32)$$

where  $\mathbf{x}$  is a vector of potentials to be solved for,  $\mathbf{b}$  is a vector dependent on the external field, and  $\mathbf{C}$  is a sparse matrix (Antunes *et al.*, 2012) (the total size of the problem is,  $N_p = N_x \times N_y \times N_z$  where  $N_x$ ,  $N_y$  and  $N_z$  represent the number of voxels in the respective dimensions) containing the conductivity and connectivity information for each of the element's surfaces and. Here,  $\mathbf{C}$  contains the terms relating to  $\beta_i$  and  $\mathbf{b}$  contains the terms relating to  $\Psi$  which represents the source current distribution and magnitudes, and  $\mathbf{x}$  is the potential,  $\Phi$ .

### 6.2.5 Analytic expressions for the Magnetic field and Vector potential

The vector potential,  $\mathbf{A}$  can be calculated from a gradient coil's wire paths (Bowtell *et al.*, 2000; Bencsik *et al.*, 2002; Bencsik *et al.*, 2007; Glover *et al.*, 2007), but for combined EEG/fMRI the head is usually positioned in the gradient coil's region of homogeneity, so that simple analytic expressions for the magnetic field and vector potential, corresponding to pure gradients, has described by Bencsik *et al.*, (2002) and Yan *et al.*, (2009), can be employed. In the following, we consider the effect of perfect transverse and longitudinal gradients with the main field ( $B_0$ ) directed along the  $z$ -axis.

#### Transverse (x) gradient:

In the case of a sphere centred at the origin of an x-gradient coil, the vector potential can be expressed, using the Coulomb gauge ( $\nabla \cdot \mathbf{A} = 0$ ), as:

$$\mathbf{A}_x = -\frac{1}{2}G_xxy\mathbf{i} + \frac{1}{4}G_x(x^2 - y^2)\mathbf{j} + G_xyz\mathbf{k} \quad (6.33)$$

where  $G_x$  is the field gradient strength.

$$\mathbf{B}_x = G_xz\mathbf{i} + G_xx\mathbf{k} \quad (6.34)$$

Let us also consider the *case of a transversally shifted sphere* where  $x_0$  denotes the shift along the  $x$ -axis then the vector potential becomes:

$$\mathbf{A}_x = -\frac{1}{2}G_x(x - x_0)y\mathbf{i} + \frac{1}{4}G_x((x - x_0)^2 - y^2)\mathbf{j} + G_xyz\mathbf{k} \quad (6.35)$$

In the *case of the longitudinally shifted sphere* by a distance  $z_0$  along the  $z$ -axis, the vector potential is modified to:

$$\mathbf{A}_x = -\frac{1}{2}G_xxy\mathbf{i} + \frac{1}{4}G_x(x^2 - y^2)\mathbf{j} + G_xy(z - z_0)\mathbf{k} \quad (6.36)$$

**Longitudinal (z) gradient:**

In the case of a sphere centred at the origin of the gradient coils then the vector potential can be expressed as:

$$\mathbf{A}_z = -\frac{1}{2}G_z yz\mathbf{i} + \frac{1}{2}G_z xz\mathbf{j} \quad (6.37)$$

where  $G_z$  is the field gradient strength in the  $z$ -direction.

$$\mathbf{B}_z = -\frac{1}{2}G_z x\mathbf{i} - \frac{1}{2}G_z y\mathbf{j} + G_z z\mathbf{k} \quad (6.38)$$

*Case of the transversally shifted sphere:*

In the case of a sphere that has been transversally shifted by a distance  $x_0$  along the  $x$ -axis, the new vector potential can be written as

$$\mathbf{A}_z = -\frac{1}{2}G_z yz\mathbf{i} + \frac{1}{2}G_z(x - x_0)z\mathbf{j} \quad (6.39)$$

We also consider a case of the sphere shifted longitudinally by a distance,  $z_0$ , along the  $z$ -axis. Again, for simplicity the field gradient was chosen to shift rather than the sphere, by writing

$$\mathbf{A}_z = -\frac{1}{2}G_z y(z - z_0)\mathbf{i} + \frac{1}{2}G_z x(z - z_0)\mathbf{j} \quad (6.40)$$

**6.3 Modelling & Methods**

A homogeneous, spherical volume conductor (VC) of 0.08m radius (mimicking the size of a human head) was used as a model system for the purpose of calculating the electric fields induced in the human head by externally applied time-varying magnetic fields gradients. A hemispherical hollow conductor with a finite thickness and similar conductivity as the spherical VC was used as the reference layer (RL) conductor. A finite volume method ( $N_p = 408 \times 408 \times 408$  voxels, at 0.5mm resolution), based on the quasi-static approximation of Maxwell's equations given by Eq. (6.29) was used in conjunction with an analytic form of the driving vector potential described in Section 6.2.5. The resulting linear system of equations given by Eq. (6.32) was solved using the biconjugate gradient stabilized method, often abbreviated as BiCGSTAB algorithm (van der Vorst 1992). This is an iterative method developed by H. A. van der Vorst for the numerical solution of nonsymmetric linear systems. It is a variant of the biconjugate gradient method (BiCG) and has faster and smoother convergence than the original BiCG.

In this study, the conductivity,  $\sigma$ , and the time derivative of the vector potential  $\frac{\partial A}{\partial t}$  are known. Therefore, the unknown scalar potential,  $\Phi$  can be calculated using  $\sigma$  and  $\frac{\partial A}{\partial t}$ . The finite volume method adopted for the volume discretization ensured that the continuity equation was satisfied for each voxel, and that each element only connects to its six nearest neighbours, turning  $C$  into a very sparse matrix, with all elements stored in seven diagonals. Once the equations have been solved for  $\Phi$ , the current density can be found by taking  $\mathbf{J} = -\sigma \nabla \Phi$ . The BiCGSTAB algorithm's stopping criterion for convergence was a residual less than  $10^{-10}$ . The algorithm execution is highly parallelizable, so C++ code (Antunes *et al.*, 2012) was used to take advantage of this feature.

We evaluated the peak voltage generated by a realistic transverse (right-left) gradient of  $10\text{mTm}^{-1}$  amplitude varying at  $1\text{kHz}$  ( $dG/dt_{peak} = 62\text{Tm}^{-1}\text{s}^{-1}$ ) on the surface of the volume and reference layer conductors at 33 electrode locations, defined by the extended 10/20 system (VC at isocentre and electrode Cz positioned on  $z$ -axis). To minimise the separation between electrodes positioned on the VC and RL, the electrode locations were modelled to be on the outer surface of the spherical VC and on the inner surface of the RL conductor. However, in a practical implementation, the electrodes have to be on the outer surface of the VC and the inner surface of the RL.

The RL geometry (Fig. 6.2), defined by the reference layer thickness (RLT), insulating layer thickness (ILT) and reference layer angular extent (RLAE) [ $90^\circ$ =hemisphere;  $180^\circ$ =sphere], was varied to identify an optimal RL design. The inner radius of the RL depends on the ILT and the depth and separation of the VC and RL electrodes. The effect of angling the head (through a nodding movement) was evaluated by rotating the whole RLAS system about the  $x$ -axis, while the effect of the RL slipping over the scalp was imitated by rotating the RL and associated sampling points, while the VC and its sampling points were not rotated.

## 6.4 Analysis

The calculation of  $\frac{\partial A}{\partial t}$  and the scalar potential are the time-consuming elements of the computation in this analytical study. At the problem size ( $408 \times 408 \times 408$  voxels, at  $0.5\text{ mm}$  resolution) chosen in this work, the calculation typically takes approximately 3 hours on a Core 2 Duo @  $3\text{GHz}$  64-bit Windows machine (8 GB RAM installed), but this time reduces

to 22 min when a Linux compiled version and GPU with 8 GB Memory, is used. The calculation of the scalar potential, electric field and current density using the C++ code on a Windows machine takes approximately 3 hours and 20 mins to execute, whereas the CPU with GPU takes 35 minutes to converge. It is worth mentioning here that calculating the scalar potential alone or calculating the scalar potential along with the electric field and current density did not increase the computation time significantly. It was found to be easier to study the effect of shifting the RLAS system in the volume of the gradient coil, by translating the gradient rather than moving the RLAS system itself.

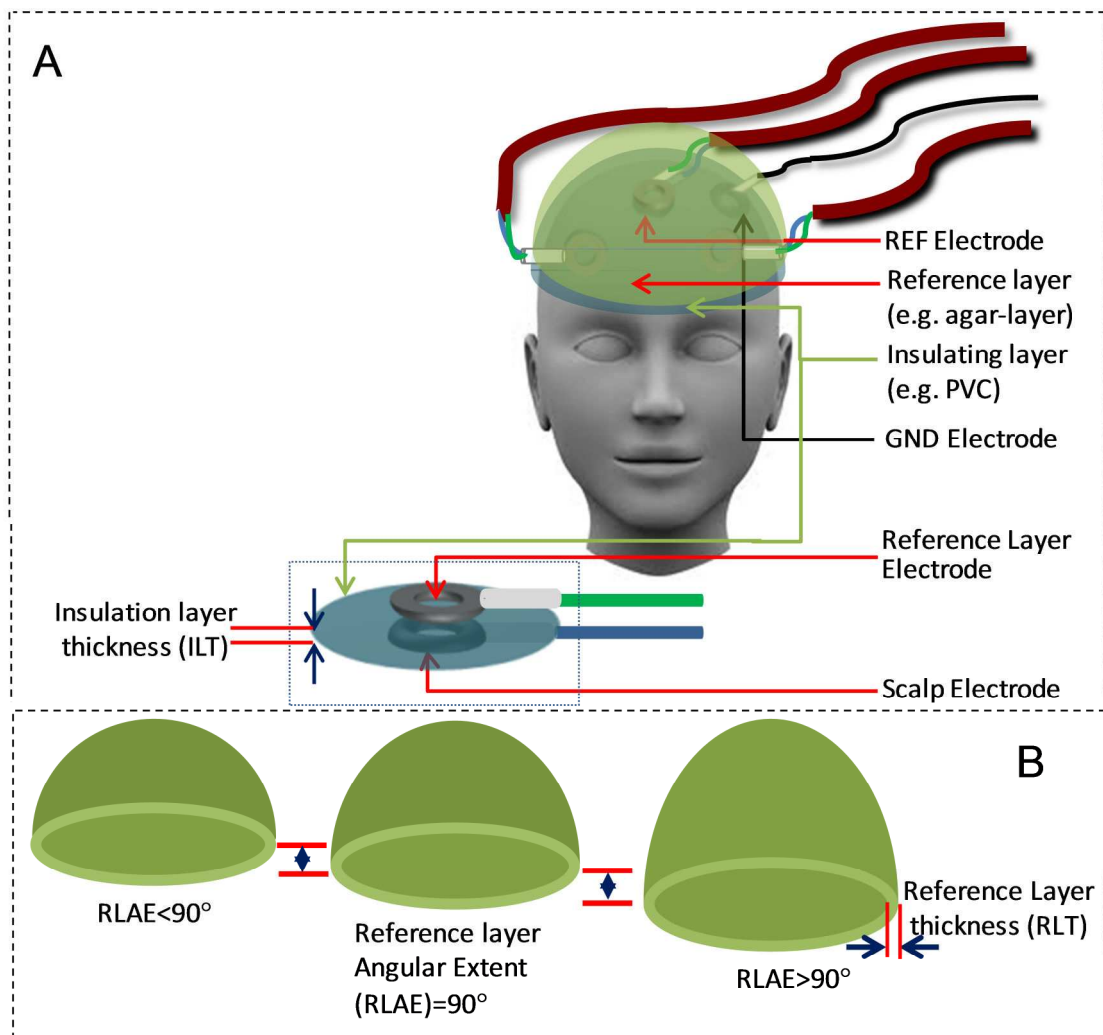


**Figure 6.2** Schematic representations of the RLAS system experimental setup (A) and RLAS parameters (B). Proposed electrode set-up on scalp and reference layer with insulating layer separating the electrodes (insert (A)).

In-house written MATLAB (The MathWorks) code was used to generate  $\frac{\partial A}{\partial t}$  and the conductivity map and C++ code was used to calculate the scalar potential,  $\Phi$ , electric field,  $E$ , and current density,  $J$ . For calculating the induced voltage at the 33 locations (31 electrode

locations, REF, GND) on the two conductors and for further quantification, in-house written MATLAB code was used. To implement RLAS, the RL and VC electrode voltages were re-referenced with respect to the reference channel used in the respective conductors. The potential values at the REF electrode locations on both conductors were used for re-referencing the potentials measured at the 31 locations on the respective conductor. For each case the voltages at the VC and RL electrodes were found and the difference calculated. The RMS amplitudes of the voltage difference and the voltage at the VC electrodes were also calculated. Brain Vision Analyzer 2 (Version 2.0.1; Brain Products, Munich, Germany) and MATLAB were used for producing artefact map using the RMS amplitudes of the voltage difference and voltage at the VC and RL electrodes.

## 6.5 Preliminary Experiments

These experiments were designed to find the voltages induced in the realistic RLAS set-up by time-varying transverse and longitudinal magnetic field gradients in order to see whether the RLAS idea was viable. In these preliminary experiments, the reference layer and insulating layer parameters were set as follows:  $RLT=5\text{mm}$ ,  $ILT=1\text{mm}$  and  $RLAE=90^\circ$ .

- **Transverse (x) gradient:** Firstly, a simulation was carried out to determine whether the voltages induced in a spherical VC and a hemispherical RL separately by a time-varying transverse magnetic field gradient are similar. Secondly, a realistic RLAS set-up was mimicked by modelling the head as a homogeneous spherical VC which was separated from the hemispherical RL by a thin insulating layer (Fig. 6.2) while a transverse field gradient was applied. This allowed the evaluation of the feasibility of the RLAS technique for artefact correction. In addition the effect on the measured gradient artefact voltages of  $1^\circ/2^\circ$  mismatch between sample locations on the VC and the RL was also tested.
- **Longitudinal (z) gradient:** With the spherical head model positioned so that its centre lay on the  $z$ -axis in the magnetic field's frame of reference, in theory no gradient artefact should be generated by a temporally varying longitudinal gradient. This is because with such an arrangement the vector potential seen by the sphere is purely azimuthal. Consequently the scalar potential,  $\Phi$ , is zero (Bencsik *et al.*, 2002) since the radial component of  $\frac{\partial A}{\partial t}$ , that is normal to the

surface of the sphere is zero. This geometry was simulated as a test of the efficacy of the software.

## 6.6 Preliminary Results

Figures 6.3A&B show the potential distributions produced by a time-varying transverse magnetic field gradient applied to a hemispherical RL and spherical VC while the centres of the VC and RL lie on the z-axis. The strong similarity of the artefact voltages on the surface of the two conductors (which forms the basis of RLAS) is evident.

To compare these results with previous work (Yan *et al.*, 2009) that used similar computational analysis, the potential distributions at the electrode positions were mapped onto a head shape using Brain Vision Analyzer 2. As expected Fig 6.4A&B show strong similarity. Fig 6.4B shows the resultant artefact map when a transverse gradient is applied to the VC, which is in line with the results obtained by Yan et al. (2009). The artefact maps of the induced voltages due to a time-varying transverse gradient for a realistic RLAS set-up on the VC and RL and the difference between the voltages on the RL and VC are shown in Fig. 6.4A, B and C, respectively. The RMS over the 31 electrode positions of the potential induced on the VC and RL, with RLT=5 mm, ILT=1 mm and RLAE=90°, took values of 3248  $\mu\text{V}$  and 3486  $\mu\text{V}$  respectively. Subtraction of the VC voltages from the RL voltages produced a large attenuation of 25 dB (RMS=183  $\mu\text{V}$ ) of the induced gradient artefact. This figure also shows the re-referenced artefact map for the difference (Fig. 6.4C) in the induced voltages

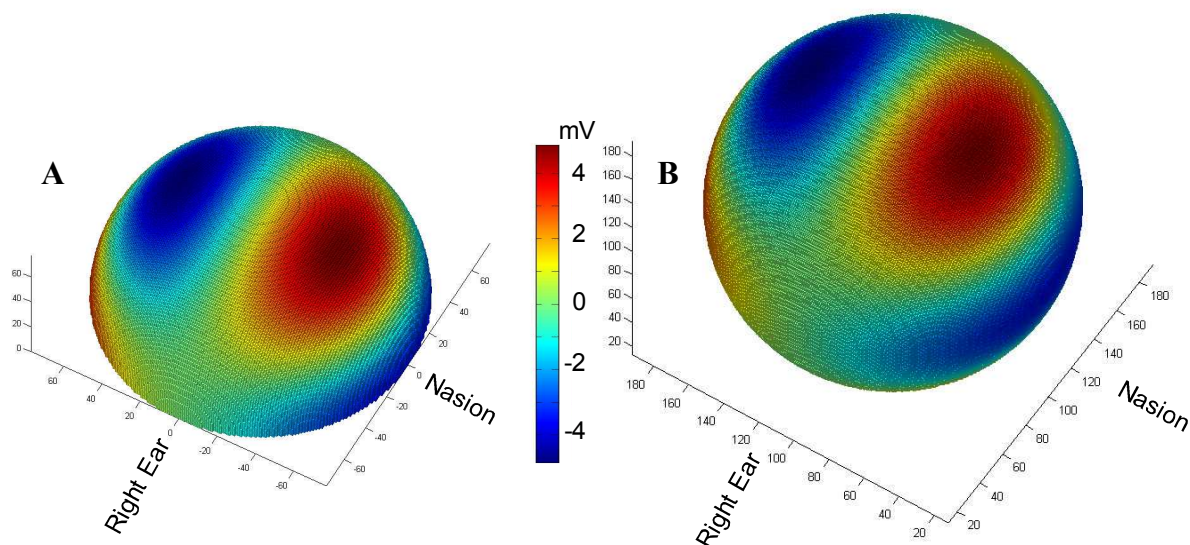


**Figure 6.3** Potential distribution due to a time-varying a transverse magnetic field for a hemi-spherical conducting RL (A) and spherical VC (B) for RLT=5 mm, ILT=1 mm and RLAE=90°.



between the RL and VC. The difference plot indicates the electrodes which measure the largest induced voltages provide the largest contribution to the artefact discrepancy between VC and RL, with the posterior electrodes exhibiting the largest residual artefact for the transverse gradient.

Given the close agreement between the RL and VC voltages (as shown in Fig. 6.4) it is unsurprising that a small mismatch between sample locations produces a large difference in the measured artefact voltages. A  $1^{\circ}/2^{\circ}$  of mismatch increased the residual RMS from  $183 \mu\text{V}$  (no mismatch) to  $232 \mu\text{V}/427 \mu\text{V}$ , respectively. This result clearly demonstrates that the sampling locations must overlay precisely.

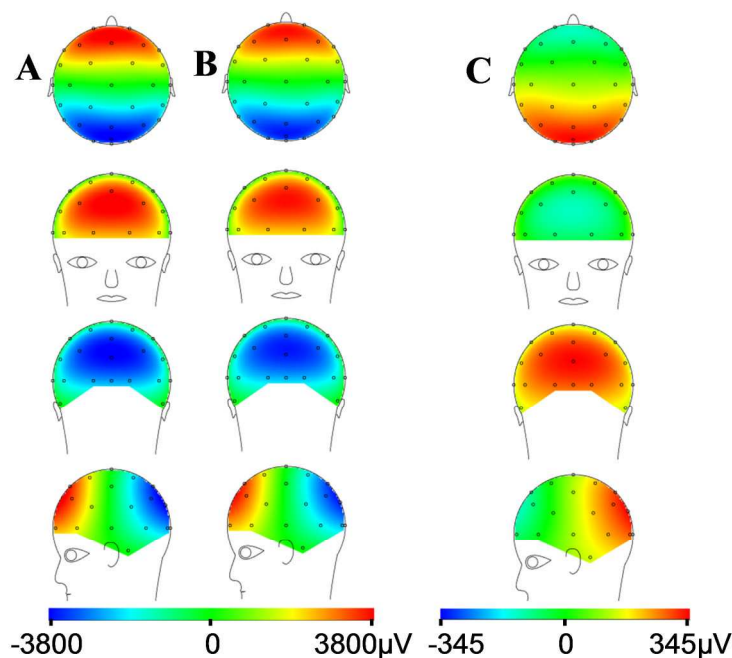


**Figure 6.4** Artefact map for RL(A) and VC(B) and the difference (C) in induced voltages between the VC and RL for  $RLT=5 \text{ mm}$ ,  $ILT=1 \text{ mm}$  and  $RLAE=90^{\circ}$ .

Figure 6.5 shows maps of the induced voltages on the VC and RL for a time-varying longitudinal gradient for a realistic RLAS set-up centred in the gradient, along with the difference in voltages on the RL and VC. As expected, the contribution of the induced voltages from the longitudinal gradient was minimal with the RMS of the potential induced on the VC and RL and of the difference in between the potentials on the RL and VC taking values of 3, 16 and  $13 \mu\text{V}$ , respectively. This result confirms the theory that little artefact is induced by the longitudinal gradient for a centred spherical VC. However, the non-zero RMS potential for the VC in this gradient and the potential mapping observed in RL indicates the minor imperfections in the calculations.

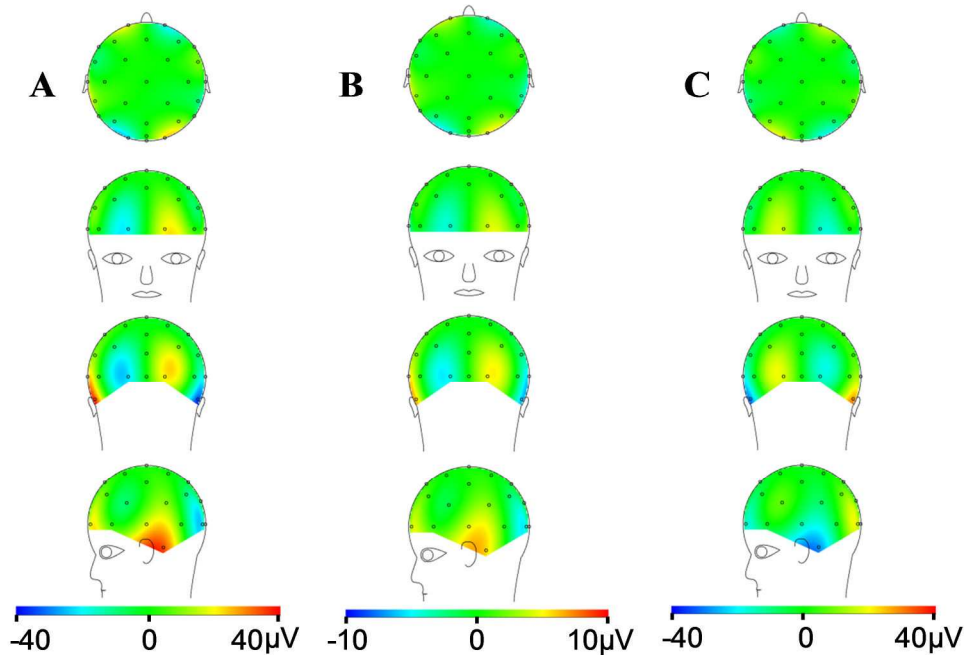


**Figure 6.5** Artefact map for RL(A) and VC(B) and the difference (C) in induced voltages between the VC and RL for  $RLT=5$  mm,  $ILT=1$  mm and  $RLAE=90^\circ$  due to a time-varying longitudinal magnetic field gradient.

The results of these preliminary experiments indicate that RLAS could be a useful artefact reduction technique if the RL and insulating layer parameters are optimized. Given the nearly zero artefact voltages produced by the longitudinal gradient, for the rest of the experiments only the gradient artefact contributions from a transverse gradient will be considered.

## 6.7 Optimization Experiments

These experiments, which were carried out with the VC and RL (separated by an insulating layer) exposed to a time-varying transverse magnetic field gradient, was designed to identify the optimum parameters for an RLAS system. The reference layer and insulating layer parameters were varied sequentially, with the optimum value for earlier parameters set in each case. The parameters were initially set to the values used for the preliminary experiments ( $RLT=5$  mm,  $ILT=1$  mm and  $RLAE=90^\circ$ ). A series of simulations were performed to evaluate the effect of varying the RL properties on the voltage induced in the VC and RL by a time-varying transverse field gradient. The induced voltage was evaluated at the same 33 electrode locations (as explained in the analysis Section 6.4) on the VC and RL in the following seven different situations:

- a.  $RLAE$  varied from  $80^\circ$  to  $155^\circ$  in steps of  $5^\circ$  (however  $RLAE$  varied in step of  $1^\circ$  when  $RLAE$  is close to  $90^\circ$ )
- b.  $RLT$  varied from 1 to 15 mm in steps of 1 mm

- c. ILT varied from 1 to 10 mm in steps of 1 mm
- d. entire system rotated about the x-axis by  $\pm 20^\circ$  in steps of  $5^\circ$
- e. RL only, rotated about the x-axis by  $\pm 20^\circ$  in steps of  $5^\circ$
- f. Shifting the RLAS system longitudinally by  $\pm 15$  cm in steps of 5 cm (however step variation is made in steps of 1 cm when the RLAS system is close to isocentre)
- g. shifting the RLAS system transversally by  $\pm 15$  cm in steps of 5 cm

## 6.8 Optimization Results

Figure 6.6 shows the RMS of the difference of the artefact voltages between the RL and VC electrodes for the range of RL and insulation layer (IL) geometry parameters investigated.

- Fig. 6.6A: Varying RLAE, which effectively changed the coverage of the RL over the VC, shows the minimum discrepancy between induced voltages is achieved at  $88^\circ$  (slightly less than a hemisphere) with a potential difference of  $76 \mu\text{V}$  (33 dB attenuation).

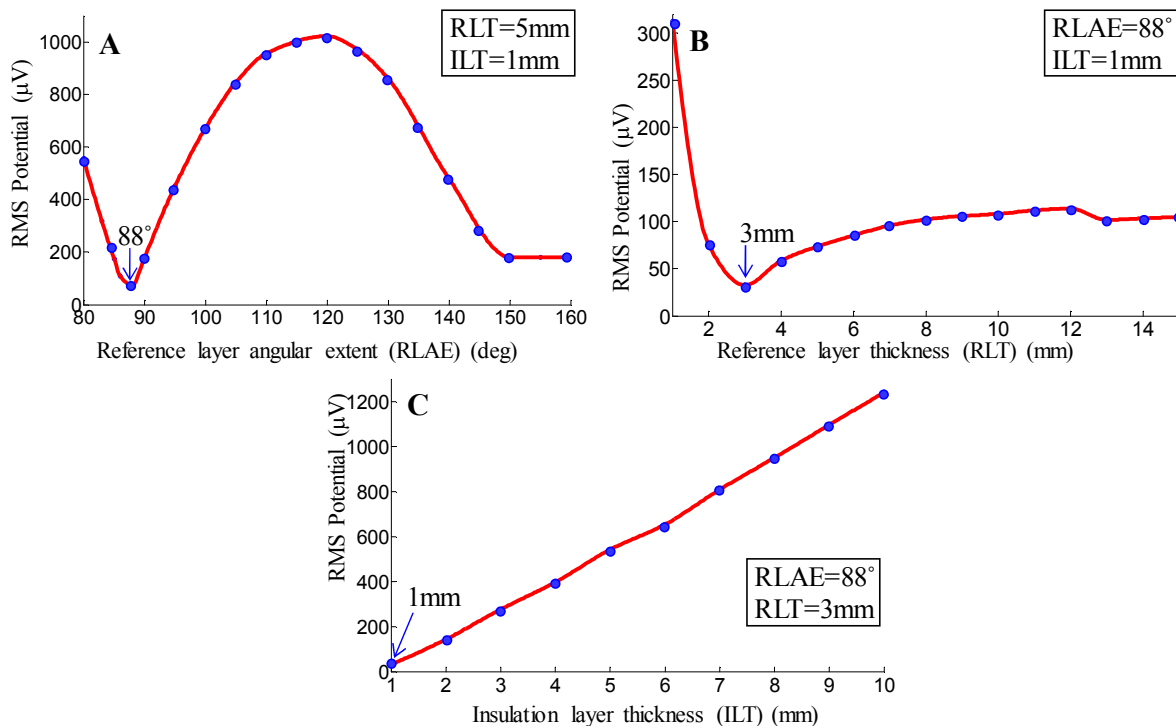


**Figure 6.6** RMS over sample locations of the difference in induced voltages between the VC and RL for a range of reference and insulation layer geometry parameters. Varying: **A)** RLAE; **B)** RLT and **C)** ILT.

- Fig. 6.6B: Varying RLT (RLAE= $88^\circ$ , ILT=1 mm) produces an almost linear increase in the difference in induced voltages between conductors for RLT in the range of 3-

8mm, then, when  $RLT > 1$  cm the voltage discrepancies become almost independent of  $RLT$ . Moreover, Fig. 6.6B shows that the discrepancy is further reduced ( $RMS=32 \mu V$ ) (40 dB attenuation) by reducing  $RLT$  to 3 mm. However, for  $RLT < 3$  mm, the  $RMS$  discrepancy increases rapidly.

- Fig. 6.6C: The potential difference between the VC and RL was found to increase linearly with  $ILT$ . Therefore, the  $ILT$  should be reduced as much as possible (1 mm) to give the minimum discrepancy in induced voltages ( $RMS=32 \mu V$ ).

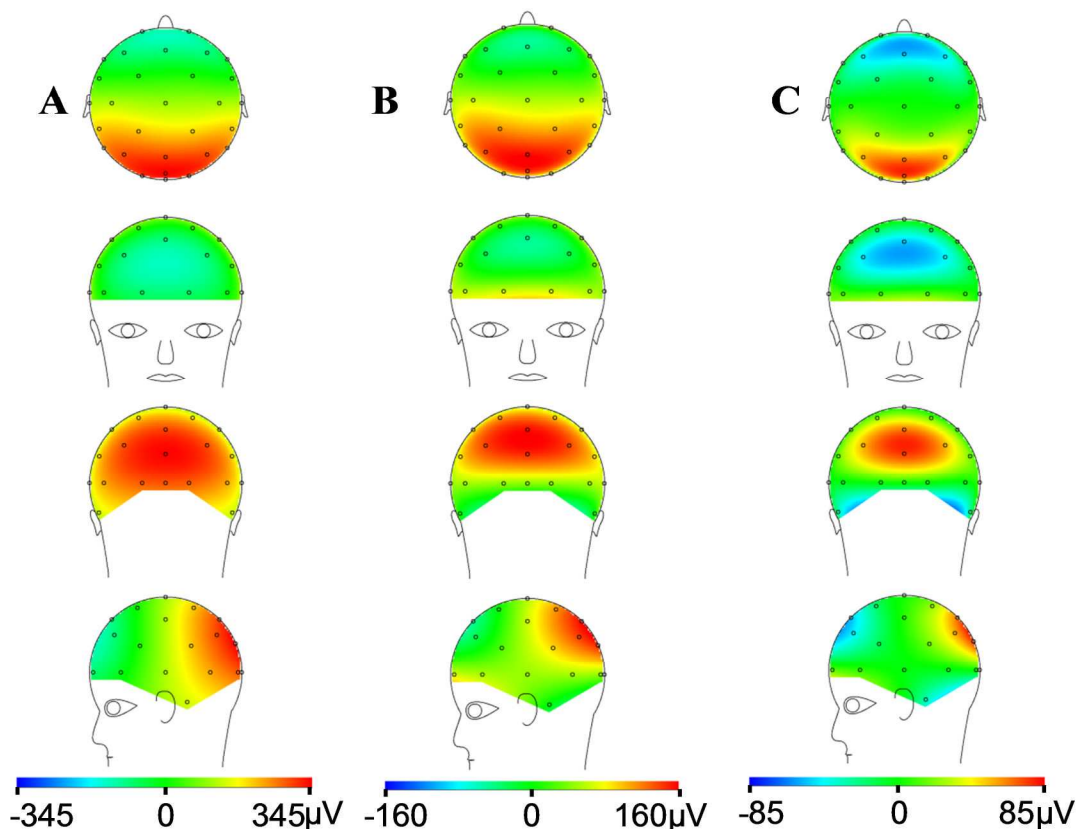


**Figure 6.7** Artefact map for the difference in induced voltages between the VC and RL for (A)  $RLT=5mm$ ,  $ILT=1mm$  and  $RLAE=90^\circ$ , (B)  $RLT=5mm$ ,  $ILT=1mm$  and  $RLAE=88^\circ$  and (C)  $RLT=3mm$ ,  $ILT=1mm$  and  $RLAE=88^\circ$ . Note that different voltage ranges have been used in each sub-plot so as to display clearly the detail of the artefacts induced in different regions.

Figure 6.7 shows maps of the  $RMS$  discrepancy obtained for each of the RL and IL optimized parameters. Varying from the initial parameters to  $RLAE=88^\circ$  while keeping  $RLT$  and  $ILT$  the same as before, the difference in induced artefact decreased considerably in the temporal and parietal lobes. This optimization reduces the overall induced artefact by 7 dB. The RLAS system exhibits the best performance with the largest artefact reduction when  $RLT=3$  mm while  $ILT=1$  mm and  $RLAE=88^\circ$ . Figure 6.8C shows that the frontal and occipital lobes

electrodes mainly contribute to the artefact difference between RL and VC for the optimized RL and IL geometry parameters.

Fig. 6.8A shows the pronounced effect of RLAS system rotation in the transverse field gradient in the induced artefact, even for 1-2° rotations, which increases almost linearly with movement away from 0°. It has been shown here that rotating about the x-axis for either **A**: the VC, RL and sample locations or **B**: the RL relative to the VC produces a reduction in the efficacy of RLAS. In fact, the effect of the RL slipping over the VC (i.e. the RL moves while the VC remains stationary, Fig 6.8B) produces more discrepancy in the induced artefact than rotation of the whole RLAS system (i.e. while VC, RL and sample location rotate, Fig 6.8A) about the x-axis. The induced artefact difference between the conductors increases more rapidly for rotations greater than  $\pm 15^\circ$  in the case where the RL slips over the VC.

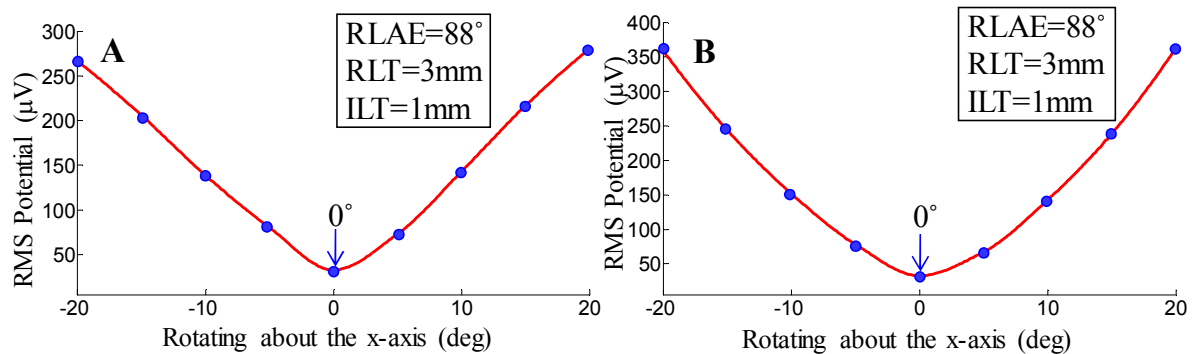


**Figure 6.8** Difference in induced voltages between conductors for rotations about the x-axis when: **A**) the RLAS system is rotated (VC, RL and all sample locations) and **B**) RL and RL sample locations are rotated (i.e. RL and RL sample locations move whilst the VC and VC sample locations remain stationary). Where 0° = sphere at isocentre with sample location Cz along the z-axis and positive values denote a nod forwards.

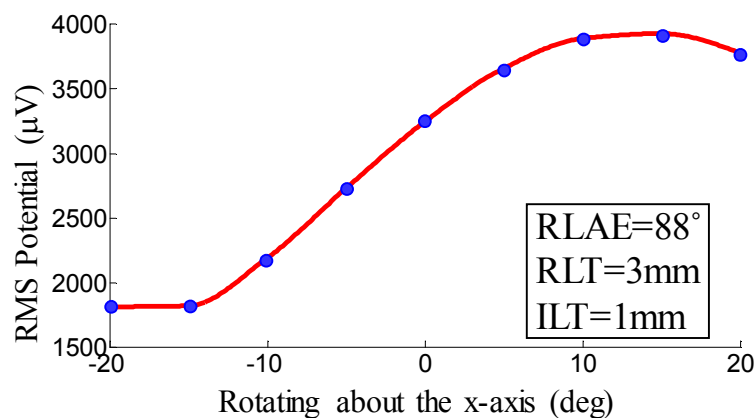


**Figure 6.9** RMS potential of the VC for rotation about x-axis when: RLAS system is rotated (VC, RL and all sample locations).

Figure 6.9 shows the variation in the residual voltages using the RLAS system when there is a rotation and the RMS potential on the VC also varies with the angle of rotation. The variation of the residual voltage is not readily obtainable from Figure 6.8 and the RMS potential of the VC needs only to be considered in the case of Fig 6.8A, as for Fig 6.8B the VC is not rotated and therefore the induced voltages in this conductor do not change. Given these differences Fig 6.10 explores the artefact attenuation when the RLAS method is employed for: A) the rotation about the x-axis of the RLAS system and B) the rotation of the RL relative to the VC. Figure 6.10A shows a difference in symmetry around 0° compared with that seen in Figure 6.8B which is brought about by the difference in the voltages induced in the VC. However, Figure 6.10 agrees with Figure 6.8 in that no further improvement in the artefact attenuation can be achieved with rotation of the system. Moreover, the performance of gradient artefact correction using the RLAS method reduces in a similar fashion when any part of the RLAS system is rotated away from 0 degree.

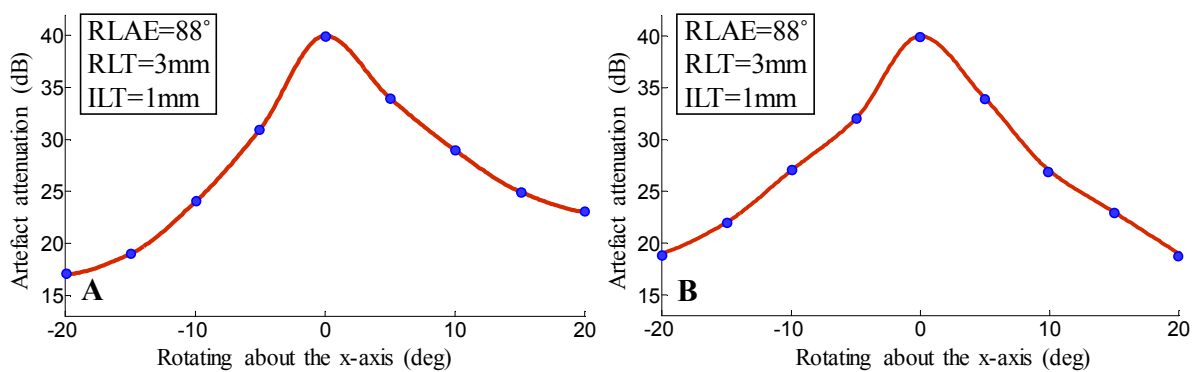


**Figure 6.10** Artefact attenuation for rotation about x-axis when: **A)** RLAS system is rotated (VC, RL and all sample locations) and **B)** RL and RL sample locations are rotated.

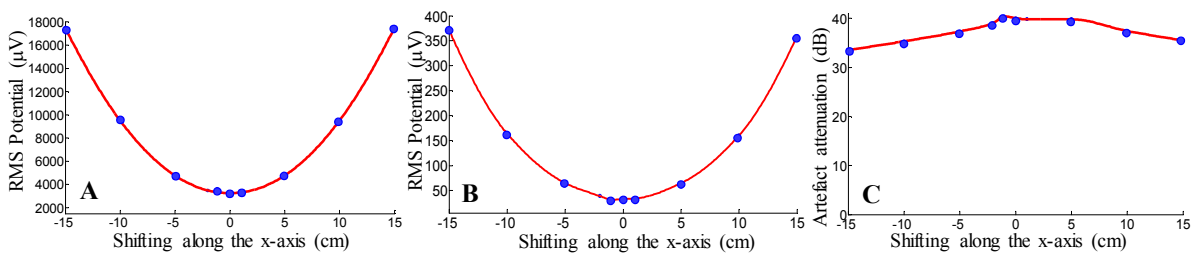


**Figure 6.11** RMS of the induced voltage on the VC (**A**) and the difference in induced voltages between conductors (**B**) when the RLAS system is shifted along the x-axis. Artefact attenuation for shifting the RLAS system along the x-axis (**C**).

Figure 6.11 shows the variation in RMS difference when the RLAS system is shifted in the x direction (right-left). Fig. 6.11 A&B shows the induced artefact variation for the VC and for the difference between the VC and RL conductor, respectively. It is evident from Figure

6.11B that the minimum artefact difference (30  $\mu\text{V}$ ) is obtained for a 1 cm shift to the left from isocentre (-1cm x-shift). The artefact attenuation shown in Figure 6.11C reflects this finding, with the maximum value of attenuation found to be 41 dB at this position. Figure 6.12 shows the RMS artefact variation for an anterior-posterior (AP) shift (y-shift) of the RLAS system. The RMS of the induced voltage of VC is smallest (2311  $\mu\text{V}$ ) when the RLAS system is shifted 2cm in the anterior direction (Figure 6.12A). However, the lowest artefact difference (32  $\mu\text{V}$ ) is found at 0cm AP shift, which is also evident from artefact attenuation plot shown in Figure 6.12C.

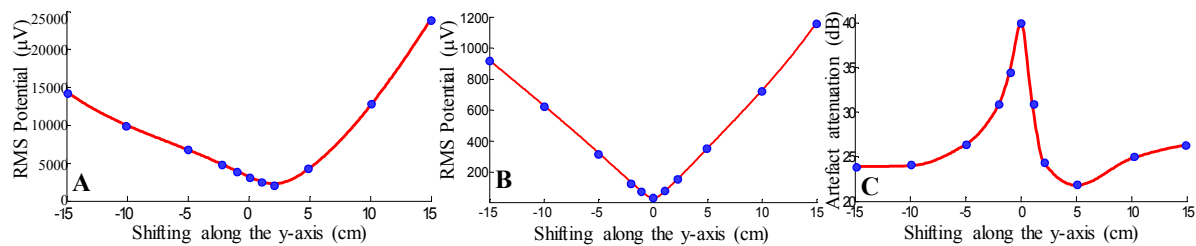


**Figure 6.12** RMS of the induced voltage on VC (A) and the difference in induced voltages between conductors (B) when RLAS system is shifted along the y-axis. Artefact attenuation for shifting the RLAS system along the y-axis (C).

The RMS of the induced artefact variation for the VC while shifting the RLAS system in the longitudinal direction (z-shift) is shown in Figure 6.14A. The lowest artefact voltage (802  $\mu\text{V}$ ) for the VC is observed at 4 cm foot shift (-4cm z-shift). However, the artefact discrepancy is found to be least at a 0 cm foot-head shift (Fig 6.13B), which is also evident from Figure 6.13C.

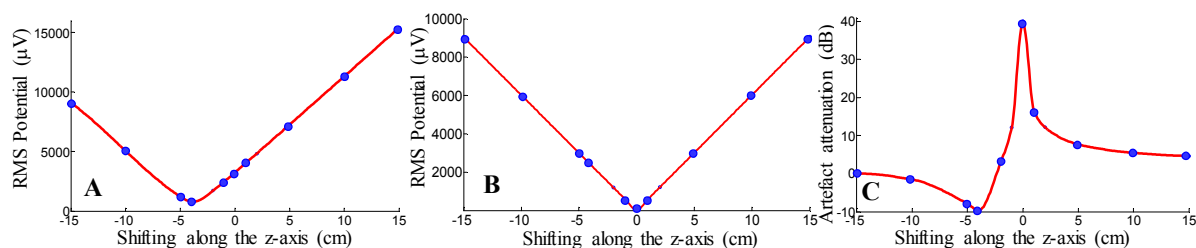


**Figure 6.13** RMS of the induced voltage on VC (A) and the difference in induced voltages between conductors (B) when RLAS system is shifted along the z-axis. Artefact attenuation for shifting the RLAS system along z-axis (C).

## 6.9 Discussions

The results of the simulations carried out using the initial realistic reference layer system (RLT=5 mm, ILT=1 mm and RLAE=90°) indicate that RLAS provides a viable method for attenuating at source the artefacts that are generated in EEG data recorded during concurrent

fMRI experiments by time-varying magnetic field gradients. The results of preliminary experiments (Fig. 6.3 & 6.4) demonstrate that in the modelled system, consisting of a separate conducting sphere and hemispherical reference layer, potential distributions resulting from a time-varying transverse gradient are very similar in both conductors. Consequently there is great potential in applying the RLAS technique to reduce time-varying gradient artefacts. For the initial RL and IL geometry parameters, it can be seen from Fig. 6.4 that the areas where the largest artefacts were induced are very similar for both the spherical VC and hemispherical RL. Therefore the subtraction of the two sets of voltages greatly attenuates the induced artefacts. For this initial set-up, RLAS resulted in an attenuation of 25 dB without any other post-processing. The difference map, shown in Figure 6.4C, depicts the spatial distribution of the residual artefact. It shows that the residual artefact is predominantly found in the occipital and parietal lobes which are also the regions that are most affected by artefacts when considering the RL and VC separately. However, the artefact difference in the frontal lobe is small despite there also being a large artefact induced in the RL and VC in this area.

Figure 6.5 shows the result of the simulations designed to find the voltages induced in the VC and RL by a time-varying longitudinal magnetic field gradient. The result observed from the simulation confirms the theory that little artefact is induced by this gradient with the RMS potential on the VC being only  $3 \mu\text{V}$ , which is very close to the theoretical value ( $0 \mu\text{V}$ ). The cubic voxel representation of the spherical volume conductor model means that the modelled VC is not completely spherical. This effect becomes pronounced for low resolution simulation models, with small problem size, and improves for high resolution, with the trade-off of a larger problem size. It is this lack of perfect sphere representation, due to the 0.5 mm voxel size, which is believed to be the source of the non-zero RMS potential for the VC in an applied longitudinal field gradient. Consequently the simulated RMS potential for a hemispherical RL shows a larger discrepancy from theoretical values due to: i) RL not being a volume conductor, rather it is hollow conductor; ii) both of its surfaces are not completely hemispherical, and this becomes pronounced for low RLT; and iii) the RL is hemispherical with probable edge distortion unlike the spherical VC.

It is apparent from Fig. 6.4 that there is a close spatial agreement between the artefacts induced for both of the conductors. Therefore a small mismatch between sample locations (i.e. electrode positions) between the VC and RL produces large difference in measured



artefact voltages. This was reflected in simulations where there was a  $1^\circ/2^\circ$  of mismatch between the conductors' sample locations which caused an RMS discrepancy of 232/427  $\mu\text{V}$  respectively; thereby reducing the artefact attenuation to 23/18 dB. Therefore the sampling locations of the two conductors must overlay precisely to get the best results from the RLAS system.

Calculation of the RMS discrepancy of the artefact voltages between the RL and VC due to the time-varying transverse gradient for the range of RL and insulation layer geometry parameters plays a substantial role in designing an optimal setup for RLAS system. It is noticed from Figure 6.7A that variation of RLAE, which effectively changes the positioning of the RL over the VC, greatly reduces the RMS discrepancy and the minimum discrepancy between induced voltages is achieved at  $88^\circ$  (slightly less than a hemisphere) with an RMS potential difference of 76  $\mu\text{V}$ . This causes an artefact attenuation of 33dB when compared to the voltages on the VC, providing an 8 dB additional gain in artefact reduction in comparison to the attenuation possible with the initial parameters used for the preliminary experiments. This result also illustrates the necessity, if possible, of making the RL from elastic material so that it can be adjusted on the subjects head depending on their head shapes. Reference layer thickness has some effect on the voltage discrepancy, with it being possible to further reduce the RMS discrepancy to 32  $\mu\text{V}$  for  $\text{RLT}=3$  mm. However, the contribution of RLT is not that critical above 2 mm, which leaves flexibility in this parameter when designing the RL. Below 2 mm, the discrepancy is large in the simulation which might be because there are very few voxels which constitute the conductive path in the RL and therefore it is difficult to make a proper spatial distribution. A RL thickness of 3mm ( $\text{RLT} = 5$  mm,  $\text{ILT} = 1$  mm,  $\text{RLAE} = 88^\circ$ ) provides an additional 7 dB attenuation in artefact correction over the RLAE correction reported above.

It was expected from theory that the potential difference between the conductors would increase with ILT, which was confirmed by the simulations shown in Fig. 6.6C. Therefore, the ILT should be made as small as possible to give the minimum discrepancy in induced voltages. However, consideration must be made to ensure proper insulation is maintained between the two conductors and the minimum ILT which is feasible, is around 1mm; this produces a maximum possible attenuation of 40 dB ( $\text{RLAE}=88^\circ$  and  $\text{RLT}=3$  mm).

The artefact maps, shown in Figure 6.7 display the effect of the RLAS geometry parameter variation on the spatial distribution of the residual induced potentials. When the initial parameters were used, the main artefact contributions come from the occipital, temporal, parietal and frontal lobe electrodes (Fig. 6.7A) whereas when the RLAE is changed to  $88^\circ$ , most of the temporal lobe electrode contributions are eliminated and the occipital, frontal and parietal lobe electrodes' contributions are also reduced (Fig. 6.7B). For RLT=3 mm, the artefact contribution is primarily from frontal and occipital lobe electrodes while the artefact contribution from the parietal lobe electrodes is diminished.

It is important to consider possible rotations and translations of the RLAS system in the MR scanner since this allows the evaluation of the change in the induced gradient artefact due to changes of head orientation and position. This will help in optimizing the RLAS design and experimental set-up. These simulations were performed using the optimised parameters obtained from the previous simulations (RLAE= $88^\circ$ , RLT=3 mm, ILT=1 mm). Figure 6.8A shows the RMS of the voltage difference between the VC and RL due to a time-varying transverse gradient for RLAS system rotations about the  $x$ -axis. It is evident from Figure 6.9 that the RMS potential for the VC was also dependent on the position of the RLAS system with respect to the  $x$ -axis. Therefore to calculate the gain of employing the RLAS system for artefact correction (Fig. 6.8A) when an  $x$ -axis rotation had occurred, results need to be considered in conjunction with the results show in Figure 6.9. Figure 6.10A clearly shows that no further improvement in the artefact attenuation was possible with rotation of the RLAS system about the  $x$ -axis. This clearly indicates that any misalignment of the RLAS system with the  $z$ -axis will increase residual artefact, with a greater difference for a backward nod than for a forward nod. This is because the VC potential increases almost linearly between  $-15^\circ$  and  $+15^\circ$  for rotation of the RLAS system about the  $x$ -axis. In the case where the RL rotates (or slips) over the VC, the VC potential remains constant whereas the RL potential changes with angle of rotation. Given the early results showing the need for electrode alignment it is unsurprising this configuration doesn't show any further improvement in artefact attenuation. This implies that the RL alignment with  $z$ -axis is also important for the best performance of the RLAS system with the optimized initial parameters. Although RLAS system rotation plots shown in Figure 6.8-10 clearly depicts that no further improvement in attenuation is possible with rotation, the position VC inside the scanner and the RLAE might have an impact on this finding. If RLAE becomes more than  $90^\circ$ , there

could be a position inside the scanner where maximum attenuation might not be produced at  $0^{\circ}$  rotation.

Mullinger *et al.*, (2011) have showed that positioning subjects so that their nasion is displaced 4 cm axially from the scanner's iso-centre towards the feet significantly reduces the gradient artefact produced by time-varying gradients applied in the RL and FH directions compared with the situation where the nasion is at the iso-centre of the scanner. It has been shown that this decrease translates into a 40% reduction in the RMS amplitude of the gradient artefacts generated during conventional multi-slice EPI acquisition, as used in most EEG-fMRI experiments. This work emphasizes the importance of studying the positioning of the RLAS system inside the MR scanner. Figure 6.13 shows the effect of the transverse magnetic field gradient in inducing artefact voltages on the VC, the discrepancy between VC and RL and its attenuation by RLAS for the same axial shift of the RLAS system. It is evident from Figure 6.13A that the 4 cm axial shift from the scanner's iso-centre towards the feet significantly reduces the VC RMS potential. The RMS voltage of VC with a 4 cm shift toward the feet is  $802\mu\text{V}$  which is 4 times smaller than that found at iso-centre ( $3248\mu\text{V}$ ). It might also be expected that the difference between the VC and RL voltages might also be a minimum at this position. However, the simulations presented here show that this is not the case, as at this position the RL RMS potential is  $2326\mu\text{V}$  and the difference between conductors is  $2447\mu\text{V}$ , and consequently no attenuation obtained at this position. Therefore although this 4cm shift toward feet showing significant improvement for a standard EEG-fMRI set-up in reducing EEG gradient artefacts, this does not apply when the RLAS system is employed. Instead the optimal position was found to be at iso-centre where the RMS artefact induced in VC and RL are  $3248$  and  $3267\mu\text{V}$  respectively and the RMS difference is  $32\mu\text{V}$  which offers 40dB artefact attenuation. This is far superior to the performance of single layer EEG system with 4 cm shift towards the feet and further demonstrates the potential benefits of the RLAS system.

Figure 6.11A shows that the RMS potential induced on the VC by a transverse gradient when the system is shifted along the  $x$ -axis (RL) is least at iso-centre, which implies that the voltage difference between conductors might be lowest at this same position. However, interestingly this was found not to be the case as the smallest discrepancy ( $30\mu\text{V}$ ) was observed 1 cm away from the iso-centre towards the left direction which results in approximately 41 dB artefact attenuation relative to the VC in that particular position. Since

the whole RLAS system need to be shifted 1cm left to produce this reduction, it be may difficult to achieve in a real EEG-fMRI study because of the limited space available inside the head RF coil . Moreover, this improvement is not very remarkable in the gradient artefact correction.

It is apparent from Figure 6.12A that the 2 cm  $y$ -axis (AP) shift from the scanner's iso-centre towards the anterior direction significantly reduces the VC RMS potential. The RMS voltage on the VC with a 2 cm shift in the anterior direction is 2311  $\mu\text{V}$  which is 29% smaller than the voltage at iso-centre (3248  $\mu\text{V}$ ). In this AP position, the RMS discrepancy between conductors might be expected to be smallest, but again Figure 6.12B&C show that this is not the case. This is because with a 2 cm anterior shift the RMS potentials on the VC and RL are 2311 and 2354  $\mu\text{V}$  respectively, and the RMS difference is 137  $\mu\text{V}$ . This 2cm shift therefore results in a 25 dB attenuation of the gradient artefact compared with the optimal 40 dB attenuation which can be achieved without this shift. Therefore it seems that there is no gain in artefact correction using the RLAS system if a shift in the AP direction is implemented and the system should be kept in the centre of the  $y$ -axis. However, the scanner bed is not exactly in the centre of the  $y$ -direction, rather for the Philip's Achieva scanner the head coil surface where the subject's head normally rests is positioned 6 cm away from the centre of the  $y$ -axis in the posterior direction. This results in 2 cm posterior shift for the centre of subject head for a subject with head diameter of 8 cm. This 2 cm AP shift in the posterior direction will not produce any gain in gradient artefact reduction; rather the artefact attenuation will become 25 dB. Therefore it is evident from the above discussion that the subject head should be lifted by 2 cm in the anterior direction to make the subject head aligned with the centre of  $y$ -axis to produce optimal gradient artefact attenuation although it might not be practically achievable in many scanners as the subject's head has to lie on the bed. However, in the Philips head coil (used in this experiment), subject has enough room to raise his/her head with the help of any support underneath as long as the shift in the anterior direction is only couple of centimetre.

## **6.10 Conclusion**

Starting from basic physical principles, this chapter describes the modelling of the spatial distribution of the gradient artefacts in EEG/fMRI for both a spherical volume conductor and a hemispherical reference layer and also the complete RLAS system with a high degree of accuracy. The work described here has also demonstrated the benefits in artefact reduction

that RLAS can provide, but clearly for these benefits to be widely realised, it is necessary to find the optimal reference layer configuration. The calculations accounted for realistic rotations and shifts of the RLAS system with respect to the gradient isocentre, thus giving insight into the optimum RLAS set-up and the potential for improved EEG cap design for an RLAS system. My work suggests the optimal set-up for an RLAS system is  $RLT = 3$  mm,  $ILT = 1$  mm,  $RLAE = 88^\circ$  with no RLAS system rotation and 1 cm left shift and 2 cm anterior shift of the whole RLAS system from isocentre. In this case the RMS difference in induced voltages between conductors was found to be  $31 \mu\text{V}$  for the model for an applied transverse gradient, a 41 dB attenuation of the VC voltages which are normally measured in a conventional EEG system. This simulation work suggests that RLAS is a viable method for removing artefacts in EEG data during simultaneous fMRI, and the RLAS approach should therefore be experimentally tested. However, the efficacy of the RLAS system is dependent upon the design of the system, thus, guidance from simulation work, will enable the best performance of an RLAS system to be realised.

## 6.11 References

- Allen, P. J., Josephs, O. and Turner, R. (2000). "A Method for removing Imaging Artifact from Continuous EEG Recorded during Functional MRI." *Neuroimage* **12**(2): 230-239.
- Allen, P. J., Poizzi, G., Krakow, K., Fish, D. R. and Lemieux, L. (1998). "Identification of EEG Events in the MR Scanner: The Problem of Pulse Artifact and a Method for Its Subtraction." *Neuroimage* **8**(3): 229-239.
- Antunes, A., Glover, P. M., Li, Y., Mian, O. S. and Day, B. L. (2012). "Magnetic field effects on the vestibular system: calculation of the pressure on the cupula due to ionic current-induced Lorentz force." *Phys. Med. Biol.* **57**: 4477-4487.
- Bencsik, M., Bowtell, R. and Bowley, R. M. (2002). "Electric fields induced in a spherical volume conductor by temporally varying magnetic field gradients." *Phys. Med. Biol.* **47**: 557-576.
- Bencsik, M., Bowtell, R. and Bowley, R. M. (2007). "Electric fields in the human body by time-varying magnetic field gradients: numerical calculations and correlation analysis." *Phys. Med. Biol.* **52**: 1-17.

- Bonmassar, G., Purdon, P. L., Jaaskelainen, I. P., Chiappa, K., Solo, V., Brown, E. N. and Belliveau, J. W. (2002). "Motion and ballistocardiogram artifact removal for interleaved recording of EEG and EPs during MRI." NeuroImage **16**(4): 1127–1141.
- Bowtell, R. and Bowley, R. M. (2000). "Analytic Calculations of the E-Fields Induced by Time-Varying Magnetic Fields Generated by Cylindrical Gradient Coils." Magnetic Resonance in Medicine **44**: 782-790.
- Dunseath, W. J. R. and Alden T. A. (2009). Electrode cap for obtaining electrophysiological measurement signals from head of subject, has measurement signal electrodes extended through electrically conductive layer and insulating layer for contacting head of subject. USA. **US 2009/0099473**.
- Glover, P. M. (2009). "Interaction of MRI field gradients with the human body." Phys. Med. Biol. **54**: R99-R115.
- Glover, P. M. and Bowtell, R. (2008). "Measurement of electric fields induced in a human subject due to natural movements in static magnetic fields or exposure to alternating magnetic field gradients." Phys. Med. Biol. **53**: 361-373.
- Glover, P. M., Cavin, I., Qian, W., Bowtell, R. and Gowland, P. A. (2007). "Magnetic-field-induced vertigo: a theoretical and experimental investigation." Bioelectromagnetics **28**: 349-361.
- Griffiths, D. J. (1981). Introduction to Electrodynamics Fourth Edition. Mishawaka, USA, Prentice Hall.
- Jackson, J. D. (1998). Classical Electrodynamics Third Edition. New York, John Willey & Sons, Inc.
- Jansen, M., White, T. P., Mullinger, K. J., Liddle, E. B., Gowland, P. A., Francis, S. T., Bowtell, R. and Liddle, P. F. (2012). "Motion-related artefacts in EEG predict neuronally plausible patterns of activation in fMRI data." Neuroimage **59**(1-3): 261-270.
- Li, Y., Hand, J. W., Wills, T. and Hajnal, J. V. (2007). "Numerically-Simulated Induced Electric Field and Current Density Within a Human Model Located Close to a z-Gradient Coil." Journal of Magnetic Resonance Imaging **26**: 1286-1295.
- Liu, F., Zhao, H. and Crozier, S. (2003). "Calculation of electric fields induced by body and head motion in high-field MRI." Journal of Magnetic Resonance Imaging **16**: 99-107.

- Liu, F., Zhao, H. and Crozier, S. (2003). "On the Induced Electric Field Gradients in the Human Body for Magnetic Stimulation by Gradient Coils in MRI." IEEE Transactions on Biomedical Engineering **50**(7): 804-815.
- Masterton, J., Abbott, D. F., Fleming, S. and Jackson, G. D. (2007). "Measurement and reduction of motion and ballistocardiogram artefacts from simultaneous EEG and fMRI recordings." NeuroImage **37**: 202-211.
- Mullinger, K. J., Yan, W. X. and Bowtell, R. W. (2011). "Reducing the Gradient Artefact in Simultaneous EEG-fMRI by Adjusting the Subject's Axial Position." NeuroImage **54**(3): 1942-1950.
- Sánchez, C. C., Glover, P. M., Power, H. and Bowtell, R. (2012). "Calculation of the electric field resulting from human body rotation in a magnetic field." Phys. Med. Biol. **57**: 4739-4753.
- van derVorst, H. A. (1992). "Bi-CGSTAB: a fast and smoothly converging variant of Bi-CG for the solution of nonsymmetric linear systems." SIAM J. Sci. Stat. Comput. **13**(2): 631-644.
- Yan, W. X., Mullinger, K. J., Brookes, M. J. and Bowtell, R. W. (2009). "Understanding Gradient Artefacts in Simultaneous EEG/fMRI." Neuroimage **46**(2): 459-471.
- Zhang, Z. (1995). "A fast method to compute surface potentials generated by dipoles within multilayer anisotropic spheres." Phys. Med. Biol. **40**: 335-349.

# Chapter 7

---

*Reference Layer Artefact Subtraction:  
experimental study*



## 7.1 Introduction

The theoretical extent by which EEG artefacts can be attenuated in a simultaneous EEG-fMRI experiment by using the novel RLAS method was evaluated through electromagnetic simulations in Chapter 6. This electromagnetic modelling allowed us to test the theoretical efficacy of GA correction that can be achieved by using the RLAS technique and helped us to optimize the RLAS system. However, RLAS can also be used to ameliorate the PA and MA which we could not easily verify through simulation.

The implementation of AAS and other techniques for GA correction are sub-optimal when subject movement occurs during a study. As already discussed in Chapter 3, changes in subject position alter the morphology of the induced GA (Mullinger *et al.*, 2011), which means that the artefact voltage waveforms recorded at each electrode vary over volume acquisitions when movements occur during an EEG-fMRI experiment. As a consequence, residual artefacts remain after AAS, since the average artefact template does not exactly characterise individual occurrences of the GA (Allen *et al.*, 2000; Becker *et al.*, 2005; Freyer *et al.*, 2009; Moosmann *et al.*, 2009). This problem is often partially resolved by using one of a number of post-processing methods which often involve reducing the number of repeats of the artefact waveform that are used in forming the subtraction template. Although these methods can improve the efficacy of artefact removal, the reduced number of repeated artefact waveforms used in forming the correction templates means that there is a greater risk that signals due to neuronal activity will be attenuated in the correction process (Mullinger *et al.*, 2008).

It would be possible to correct the GA with the help of motion information if there was a model of how the GA changed with motion— but most motion sensors wouldn't really give enough information to do this (e.g. the piezo sensors that Bonmassar *et al.* (2002) used) and it's hard to generate a useful model without making a lot of additional experimental measurements. Therefore reference signals recorded using motion sensors cannot address the GA, and more particularly changes in the GA due to head movement. The performance of the reference signal approach proposed by Dunseath *et al.*, (2009) is not described in the literature. It is evident from the simulation work described in Chapter 6 that deploying the reference layer approach can significantly remove the gradient induced artefacts from EEG data. However, since the exact cause of the PA is still uncertain (Yan *et al.*, 2010; Mullinger

*et al.*, 2013) with some suggestion that it is in part due to blood-flow-induced Hall voltages which would not appear on the reference layer, it is unclear how successfully the reference layer approach can attenuate the PA.

The aim of the work described here was therefore to develop an experimental set-up in which gradient, movement and pulse artefacts could be simultaneously recorded on the scalp and on a reference layer, thus allowing the efficacy of artefact correction that can be achieved by using RLAS to be properly tested. Preliminary experiments were carried out on simple spherical phantoms using different cable configurations to test the feasibility of RLAS, and recordings were also made on a head-shaped agar phantom using the original fEEG cap system (Dunseath *et al.*, 2009) in conjunction with a BrainAmp MR-plus amplifier (Brain Products, Munich, Germany) so as to compare with the preliminary results produced using the new set-up developed here. Subsequently, a series of experiments were carried out on spherical phantoms and human subjects in conjunction with our prototype reference layer system to test how well RLAS eliminates the GA, PA and MA when these artefacts are present individually and in combination. In this prototype system, we formed the reference layer using saline-doped agar and recorded the signals from electrode pairs in which one electrode made contact with the reference layer, while the other contacted the scalp or spherical phantom. Using the resulting data, we evaluated the level of artefact attenuation which could be achieved by using AAS, RLAS and the combination of RLAS and AAS.

### 7.2 General Equipment and Data Acquisition

The conducting spherical phantom employed in this work was 0.14 m in diameter and constructed from 4% (by total weight) agar (Sigma Aldrich) in distilled water. 0.5% NaCl was added to the water to yield a conductivity of about  $0.5 \Omega^{-1} \text{ m}^{-1}$ , which approximately reflects the conductivity of tissues of the human head (blood  $\sim 0.6 \Omega^{-1} \text{ m}^{-1}$  and gray/white matter  $\sim 0.12 \Omega^{-1} \text{ m}^{-1}$ ) (Bencsik *et al.*, 2007), along with 4 ml/l of Milton sterilizing fluid which was added to prevent bacterial growth (Yan *et al.*, 2009). The contents were boiled to make a viscous gel, which was then poured into a spherical fibre-glass mould with an inner radius of 0.14 m. After the agar had set, the mould was removed to yield the desired spherical phantom (Figure 7.1A). The approximately 5-mm-thick reference layer (Figure 7.6B) was constructed from saline-doped agar, which was produced using the same recipe as employed for manufacturing the spherical phantom. Since agar layer becomes more fragile if it makes

thinner, the thickness of the reference layer is more than the optimal thickness (3 mm) identified in Chapter 6. Hemispherical or head-shaped layers (for use with the spherical phantom or human subjects respectively) were produced by using appropriately shaped fibre-glass moulds. A head-shaped, agar phantom (Figure 7.1B) was constructed using the head-shape mould and the agar recipe described above to allow the performance of the fEEG system to be tested.

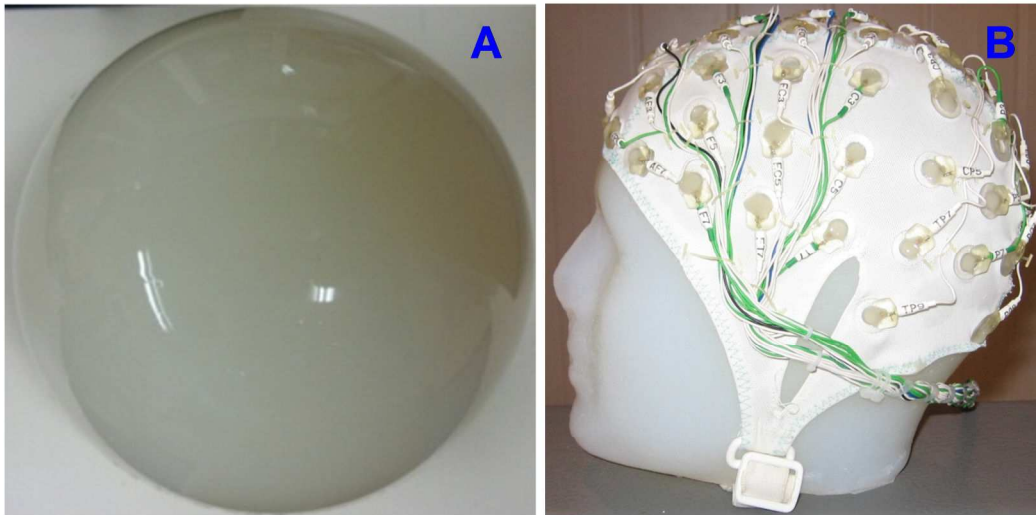


**Figure 7.1** Pictures depicting the phantoms used for the experiments described in this Chapter. A: Spherical agar phantom; B: Human head-shaped agar phantom.

Experiments were carried out in a Philips Achieva 3 T MR Scanner (Philips Medical Systems, Best, Netherlands) using a whole-body radiofrequency (RF) transmit coil and an eight-channel, head receiver coil.

EEG data were recorded using a BrainAmp MRplus EEG unipolar amplifier and Brain Vision Recorder software (Brain Products, Gilching, Germany). The EEG system allowed recording of signals in the frequency range 0.016–250 or 1000 Hz (used only for customized EPI; described in Section 7.2.2) with a sampling rate of 5 kHz. The MR scanning and EEG sampling were synchronized by driving the EEG amplifier clock using a 5 kHz signal derived from a 10 MHz reference signal from the MR scanner (discussed in detail in Chapter 4) (Mandelkow *et al.*, 2006; Mullinger *et al.*, 2008c). A TTL pulse generated by the scanner at the start of each slice acquisition was recorded by the EEG software. The pulse timing information was used to facilitate GA correction using AAS and to inform the analysis of average residual artefacts after application of the different correction methods.

For recordings on human subjects, a pair of electrodes were attached to the chest (one at the mid-line and the other to the left of the heart) and used in conjunction with a BrainAmp ExG MR bipolar amplifier and Brain Vision Recorder software (Brain Products, Munich, Germany) to record the subject's ECG during those experiments which were designed to evaluate the PA correction. The ECG trace was used for the R-peak detection that is required for PA correction when using the AAS technique.

### 7.3 Preliminary Experiment

In most commercial EEG caps, twisted wires are used to form the cable between the cap and the amplifier (or the amplifier's break-out box). The reference layer approach requires the paths of the leads connected to the electrodes on the scalp or phantom surface to follow exactly the same path as the leads connected to the corresponding electrodes on the reference layer all the way from the electrodes to the EEG amplifier. This is to ensure that the artefact voltages induced in the two associated leads by movement or temporally-varying magnetic fields are identical.

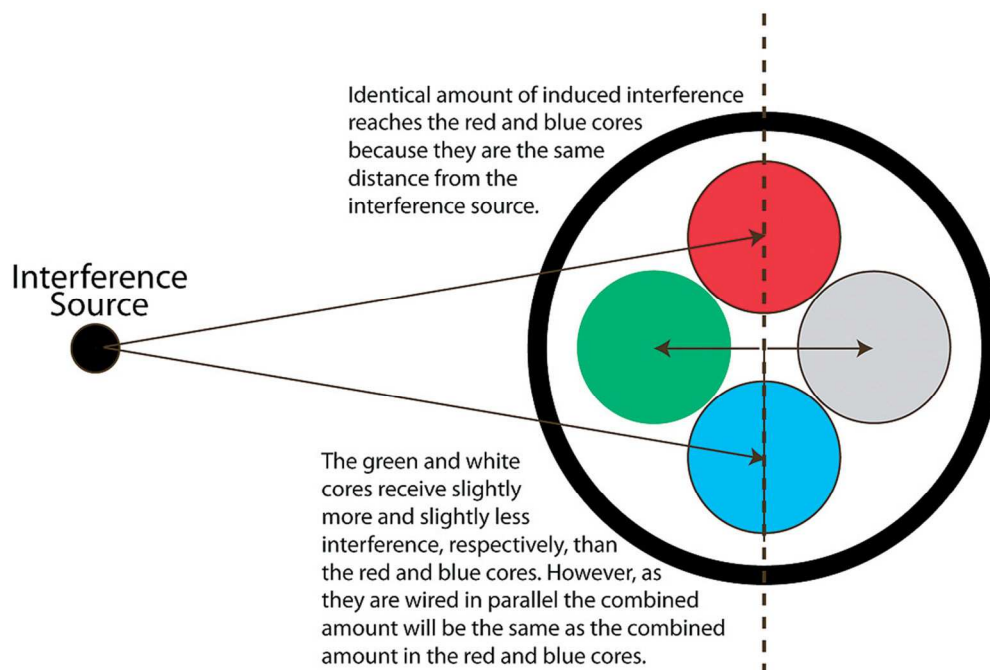


**Figure 7.2** A schematic representation of the pairs of cores and how they are arranged in a star-quad cable. Taken from (Robjohns 2009).

Theoretically, standard two-core twisted cable should ensure that this requirement is fulfilled, however much better rejection of low frequency electromagnetic interference can be achieved by using star-quad cable (Robjohns 2009). This cable comprises four cores, which are wired

as two pairs with opposing conductors in the star connected at each end, and which are tightly twisted with a short lay length. As the Figure 7.2 shows, the four cores are arranged in a cross formation and the opposite cores are wired in parallel to form a single balanced pair. The advantage of star-quad cable over twisted cable is better rejection of electromagnetically induced interference.

### 7.3.1 Method

A preliminary experiment was carried out with the spherical phantom positioned inside the scanner to test whether standard two-core twisted cable or star-quad cable was the most suitable for making connections between the electrode and amplifier in the RLAS set-up. Two electrode pairs were employed in this preliminary work: standard two-core twisted cable was used to connect one electrode pair to the amplifier, whereas star-quad cable (LSZH Star-quad Installation, Van Damme Cable, [www.van-damme.com](http://www.van-damme.com)) was employed for connection of the other pair. Each electrode pair was formed from two sintered Ag/AgCl (EasyCap, Herrsching, Germany) ring-electrodes which were connected to either the single cores of a standard twisted pair or to the wire pairs of the star-quad cable.

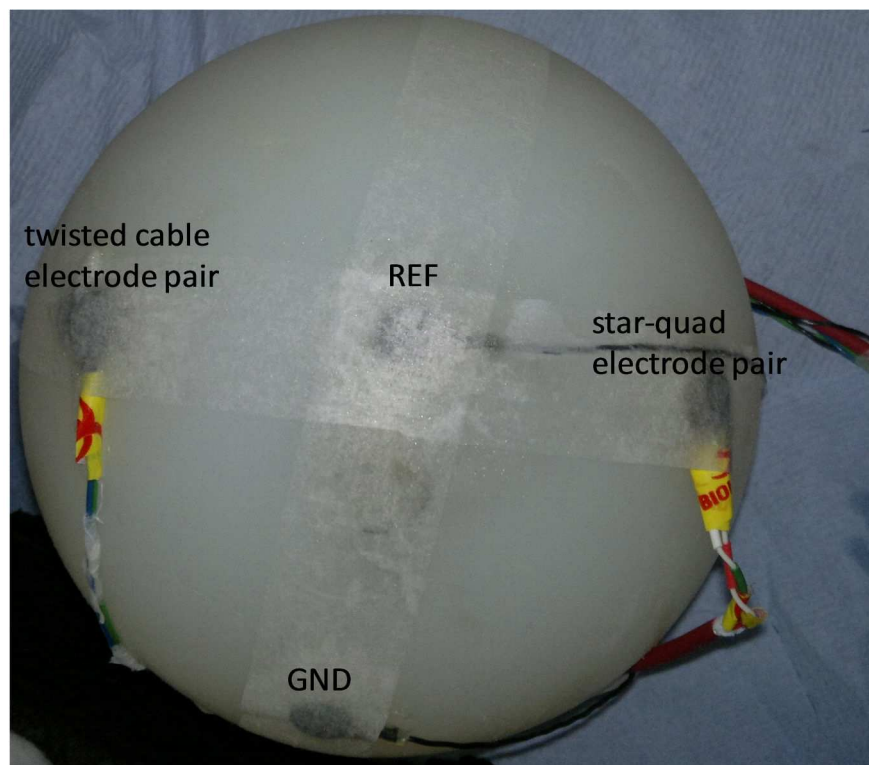


**Figure 7.3** Experimental set-up of the phantom for evaluating the performance of star-quad cable (right of the image) in comparison to standard twisted pair cable (left of the image).

As it was not possible to make connections directly onto the electrodes, short sections (less than 7 cm in length) of standard single core wire, which had been attached to the electrodes by the manufacturer, were used (Fig. 7.3). Reference (REF) and ground (GND) electrodes were also attached to the phantom as shown in Figure 7.3. 1-m-long star-quad cables/twisted wire pairs were run axially along the magnet bore and used to connect the electrodes to the EEG amplifier via a break-out box. We took a number of steps to isolate the cables, break-out box and EEG amplifier from the vibrations produced by the scanner during imaging, in order to limit the generation of additional artefacts as a result of movement of these components in the strong magnetic field. Specifically, the break-out box and EEG amplifier were placed on a table positioned just outside the bore of the magnet. The cables were tied together and attached to a cantilevered beam which was fixed to the table, similar to the set-up shown in Mullinger *et al.*, (2013).

In order to assess how the two different cable configurations (standard twisted pair and star-quad cable) affected the magnitude of GA produced by each of the three orthogonal gradients, EEG recordings were made during execution of a modified EPI sequence (as described in Chapter 5, Section 5.2.1) while the pair of electrodes for both cables was electrically shorted together using abrasive and conductive gel (Abralyte 2000 EEG gel). The electrodes were electrically connected to the surface of spherical agar phantom using more of the gel. Six volumes (each composed of 5 slices) were acquired using the modified EPI sequence providing a total of 30 pulse repetitions.

### 7.3.2 Analysis

Initial data processing and analysis were carried out in Brain Vision Analyzer2 (Version 2.0.1; Brain Products, Munich, Germany), while MATLAB (The MathWorks) was used for further quantification of differences in induced GAs between cables.

The modified sequence allowed easy separation of the effects of the three different gradients by providing clearly defined periods during which each single gradient varied in time in a well-defined manner. The EEG recordings were then segmented using the scanner's slice markers (-150 ms to 0 ms relative to slice marker) and the EEG data from each channel pair of the two different cables were baseline-corrected (-150 ms to 0). To measure the artefact induced by each single gradient on each channel of two cables, the difference in the GA

voltage (the difference between the positive and negative lobes of the induced artefacts on each lead) between the two leads in each cable were taken and averaged over the 30 repetitions. By taking the difference between the artefacts induced in the two leads, any artefact voltages generated in the break-out box and amplifier were removed, revealing the differences in the voltages induced in the two different cables.

### 7.3.3 Results and Discussion of the Preliminary Experiment

Figure 7.4 shows the artefact remaining after subtraction of the signals on the two leads forming a pair for the star-quad (A) and twisted pairs cable (B). These results clearly show that the star-quad cable outperforms standard twisted pair cable in reducing the remaining GA after subtraction of the contribution of the two leads. The maximum residual artefact amplitude for different gradients when the star-quad cable was used were considerably reduced compared with the twisted pair cable. This was reflected in the RMS of the difference voltages which were: 194/562, 90/232 and 86/34  $\mu\text{V}$  for star-quad cable/twisted pair cable for the AP, RL and FH gradients respectively.

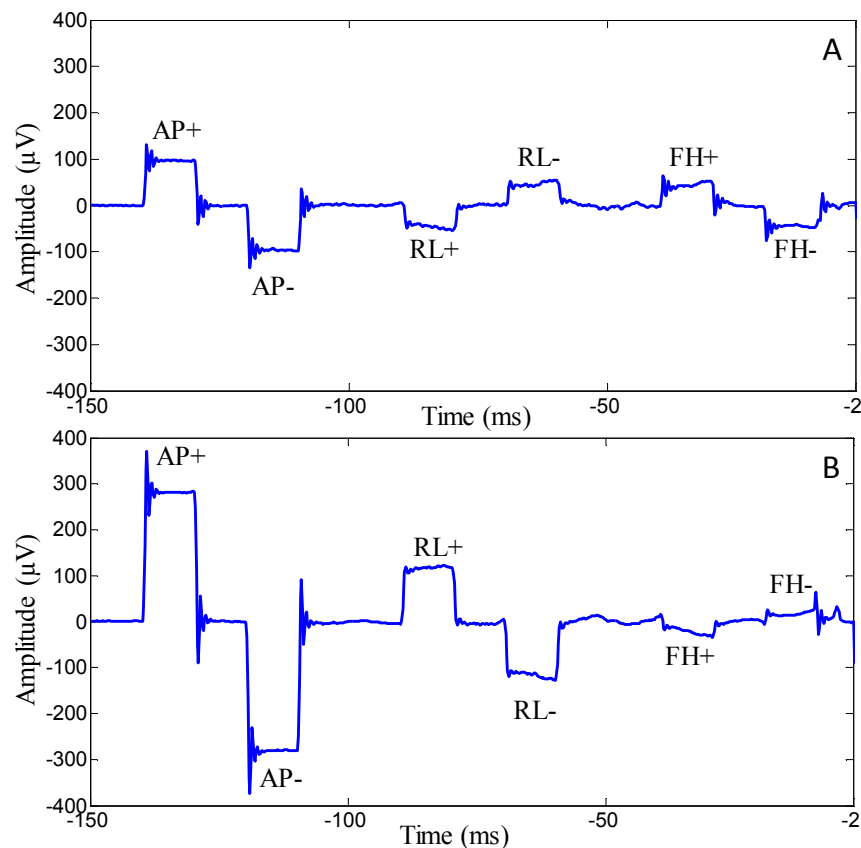


**Figure 7.4** The remaining induced artefact for AP, RL and FH gradients after subtraction of the contributions in the pairs of leads in each cable for **A**: star-quad cable & **B**: twisted pair cable when the electrode pairs were shorted on the surface of the phantom.

### 7.3.4 Conclusion to Preliminary Experiment

Figure 7.4 clearly demonstrates larger differences in the induced voltages between leads when the twisted pair cable is employed rather than the quad-star cable. This reveals the advantage of using a star-quad cable between the electrode and the break-out box of the EEG amplifier in the RLAS set-up. From this preliminary work it can be stated that the use of star-quad cable should improve the performance of the reference layer based artefact correction system, which could consequently help in better detection of neuronal activity.

### 7.4 Constructing the Reference Layer set-up

On the basis of the findings of the preliminary experiment described in the previous section, to provide the best possible matching of wire paths, the balanced pairs of wires in star-quad cable were employed for each scalp-reference lead pair. One electrode from each pair was

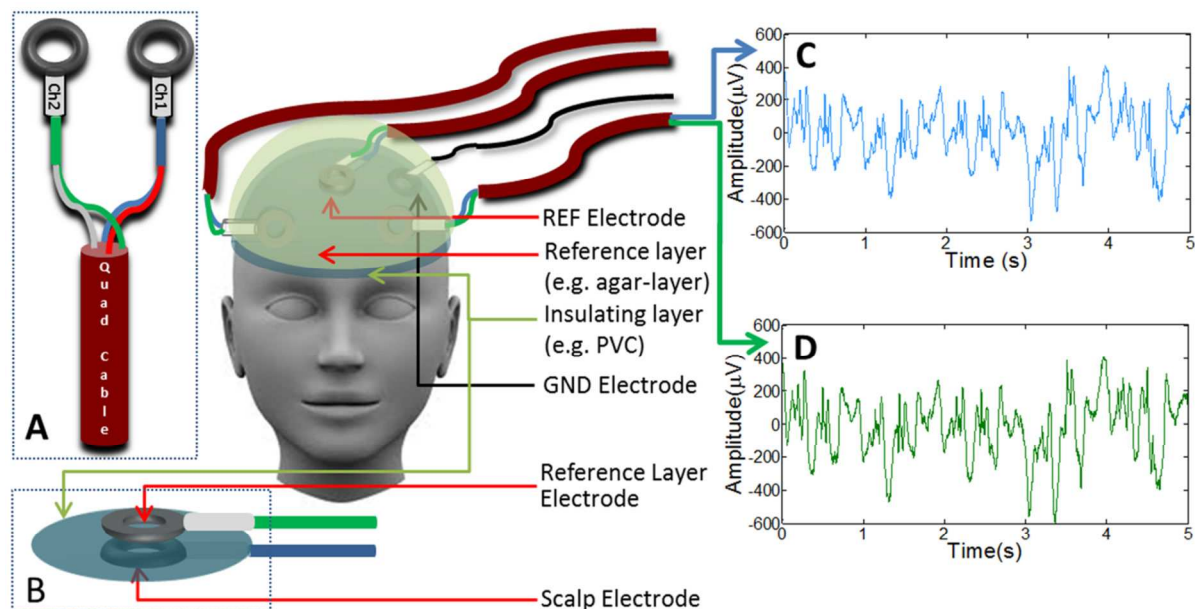


**Figure 7.5** Schematic representation of the reference layer experimental set-up. A: Electrode connections to star-quad cable; B: Electrode set-up on scalp and reference layers; EEG traces recorded simultaneously from C: phantom and D: reference channels during movement of the phantom.

attached to the scalp/phantom surface using abrasive and conductive gel (Abralyte 2000 EEG gel) and each reference layer electrode was positioned atop the corresponding scalp/phantom electrode (Fig. 7.5B) with the short sections of standard wire from the two electrodes laid on top of one another. A thin (less than 0.5mm thickness according to the findings of Chapter 6) insulating layer of polyvinyl chloride (PVC) was used to separate the electrodes on the scalp/phantom from those on the reference layer (Fig. 7.5B). The reference layer was then



placed over the electrode assembly with conductive gel used to create good connections between the reference layer electrodes and the reference layer. The ground (GND) electrode was attached to the scalp/phantom and also shorted to the reference layer by using conductive gel to form a bridge between the scalp/phantom and the reference layer through a small hole in the insulating layer, thus providing a common ground in the two layers.

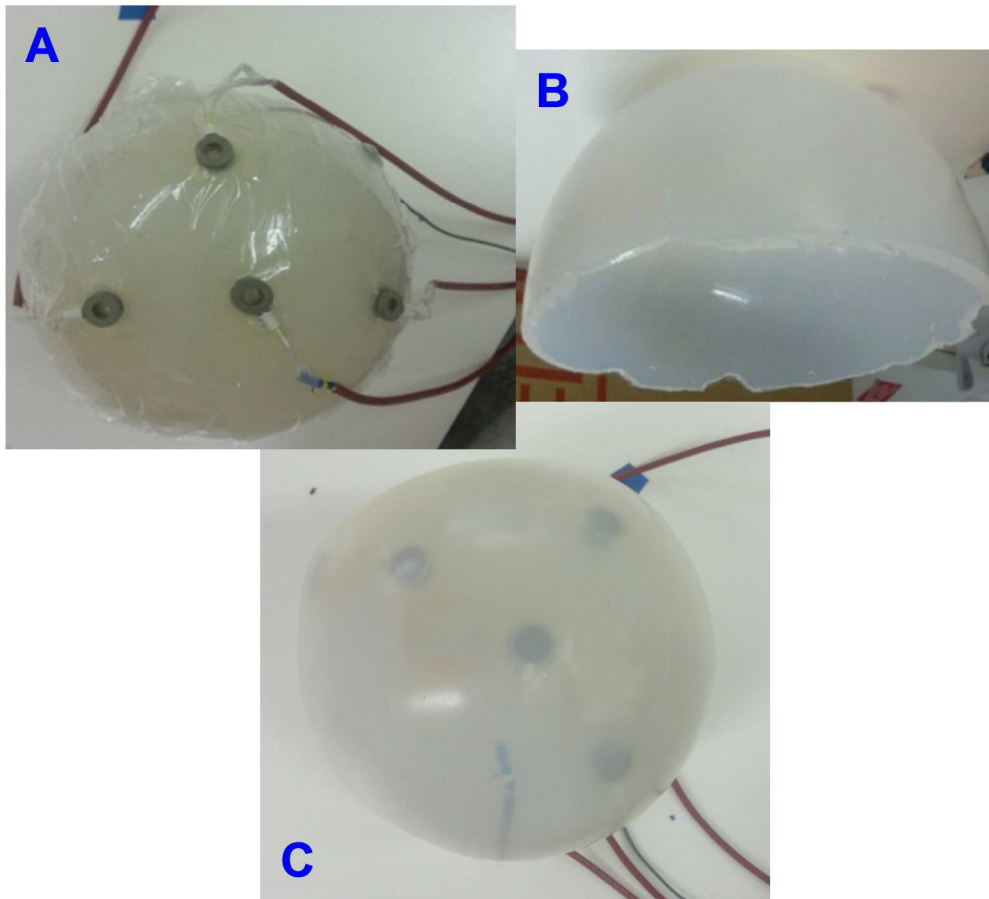


**Figure 7.6** Pictures depicting the assembly of the reference-layer set-up for use with the spherical phantom. **A:** Electrode pairs placed on the spherical phantom, along with the PVC, insulating layer which separates the scalp and reference layer electrodes. The red, quad star cables, which are connected to the electrode pairs, can also be seen. **B:** Hemispherical agar layer used to form the conductive reference layer of the cap; **C:** Reference agar layer (**B**) placed over the phantom set-up shown in (**A**).

Five electrode pairs were employed in this work. One pair formed the reference electrode pair (where the electrode used as the amplifier's reference input was attached to the scalp) which was placed centrally on the scalp. The remaining electrode pairs were positioned approximately equidistant from the reference electrode pair. The star-quad leads connected to each electrode pair were routed under the gel layer before exiting at the left or right side of

the head/phantom, coming together under the chin to form a cable bundle, which then curved behind the receiver RF coil to run axially along the bore to the rear of the magnet. Leads attached to electrodes positioned on the right (left) side of the head/phantom exited from under the reference layer on the right (left) side of the head/phantom. The lead attached to the centrally positioned reference electrode pair exited on the right hand side of the head/phantom. Figure 7.6 illustrates the steps followed in assembling the prototype reference layer set-up, when carrying out experiments on the spherical phantom (shown in Figure 7.1). The cable paths were kept as similar as possible for all recordings so as to limit variation of any voltages induced in the cables.

### 7.5 RLAS Experiments

#### 7.5.1 General Set-up

A standard, axial multi-slice EPI sequence was implemented with TR= 2 s, TE=35 ms, SENSE factor 2, a 36×36 matrix, 7 mm isotropic resolution and a five slice volume. A relatively coarse resolution was used so as to limit the maximum rate of change of the applied gradients, thus ensuring that the GA induced on the scalp or reference leads never exceeded the amplifier's dynamic range. This is not a pre-requisite of the RLAS approach, but was important here as we wanted to compare directly the voltages induced in the scalp and reference layer leads. As the cap was constructed without series safety resistors, the imaging sequence for studying human subjects was designed without RF (without this resistor if RF applied, large current flows in the wire loop which will produce highest potential at the scalp and electrode contact point making it dangerous for human subject). Seventy volumes were acquired and the five slice acquisitions were equally spaced within each TR-period. The TR and number of slices were chosen to ensure that the duration of each slice acquisition was an integer number of EEG-clock periods (the clock period was 200  $\mu$ s) as is required to allow optimal GA correction using AAS (Mandelkow *et al.*, 2006; Mullinger *et al.*, 2008c).

A series of experiments were carried out where artefact voltages were first measured using the conducting spherical/head-like phantom in order to test the efficacy of the RLAS technique under controlled conditions. Subsequently, similar measurements were made on two human volunteers (with the approval of the local ethics committee and informed consent of the subjects).

### 7.5.2 Experiment 1: RLAS vs. fEEG

An initial experiment was carried out on a spherical phantom (shown in Figure 7.1A) using the RLAS set-up described in Section 7.4 and compared with the Kappametrics (fEEG) cap (Dunseath *et al.*, 2009) (connected to a BrainAmp MR plus EEG amplifier using an in-house built connection interface) on a head-shaped phantom (as shown Figure 7.1B) to give a better fit to the fEEG cap (shown in Figure 7.7). This experiment was designed to evaluate the relative performance of RLAS and fEEG systems. EEG data were collected during the execution of the modified EPI sequence, used in Section 7.3, using both the fEEG cap and RLAS proto-type cap. The unipolar amplifier was employed so that the scalp and reference layer signals could be analysed separately and compared between set-ups.



*Figure 7.7 Picture of fEEG cap (Photo courtesy Kappametrics)*

### 7.5.3 Experiment 2: Verifying the fidelity of the RLAS approach

To test whether the use of RLAS with the prototype reference layer set-up compromised the detection of neuronal signals, an experiment was carried out on the spherical phantom outside the scanner. A primary assumption of the RLAS method is that the electrical isolation between the two layers ensures that signals generated in the brain (or phantom) are not detected at the reference layer electrodes and so are not affected when the difference of the scalp and reference layer signals is calculated. To test if any activity coming from the phantom was also detected by the reference layer, a 1 cm long current dipole was embedded in a spherical agar phantom with the dipole positioned close to the surface of the sphere. Outside the MR scanner environment, signals from the scalp and reference layer electrodes were recorded from the phantom while a 10.2 Hz sinusoidal oscillating current was applied to

the dipole so as to simulate a neuronal signal from the brain corresponding to peak–peak (p–p) dipole strength  $20 \pm 2 \text{ nAm}$ .

#### 7.5.4 Experiment 3: Phantom

This experiment, which was carried out with the phantom in the scanner, was designed to compare the efficacy of GA and MA correction using RLAS alone, RLAS followed by AAS (RLAS-AAS) and AAS only. In addition we tested the effectiveness of using RLAS and RLAS-AAS in comparison to the use of AAS alone in recovering a sinusoidal signal produced by a current dipole embedded in the phantom from EEG data affected by both GA and MA. For this purpose, EEG data were recorded from the phantom in four different situations:

**Experiment 3a - GA only:** EEG data were recorded from the stationary phantom during execution of the multi-slice EPI sequence.

**Experiment 3b - MA only:** To simulate the effects of the head movements that occur during fMRI, data were recorded while the phantom was moved, in a continuous, periodic manner, inside the magnetic bore continuously for approximately 30s without the application of MR gradients. The amplitude of movements was limited so that the maximum displacement of points of the sphere's surface was around 7 mm or less. In these and other phantom experiments involving MA generated movements by lightly pushing and then releasing the phantom, so as to cause small rotations and translations.

**Experiment 3c - GA and MA:** In this case, data were recorded while the phantom underwent controlled movements during execution of the EPI sequence. The phantom was moved up to three times during the whole acquisition with the number and size of the rotational and translational movements varied across the four datasets which were acquired (1 small movement of  $<0.2$  mm magnitude, 3 small movements of  $<0.5$  mm, 1 large movement of  $<5$  mm and 3 large movements of  $<7$  mm over the whole acquisition). The duration of each period of movement was approximately 4 seconds.

**Experiment 3d - GA and MA with sinusoidal current present:** The recordings described under Experiment 3c were repeated (1 small movement of  $<0.2$  mm magnitude, 1 large movement of  $<1$  mm, 3 small movements of  $<0.5$  mm and 3 large movements of  $<3$  mm over the whole acquisition) using the phantom containing a current dipole, while the dipole was driven with a sinusoidal current at a frequency of 11 Hz (as described in Experiment 2, Section 7.5.2) so as to mimic neuronal activity.

### 7.5.5 Experiment 4: Human Subjects

The final set of experiments was designed to assess the effectiveness of RLAS and RLAS-AAS compared with AAS when applied to data recorded from human subjects in the presence of GA, MA and PA. Two of the electrodes were placed over the visual cortex (to measure alpha power) and the other two either placed over the temples (to maximise sensitivity to the PA) or over the frontal lobe. To ensure subject safety, the RF pulse amplitude was set to zero, as the cap configuration had not fully been tested for RF heating effects and there were no series resistors between the electrodes and leads in this prototype cap (as described in Chapter 4, Section 4.3.1). All EEG measurements described below were made on two healthy volunteers in four different situations:

**Experiment 4a - PA:** Recordings were made from two subjects inside the MR scanner with no MR gradients applied. The subjects were asked to remain still so that the PA was the dominant artefact.

**Experiment 4b - MA only:** To simulate the effects of the head movements that occur during fMRI, data were recorded while the subject moved (gentle nodding or shaking of the head, causing head movement of less than 5 mm in magnitude) inside the magnetic bore continuously for approximately 30s without the application of MR gradients. This experiment was carried out on both subjects.

**Experiment 4c- GA and PA:** Recordings were made from both subjects during the execution of the multi-slice EPI sequence. In each case, the subject was asked to remain still, so that the GA was the dominant artefact.

**Experiment 4d - GA, PA and MA:** Two recordings were made from the subjects during execution of the multi-slice EPI sequence. During the first recording, the subject was asked to make one head movement (gentle head nod) during the acquisition, while in the second recording, three movements (gentle head nods) were made during the acquisition. The approximate duration of each period of movement was five seconds.

**Experiment 4e - GA, PA and MA with changes in neuronal activity:** It is well known that alpha activity (8-13Hz neuronal oscillations) measured with EEG is strong in healthy individuals at rest with their eyes closed, and is suppressed by opening the eyes (Adrian *et al.*, 1934). Therefore to test the effect of RLAS on the detection of neuronal activity, an experiment was carried out in which changes in alpha activity were induced by asking the subjects to open their eyes for 30 seconds and then to close them for 30 seconds (as mentioned in Chapter 2, Section 2.6.1). During this period, EEG recordings were made while

the multi-slice EPI sequence was executed. The subject was also asked to move their feet (to cause small head rotations and translations typical of longer fMRI experiments) (Mullinger *et al.*, 2011) for a five second period during the recording.

## 7.6 Analysis of RLAS Experiments

Initial analysis steps for RLAS and AAS were carried out using Brain Vision Analyzer 2 (Version 2.0.1; Brain Products, Munich, Germany) while MATLAB (The MathWorks) was used for further quantification of the efficacy of artefact correction that could be achieved using the different methods.

### 7.6.1 Artefact removal using RLAS

To implement RLAS, the reference layer signals were re-referenced using Brain Vision Analyzer 2 to the channel in the reference layer which overlaid the electrode on the scalp/phantom that was connected to the amplifier's reference input. Raw EEG signals were high-pass filtered with a 0.02 Hz cut-off frequency to remove any slow drifts. The signal from each reference layer electrode was then subtracted from the corresponding scalp electrode signal to yield RLAS-corrected EEG signals.

### 7.6.2 Artefact correction using AAS

The GA correction process used an average artefact waveform of 400 ms duration, formed from the average over all of the slice periods that were identified using the scanner-generated markers. This average slice artefact template was then subtracted from each occurrence of the GA. AAS was carried out on the raw scalp recordings (AAS<sub>GA</sub>) and RLAS corrected data (RLAS-AAS<sub>GA</sub>). No additional filtering or down-sampling was applied during the artefact removal process.

PA correction was carried out on the data that had been acquired on the human subjects after gradient artefact correction. Here, the AAS method (Allen *et al.*, 1998) used templates of the PA formed from the preceding 10 s of data recorded on each channel. These were formed by using R-peak markers derived from the ECG trace in conjunction with the direct detection method (Allen *et al.*, 1998) in the Brain Vision Analyzer2 software. Any incorrectly positioned R-peak markers were manually repositioned. The EEG recordings were then segmented using the R-peak markers (-100 ms to +600 ms in extent relative to the R-peak)

and baseline-corrected based on the 100 ms of data recorded before each R-peak (-100 ms to 0). The template on each channel was then subtracted from the data to eliminate each occurrence of the PA. PA correction via AAS was carried out on the  $AAS_{GA}$  data ( $AAS_{GA}-AAS_{PA}$ ) and the RLAS- $AAS_{GA}$  data ( $RLAS-AAS_{GA}-AAS_{PA}$ ) to enable assessment of the total possible gain in performance of artefact corrections which can be achieved by using RLAS in conjunction with post processing methods.

### 7.6.3 Evaluation of correction methods

To determine the efficacy of the new RLAS system compared with the fEEG cap, the differences between the artefacts induced in each of the layers for the fEEG and RLAS systems were calculated. The C3 electrode was chosen in analysing the signals from the fEEG system, as this electrode position was most similar to the electrode position used in the RLAS set-up.

To evaluate the efficacy of GA correction, the corrected data from Experiments 3 and 4 were exported to MATLAB, where the RMS magnitude of the artefact voltages over time was calculated from the raw data and then from data that had been subjected to: (i)  $AAS_{GA}$ , (ii) RLAS and (iii)  $RLAS-AAS_{GA}$ . Results were converted to attenuation relative to the raw signal for each channel for each data set and the mean, maximum and minimum attenuation over channels was evaluated.

The effectiveness of PA correction was assessed by calculating the average and standard deviation of the pulse artefact waveform (from data acquired in Experiment 4a), before and after PA correction using  $AAS_{PA}$ , RLAS and  $RLAS-AAS_{PA}$ . In addition the reduction in the RMS of the artefact voltages due to application of  $AAS_{GA}-AAS_{PA}$ , RLAS and  $RLAS-AAS_{GA}-AAS_{PA}$  was calculated from the data acquired in Experiment 4c to allow evaluation of the efficacy of the artefact correction in the presence of pulse and gradient artefacts.

Motion artefacts cannot be corrected using AAS, so our analysis of MA correction focused on testing the efficacy of RLAS. This was done by calculating the RMS amplitude of the signal during periods of movement before and after application of RLAS. To test the capability of RLAS to remove the artefacts without affecting signals of interest, power

spectra were calculated from the data acquired in Experiments 3d and 4e before and after correction using the different approaches.

## 7.7 RLAS Results

### 7.7.1 RLAS vs. fEEG

Figure 7.8A demonstrates that the signal recorded from the phantom using the fEEG system (blue) does not closely follow that recorded on the reference layer (red); whereas, for the RLAS system (Figure 7.8B) the scalp and reference layer signals closely follow one another.

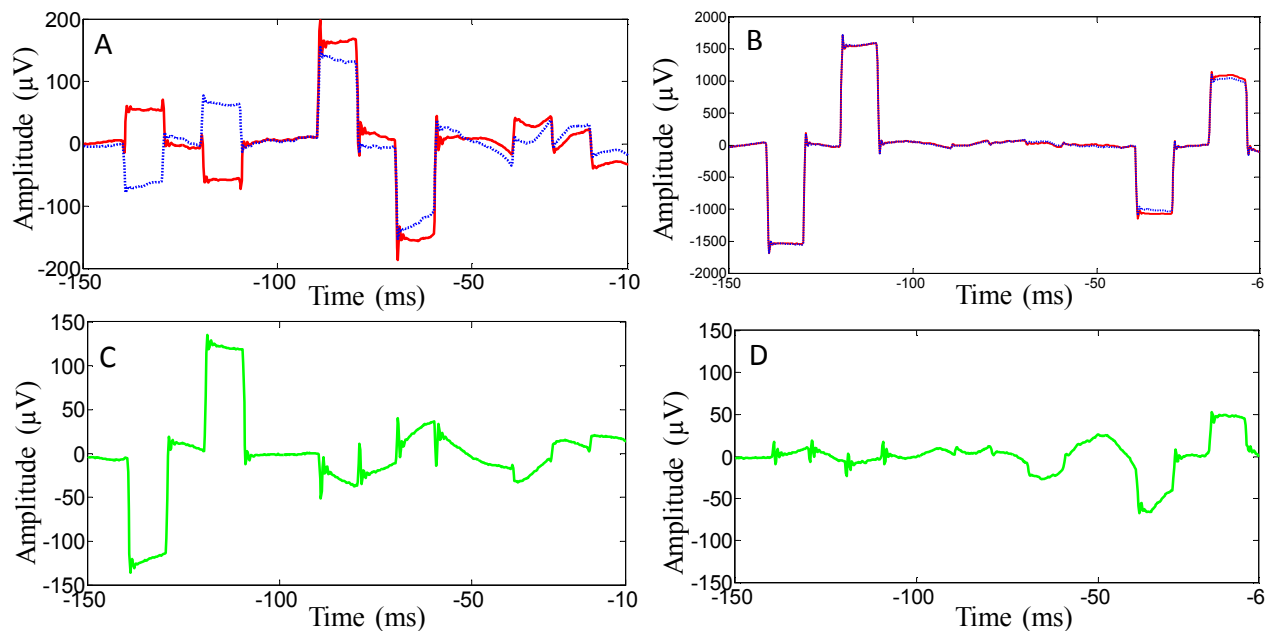


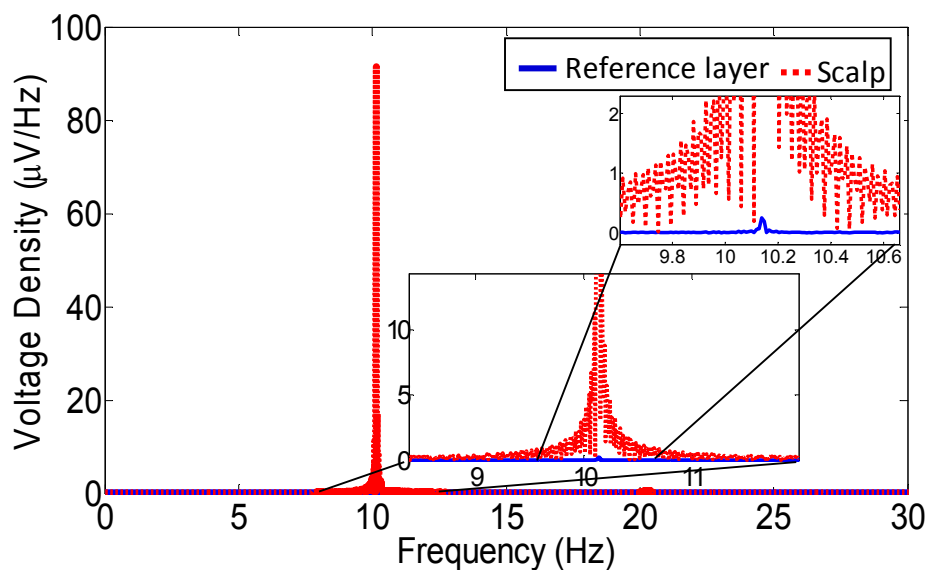
**Figure 7.8** EEG traces recorded on a phantom from the scalp electrode (blue) and reference layer electrode (red) for the three orthogonal gradients (AP, RL, and FH) for **A**: fEEG system & **B**: RLAS system. Difference (green) between the scalp and reference layer recorded signals for **C**: fEEG system & **D**: RLAS system. Note the different scales in **A**&**B**.

By taking the difference between the artefacts induced in each of the layers for the fEEG (Fig. 7.8C) and RLAS systems (Fig. 7.8D) the differences in the performance of the two reference layer approaches (fEEG and RLAS) can be seen. This was reflected in the RMS of the difference voltages between the scalp and reference layer electrodes which took values of: 242/13, 54/29, 41/109  $\mu\text{V}$  for the fEEG/RLAS systems for the AP, RL and FH gradients respectively. In these data, the percentage reduction from the uncorrected signal (measured on the scalp) of each of the gradients (AP, RL and FH) were 182/0.4 %, 16/74 % and 256/5% respectively for fEEG/RLAS system. It might be worth mentioning here that the artefact due to the RL gradient was very small in magnitude for the RLAS system so the percentage reduction is not very meaningful for this gradient.



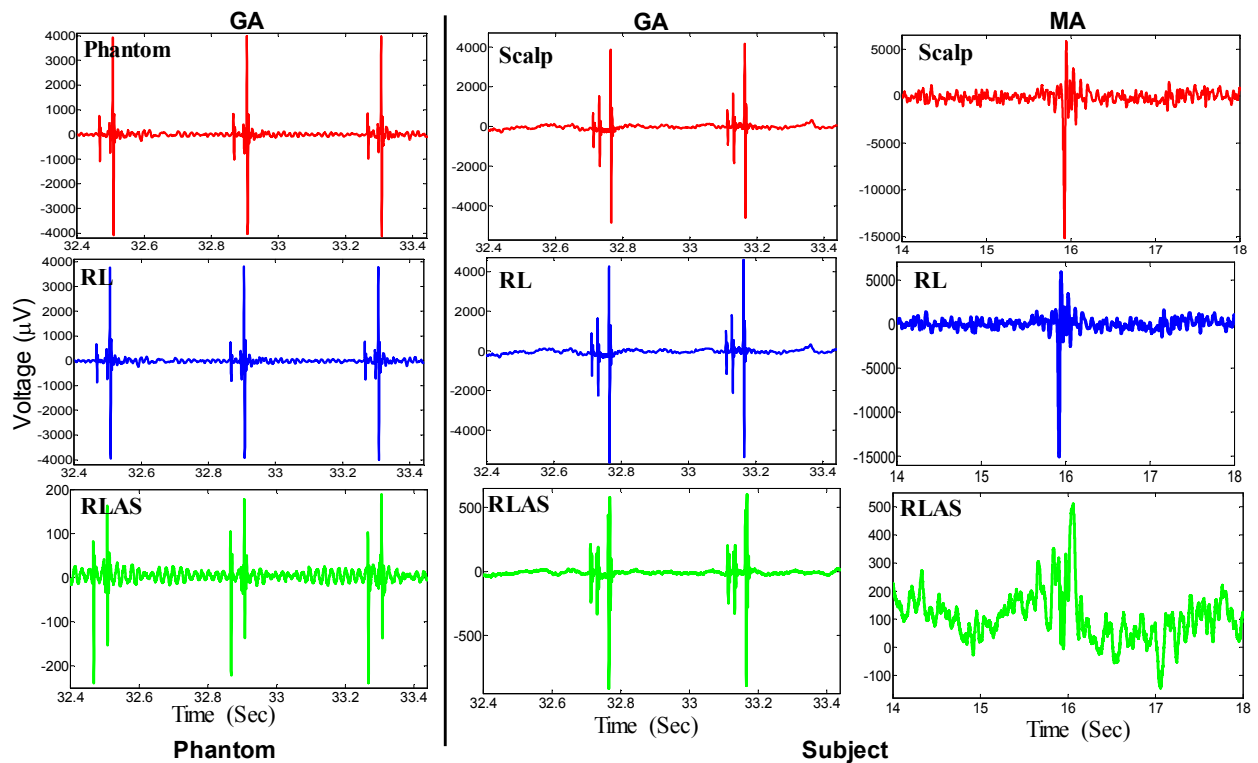
### 7.7.2 Verifying the fidelity of the RLAS approach

Figure 7.9 shows spectra of the signals sampled from electrodes on the spherical phantom and reference layer in Experiment 2. A strong peak resulting from the 10.2 Hz current that was applied to the dipole embedded in the agar sphere is evident in the spectrum from the “scalp” electrode, but is almost absent (91 dB attenuation compared with the scalp signal) in the spectrum of the signal from the reference layer electrode.



**Figure 7.9:** FFT of the EEG signals recorded from an electrode on the surface of the spherical phantom (red) and on the reference layer (blue) when the dipole embedded in the phantom was driven at 10.2 Hz.

Figures 7.5C&D show example traces recorded from a reference layer electrode and associated scalp electrode on the phantom while the phantom underwent small continuous movements inside the scanner in Experiment 3b. The strong similarity of the artefact voltages in the two traces, which forms the basis of RLAS, is evident. Figure 7.10 shows that the artefact voltages appearing in the reference and scalp traces are similar during multi-slice EPI acquisition for the phantom (Experiment 3) and human subject (Experiment 4c), and also show a high degree of similarity during the head movements that were made in the absence of time-varying MR gradients in Experiment 4b.



**Figure 7.10** *Left column:* EEG signal recorded from an electrode on the spherical phantom during the execution of the multi-slice EPI sequence (red); re-referenced signal from the corresponding reference layer electrode (blue); the difference of phantom and RL produced by RLAS (green). *Middle column:* similarly colour-coded signals recorded from a human subject during execution of the multi-slice EPI sequence. *Right column:* similar signals recorded from human subject undergoing head movements in the 3 T static magnetic field. Note that different voltage ranges have been used for these plots, since the RLAS data spans a much smaller voltage range than the recordings from the scalp or reference layer.

### 7.7.3 Comparing artefact removal methods:

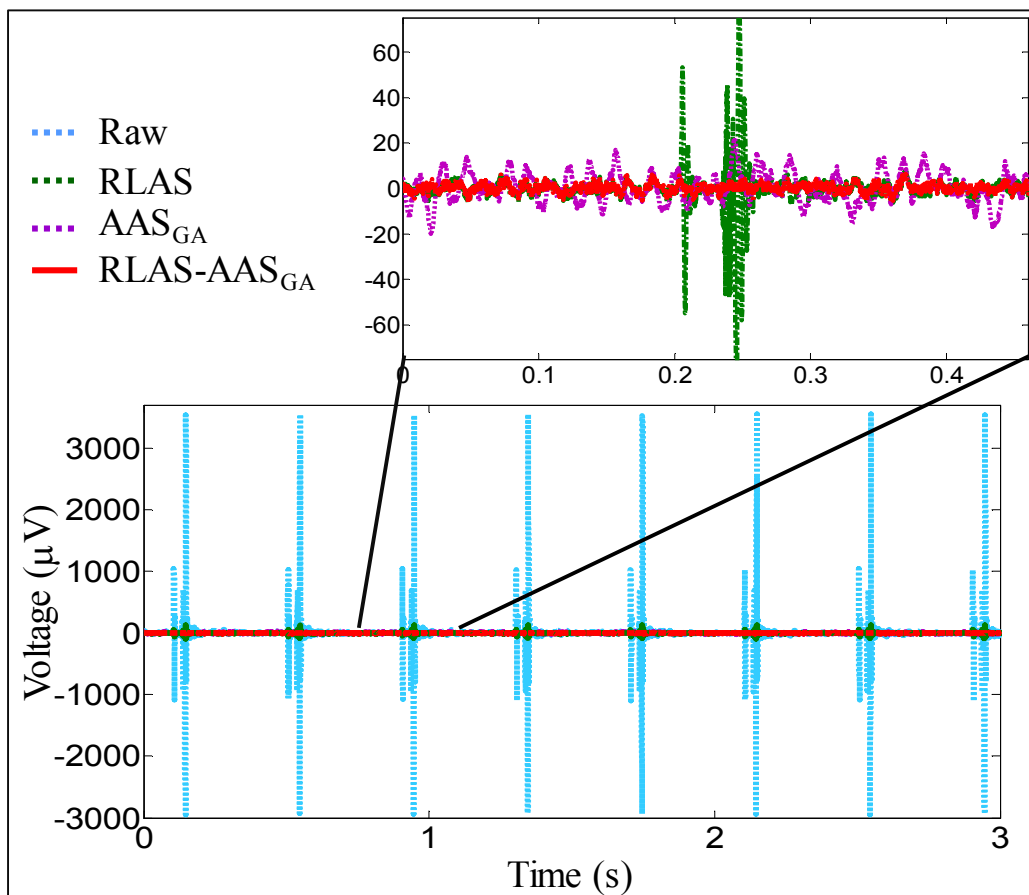
#### 7.7.3.1 Phantom Data:

Figure 7.11 shows a portion of the EEG trace recorded from a scalp electrode on the stationary phantom during the multi-slice EPI acquisition of Experiment 3a. Corresponding traces produced after correction using  $AAS_{GA}$ , RLAS and  $RLAS-AAS_{GA}$  are also shown. The strong gradient artefacts, repeated five times in each 2s TR period, can be seen clearly in the raw trace (blue) and in a greatly attenuated form in the trace produced after RLAS (green). With the phantom stationary, the GA is highly reproducible across repeated slice acquisitions and  $AAS$  (pink) consequently performs very well producing a reduction of the RMS voltage averaged across lead pairs of 26 dB (maximum/minimum = 31/21 dB) compared to the raw data, whilst RLAS yields a 24 dB attenuation (maximum/minimum = 29/17 dB). Further attenuation of the artefacts was achieved by performing RLAS followed by  $AAS_{GA}$  (red

trace), yielding an average 41 dB reduction (maximum/minimum = 44/38 dB) of the RMS voltage relative to the raw data, and leaving the cleanest signal (as shown in Table 7.1) with a maximum (peak-to-peak) signal range of 20  $\mu\text{V}$ .

Phantom			
Correction Method/ Artefacts	AAS <sub>GA</sub>	RLAS	RLAS-AAS <sub>GA</sub>
GA Only (Experiment 3a)	26	24	41
MA Only (Experiment 3b)	n/a	30	n/a
GA-MA (Experiment 3c)	16	22	31

**Table 7.1** Average attenuation in dB, over all relevant datasets acquired from the phantom, which was achieved by using each of the correction set methods. “n/a” indicates when a correction method was not applied to the specific data set.



**Figure 7.11** Raw EEG signals recorded over 3 s from the stationary phantom during execution of multi-slice EPI sequence (blue) and after correction using AAS<sub>GA</sub> (purple), RLAS (green) and RLAS-AAS<sub>GA</sub> (red). Inset shows expanded plots of AAS<sub>GA</sub>, RLAS and RLAS-AAS<sub>GA</sub> data from a 0.45 s period.

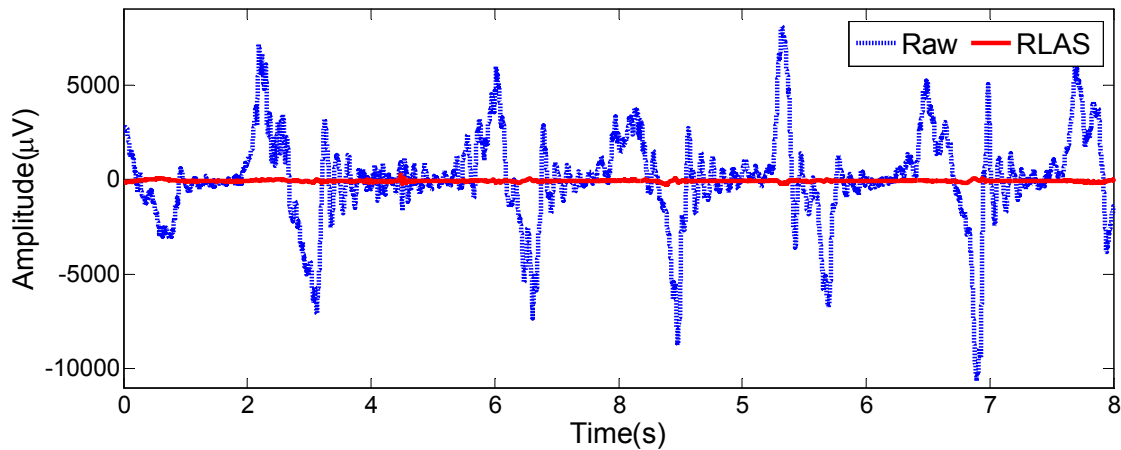


**Figure 7.12** Raw EEG data recorded from the spherical phantom over an 8 s period of movement in the static magnetic field (blue) and after RLAS (red).

Figure 7.12 shows the effect of RLAS on the MA produced when the phantom was moved inside the scanner (in the absence of scanning) in Experiment 3b. Movement-induced voltages of more than 10 mV in amplitude are evident in the raw data (blue trace), but are greatly attenuated by the application of RLAS. In these data, the RMS artefact voltage over the whole acquisition was attenuated by 30 dB (maximum/minimum = 35/25 dB) by RLAS.

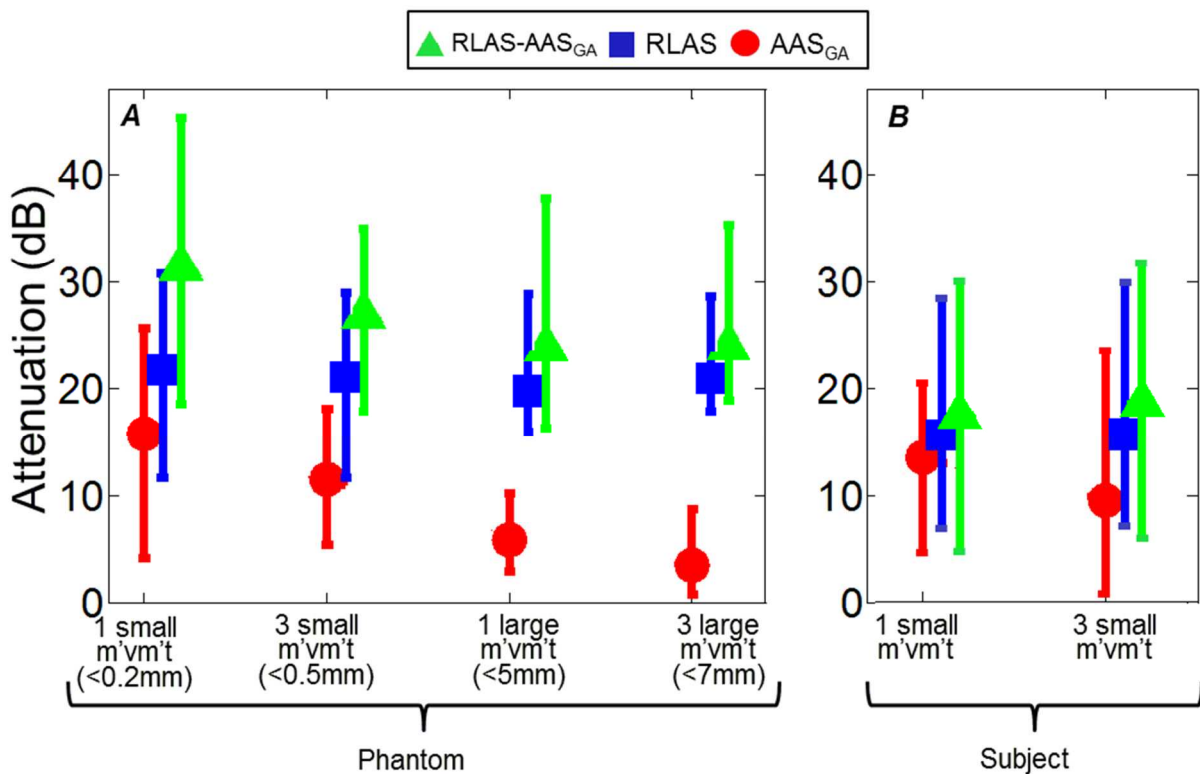


**Figure 7.13** Mean RMS attenuation over channels for the phantom (A) and subject (B) data after correction with  $AAS_{GA}$  (red), RLAS (blue) and  $RLAS-AAS_{GA}$  (green) for varying degrees of movement ( $m'vm't$ ). Error bars denote the range of attenuation values across channels (maximum–minimum).

Figure 7.13A characterises the efficacy of artefact correction that was produced by applying the different correction methods to data recorded from the phantom in Experiment 3c, in which the phantom underwent different degrees of movement during a multi-slice EPI acquisition. The markers indicate the average over channels of the attenuation of the RMS voltage, while the tips of the error bars indicate the maximum and minimum attenuation across channels. This figure indicates that RLAS outperforms  $AAS_{GA}$  in all experiments and that implementing  $AAS_{GA}$  after RLAS provides further attenuation of artefacts. The performance of  $AAS_{GA}$  is particularly compromised when multiple, large movements occur.

Figure 7.14 shows data that were recorded from one electrode pair attached to the phantom containing the current dipole in Experiment 3d, during which the phantom was moved whilst the multi-slice EPI acquisition was executed. Raw data (blue trace) from a 1.2 s period of the recording (within the 4 s movement epoch) are shown in Fig. 7.14A, along with corresponding traces produced after correction using  $AAS_{GA}$  (purple), RLAS (green) or RLAS- $AAS_{GA}$  (red). The GA's occurring every 0.4 s are strongly evident in the raw data (the 988  $\mu\text{V}$  peak-to-peak amplitude of the GA exceeds the  $\pm 400 \mu\text{V}$  range shown in the plot). Residual GA's appear with much reduced amplitude in the RLAS data, but are removed by the subsequent application of AAS. There are significant residual motion artefacts in the

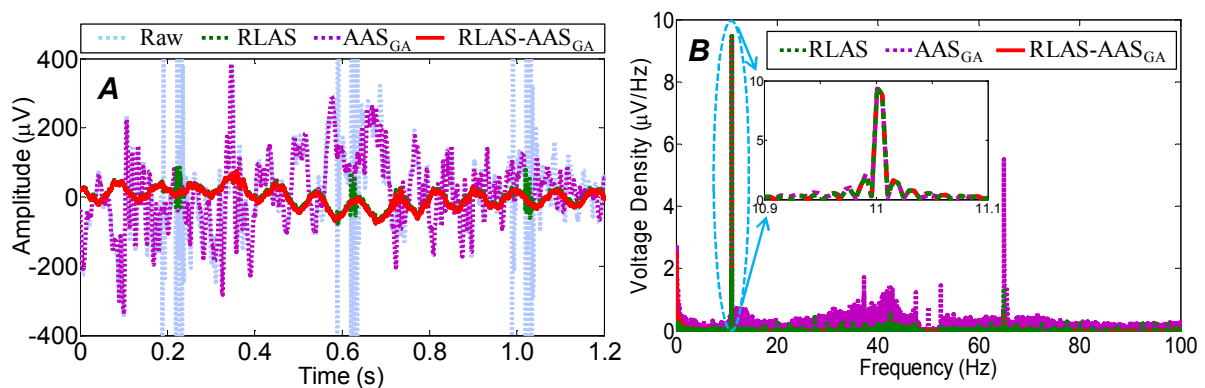


**Figure 7.14** EEG signals recorded from the spherical phantom containing a current dipole, which was driven with a current varying at 10.2 Hz, during execution of the multi-slice EPI sequence and movement of the phantom. Raw data (light blue) and data formed after correction using  $AAS_{GA}$  (purple), RLAS (green) and RLAS- $AAS_{GA}$  (red) are shown over a 1.2 s period (A) along with the square root of the power spectra (B).

$AAS_{GA}$  data which mask the 11 Hz signal from the current dipole, but this signal is evident in the RLAS data even before application of AAS. For the phantom data of Experiment 3d, the RMS artefact voltages averaged over all channels were attenuated on average by 19 dB (maximum/minimum= 23/15 dB), 20dB (maximum/minimum= 26/12 dB) and 25 dB

(maximum/minimum= 29/19 dB) by using  $AAS_{GA}$ , RLAS and RLAS- $AAS_{GA}$  respectively (as shown in Table 7.1). Figure 7.14B shows the power spectra calculated from the data recorded over the whole 140 s of the experiment.

### 7.7.3.2. Human Subject Data:

Figure 7.10 clearly shows the similarity of the GA and MA in the traces from the reference layer and scalp leads in data from Subject 1. This indicates that the voltages generated by temporally varying magnetic field gradients are similar on the reference layer and scalp leads, despite the non-spherical shape of the head and reference layer, and that this is also the case for voltages due to rotation in a uniform magnetic field.

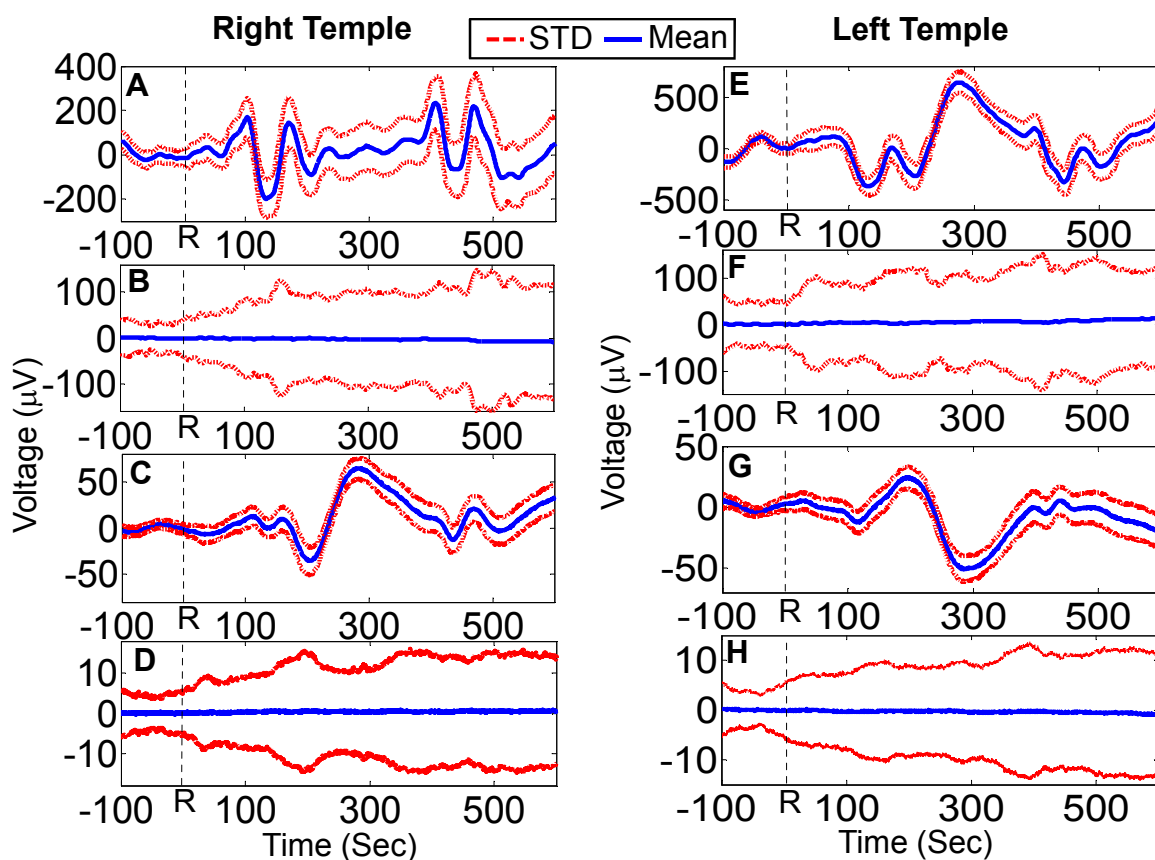


**Figure 7.15** A representative single subject EEG trace from a right/left temple channel averaged over all cardiac cycles occurring in a 2-min period before (A/E) and after correction using  $AAS_{PA}$  (B/G), RLAS (C/F) and RLAS- $AAS_{PA}$  (D/H), with the red dashed lines indicating the standard deviation of each average waveform. In these traces, R corresponds to the occurrence of the R-peak in the ECG recording. R-markers derived from the ECG recordings were used in carrying out AAS. Note that different voltage ranges are used in the different plots.

Figure 7.15 shows data from Experiment 4a in which recordings were made while Subject 1 lay stationary in the scanner with no scanning occurring, so that the PA was the dominant

artefact. Raw data from electrodes attached to the right and left temples are shown, along with data corrected using  $AAS_{PA}$ , RLAS and RLAS- $AAS_{PA}$ . Figure 7.15A/E shows the average PA waveform recorded from the scalp electrode positioned on the right/left temple over 150 cardiac cycles occurring in a 2-min period. The standard deviation of the voltage across the 150 cardiac cycles is also indicated at each time point using red dotted lines. Figure 7.15B/F shows the average and standard deviation of the PA after application of  $AAS_{PA}$  to the raw data from the right/left temple, while Fig. 7.15C/G shows data after application of RLAS and Fig. 7.15D/H shows data resulting from the application of RLAS and  $AAS_{PA}$ . As expected, AAS reduces the average PA approximately to zero, but there is a significant variation of the residual PA across cardiac cycles, which is indicated by the standard deviation of around  $100 \mu V$  shown in Fig. 7.15B & F. After application of RLAS the amplitude of the average PA is significantly attenuated (right/left peak-to-peak voltage in raw data  $402/1013 \mu V$  versus  $85/76 \mu V$  in RLAS data) and the standard deviation of the PA is also reduced (Fig. 7.15C & G). The reduced variability of the PA is particularly evident in the RLAS- $AAS_{PA}$  data produced by applying both RLAS and AAS to the data. Comparing the plots shown in Fig. 7.15D/H to those in 7.15B/F indicates that the standard deviation across cardiac cycles is reduced by a factor of around 10 by the use of RLAS.

Figure 7.16 shows EEG data recorded from an electrode pair located on the right temple in Experiment 4c in which Subject 1 remained still during execution of the multi-slice EPI sequence, yielding maximally reproducible GA and PA. Raw data (pale blue) recorded over a 2 s period is shown in Fig. 7.16A along with data corrected using the following combinations of correction methods:  $AAS_{GA}$  (purple),  $AAS_{GA}$ - $AAS_{PA}$  (light green), RLAS (dark green), RLAS- $AAS_{GA}$  (red) and RLAS- $AAS_{GA}$ - $AAS_{PA}$  (blue). The corrected data are shown on an expanded scale in Fig. 7.16B. GA with peak-to-peak amplitude of more than 4 mV is evident in the raw data (Fig. 7.16A) and also appears with much reduced amplitude in the RLAS data (Fig. 7.16A&B). After GA correction using AAS, a PA of around  $400 \mu V$  peak-to-peak amplitude is evident in the  $AAS_{GA}$  data and is also seen, but with a significantly reduced amplitude in the RLAS- $AAS_{GA}$  data. The latencies of the peaks of the PA relative to the occurrence of the R-peak, which can be gauged by comparison to the ECG trace shown in Fig. 7.16C, are similar to those shown in Fig. 7.15. The PA is significantly attenuated by

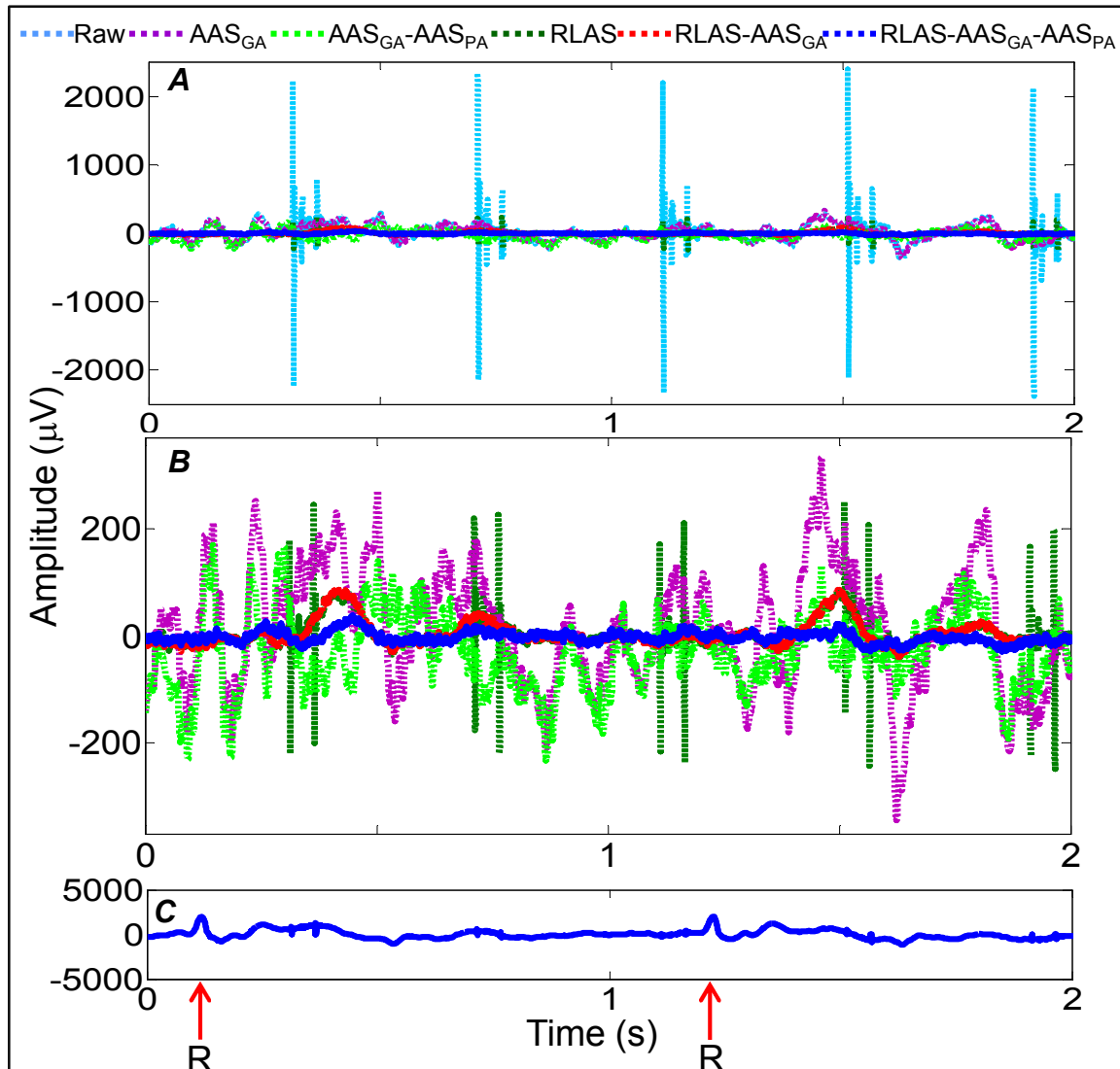


**Figure 7.16** (A) EEG signal recorded from an electrode on the left temple over a 2 s period during execution of the multi-slice EPI sequence (blue) and (B) after correction using AAS<sub>GA</sub> (purple), AAS<sub>GA</sub>-AAS<sub>PA</sub> (light green), RLAS (dark green), RLAS-AAS<sub>GA</sub> (red) and RLAS-AAS<sub>GA</sub>-AAS<sub>PA</sub> (blue). (C) Corresponding ECG trace with R peaks, marking the onset of each cardiac cycle, depicted. Note that different voltage ranges have been used in each sub-plot so as to display clearly the detail of the signal waveforms.

application of AAS, yielding the AAS<sub>GA</sub>-AAS<sub>PA</sub> (light blue) and RLAS-AAS<sub>GA</sub>-AAS<sub>PA</sub> (blue) data. Comparison of these two traces indicates that the noise level in the data that has been subjected to RLAS is significantly reduced, presumably due to a reduction of residual GA and PA, as well as MA due to small subject movements. Analysing the data from all leads over the whole recording we found that the RMS voltages were attenuated relative to the raw data by 11 dB (maximum/minimum = 14/5 dB), 14 dB (max./min. = 17/8 dB), 15 dB (max./min. 16/14 dB), 25 dB (max./min.= 28/20 dB) and 27dB (max./min. 29/24 dB) by AAS<sub>GA</sub>, AAS<sub>GA</sub>-AAS<sub>PA</sub>, RLAS, RLAS-AAS<sub>GA</sub> and RLAS-AAS<sub>GA</sub>-AAS<sub>PA</sub>, respectively (as



shown in Table 7.2). The aspects of these findings related to the GA are confirmed by the plots shown in Fig. 7.13B, which depict the efficacy of GA correction that was produced by applying the different correction methods to data recorded in Experiment 4d, in which the two subjects executed different degrees of movement during a multi-slice EPI acquisition. As was found in the case of the moving phantom (Fig. 7.13A) RLAS outperforms  $AAS_{GA}$  in all experiments and implementing  $AAS_{GA}$  after RLAS provides further attenuation of artefacts.

Figure 7.17 shows the results from Experiment 4e in which changes in alpha activity between eyes-open and eyes-closed conditions were measured during scanning, with Subject 2 executing foot movements over a 5s period during the minute. Figure 7.17A shows power spectra from the 30s-epoch during which the subject’s eyes were open. These were produced using RLAS and are shown before (red) and after (blue) application of AAS for correction of the GA and PA. Spectra produced from scalp data after application of only AAS for GA and PA correction (green) are also shown. Data were taken from an electrode pair located over the occipital lobe, while the reference channel was positioned close to the Cz position in the 10/20 system. Figure 7.17B shows similar data for the 30 s eyes-closed period. Inspection of the expanded plots spanning the 8-12 Hz frequency range shows similarly increased power in the alpha frequency range in the eyes-close condition in all data, indicating that application of RLAS has not significantly affected the measurement of brain signals. In particular, the increase in alpha power is clear in the RLAS data (red) which has not been subject to any additional post-processing.

Correction Method/ Artefacts	Subjects						
	$AAS_{PA}$	$AAS_{GA}$	RLAS	$AAS_{GA} - AAS_{PA}$	RLAS- $AAS_{PA}$	RLAS- $AAS_{GA}$	RLAS- $AAS_{GA} - AAS_{PA}$
PA Only (Experiment 4a)	3	n/a	18	n/a	19	n/a	n/a
GA-PA (Experiment 4c)	n/a	11	15	14	n/a	25	27
GA-MA-PA (Experiment 4d)	n/a	14	16	n/a	n/a	18	n/a

**Table 7.2** Average attenuation in dB, over all relevant datasets acquired from the human subjects, which was achieved by using each of the correction methods. “n/a” indicates when a correction method was not applied to the specific data set.

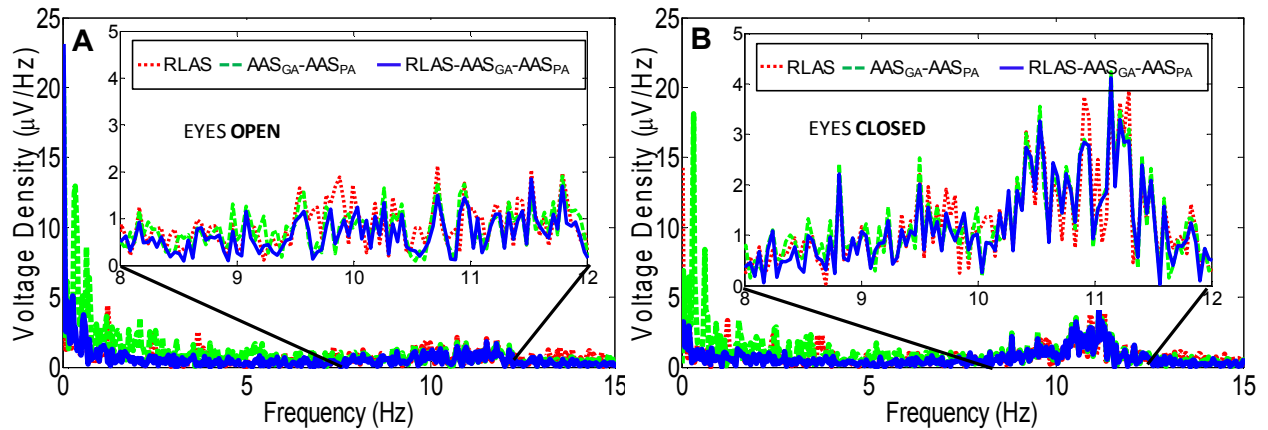


**Figure 7.17** FFT of the corrected EEG signal from a channel over the left visual cortex of a representative subject for the eyes open (A) and eyes closed data (B): correction using RLAS (red) AAS<sub>GA</sub>-AAS<sub>PA</sub> (green) and RLAS-AAS<sub>GA</sub>-AAS<sub>PA</sub> (blue). Note that here RLAS correction is shown in red.

## 7.8 Discussion

The results of the experiments carried out using the prototype reference layer system indicate that RLAS forms a viable method for attenuating at source the artefacts that are generated in EEG data recorded during concurrent fMRI experiments by time-varying magnetic field gradients, cardiac pulsation and head movements. The results also demonstrate that RLAS can be used in conjunction with AAS further to attenuate gradient and pulse artefacts and that the use of RLAS does not confound the recording of brain signals.

The findings from Experiment 1 show (Fig. 7.8) that the proto-type RLAS system developed in this chapter has superior performance to the fEEG system. It is clear that the artefacts induced in the scalp and reference layers by the AP and FH gradients are much larger in amplitude for the RLAS system than for the fEEG system. This difference in induced artefact might be linked with the arrangement of the leads running over the surface of the fEEG cap (Figure 7.7) which come together in a cable bundle at the crown of the head, like the standard EasyCap EEG cap (Chapter 4, Figure 4.4A). In contrast, the leads in the RLAS set-up come out of cap differently; leads ran in an inferior direction from the electrodes and left the scalp on the left or right side of the head depending on the location of the electrode (Figure 7.6C). This causes the wire paths to be longer, thereby increasing the raw artefact amplitude. Despite the larger induced artefacts in the RLAS system the similarity of the artefacts in the two layers was greater than in the fEEG system, resulting in the improved performance in artefact elimination. This difference in performance occurs despite the fundamental concept

of using a reference layer to replicate the artefact induced in scalp being same in both systems. The differences are likely to arise from the materials and set-up of the systems and primarily the cable used between the cap and amplifier: i.e. a twisted-pair cable for the fEEG system and star-quad cable for the RLAS system. The differences in performance could also be due to the materials used (size/thickness) for the insulating layer which the reference layer system is known to be sensitive to, as shown in the simulation work described in Chapter 6. Therefore the RLAS system developed here shows the potential to provide superior correction of all artefacts and was used in all of the further experiments.

The results of Experiment 2 (Fig. 7.9) demonstrate that in the model system consisting of a current dipole embedded in a conducting agar sphere, voltages resulting from a time-varying current in the dipole are not sensed by reference layer electrodes, although they are picked up by electrodes on the phantom's surface. Consequently RLAS does not attenuate the voltage produced by the current dipole inside the sphere and can be expected similarly to preserve brain signals generated at the scalp surface in human studies. This is borne out by the results of Experiment 4e (Fig. 7.17) in which an elevation in the alpha power as a result of the subject closing their eyes, is still clearly detected when RLAS is applied.

The results of Experiment 3 demonstrate the efficacy of RLAS in attenuating the GA and MA under ideal conditions, in which: (i) the reference layer forms a hemisphere which accurately overlays a spherical conductor; (ii) there are no brain signals nor PA to add to the signal variance; (iii) movements are under the control of the experimenter. The similarity of the artefact voltage waveforms recorded from the scalp and reference layer electrodes when the phantom is moved in the 3 T magnetic field or the time-varying gradients needed for implementation of multi-slice EPI are applied, is evident from the plots shown in Figs. 7.5 and 7.10, respectively. This similarity underlies the large reduction in the artefact voltages which are produced when RLAS is applied (Figs. 7.10-7.12). Figure 7.12 shows clearly that MA produced by random movements, which cannot be corrected using post-processing methods, are greatly reduced (30 dB attenuation) by RLAS, while Figs. 7.10 and 7.11 show that RLAS also greatly attenuates the GA. The residual GA in the RLAS data shown in Figs. 7.10 and 7.11 indicate that the cancellation is not perfect, but it is evident from these figures that the peak artefact is reduced by more than an order of magnitude by application of RLAS. Quantitative analysis of the data from Experiment 3a shows that  $AAS_{GA}$  slightly outperforms

RLAS in attenuating the GA produced when the phantom is stationary (26 dB vs 24 dB). The conditions of Experiment 3a form an ideal basis for the implementation of  $AAS_{GA}$ , since the GA is expected to be highly reproducible across repeated acquisitions in a stationary phantom. However the largest attenuation of the GA (41 dB) was produced when  $AAS_{GA}$  was applied in conjunction with RLAS, indicating that the residual artefacts remaining after RLAS are stable across repeated image acquisitions. These artefacts most likely result from small differences in the voltages induced in the reference layer compared with those appearing at the surface of the spherical phantom and also from the effect of small differences in the paths followed by the leads joining the two electrodes to the star-quad cable. This is expected given the results of Chapter 6 and the preliminary experiment presented in this chapter. The greater reduction in GA produced by using RLAS and  $AAS_{GA}$  together compared with the use of  $AAS_{GA}$  alone, implies that there are some GA contributions which vary across repeated acquisitions, but which are similar in the reference layer and scalp channels. Such artefacts could arise from small movements of the phantom in the static field resulting from gradient coil vibrations.

When the phantom was moved during multi-slice EPI acquisition (Experiment 3c) the performance of  $AAS_{GA}$  was compromised, with the artefact attenuation reducing from 16 dB for the case where one small movement was made during the course of the 140 s recording to a value of 3 dB when three large movements occurred (Fig. 7.13). This failure of  $AAS_{GA}$  results from changes in the GA waveform resulting from changes in the position of leads and electrodes in the applied field gradients, which mean that an average artefact template does not provide a good representation of individual artefact occurrences. In addition, the large, variable MA corrupts the average artefact template and leaves residual variance in the signal. In contrast, the performance of RLAS is relatively insensitive to the degree of movement, yielding a reduction of more than 20 dB over the full range of movements that were employed (Fig. 7.13). The additional artefact attenuation produced by applying AAS after RLAS is reduced as the degree of movement increases, presumably because the residual artefacts after application of RLAS are also sensitive to the positions of the lead and electrode pairs in the applied field gradients. However even when the phantom was moved three times in the 140 s acquisition yielding electrode displacements of up to 7 mm, it was still possible to attenuate the artefacts by 25 dB using RLAS in combination with  $AAS_{GA}$ . This is a

significant improvement compared with the 3 dB attenuation which the application of AAS<sub>GA</sub> alone yielded from these data.

The results of Experiment 3d in which recordings were made from a spherical phantom containing a current dipole while the multi-slice EPI sequence was executed and the phantom was moved indicate that even in the presence of large GA and MA, RLAS is able to reveal the temporal evolution of a 11 Hz signal of  $\sim 50 \mu\text{V}$  peak to peak amplitude from the embedded dipole (Fig. 7.14). Whilst AAS<sub>GA</sub> also preserves the oscillatory 11 Hz signal it leaves residual artefacts across a broad frequency spectrum, so that it is possible to identify the signal from the dipole in the spectrum, but not in the time domain (Fig. 7.14). When making *in vivo* measurements of rhythmic neuronal activity, which typically span a broader frequency range and have lower amplitude than the signal from the current dipole, the residual artefacts after AAS are likely to dominate in the time domain and may make it difficult to identify the signal of interest in the frequency domain as well. This is demonstrated in Figure 7.17, where, whilst it is possible to identify activity in the alpha band (enhanced by the subject closing their eyes) the amplitude of this activity suggests that if the frequency of interest was in the delta band ( $< 4$  Hz) then the residual MA and PA in data corrected using AAS only would most likely swamp the neuronal signals. It is important to reiterate the point first made in Chapter 3, Section 3.2, that, using standard methods of artefact correction it is generally not possible to recover brain signals from EEG data recorded during a period of significant head motion. Here, however, we have demonstrated that with the application of RLAS-AAS<sub>GA</sub> the underlying signals can be recovered (Fig. 7.14). In future EEG-fMRI studies this could have the benefit of reducing the number and duration of epochs where brain signals are inaccessible and could also reduce the occurrence of movement-induced spurious correlations between EEG and BOLD signals that have previously been reported (Jansen *et al.*, 2012).

The measurements on human subjects show that RLAS also significantly attenuates MA and GA in the more complex situation where the reference layer must replicate the artefact voltages induced in the heterogeneous volume conductor formed by the human head and where the reference layer no longer has a simple hemispherical shape. Figure 7.10 shows that the artefacts recorded from scalp electrodes when time-varying gradients are applied, or head movements occur, are still very similar to those recorded from the corresponding reference

layer electrodes. Taking the difference of these recordings in RLAS thus significantly attenuates the MA and GA. Analysis of the data recorded from the stationary subjects (Experiment 4c) showed slightly different relative performances of the different artefact correction approaches compared with the data from the phantom: in the human subjects, the GA was better corrected by RLAS (15 dB attenuation) than AAS<sub>GA</sub> (11 dB attenuation), but RLAS-AAS<sub>GA</sub> (25 dB attenuation) still provided the best result. The better performance of RLAS compared with AAS<sub>GA</sub> in the human data, most likely results from the effect of small involuntary movements of the subject's head, including those due to pulsatile blood flow (Mullinger *et al.*, 2013). These cause small MA that cannot be corrected by AAS and also produce slice-to-slice variation of the GA that confounds the operation of AAS<sub>GA</sub>. The results of Experiment 4d (Fig. 7.13B) indicate that the performance of RLAS in reducing the signal variance in the presence of MA and GA is also better than that of AAS<sub>GA</sub> in the presence of cued head movements, and in addition the performance of AAS<sub>GA</sub> degrades as the degree of movement increases, while the attenuation achieved by using RLAS or RLAS-AAS<sub>GA</sub> is similar for the cases where the subject makes 1 or 3 movements. Figure 7.13 also shows that in general the fractional reduction of the mean RMS voltage that was produced by using RLAS was less in the human data than recordings from the phantom. This is in part because of the presence of other sources of signal variance, including voltages from brain activity, which also affect the fractional reduction produced using AAS, but may also reflect greater differences between the gradient and movement artefact voltages induced in the human head and head-shaped reference layer compared with those occurring in the model system formed by the hemispherical reference layer and homogenous spherical phantom.

The data shown in Fig. 7.15 indicates that RLAS can reduce the peak to peak amplitude of the PA by more than a factor of four and also reduces the standard deviation of the PA across cardiac cycles by about a factor of 10. Since it is the variability of the PA, which often causes problems with its correction in EEG-fMRI experiments, this finding promises significant benefit from use of RLAS in future studies. Overall, these measurements are consistent with the idea that the dominant source of the PA is cardiac-pulse-driven head movement (whose effect can be cancelled using RLAS) rather than Hall voltages due to blood flow in the strong static field (which will not be affected by RLAS) (Yan *et al.*, 2010; Mullinger *et al.*, 2013). In addition, the fact that the reduction of the standard deviation of the PA across cardiac cycles due to RLAS is larger than the reduction of the average magnitude of the PA implies that the

artefact voltages due to cardiac-pulse-driven head movements contribute disproportionately to the variability of the PA.

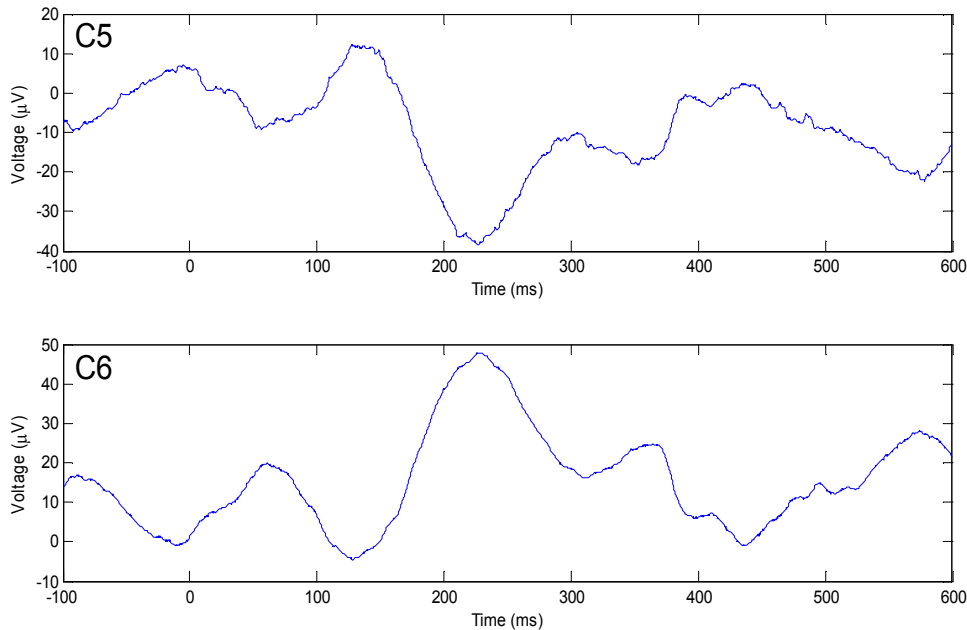


**Figure 7.18** Average PA on channels C5 and C6 from 120 cardiac cycles for Subject 1 when using a conventional 64 channel EasyCap EEG cap and same 3 T MR scanner used for acquisition of the reference layer EEG data shown in Figure 7.15. 0 ms denotes time of R-peak.

As described in Chapter 3, there can be large differences in the PA between subjects and indeed there were differences in the PA waveforms that were recorded on the two subjects. It is interesting to note that the temporal form of the PA shown in the raw data recordings in Fig. 7.15 is quite different from that previously reported (Debener *et al.*, 2008) and its amplitude is also larger than in previously reported 3 T data. To evaluate the differences of PA recorded using a conventional cap and the RLAS set-up, EEG data were collected from Subject 1 using a conventional 64 channel EasyCap EEG cap. The resulting data from electrodes C5 and C6 (whose positions are most similar to the electrode positions used in the RLAS set-up) are shown in Figure 7.18 and are clearly very different in form compared with the PA shown in Figure 7.15. This difference in the temporal form of the PA compared with that found in recordings made using a conventional cap was seen on both subjects. A similar pattern of differences between the right- and left-sided channels was seen in the PA for Subject 2 as well. These results lead us to suggest that the differences in the PA recorded from the scalp with the reference layer set-up are due to the wire paths. There is a significant difference between the lead paths used here and those which are employed in most EEG-

fMRI experiments with commercially available EEG caps. The standard arrangement has the leads running over the surface of the head in a generally superior direction (as shown in Chapter 4, Figure 4.4A), starting from the electrodes and coming together in a cable bundle at the crown of the head, while in our RLAS experiments the leads ran in an inferior direction from the electrodes and left the scalp on the left or right side of the head depending on the location of the electrode (Figure 7.6C). The voltages induced in the leads by head movements and pulse-driven scalp expansion and are likely to be quite different for these two arrangements and when combined with flow-induced Hall voltages could produce very dissimilar PA waveforms.

Figure 7.16 shows that applying  $AAS_{PA}$  to the RLAS- $AAS_{GA}$  data produces an additional significant reduction of the pulse artefact, implying that the residual PA in the RLAS data, which most likely arises from flow-induced Hall voltages, is consistent across cardiac cycles. Applying average artefact subtraction for PA and GA correction to the RLAS data from the stationary subject (Fig. 7.16) produces an overall 27 dB attenuation of the RMS voltage. This is a significant reduction of the signal variance, but less than the 41 dB reduction which could be achieved in similar data from the stationary spherical phantom. This difference is most likely due to the contribution of brain signals to the RMS voltage. The greater reduction of artefact voltages that can be produced when RLAS is used in conjunction with AAS compared with use of AAS alone is particularly evident in the  $< 4\text{Hz}$  frequency range in the data shown in Fig. 7.17. This mainly results from the additional attenuation of the PA and MA that the use of RLAS provides.

A small component of the GA is known to result from the RF pulses that are applied during MRI (Spencer *et al.*, 2012). This contribution to the GA would have been present in the data recorded from the phantom, but not in the data acquired from the human subjects, as the RF pulses were not applied in these experiments. Since the artefact reduction produced by applying RLAS to the data from the phantom was excellent, we have no reason to believe that the performance of RLAS on data recorded from human subjects would be compromised by the presence of small RF pulse artefacts. However, further subject studies involving EPI acquisitions with the RF pulses enabled are needed to test this expectation, which will be discussed in more detail in Chapter 8.



## 7.9 Conclusion

In conclusion we have shown that the RLAS technique is a viable method by which to remove artefacts in EEG data during simultaneous fMRI with no signal loss or distortion of the neuronal signals of interest. We have shown that the RLAS system built here performs better than the fEEG system previously developed and that system design is very important for performance. We have also shown that RLAS generally outperforms AAS in the removal of the GA and PA when motion is present and that using AAS in conjunction with RLAS produces the highest attenuation of artefacts. In addition we have demonstrated the power of RLAS in removing MA, which generally cannot be corrected using post-processing methods, because their occurrence is unpredictable and they are highly variable in their temporal and spatial form. Therefore this proto-type system shows great promise and should be developed further, as discussed in more detail in Chapter 8.

## 7.10 References

- Adrian, E. D. and Matthews, B. H. C. (1934). "The Berger rhythm: potential changes from the occipital lobes in man." Brain **57**: 355-385.
- Allen, P. J., Josephs, O. and Turner, R. (2000). "A Method for removing Imaging Artifact from Continuous EEG Recorded during Functional MRI." Neuroimage **12**(2): 230-239.
- Allen, P. J., Poizzi, G., Krakow, K., Fish, D. R. and Lemieux, L. (1998). "Identification of EEG Events in the MR Scanner: The Problem of Pulse Artifact and a Method for Its Subtraction." Neuroimage **8**(3): 229-239.
- Becker, R., Ritter, P., Moosmann, M. and Villringer, A. (2005). "Visual Evoked Potentials Recovered From fMRI Scan Period." Human Brain Mapping **26**: 221-230.
- Bencsik, M., Bowtell, R. and Bowley, R. M. (2007). "Electric fields in the human body by time-varying magnetic field gradients: numerical calculations and correlation analysis." Phys. Med. Biol. **52**: 1-17.
- Bonmassar, G., Purdon, P. L., Jaaskelainen, I. P., Chiappa, K., Solo, V., Brown, E. N. and Belliveau, J. W. (2002). "Motion and ballistocardiogram artifact removal for interleaved recording of EEG and EPs during MRI." NeuroImage **16**(4): 1127-1141.
- Debener, S., Mullinger, K. J., Niazy, R. K. and Bowtell, R. W. (2008). "Properties of the ballistocardiogram artefact as revealed by EEG recordings at 1.5, 3 and 7 Tesla static magnetic field strength." International Journal of Psychophysiology **67**(3): 189-199.

- Dunseath, W. J. R. and Alden, T. A. (2009). Electrode Cap for Obtaining Electrophysiological Measurement Signals from Head of Subject, has Measurement Signal Electrodes Extended through Electrically Conductive Layer and Insulating Layer for Contacting Head of Subject. USA. US 2009/0099473.
- Freyer, F., Becker, R., Anami, K., Curio, G., Villringer, A. and Ritter, P. (2009). "Ultra-high-frequency EEG during fMRI: Pushing the limits of imaging-artifact correction." *Neuroimage* **48**(1): 94-108.
- Jansen, M., White, T. P., Mullinger, K. J., Liddle, E. B., Gowland, P. A., Francis, S. T., Bowtell, R. and Liddle, P. F. (2012). "Motion-related artefacts in EEG predict neuronally plausible patterns of activation in fMRI data." *Neuroimage* **59**(1-3): 261-270.
- Mandelkow, H., Halder, P., Boesiger, P. and Brandeis, D. (2006). "Synchronisation facilitates removal of MRI artefacts from concurrent EEG recordings and increases usable bandwidth." *Neuroimage* **32**(3): 1120-1126.
- Moosmann, M., Schonfelder, V. H., Specht, K., Scheeringa, R., Nordby, H. and Hugdahl, K. (2009). "Realignment parameter-informed artefact correction for simultaneous EEG-fMRI recordings." *Neuroimage* **45**(4): 1144-1150.
- Mullinger, K. J., Brookes, M. J., Geirsdottir, G. B. and Bowtell, R. (2008). Average gradient artefact subtraction: the effect on neuronal signals. Human Brain Mapping, Elsevier, Melbourne.
- Mullinger, K. J., Castellone, P. and Bowtell, R. W. (2013). "Best current practice for obtaining high quality EEG data during simultaneous fMRI." *Journal of Visualized Experiments (JoVE)*.
- Mullinger, K. J., Havenhand, J. and Bowtell, R. W. (2013). "Identifying the sources of the pulse artefact in EEG recordings made inside an MR scanner." *Neuroimage* **71**: 75-83.
- Mullinger, K. J., Morgan, P. S. and Bowtell, R. W. (2008c). "Improved Artefact Correction for Combined Electroencephalography/Functional MRI by means of Synchronization and use of VCG Recordings." *Journal of Magnetic Resonance Imaging* **27**(3): 607-616.
- Mullinger, K. J., Yan, W. X. and Bowtell, R. W. (2011). "Reducing the Gradient Artefact in Simultaneous EEG-fMRI by Adjusting the Subject's Axial Position." *NeuroImage* **54**(3): 1942-1950.

- Robjohns, H. (2009). "What's special about star-quad cable?". Retrieved on 12 Jun, 2011, from [http://www.soundonsound.com/sos/nov09/articles/qa1109\\_4.htm](http://www.soundonsound.com/sos/nov09/articles/qa1109_4.htm).
- Spencer, S. G., Mullinger, K. J., Peters, A. and Bowtell, R. W. (2012). Modelling and Removing the Gradient Artefact using a Gradient Model Fit (GMF). Proc. Intl. Soc. Mag. Reson. Med. 20, Abstract#2083, Melbourne.
- Yan, W. X., Mullinger, K. J., Brookes, M. J. and Bowtell, R. W. (2009). "Understanding Gradient Artefacts in Simultaneous EEG/fMRI." Neuroimage **46**(2): 459-471.
- Yan, W. X., Mullinger, K. J., G.B., G. and Bowtell, R. W. (2010). "Physical Modeling of Pulse Artefact Sources in Simultaneous EEG/fMRI." Human Brain Mapping **31**: 604-620.

# Chapter 8

---

## *Conclusion*

## **8.1 Summary**

The work described in this thesis was directed towards developing and applying novel techniques to reduce the EEG artefacts at source during the simultaneous acquisition of EEG-fMRI. This involved obtaining a detailed understanding of the different artefacts produced in simultaneous EEG-fMRI recordings that currently prevent an in-depth exploration of the neural activity measured over all frequency bands.

The premise behind using EEG and fMRI techniques to study brain function and the relative advantages and disadvantages of these methods and the complementary information which the two techniques provide are explored in Chapter 2. The difficulties of combining EEG and fMRI are discussed in Chapter 3 with particular attention given to the sources of artefact in the EEG data in combined EEG-fMRI experiments and current methods for overcoming these problems. The periodicity of artefact voltages from the MR gradients and cardiac pulsation makes it possible to remove the majority of these artefacts from the EEG data. Unfortunately subject movement and any form of temporal instability of the artefact waveforms lead to failure of the artefact correction procedure and consequently the presence of large residual artefact signals after correction. Chapter 4 summarizes the best current practice for implementing combined EEG-fMRI experiments based upon the findings of various research groups. This chapter highlights the best possible characterization of the spatial distribution and expected temporal characteristics of the EEG artefacts along with the highest achievable EEG data quality possible with these current methods.

Chapter 5 introduces experimental work exploring the effects of the cable configuration on the characteristics of the GA. This work demonstrates that the artefacts induced in a ribbon cable are much larger and more sensitive to movement than those produced in a twisted cable. These results highlight the importance of ensuring the ribbon cable is fixed in a way that decouples it from subject movement and MR scanner vibrations when performing EEG-fMRI experiments. If this is not possible, a twisted cable should be used to attach the EEG cap to the amplifier. These measures ensure a reduction in the variation of the GA during an fMRI data acquisition, which is highly advantageous since residual GA can easily swamp brain signals. The work described in Chapter 5 also demonstrates how the presence of the ribbon cable when considered in conjunction with the EEG cap may actually be advantageous in reducing the GA artefact due to the interaction of the artefacts induced in the two sections

of the hardware and therefore, with a carefully designed setup, could either prevent saturation of amplifier channels and/or reduce the required dynamic range of the amplifier.

There are still significant limitations on the frequency bands and low-voltage signals which can be investigated confidently using simultaneous EEG-fMRI. Available post-processing methods are not suited to removal of artefacts related to motion. New methods are required to reduce the amplitude and the variability of the EEG artefacts at source with the aim to minimise residual artefacts after post-processing. Chapter 6 explores the theoretical efficacy of artefact correction that can be achieved by using a new method, Reference Layer Artefact Subtraction (RLAS). This is done via analysis of the results of electromagnetic simulations of the artefacts induced in a hemispherical reference layer and a spherical volume conductor by time-varying magnetic field gradients. A series of simulations were carried out to find the optimal reference layer configuration thus providing an insight into the best EEG cap design for a practical RLAS system. This chapter shows that the optimal set-up for an RLAS system has a reference layer thickness = 3 mm, insulation layer thickness = 1 mm, reference layer angular extent =  $88^\circ$  with no RLAS system rotation and 1 cm shift to the left and 2 cm shift in the anterior direction of the whole RLAS system from iso centre. The simulations indicated that with this set-up, RLAS could produce a 41dB attenuation of the voltages induced in the model spherical conductor conduction by an applied transverse gradient. This simulation work suggests that RLAS is a viable method for removing artefacts in EEG data during simultaneous fMRI, and that the RLAS approach should therefore be experimentally tested.

Chapter 6 describes the investigation of the feasibility of implementing an RLAS system experimentally for reducing EEG artefacts in simultaneous EEG-fMRI. Chapter 7 explores the development of an experimental RLAS set-up in which gradient, movement and pulse artefacts could be simultaneously recorded on the scalp and on a reference layer. This allowed experimental testing of the efficacy of artefact correction that can be achieved using RLAS. A preliminary experiment showed that the use of star-quad cable can give an additional advantage in designing the reference layer based artefact correction system. The prototype RLAS system built in this work performs better than the fEEG system previously developed. The results of the series of experiments carried out using the prototype system indicate that RLAS forms a viable method for attenuating the EEG artefacts at source that are generated by time-varying magnetic field gradients, cardiac pulsation and head movements. The results also demonstrate that RLAS can be used in conjunction with post processing

artefact correction methods such as AAS further to attenuate gradient and pulse artefacts and that the use of RLAS does not confound the recording of brain signals. RLAS can reduce the peak-to-peak amplitude of the PA by more than a factor of four and also reduces the standard deviation of the PA across cardiac cycles by about a factor of 10. It is generally not possible to recover brain signals from EEG data recorded during a period of significant head motion using standard methods of artefact correction. RLAS can significantly attenuate MA and GA in the more complex situation of artefact induction in the heterogeneous volume conductor, namely the human head. Employing the RLAS technique could therefore reduce the occurrence of movement-induced spurious correlations between EEG and BOLD signals. The results obtained using this prototype RLAS system show great promise and imply that the RLAS approach should be developed further.

## 8.2 Future Work

Although the focus of the research presented in Chapter 7 has been the quality of the EEG recording produced using the RLAS approach, it is also important to note that the reference layer set-up used here does not necessarily compromise the quality of the fMRI data. The conductivity of the reference layer used in this experimental work is similar to that of brain tissue and so its addition does not produce any significant additional RF screening effects. The lead pairs and electrodes can also potentially be made of similar material to that used in current MR-compatible EEG systems and so would be expected to produce similar, minimal levels of RF and static field inhomogeneity. In the studies reported here, we used commercially available star-quad cable to form the lead pairs and since the configuration we employed had not been fully tested for RF heating effects (Mullinger *et al.*, 2008d), the RF pulse amplitude was set to zero in the recordings made on the human subjects so as to avoid any risk of heating: the impact of any MR artefacts due to RF has thus not been tested in the work described in this thesis. A full evaluation of RF heating and effects on MR image quality will be carried out in future as part of the development of an improved reference layer set-up.

For the work described in this thesis, a unipolar EEG amplifier with a common reference was used, so as to allow the artefact voltages from the reference layer and scalp electrodes to be separately recorded and analysed. This meant that the maximum difference in voltage between the reference channel amplifier input and the inputs associated with all other

electrodes had to be kept less than the amplifiers' dynamic range (32 mV). Consequently we used a multi-slice EPI sequence with a relatively coarse resolution when generating GA and also used a conservative, 250 Hz low-pass filter setting, to ensure that there was no clipping of signals. However, it is also possible to use the reference layer approach in conjunction with bipolar EEG amplifiers that are configured to measure the voltage differences between each reference layer and scalp electrode pair. Since the artefact voltages appearing on the inputs linked to the reference layer and scalp electrodes will be very similar for each lead-pair of the RLAS set-up it would be possible to reduce the dynamic range required of the amplifiers compared with current MR-compatible EEG systems, and also to open up the bandwidth of the system to allow recording of high frequency electric signals from the brain (Freyer *et al.*, 2009) without causing saturation of the amplifier due to the increased peak amplitudes of the GA.

The work described in Chapter 7 has demonstrated the benefits in artefact reduction that RLAS can provide, but clearly for these benefits to be widely realised, it will be necessary to devise a more robust reference layer arrangement that is also easier to use. This will require the use of a reference layer material that is tougher than saline-doped agar, but which still has a similar conductivity to tissue. Carbon-fibre-loaded rubber and hydrogel form two candidate materials but it is necessary to ensure the chosen material used does not cause any RF shielding effects. In addition the electromagnetic simulation work, described in Chapter 6, indicates how the geometry and shape of the reference layer affect the similarity of the artefact voltages induced in the reference layer and scalp. This work will guide the design of the more robust optimal reference layer configuration in future.

The reference layer, used in the experiments discussed in Chapter 7, was a solid, thin, electrically conducting layer. The solid reference layer provides some practical difficulties in attaching the EEG cap to the scalp and working on reducing impedances once the reference layer is in place. In addition the solid layer causes substantial difficulties in channelling the cables from the electrodes away from the head, with this problem likely to increase with the addition of more EEG channels that is required to make a full EEG cap. However if the reference layer could be formed from a mesh rather than a solid hemisphere then the set-up of the cap on the subject's head would potentially be easier and the wires could come away from the head quicker reducing the chances of a safety problems occurring. A mesh reference layer would have the additional advantage that due to the reduction in conductive material



present the potential, for RF shielding effects from this layer would be reduced. However, it is not known whether a meshed hemispherical layer could replace a solid hemispherical layer and still experience the same induced artefacts due to the MR gradients and therefore produce the same artefact reduction via RLAS as shown in Chapter 7. Preliminary simulation work has been done to measure the potential induced in a meshed hemisphere on the top of a conducting sphere and to compare these results with those presented for a solid hemispherical layer overlaid on a sphere presented in Chapter 6. The results from these simulations are promising, as shown in Figure 8.1, and suggest it may be possible to use a mesh reference layer in the RLAS setup.

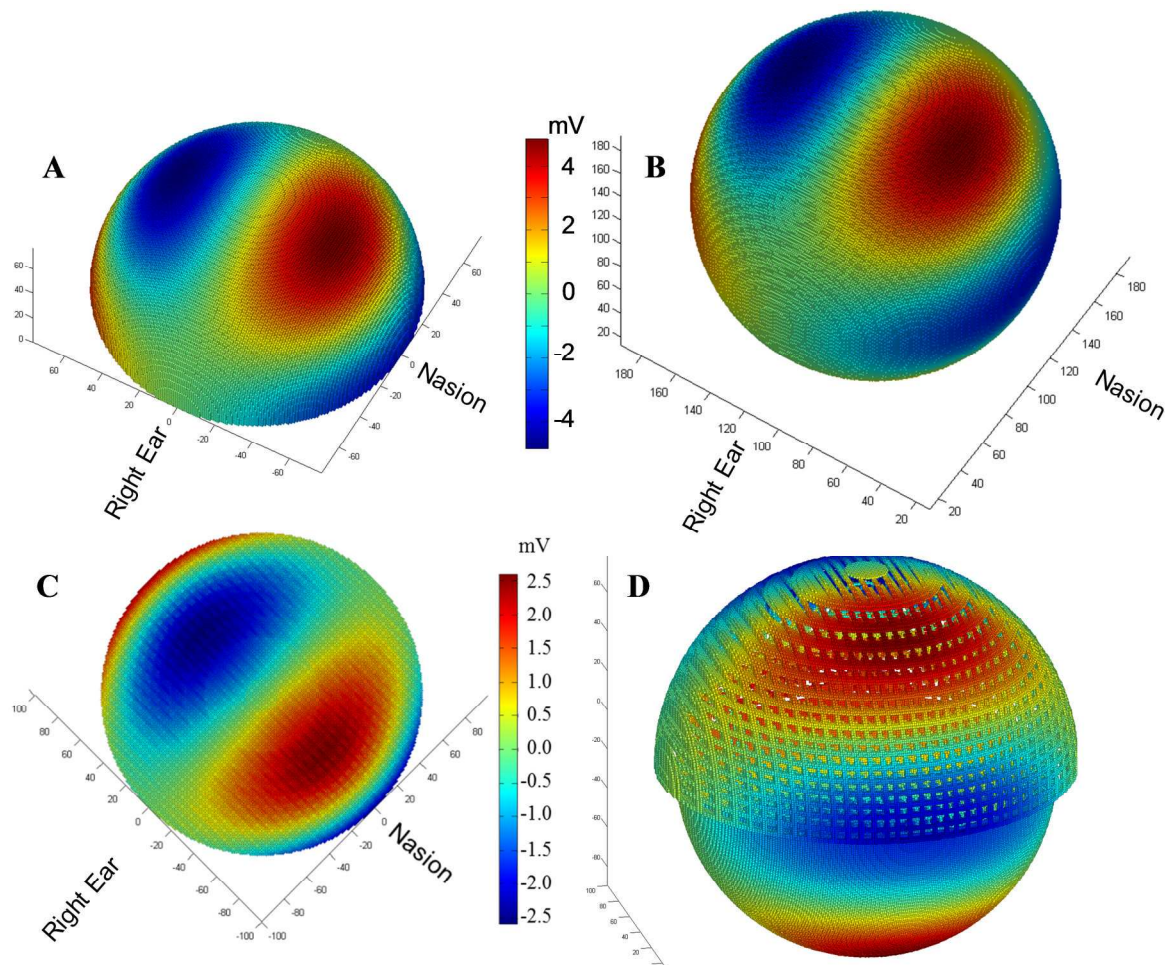


**Figure 8.1** Potential distribution due to a time-varying a transverse magnetic field gradient for a solid hemi-spherical conducting reference layer (A), a conducting sphere (B) and hemispherical conducting mesh reference layer overlaid on sphere, top view (C) and front view (D).

The simulation results described in Chapter 6 show that there is a significant difference in the induced voltages on the volume conductor and reference layer if there is a significant gap between these two conductors. With the current RLAS set-up, shown in Chapter 7, practical

limitations meant that the separation between the two conductors is approximately 7 mm due to the thickness of the electrodes used and the separation of these by the insulating layer. To minimize the separation between the electrodes, it is important to design a new set of electrodes in which the reference layer and scalp electrodes will not be separate, but rather a single entity incorporating a thin insulation layer. A possible set-up for the electrodes is shown in Figure 8.2.

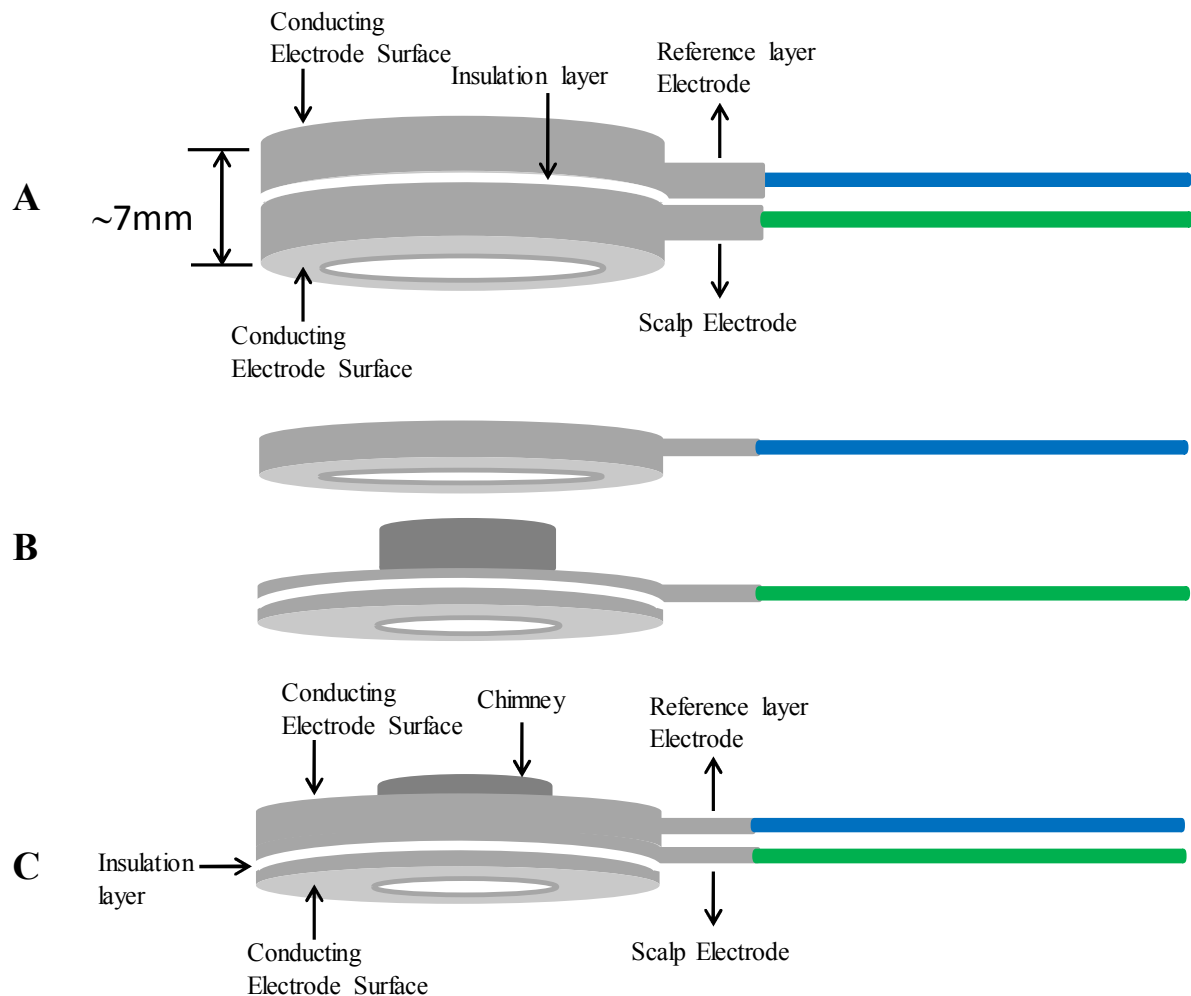


**Figure 8.2** Schematic representation of the current overlaid electrode pair (A) and scalp electrode (with chimney to put gel on scalp) and reference layer electrode shown separately (B) and electrodes after combining as one unit (C).

It is evident from previous simulation work (Yan *et al.*, 2009; Yan *et al.*, 2010) and the experimental work shown in Chapter 5 of this thesis that the cable tree running from the electrodes and the ribbon cable running from the break-out box to the amplifier both produce a significant contribution to the total MR gradient and motion artefact induced. This work therefore indicates that it would much better, if possible, to remove the metallic cabling from inside the MR bore and replace this arrangement with an optical fibre arrangement. In this

case, there would not be any issue of wire movement which produces a significant contribution to the residual gradient and motion artefacts in the EEG data. However, the challenging task is recording and amplifying the tiny brain signals and then converting this signal from the electrical domain to the optical domain on the EEG cap. Here, the challenge is making an electronic circuit, which does not contain any ferromagnetic components and at the same time does not distort the MR images. An additional challenge would be coupling the signal to the fibre which will carry the signal. Although it seems very challenging in implementation, it could provide a break-through in EEG signal recording for simultaneous EEG-fMRI.

### 8.3 Concluding Remarks

Successful implementation of simultaneous EEG-fMRI allows an investigator to take full advantage of these complementary imaging techniques, with the high spatial resolution of the fMRI and the superior temporal resolution of the EEG. The RLAS technique is shown here as a viable novel method of attenuating EEG artefacts at source during simultaneous fMRI with no signal loss or distortion of the neuronal signals of interest and the ability to apply post-processing methods to the data collected with this system. RLAS therefore provides the potential to enable us to better detect neuronal activity during simultaneous EEG-fMRI and consequently it will help in increasing our understanding of neurovascular coupling and brain function.

### 8.4 References

- Freyer, F., Becker, R., Anami, K., Curio, G., Villringer, A. and Ritter, P. (2009). "Ultrahigh-frequency EEG during fMRI: Pushing the limits of imaging-artifact correction." Neuroimage **48**(1): 94-108.
- Mullinger, K. J., Debener, S., Coxon, R. and Bowtell, R. W. (2008d). "Effects of simultaneous EEG recording on MRI data quality at 1.5, 3 and 7 tesla." International Journal of Psychophysiology **67**: 178-188.
- Yan, W. X., Mullinger, K. J., Brookes, M. J. and Bowtell, R. W. (2009). "Understanding Gradient Artefacts in Simultaneous EEG/fMRI." Neuroimage **46**(2): 459-471.
- Yan, W. X., Mullinger, K. J., Geirsdottir, G. B. and Bowtell, R. W. (2010). "Physical Modeling of Pulse Artefact Sources in Simultaneous EEG/fMRI." Human Brain Mapping **31**: 604-620.

## **Publications of Author**

### **Articles in Journals:**

1. **M. E. H. Chowdhury**, Karen J. Mullinger, Paul M. Glover, Richard W. Bowtell, “**Reference Layer Artefact Subtraction (RLAS): a novel method of minimizing EEG artefacts during simultaneous fMRI**”, Neuroimage, 2014; 84C:307-319.
2. Bulbul Ahmed, Arif Ul Alam, Md. Abdullah-Al-Mamun, **Md. Enamul Hoque Chowdhury** and Tamnun E Mursalin “**Analysis of Visual Cortex Event Related FMRI Data using ICA Decomposition**” in the International Journal of Biomedical Engineering and Technology, Inderscience Publications, Vol-7(4), 2011, P. 365-376.
3. Md. Shafiul Islam, Saadia Binte Alam, Rabeya Ferdousy, **Md. Enamul Hoque Chowdhury**, “**Analysis of morphological brain change of Alzheimer disease (AD) patients**” in the Canadian Centre of Science and Education, Vol. 2(II), Nov, 2010, p. 148-155.
4. [Prepared] **M. E. H. Chowdhury**, Karen J. Mullinger, Richard W. Bowtell, “**Simultaneous EEG-fMRI: evaluating the effect of the cabling configuration on the gradient artefact**”, Physics in Medicine and Biology, IOP Publishing.

### **Conference Contributions:**

#### **2013:**

##### **ESMRMB 2013**

1. **Chowdhury, M. E. H.**, Karen J. Mullinger, Paul M. Glover, Richard W. Bowtell (2013), “**Reference Layer Artefact Subtraction (RLAS): a novel method of minimizing EEG artefacts during simultaneous fMRI**”, 19th Annual Meeting of the Organization for Human Brain Mapping, Abstract#47935, Toulouse, France.
2. **Chowdhury, M. E. H.**, Mullinger, K. J., Antunes, A., Glover, P.M. and Bowtell, R. W. (2013), “**A novel method of minimizing EEG artefacts during simultaneous fMRI: a simulation study**”, 19th Annual Meeting of the Organization for Human Brain Mapping, Abstract#47937, Toulouse, France.

##### **OHBM 2013**

3. **Chowdhury, M. E. H.**, Karen J. Mullinger, Paul M. Glover, Richard W. Bowtell (2013), “**Reference Layer Artefact Subtraction (RLAS): a novel method of minimizing EEG artefacts during simultaneous fMRI**”, 19th Annual Meeting of the Organization for Human Brain Mapping, Abstract#1242, Seattle, USA.
4. **Chowdhury, M. E. H.**, Mullinger, K. J., Antunes, A., Glover, P.M. and Bowtell, R. W. (2013), “**A novel method of minimizing EEG artefacts during simultaneous fMRI: a simulation study**”, 19th Annual Meeting of the Organization for Human Brain Mapping, Abstract#1783, Seattle, USA.

### ISMRM 2013

5. K. J. Mullinger, **M.E.H. Chowdhury**, R. Bowtell (2013), “**Reducing the gradient artefact in simultaneous EEG-fMRI by adjusting the EEG cap lead configuration**” 21<sup>st</sup> Annual Meeting and Exhibition of the ISMRM, Abstract#2763, Salt lake, USA.

### bcISMRM Symposium 2013

6. **Chowdhury, M. E. H.**, Mullinger, K. J., Antunes, A., Glover, P.M. and Bowtell, R. W. (2013), “**A novel method of minimizing EEG artefacts during simultaneous fMRI: a simulation study**”, 22<sup>nd</sup> British Chapter ISMRM Postgraduate Symposium, Abstract#20, London, UK.

### 2012:

7. **M. E. H. Chowdhury**, K. J. Mullinger, R. W. Bowtell (2012), “**Reference Layer Artefact Subtraction (RLAS): a novel method of minimizing EEG artefacts during simultaneous fMRI**” ERNI-HSF Budapest Meeting 'Brain Oscillations in Health and Disease', Abstract#13, Budapest, Hungary.

### ISMRM 2012

8. **M. E. H. Chowdhury**, K. J. Mullinger, R. W. Bowtell (2012), “**Reference Layer Artefact Subtraction (RLAS): a novel method of minimizing EEG artefacts during simultaneous fMRI**” 20th Annual Meeting and Exhibition of the ISMRM, Abstract#3965, Melbourne, Australia.
9. **M. E. H. Chowdhury**, K. J. Mullinger, R. W. Bowtell (2012), “**Simultaneous EEG-fMRI: Gradient artefact reduction through cabling configuration**” 20th Annual Meeting and Exhibition of the ISMRM, Abstract#2322, Melbourne, Australia.

### bcISMRM Symposium 2012

10. **M. E. H. Chowdhury**, K. J. Mullinger, R. W. Bowtell (2012), “**Reference Layer Artefact Subtraction (RLAS): a novel method of minimizing EEG artefacts during simultaneous fMRI**” 21<sup>st</sup> British Chapter ISMRM Postgraduate Symposium, Abstract#05, Bristol, UK.

### 2011:

11. **M. E. H. Chowdhury**, K. J. Mullinger, R. W. Bowtell (2011), “**Simultaneous EEG-fMRI: Gradient artefact reduction through cabling configuration**” in the preceding of Combining Human Brain Imaging techniques, Abstract#06, Galway, Ireland.

### bcISMRM 2011

12. **M. E. H. Chowdhury**, K. J. Mullinger, R. W. Bowtell (2011), “**Simultaneous EEG-fMRI: Gradient artefact reduction through cabling configuration**” 17th British Chapter ISMRM annual meeting, Abstract#29, Manchester, UK.

### 2010:

13. Rabeya Ferdousy, Anisul Islam Choudhory, **Md. Enamul Hoque Chowdhury** and Subrata Kumar Aditya “**Electrooculographic and Electromyographic Artifacts Removal from EEG**” in the 2010 2nd International Conference on Chemical, Biological and Environmental Engineering (ICBEE 2010), 2-4 Nov. 2010. p. 163-167.